

# MODELING HUMAN BRAIN DISEASES USING PLURIPOTENT STEM CELLS

SHASHINI MUNSHI

THESIS



# **Modeling Human Brain Diseases using Pluripotent Stem Cells**

**Shashini Thischa Munshi**





# **Modeling Human Brain Diseases using Pluripotent Stem Cells**

Het modelleren van humane hersenziektes  
met behulp van pluripotente stamcellen

## **Thesis**

To obtain the degree of Doctor from the  
Erasmus University Rotterdam by  
command of the rector magnificus  
Prof.dr. R.C.M.E. Engels

And in accordance with the decision of the Doctorate Board  
The public defense shall be held on  
Wednesday 6 November 2019, 11.30h

**Shashini Thischa Munshi**

born Tuesday 13 December 1988  
in Schiedam

**Erasmus University Rotterdam**



**promotor**

Prof.dr. S.A. Kushner

**other members**

Prof.dr. Y. Elgersma

Prof.dr. R. Willemsen

Dr. N.N. Kasri

**copromotor**

Dr. F.M.S. de Vrij

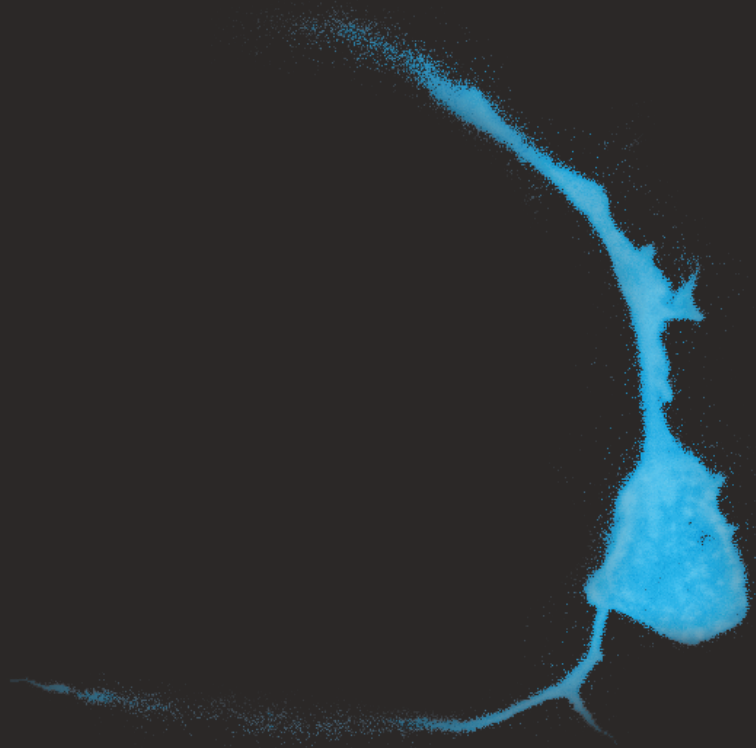
## TABLE OF CONTENTS

Chapter 1	General Introduction	7
Chapter 2	A simplified protocol for differentiation of electrophysiologically mature neuronal networks from human induced pluripotent stem cells	25
Chapter 3	Identification of novel activity-dependent human <i>BDNF</i> transcripts	49
Chapter 4	Subcellular localization of mouse and human UBE3A protein isoforms	75
Chapter 5	Epigenetic characterization of the <i>FMRI</i> promoter in induced pluripotent stem cells from human fibroblasts carrying an unmethylated full mutation.	91
Chapter 6	A functional variant in the miR-142 promoter modulating its expression and conferring risk of Alzheimer's disease	115
Chapter 7	General Discussion	143
	Summary	165
	Samenvatting	167
	PhD Portfolio	169
	Curriculum Vitae	170
	List of Publications	171
	Acknowledgements	172



# Chapter 1

## General Introduction





Well into the 21<sup>st</sup> century, the human brain remains a mystery. Although human brain development follows the same principles as that of all mammals<sup>1,2</sup>, there are clear interspecies differences that ultimately lead towards the unique cognitive and behavioral features of humans<sup>3,4</sup>. Primarily the cerebral cortex is responsible for the higher cognitive, abstract thinking and language capacities humans contain<sup>3,4</sup>.

Humans have an exceptionally long gestational time, childhood and adolescence<sup>2,5-7</sup>. Anatomically the human brain has an extended surface area and the amount of vertical columns in the cortex has increased in number, size and complexity<sup>1,8</sup>. This has resulted in a large change in cell number<sup>9,10</sup>, morphology and composition of brain cells<sup>11,12</sup>.

Genetic differences between humans and our closely related ancestors<sup>9,13-16</sup> and the latest humans to become extinct, Neanderthals and Denisovans<sup>17,18</sup>, are reflected in single-nucleotide variants, insertions, deletions and structural chromosomal rearrangements<sup>18</sup>. The majority of alterations are found in developmental genes and their regulatory regions<sup>18-20</sup>. Especially the latter may have significantly contributed to human brain evolution, as regulatory genes function selectively in cell types and during specific cell cycles, adding extra layers of control of expression<sup>13,18,21,22</sup>.

Nonetheless, human brain evolution and extended life span also appears to have given rise to susceptibility for brain diseases, such as neurodegenerative diseases<sup>23</sup> and psychiatric disorders<sup>24-26</sup>. In humans amongst others the processes of dendritic and synaptic maturation and synaptic pruning are prolonged<sup>27</sup>. This prolonged period links it to various neuropsychiatric disorders and intellectual disabilities<sup>28-30</sup>. Also many genes associated with neuropsychiatric disorders are involved in brain development and its regulation, which contains several human-specific processes<sup>31,32</sup>. Similarly, white matter volume in the prefrontal cortex is disproportionately larger in human brains<sup>33,34</sup>, but progressively declines in the aging brain, linking human oligodendrocyte function to several neurodegenerative diseases<sup>35</sup>.

To shed light on the molecular mechanisms of human brain diseases, studies are commonly performed in animal models, the mouse being highly suitable for its genetic resemblance and ease to work with<sup>2</sup>. Yet, the human brain is over 1000 times larger than the mouse brain<sup>3</sup>, its cortical genesis takes roughly 20 times longer<sup>3</sup>, its cell cycle time is 3-4 times longer<sup>3</sup>, birth occurs during later stages of brain development and postnatal maturation takes longer before reproduction. Also, in development there is compartmentalization of the different neural progenitors and layers, such as a larger transient subplate zone and an outer subventricular zone as well as expanded superficial layers of the cortex. Also human glia are unique and distinctively different from rodent glia<sup>36-38</sup>. They are considerably larger in size, have more elaborate processes and physiology and form more connections.

One way to study particularly human brain development and the cells of the human brain is by using human embryonic stem (hES) cell technology. Human embryonic stem cell technology emerged in the late 1990s. It comprises the use of pluripotent stem cells from pre-implanted embryos. These cells in theory have the capacity to differentiate into the different

cell types that can be found in the human brain. A couple of commonly used hES cell lines are the H1, H9 and H11 lines<sup>39</sup> and protocols to tweak these cells towards the neural lineages appeared soon after their establishment in 1998. Most of these protocols are based on existing procedures to derive neural precursor cells (NPCs) from mouse stem cells<sup>40</sup>. Fundamental studies on human stem cell-derived neural cells though stayed surprisingly limited. A reason for this may have been the ethical and limited disease-modeling capacity of hES cells.

In 2006 Yamanaka et al. published their work on *in vitro* reprogramming of somatic cells towards induced pluripotent stem (iPS) cells<sup>41</sup>. With the overexpression of the four embryonic transcription factors Oct3/4, Sox2, Klf4, and c-Myc in terminally differentiated cell types, somatic cells are driven back to an induced pluripotent state. In many ways, iPS cells are morphologically and transcriptionally similar to hES cells<sup>42</sup>. They have the capacity to differentiate to different germ layers and terminally differentiate towards specific cell types. This has offered a less ethically controversial way to generate human brain cell types and allowed diseasemodeling in which the differentiated neural cells retain the genome of the donor.

## DEVELOPMENT OF THE HUMAN CEREBRAL CORTEX

The question that emerged however is to what extent iPS technology could be applied to study human brain development and model human brain diseases.

Cortical development involves neurogenesis, differentiation, migration, synaptogenesis, and establishment and refinement of connections<sup>4</sup>. In humans it spans early to mid-gestational periods, although myelination takes up to the 2<sup>nd</sup> and 3<sup>rd</sup> decade of life. Human neurodevelopment starts with the formation of the neural tube from the embryonic ectoderm<sup>7,43</sup>. The wall of the neural tube contains a pseudostratified layer of neuroepithelial cells called the ventricular zone (VZ). These cells are the progenitors for all neurons and glial cells (astrocytes and oligodendrocytes) in the brain and spinal cord. Rounds of symmetric division of the neuroepithelial cells which give rise to two identical progenitor daughter cells, each round of replication increasing the pool of neural progenitor cells. Rounds of asymmetric division produce one progenitor cell and one post-mitotic neuron per division. To form the cortical plate, cells radially migrate from the VZ<sup>44</sup>. The cortex is shaped in an inside-out fashion. Neurons residing in deeper layers emerge first and newly generated neurons migrate through these layers to form the more superficial layers<sup>44</sup>.

Every cell in the different layers of the cortex has a distinct transcriptional profile related to its cellular composition and relative maturity. Neurons find their place in the cortex using somal translocation. The neuron extends one process, which is an extension of the cell body beyond the VZ into the outer region. The process then attaches to the pial surface, the outer surface of the brain. Subsequently, the nucleus then moves up the process and migrates out of the VZ. When the brain becomes larger, radial glial (RG) cells serve as guides for migrating



neurons. Their nucleus remains in the VZ and they extend their processes to the pial surface. Migrating neurons use their process as a scaffold to migrate into the brain. RGs themselves also serve as a neural progenitor pool. Next, a second proliferative zone emerges above the VZ, called the subventricular zone (SVZ). These cells give rise to the majority of the glutamatergic neurons within the telencephalon.

During development, several layers are discernable (**Figure 1**)<sup>7,43</sup>. The first neurons that leave the VZ form the preplate (PP). The next wave of migrating neurons splits the PP in the marginal zone (MZ) and the subplate (SP). The neurons that establish between these layers are the first cells of the cortical plate (CP). Both the MZ and the CP are transient layers, and disappear with development. The MZ moreover contains Cajal-Retzius cells, a heterogeneous population of cells that produce reelin, a secreted extracellular matrix protein responsible for migration and positioning of neurons into layers of the neocortex<sup>45</sup>. Subsequently, the SVZ emerges and from the VZ up to the MZ the following layers are present: VZ, SVZ, intermediate zone (IZ), SP, CP, MZ. The VZ and SVZ will eventually reduce to a one-cell-layer thick region and the IZ will develop into a white matter layer above which the 6 layers of the cortex have developed.

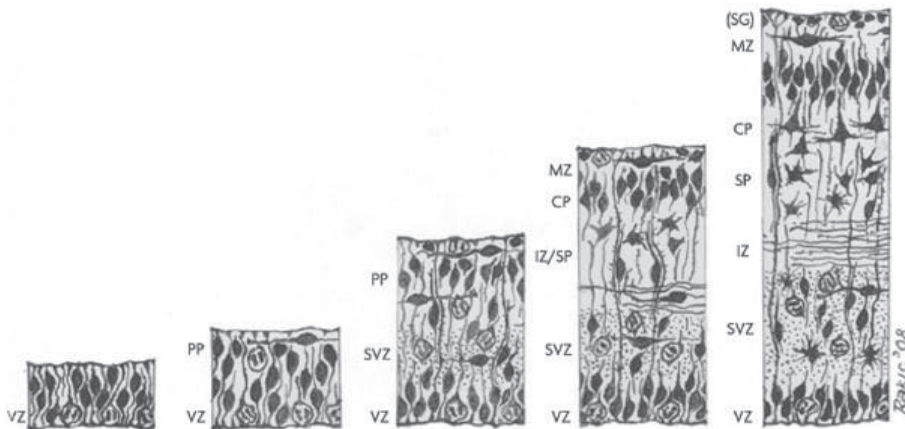


**Figure 1**, schematic model of human neocortical development (adapted from Bystron et al. 2008<sup>43</sup>). CP, cortical plate; IZ, intermediate zone; SP, subplate zone; MZ, marginal zone; SVZ, subventricular zone; (SG), subpial granular layer (part of the MZ); VZ, ventricular zone.

Another proliferative zone in the developing brain is the ganglionic eminence (GE). Here important classes of inhibitory neurons and oligodendrocytes precursor cells (OPCs) are generated. These cells migrate tangentially into the cortex<sup>44</sup>.

Most of the knowledge regarding early brain development is derived from rodents where tracing studies with labeled virus can indicate cell progeny. Limited evidence exists on early human VZ/SVZ development. A few studies however confirm and highlight similarities and dissimilarities between rodents and human VZ development. Most knowledge is obtained by

immunostaining of primary cell cultures and slice cultures from human fetal brains. More recently, with the development of single-cell RNA sequencing technology progenitors and neurons are re- and sub-classified on the basis of their RNA expression next to their immunogenic profile<sup>46</sup>.

## THE VENTRICULAR ZONE

Several groups have described different cell types in the VZ during human brain development. The first cell types to be identified were RG and neuron-restricted progenitors<sup>47–50</sup>. At 4,5 gestational weeks (gw) RG are exclusively present in the VZ<sup>47</sup>. Immunophenotypically, RG are characterized by the expression of glia-specific antigens, such as the intermediate filament vimentin<sup>51</sup> or nestin, astrocyte-specific glutamate transporter (GLAST)<sup>52</sup> and glial fibrillary acidic protein (GFAP)<sup>47,49</sup>. Actively dividing RGs are visualized using the 4A4 antibody, which recognizes vimentin phosphorylated by a mitosis-specific kinase, cdc2 kinase<sup>53</sup>. When RG divide, their cell bodies descend to the ventricular surface to undergo mitosis (interkinetic nuclear migration)<sup>1</sup>. RG serve as a guide for migrating neurons, but eventually develop into neurons, astrocytes or oligodendrocyte precursor cells (OPCs). Occasionally therefore RGs in this stage are also found to express SMI-31, a marker of nonphosphorylated intermediate filament proteins, present in cells of neuronal lineage<sup>47</sup>.

At similar ages neuron-restricted progenitors are also found<sup>47–50</sup>. These are dividing cells that stain positive for neuronal markers such as SMI-31,  $\beta$ -III-tubulin, MAP2 and doublecortin (DCX) and negative for any of the RG markers. They are also present in the pro-encephalon, where no RGs are present<sup>47</sup>.

At 5–6 gw neurogenesis starts in humans<sup>48</sup>. At 5,5 gw mitotically active RG are found about 100  $\mu$ m above the VZ surface<sup>47</sup>. At 6 gw active RGs are found throughout the entire pro-encephalon. Next to this, neurogenic progenitors are found throughout the VZ and SVZ. They are dividing vertically or horizontally with respect to the VZ surface. There is also an actively dividing GLAST<sup>+</sup> and  $\beta$ -III-tubulin<sup>+</sup> population at the ventricular surface, perhaps indicating RG that will develop into neurons.

By 9–10 gw the cortical plate, a layer of 6 cells thick, is visible in the entire telencephalic wall<sup>47</sup>. RG are abundant and dividing. Many also have migrated to the SVZ and IZ. RG are reaching up into the SVZ, the IZ and CP<sup>47</sup>. These RG do not express neuronal and glial markers simultaneously<sup>49</sup>.

That RG become restricted in their fate was also indicated by Mo et al<sup>50</sup>. They isolated RG from 14 and 20 gw VZ/SVZ using immunopanning with CD15, an extracellular matrix-associated carbohydrate<sup>50</sup>. Over 90% of the CD15<sup>+</sup> population co-labeled for one of the following RG markers: BLBP, vimentin or GFAP. Only less than 10% of the CD15<sup>+</sup> co-stained for  $\beta$ -III-tubulin. When clonal cultures of individual CD15<sup>+</sup> cells were analyzed, four types of clones

were discernable: pure GFAP<sup>+</sup> clones, pure MAP2<sup>+</sup> clones, mixed clones with a majority of GFAP<sup>+</sup> cells, and mixed clones with a majority of MAP2<sup>+</sup> clones. More glia were generated in cultures derived from the 20 gw-old VZ/SVZ than from the 14 gw-old VZ/SVZ, indicating that stage differences may play a part in their fate determination.

That the RG population itself is heterogeneous was also confirmed by Howard et al. who studied dissociated cell cultures obtained from VZ/SVZ of 19-22 gw fetuses<sup>47</sup>. Of the total population of dividing cells in culture roughly 30% was vimentin<sup>+</sup> or GFAP<sup>+</sup> and about 15% was GLAST<sup>+</sup>. Many glial cells would simultaneously express several markers. It was unclear though if the expression of different antigens determines RGs ability to develop into either neurons, astrocytes or OPCs or that it is a function of cell differentiation.

Which factors play a part in fate-determination remains largely unknown. One however entails regional cues<sup>50</sup>. Mo et al. co-cultured CD15<sup>+</sup> cells with GE and cortical cells. They showed that CD15<sup>+</sup> cells co-cultured with the GE developed into calretinin<sup>+</sup> interneurons considerably more often than when CD15<sup>+</sup> cells were co-cultured with cortical cells<sup>50</sup>. They also found that growth factors EGF and FGF were higher in cultures containing neurogenic RGs, pointing towards which cues specifically play a role in fate-determination.

At 17-24 gw RG are still dividing but less so than at 9-10 gw<sup>47</sup>. In midgestation RGs are in all compartments of the telencephalon, such as the IZ and the most superficial subpial granule layer. In the VZ some calretinin<sup>+</sup> 4A4<sup>+</sup> cells are visible. They are closely apposed to the RG fibers as if using them as a guide.

By midgestation 20 gw, most of neurogenesis has taken place. RG start to transform into GFAP<sup>+</sup> astrocytes in the intermediate zone and the cortical plate<sup>48</sup>. Occasionally there is mitosis of the RG, but by 23 gw proliferation has finished<sup>49</sup>. An ependymal layer forms on the VZ. Thin GFAP<sup>+</sup> fibers cross it to attach to the VZ surface<sup>49</sup>.

## THE SUBVENTRICULAR ZONE

From 5-6 gw the VZ is the only proliferative zone. At 7-8 gw the SVZ emerges above the VZ<sup>54,55</sup>. Cells that are generated from the ventricular epithelium populate it. Here proliferation continues until the 40 gw-long intra-uterine period. From 10-24 gw the appearance of the SVZ changes because of tangentially incoming fibers from subcortical regions and those crossing the corpus callosum<sup>54</sup>. There are cell fibers visible that stretch to the subplate. The fibers divide the SVZ in the inner (iSVZ) and outer SVZ (oSVZ).

Several classes of progenitors are found in the SVZ<sup>56</sup>. One resembles RG in phosphovimentin, nestin and GFAP expression and is also Pax6<sup>+</sup> and Sox2<sup>+</sup><sup>56</sup>. In contrast to RG though these cells have basal processes extending to the pia, but lack an apical process that is connected to the surface of the VZ. They are termed outer radial glia cells (oRG). In contrast to RG that show interkinetic nuclear migration, these cells show mitotic somal translocation

where the nucleus moves up the basal fiber before cell division. As the cell divides the upper cell inherits the basal process, whereas the lower cell becomes bipolar, generating an oRG and an oSVZ progenitor. This is an example of asymmetric self-renewing division. Both oRG and oSVZ progenitors are able to divide again. The oRG is able to yet again asymmetrically divide, whereas the oSVZ generates two similar daughter cells. This process ensures rapid expansion of the progenitor pool. Hansen et al. also found that daughter oSVZ cells can readapt oRG morphology<sup>56</sup>.

Outer RG develop into excitatory neurons<sup>54-56</sup>. From 7-27 gw  $\beta$ -III-tubulin<sup>+</sup>, PSA-NCAM<sup>+</sup> and MAP2<sup>+</sup> immature neurons are present in the SVZ<sup>56</sup>. TBR-1<sup>+</sup> and glutamate<sup>+</sup> cells are present, labeling projection neurons, which were migrating radially to the upper cortical layers<sup>54</sup>. NeuN<sup>+</sup> and NSE<sup>+</sup> cells are mostly visible away from the SVZ in the subplate, the cortical plate and layer I<sup>54</sup>.

However, from 7-22 gw Zecevic et al. also found GABA<sup>+</sup>, calretinin<sup>+</sup>, and calbindin<sup>+</sup> inhibitory neurons<sup>54</sup>. They had unipolar or bipolar morphology, suggestive of their migration. In slice cultures of 22 gw-old VZ/SVZ a BrdU-incorporation proliferation assay showed that 25% of the BrdU<sup>+</sup> cells expressed *Dlx* and 19% expressed *Nkx2.1*, indicating these cells were progenitors to interneurons. Yet, 55% of the *Dlx*<sup>+</sup> cells and 80% of the *Nkx2.1*<sup>+</sup> were also PDGFR $\alpha$ <sup>+</sup>, an early oligodendrocyte progenitor marker, signifying that in the SVZ progenitors to both interneurons and OPCs are present.

Hansen et al. similarly found progenitors of interneurons. By following division of oRG in real-time and determining daughter cell fate by immunostaining, they showed that daughter cells can start to express TBR-2, an indicator of commitment to the neuronal lineage and newly-born neurons of the excitatory lineage, or ASCL1, a transcription factor to indicate GABAergic fate.

At 25-27 gw the VZ becomes a one-cell-layer thick ependymal layer whereas the SVZ is still present around the lateral ventricle<sup>54</sup>. The subependymal zone contains neural stem cells, which then remain throughout adulthood for repair processes<sup>57</sup>.

## INTERNEURONS

In contrast to rodents, in humans two-thirds of the interneurons are generated in the SVZ<sup>58-64</sup>.

The first-born GABAergic interneurons are generated in the GE in the basal ganglia and migrate tangentially into the CP. The first wave of migration contains pioneer neurons that make up the early PP. These contain different types of cells, including Cajal-Retzius cells. Production of interneurons in the GE is followed by generation of interneurons in the SVZ. In the mature brain several classes of interneurons are found. They are roughly divided by their expression of the neurochemical markers parvalbumin (PV), somatostatin (STT) and serotonin receptor 3A (Htr3a) and are further subdivided based on morphological features,

cellular and subcellular targeting, electrophysiological and synaptic properties as well as expression of other markers<sup>65–67</sup>. This classification is largely based on studies in mice and serves as a starting point for understanding the interneuron diversity in humans.

Several studies shed light on the development of interneurons in the human brain. The GE is the main source of interneurons in early brain development (6–15 gw)<sup>42,50–52</sup>. In mice a regulatory network of the transcription factors *Dlx1*, *Dlx2*, *Ascl1*, *Gsx1* and *Gsx2* is required for the generation of interneurons in the subpallium<sup>70,71</sup>. In humans *Dlx*<sup>+</sup> and *Nkx2.1*<sup>+</sup> progenitors for interneurons are also found and migrate tangentially to the developing neocortex. They develop into calretinin<sup>+</sup> and calbindin<sup>+</sup> interneurons in the deeper layers V and VI of the neocortex<sup>58</sup>. At 15 gw the GE is still the main source of cortical interneurons, as indicated by calretinin labeling<sup>58</sup>. From 16–24 gw however, *Dlx*<sup>+</sup><sup>63</sup>, *Nkx2.1*<sup>+</sup><sup>63</sup>, *Ascl1*<sup>+</sup><sup>60</sup> and *Gsx2*<sup>+</sup><sup>64</sup> populations are also discernable in the VZ/SVZ. These cells regularly co-localize with markers GABA, GAD2 or calbindin. VZ/SVZ RG that are *Pax6*<sup>+</sup> and *BLBP*<sup>+</sup> are also able to produce interneurons<sup>64</sup>. Yu et al. also confirmed the presence of RG that are GABA<sup>+</sup> and calretinin<sup>+</sup><sup>63</sup>.

At midgestatin *Ascl1*<sup>+</sup> cells are also found in the GE. There they co-label with *Dlx*<sup>59,62</sup>. In the VZ however, *Ascl1*<sup>+</sup> and *Dlx*<sup>+</sup> cells do not co-localize, nor do *Ascl1*<sup>+</sup> and *Nkx2.1*<sup>+</sup> cells, indicating distinct populations of precursor interneurons. Also, there was very little overlap between *Ascl1*<sup>+</sup> and calretinin<sup>+</sup> progenitors. *Ascl1*<sup>+</sup> cells however were GABA<sup>+</sup>, so they may give rise to another interneuron subtype. *Ascl1*<sup>+</sup> cells were however sometimes also labeled with PDGFR $\alpha$ , but most of these cells were seen in the cortical plate, especially in the subplate<sup>59</sup>. Its percentage was much lower in the VZ/SVZ. Therefore in midgestation *Ascl1*<sup>+</sup> interneurons and *Ascl1*<sup>+</sup> OPC progenitors are present. There are also *Ascl1*<sup>+</sup> cells that express neither of these markers and therefore they are either not committed to cell fate yet or part of the interneuron and OPC lineage but at time of examining not expressing GABA or PDGFR $\alpha$ .

Neuropeptide Y<sup>+</sup>, somatostatin<sup>+</sup> and parvalbumin<sup>+</sup> interneurons are sparse in midgestation<sup>58</sup> and are generated later in human neurodevelopment.

## GLIAL CELLS: OLIGODENDROCYTES AND ASTROCYTES

Oligodendrocyte lineage cells have the highest turnover in the central nervous system and all ages of the cell are present throughout the brain at all times. OPC development starts in 2<sup>nd</sup> trimester and continues after birth<sup>72,73</sup>. PDGFR $\alpha$ <sup>+</sup> cells are visualized at 10 gw in the forebrain for the first time, but the highest number of these cells is around 15 gw, when they are present mostly in the GE and VZ/SVZ. Cells with similar morphology as PDGFR $\alpha$ <sup>+</sup> cells were often also labeled with NG2-chondroitin sulfate proteoglycans<sup>72</sup>. By midgestation 19–22 gw OPCs invade more dorsal areas as well as the cortical plate. During the majority of development OPCs are most dense in the SVZ. At around 20–22 gw O4<sup>+</sup> and O1<sup>+</sup> OPCs are present in the subplate layer, immediately below the cortical plate. As they mature they start to express MBP

and PLP. The first MBP<sup>+</sup> cells with mature morphology are seen at 18 gw. There is a ventral to dorsal progression of oligodendrogenesis. During development several classes of OPCs are discernable: there is a population that expresses Dlx2, Nkx2.1, present in both GE and VZ, a Dlx2<sup>-</sup> and Nkx2.1<sup>-</sup> class, and a class of OPCs expressing PDGFR $\alpha$ , NG2, Olig1, nestin, and also CD34 and CD68<sup>72,73</sup>. Next to this humans contain a subpopulation of NPCs that are Olig2<sup>+</sup> and Pax6<sup>+</sup> in cryosections of 15-20gw in GE and SVZ, indicating human-specific OPC populations.

Human astrocyte development is mostly unknown. In rodents astrocytes develop from transformation of RG, glial progenitors in the SVZ, glial progenitors in the MZ/layer I or from progenitors in the superficial layers of the cortex<sup>74</sup>. DeAzevedo et al. describes the transition of RG into astrocytes in human brain from 18 to 39 gw<sup>75</sup>. Transition is described by detachment of the ventricular process, followed by detachment of the pial process. However, also pial detachment before ventricular detachment is seen. In the late stages of astrocytes development stellate morphology is discerned. From 38-39 gw astrocytes are bilaminarily distributed. GFAP<sup>+</sup> and vimentin<sup>+</sup> astrocytes are seen in the upper CP and MZ and in the SP/IZ. After detachment of either of the processes, nuclei of the astrocytes migrate radially to their place in the cortex.

Most astrocytes nonetheless are generated after birth<sup>36</sup>. In adult humans four classes of astrocytes are found: protoplasmic astrocytes, interlaminar astrocytes, polarized astrocytes and varicose projection astrocytes<sup>37,38</sup>. It is unclear though how and when these develop.

## MODELING HUMAN NEURAL CELLS WITH IPS CELLS

Regardless of the complexity of the human brain, the generation of neural cell types that resemble bona fide neural cells at the level of RNA, antigen expression and/or functionality have been generated using iPS as cell source.

Most protocols to classically differentiate neural cells from iPS are based on or modified from protocols to generate neural cells from mouse ES or hES cells. The majority of the protocols rely on mimicking the extracellular environment *in utero*<sup>76</sup>. In short, two pathways exist: guiding towards neuroepithelium with growth-factors and morphogens versus dual-SMAD inhibition<sup>76</sup>. In such a way neural progenitor cells (NPCs) are produced. They are then cultured for terminal differentiation into neurons or glial cells<sup>77,78</sup>. Protocols are also available to enrich for specified neurons such as cholinergic<sup>79</sup>, dopaminergic<sup>79</sup>, GABAergic<sup>80</sup> and serotonergic<sup>81,82</sup> populations. By combination of growth factors and mere time, cell populations could also be enriched for astrocytes<sup>83,84</sup>, OPCs<sup>85</sup> and oligodendrocytes<sup>86</sup>.

It became clear that the development *in vitro* was mimicking the order of development *in vivo*<sup>87</sup>. Many neuron-generating protocols show a neural rosette stage resembling neural tube formation<sup>76,88</sup>. This stage recapitulates progenitor zones similar to the VZ and SVZ including

its mixed population of progenitors. *In vitro* emergence of astrocytes and myelination takes place after terminal neuronal division also mimicking *in vivo* neurodevelopment. As a consequence, more so than a model for adult human brain neurons, stem cell-derived neurons *in vitro* represent best first trimester (up to 12gw) human fetal neurons<sup>89,90</sup>, which are generated in at least 6 weeks *in vitro* from a neural progenitor stage<sup>91</sup>. Also, certain protocols recapitulate some structures of second trimester brain development<sup>92</sup>. As such, next to modeling specific cell types, human iPS technology allows modeling early human brain development<sup>93</sup>.

Enhanced maturation is seen by using 3D culturing techniques<sup>92,94,95</sup>. Combinations of growing iPS in gels and scaffolds<sup>96</sup>, or the self-organizing capacity of iPS in suspension are used to generate adherent 3D neural cultures, or free-floating brain organoids respectively<sup>97</sup>. The 3D environment allows next-level development of structures with enhanced and more mature capabilities<sup>84</sup> and model gene expression programs of fetal brain development<sup>98</sup>. 3D models have come as far as modeling hippocampal and cortical layers<sup>99,100</sup> as well as forebrain, midbrain and hypothalamic structures<sup>92,101</sup>, where further development of the culture is commonly held back by lack of *in vitro* vascularization capacity<sup>99</sup>. However, recently Mansour et al.<sup>102</sup> implanted brain organoids in the mouse brain and showed enhanced development and vascularization, paving the way towards developmental progression of iPS-derived neural models and enhanced understanding of the brain and brain-related disease using iPS-based models.

## SCOPE OF THIS THESIS

In this thesis we explore the use of IPS for modeling human brain development and disease.

In chapter 2 we describe a neural differentiation protocol that produces electrophysiological functional neural networks. This protocol allows for examination of iPS-derived neural networks for disease-related studies.

In chapter 3 we study the transcriptional regulation of human *BDNF*. Using our protocol described in chapter 2 we find novel *BDNF* transcripts in humans that are expressed upon activity of neural cells.

In chapter 4 we study the subcellular localization of mouse and human UBE3A in neurons, the lack of which in neurons causes the neurodevelopmental disorder Angelman Syndrome. We find differential localization of mouse and human UBE3A protein isoforms.

In chapter 5 we study the epigenetic modifications of the *FMRI1* gene. The absence of the *FMRI1* gene product, fragile X mental retardation protein (FMRP), causes the intellectual disability disorder Fragile X syndrome. We find that standard reprogramming procedures lead to epigenetic silencing of the fully mutated *FMRI1* gene also in rare healthy individuals who carry a full mutation of *FMRI1* but show no hypermethylation of the gene's CGG repeats and promoter.

In chapter 6 we study long non-coding RNA (lncRNA) variants associated with Alzheimer's disease (AD). We find an associated variant that mediates regulation of AD-related genes in iPS-derived neural cells.

In chapter 7 I discuss the limitations of iPS technology that influence its capacity to model human brain diseases. I also discuss potential solutions.



## REFERENCES

1. Lui, J. H., Hansen, D. V & Kriegstein, A. R. Development and evolution of the human neocortex. *Cell* **146**, 18–36 (2011).
2. Semple, B. D., Blomgren, K., Gimlin, K., Ferriero, D. M. & Noble-Haeusslein, L. J. Brain development in rodents and humans: Identifying benchmarks of maturation and vulnerability to injury across species. *Prog. Neurobiol.* **106–107**, 1–16 (2013).
3. Geschwind, D. H. & Rakic, P. Cortical evolution: Judge the brain by its cover. *Neuron* **80**, 633–647 (2013).
4. Silbereis, J. C., Pochareddy, S., Zhu, Y., Li, M. & Sestan, N. The Cellular and Molecular Landscapes of the Developing Human Central Nervous System. *Neuron* **89**, 248–268 (2016).
5. Gogtay, N. *et al.* Dynamic mapping of human cortical development during childhood through early adulthood. *Proc. Natl. Acad. Sci.* **101**, 8174–8179 (2004).
6. Petanjek, Z., Judaš, M., Kostović, I. & Uylings, H. B. M. Lifespan alterations of basal dendritic trees of pyramidal neurons in the human prefrontal cortex: A layer-specific pattern. *Cereb. Cortex* **18**, 915–929 (2008).
7. Stiles, J. & Jernigan, T. L. The basics of brain development. *Neuropsychol. Rev.* **20**, 327–348 (2010).
8. Rakic, P. Evolution of the neocortex: A perspective from developmental biology. *Nat. Rev. Neurosci.* **10**, 724–735 (2009).
9. Dehay, C., Kennedy, H. & Kosik, K. S. The Outer Subventricular Zone and Primate-Specific Cortical Complexification. *Neuron* **85**, 683–694 (2015).
10. Howard, B. M., Mo, Z., Filipovic, R., Moore, A. R. & Antic, S. D. Radial Glia Cells in the Developing Human Brain. *Neuroscientist* **14**, 459–473 (2009).
11. Bystron, I., Rakic, P., Molnár, Z. & Blakemore, C. The first neurons of the human cerebral cortex. *Nat. Neurosci.* **9**, 880–886 (2006).
12. Semendeferi, K. *et al.* Spatial organization of neurons in the frontal pole sets humans apart from great apes. *Cereb. Cortex* **21**, 1485–1497 (2011).
13. Bae, B. Il, Jayaraman, D. & Walsh, C. A. Genetic changes shaping the human brain. *Dev. Cell* **32**, 423–434 (2015).
14. Cheng, Z. *et al.* A genome-wide comparison of recent chimpanzee and human segmental duplications. *Nature* **437**, 88–93 (2005).
15. Prüfer, K. *et al.* The bonobo genome compared with the chimpanzee and human genomes. *Nature* **486**, 527–531 (2012).
16. Sudmant, P. H. *et al.* Evolution and diversity of copy number variation in the great ape lineage. *Genome Res.* **23**, 1373–1382 (2013).
17. Somel, M., Liu, X. & Khaitovich, P. Human brain evolution: transcripts, metabolites and their regulators. *Nat. Rev. Neurosci.* **14**, 112–127 (2013).
18. Franchini, L. F. & Pollard, K. S. Genomic approaches to studying human-specific developmental traits. *Development* **142**, 3100–3112 (2015).
19. Haygood, R., Babbitt, C. C., Fedrigo, O. & Wray, G. A. Contrasts between adaptive coding and noncoding changes during human evolution. *Proc. Natl. Acad. Sci.* **107**, 7853–7857 (2010).
20. McLean, C. Y. *et al.* Human-specific loss of regulatory DNA and the evolution of human-specific traits. *Nature* **471**, 216–219 (2011).
21. Javierre, B. M. *et al.* Lineage-Specific Genome Architecture Links Enhancers and Non-coding Disease Variants to Target Gene Promoters. *Cell* **167**, 1369–1384.e19 (2016).

22. Long, H. K., Prescott, S. L. & Wysocka, J. Ever-Changing Landscapes: Transcriptional Enhancers in Development and Evolution. *Cell* **167**, 1170–1187 (2016).
23. Finch, C. E. Evolution of the human lifespan and diseases of aging: Roles of infection, inflammation, and nutrition. *Proc. Natl. Acad. Sci.* **107**, 1718–1724 (2010).
24. Khaitovich, P. *et al.* Metabolic changes in schizophrenia and human brain evolution. *Genome Biol.* **9**, 1–11 (2008).
25. Song, J. H. T., Lowe, C. B. & Kingsley, D. M. Characterization of a Human-Specific Tandem Repeat Associated with Bipolar Disorder and Schizophrenia. *Am. J. Hum. Genet.* **103**, 421–430 (2018).
26. Crow, T. J. Schizophrenia as the price that Homo sapiens pays for language: a resolution of the central paradox in the origin of the species 1. *brain Res. Rev.* **31**, 118–129 (2000).
27. Bianchi, S. *et al.* Synaptogenesis and development of pyramidal neuron dendritic morphology in the chimpanzee neocortex resembles humans. *Proc. Natl. Acad. Sci.* **110**, 10395–10401 (2013).
28. Giedd, J. N., Keshavan, M. & Paus, T. Why do many psychiatric disorders emerge during adolescence? *Nat. Rev. Neurosci.* **9**, 947–957 (2008).
29. Kessler, R. C. *et al.* Age of onset of mental disorders: A review of recent literature. *Curr. Opin. Psychiatry* **20**, 359–364 (2007).
30. Lee, F. S. *et al.* Adolescent mental health--Opportunity and obligation. *Science (80-. )*. **346**, 547–549 (2014).
31. Lein, E. S., Belgard, T. G., Hawrylycz, M. & Molnár, Z. Transcriptomic Perspectives on Neocortical Structure, Development, Evolution, and Disease. *Annu. Rev. Neurosci.* **40**, 629–652 (2017).
32. Tebbenkamp, A. T. N., Willsey, A. J., State, M. W. & Šestan, N. The developmental transcriptome of the human brain: Implications for neurodevelopmental disorders. *Curr. Opin. Neurol.* **27**, 149–156 (2014).
33. Smaers, J. B., Schleicher, A., Zilles, K. & Vinicius, L. Frontal white matter volume is associated with brain enlargement and higher structural connectivity in anthropoid primates. *PLoS One* **5**, (2010).
34. Schoenemann, P. T., Sheehan, M. J. & Glotzer, L. D. Prefrontal white matter volume is disproportionately larger in humans than in other primates. *Nat. Neurosci.* **8**, 242–252 (2005).
35. Ettle, B., Schlachetzki, J. C. M. & Winkler, J. Oligodendroglia and Myelin in Neurodegenerative Diseases: More Than Just Bystanders? *Mol. Neurobiol.* **53**, 3046–3062 (2016).
36. Robertson, J. M. Astrocytes and the evolution of the human brain. *Med. Hypotheses* **82**, 236–239 (2014).
37. Oberheim, N. A. *et al.* Uniquely hominid features of adult human astrocytes. *J. Neurosci.* **29**, 3276–87 (2009).
38. Oberheim, N. A., Wang, X., Goldman, S. & Nedergaard, M. Astrocytic complexity distinguishes the human brain. *Trends Neurosci.* **29**, 547–553 (2006).
39. Thomson, J. A. *et al.* Embryonic Stem Cell Lines Derived from Human Blastocysts. *Science (80-. )*. **282**, (1998).
40. Carpenter, M. K. *et al.* Enrichment of neurons and neural precursors from human embryonic stem cells. *Exp. Neurol.* **172**, 383–97 (2001).
41. Takahashi, K. & Yamanaka, S. Induction of pluripotent stem cells from mouse embryonic and adult fibroblast cultures by defined factors. *Cell* **126**, 663–76 (2006).
42. Takahashi, K. *et al.* Induction of pluripotent stem cells from adult human fibroblasts by defined factors. *Cell* **131**, 861–72 (2007).
43. Bystron, I., Blakemore, C. & Rakic, P. Development of the human cerebral cortex: Boulder Committee revisited. *Nat. Rev. Neurosci.* **9**, 110–122 (2008).
44. Marin, O. & Rubenstein, J. L. R. Cell Migration in the Forebrain. *Annu. Rev. Neurosci.* **26**, (2003).
45. Meyer, G., Schaaps, J. P., Moreau, L. & Goffinet, A. M. Embryonic and early fetal development of the human neocortex. *J. Neurosci.* **20**, 1858–1868 (2000).

46. Nowakowski, T. J. *et al.* Spatiotemporal gene expression trajectories reveal developmental hierarchies of the human cortex. *1323*, 1318–1323 (2017).
47. Howard, B., Chen, Y. & Zecevic, N. Cortical progenitor cells in the developing human telencephalon. *Glia* **53**, 57–66 (2006).
48. Howard, B. M. *et al.* Radial glia cells in the developing human brain. *Neuroscientist* **14**, 459–473 (2008).
49. Zecevic, N. Specific characteristic of radial glia in the human fetal telencephalon. *Glia* **48**, 27–35 (2004).
50. Mo, Z. *et al.* Human cortical neurons originate from radial glia and neuron-restricted progenitors. *J Neurosci* **27**, 4132–4145 (2007).
51. Dahl, D., Rueger, D. C., Bignami, A., Weber, K. & Osborn, M. Vimentin, the 57 000 molecular weight protein of fibroblast filaments, is the major cytoskeletal component in immature glia. *Eur. J. Cell Biol.* **24**, 191–6 (1981).
52. Shibata, T. *et al.* Glutamate Transporter GLAST Is Expressed in the Radial Glia–Astrocyte Lineage of Developing Mouse Spinal Cord. *J. Neurosci.* **17**, 9212–9219 (1997).
53. Kamei, Y. *et al.* Visualization of mitotic radial glial lineage cells in the developing rat brain by Cdc2 kinase-phosphorylated vimentin. *Glia* **23**, 191–9 (1998).
54. Zecevic, N., Chen, Y. & Filipovic, R. Contributions of cortical subventricular zone to the development of the human cerebral cortex. *J. Comp. Neurol.* **491**, 109–22 (2005).
55. Bayatti, N. *et al.* A molecular neuroanatomical study of the developing human neocortex from 8 to 17 postconceptional weeks revealing the early differentiation of the subplate and subventricular zone. *Cereb. Cortex* **18**, 1536–1548 (2008).
56. Hansen, D. V., Lui, J. H., Parker, P. R. L. & Kriegstein, A. R. Neurogenic radial glia in the outer subventricular zone of human neocortex. *Nature* **464**, 554–561 (2010).
57. Barbaro, N. M. *et al.* Unique astrocyte ribbon in adult human brain contains neural stem cells but lacks chain migration. *Nature* **427**, 740–744 (2004).
58. Zecevic, N., Hu, F. & Jakovcevski, I. Interneurons in the developing human neocortex. *Dev. Neurobiol.* **71**, 18–33 (2011).
59. Jakovcevski, I., Mayer, N. & Zecevic, N. Multiple origins of human neocortical interneurons are supported by distinct expression of transcription factors. *Cereb. Cortex* **21**, 1771–1782 (2011).
60. Al-Jaberi, N., Lindsay, S., Sarma, S., Bayatti, N. & Clowry, G. J. The early fetal development of human neocortical GABAergic interneurons. *Cereb. Cortex* **25**, 631–645 (2015).
61. Petanjek, Z. Primate-specific origins and migration of cortical GABAergic neurons. *Front. Neuroanat.* **3**, 1–12 (2009).
62. Letinic, K., Zoncu, R. & Rakic, P. Origin of GABAergic neurons in the human neocortex. *Nature* **417**, 645–649 (2002).
63. Yu, X. & Zecevic, N. Dorsal Radial Glial Cells Have the Potential to Generate Cortical Interneurons in Human But Not in Mouse Brain. *J. Neurosci.* **31**, 2413–2420 (2011).
64. Radonjic, N. V. *et al.* The complexity of the calretinin-expressing progenitors in the human cerebral cortex. *Front. Neuroanat.* **8**, 1–12 (2014).
65. Tremblay, R., Lee, S. & Rudy, B. GABAergic Interneurons in the Neocortex: From Cellular Properties to Circuits. *Neuron* **91**, 260–292 (2016).
66. Wamsley, B. & Fishell, G. Genetic and activity-dependent mechanisms underlying interneuron diversity. *Nat. Rev. Neurosci.* **18**, 299–309 (2017).
67. Lim, L., Mi, D., Llorca, A. & Marín, O. Development and Functional Diversification of Cortical Interneurons. *Neuron* **100**, 294–313 (2018).
68. Rakic, S. & Zecevic, N. Emerging complexity of layer I in human cerebral cortex. *Cereb. Cortex* **13**, 1072–1083 (2003).

69. Zecevic, N., Milosevic, A., Rakic, S. & Marín-Padilla, M. Early development and composition of the human primordial plexiform layer: An immunohistochemical study. *J. Comp. Neurol.* **412**, 241–254 (1999).
70. Wang, B. *et al.* Loss of Gsx1 and Gsx2 function rescues distinct phenotypes in Dlx1/2 mutants. *J. Comp. Neurol.* **521**, 1561–1584 (2013).
71. Long, J. E., Cobos, I., Potter, G. B. & Rubenstein, J. L. R. Dlx1&2 and Mash1 Transcription Factors Control MGE and CGE Patterning and Differentiation through Parallel and Overlapping Pathways. *Cereb. Cortex* **19**, i96–i106 (2009).
72. Jakovcevski, I. & Zecevic, N. Sequence of oligodendrocyte development in the human fetal telencephalon. *Glia* **49**, 480–491 (2005).
73. Jakovcevski, I. Oligodendrocyte development and the onset of myelination in the human fetal brain. *Front. Neuroanat.* **3**, 1–15 (2009).
74. Schitine, C., Nogaroli, L., Costa, M. R. & Hedin-Pereira, C. Astrocyte heterogeneity in the brain: from development to disease. *Front. Cell. Neurosci.* **9**, 1–11 (2015).
75. DeAzevedo, L. C. *et al.* Cortical radial glial cells in human fetuses: Depth-correlated transformation into astrocytes. *J. Neurobiol.* **55**, 288–298 (2003).
76. Dhara, S. K. & Stice, S. L. Neural differentiation of human embryonic stem cells. *J. Cell. Biochem.* **105**, 633–40 (2008).
77. Falk, A. *et al.* Capture of Neuroepithelial-Like Stem Cells from Pluripotent Stem Cells Provides a Versatile System for In Vitro Production of Human Neurons. *PLoS One* **7**, e29597 (2012).
78. Kozhich, O. A., Hamilton, R. S. & Mallon, B. S. Standardized Generation and Differentiation of Neural Precursor Cells from Human Pluripotent Stem Cells. *Stem Cell Rev. Reports* **9**, 531–536 (2013).
79. Engel, M., Do-Ha, D., Mu??oz, S. S. & Ooi, L. Common pitfalls of stem cell differentiation: a guide to improving protocols for neurodegenerative disease models and research. *Cell. Mol. Life Sci.* **73**, 3693–3709 (2016).
80. DeBoer, E. M. & Anderson, S. A. Fate determination of cerebral cortical GABAergic interneurons and their derivation from stem cells. *Brain Res.* **1655**, 277–282 (2017).
81. Kumar, M., Kaushalya, S. K., Gressens, P., Maiti, S. & Mani, S. Optimized derivation and functional characterization of 5-HT neurons from human embryonic stem cells. *Stem Cells Dev.* **18**, 615–27 (2009).
82. Vadodaria, K. C., Marchetto, M. C., Mertens, J. & Gage, F. H. Generating human serotonergic neurons in vitro: Methodological advances. *BioEssays* **38**, 1123–1129 (2016).
83. Chandrasekaran, A., Avci, H. X., Leist, M., Kobolák, J. & Dinnyés, A. Astrocyte Differentiation of Human Pluripotent Stem Cells: New Tools for Neurological Disorder Research. *Front. Cell. Neurosci.* **10**, (2016).
84. Sloan, S. A. *et al.* Human Astrocyte Maturation Captured in 3D Cerebral Cortical Spheroids Derived from Pluripotent Stem Cells. *Neuron* **95**, 779–790.e6 (2017).
85. Goldman, S. A. & Kuypers, N. J. How to make an oligodendrocyte. *Development* **142**, 3983–3995 (2015).
86. Madhavan, M. *et al.* Induction of myelinating oligodendrocytes in human cortical spheroids. *Nat. Methods* **15**, 700–706 (2018).
87. Duan, L., Peng, C.-Y., Pan, L. & Kessler, J. Human pluripotent stem cell-derived radial glia recapitulate developmental events and provide real-time access to cortical neurons and astrocytes. *Stem Cells Transl Med.* **4**, 1–11 (2015).
88. Zhang, S. C., Wernig, M., Duncan, I. D., Brüstle, O. & Thomson, J. a. In vitro differentiation of transplantable neural precursors from human embryonic stem cells. *Nat. Biotechnol.* **19**, 1129–33 (2001).

89. Mariani, J., Vittoria, M., Palejev, D. & Tomasini, Livia; Coppola, G.; Szekeley, A.M.; Horvath, T.L.; Vaccarino, M. V. Modeling human cortical development in vitro using induced pluripotent stem cells. *Proc. Natl. Acad. Sci.* **109**, 12770–12775 (2012).
90. van de Leemput, J. *et al.* CORTECON: A Temporal Transcriptome Analysis of In Vitro Human Cerebral Cortex Development from Human Embryonic Stem Cells. *Neuron* **83**, 51–68 (2014).
91. Gunhanlar, N. *et al.* A simplified protocol for differentiation of electrophysiologically mature neuronal networks from human induced pluripotent stem cells. *Mol. Psychiatry* 1–9 (2017). doi:10.1038/mp.2017.56
92. Qian, X. *et al.* Brain-Region-Specific Organoids Using Mini-bioreactors for Modeling ZIKV Exposure. *Cell* **165**, 1238–1254 (2016).
93. Kelava, I. & Lancaster, M. A. Stem Cell Models of Human Brain Development. *Cell Stem Cell* **18**, 736–748 (2016).
94. Paşca, A. M. *et al.* Functional cortical neurons and astrocytes from human pluripotent stem cells in 3D culture. *Nat. Methods* **12**, 671–678 (2015).
95. Kadoshima, T. *et al.* Self-organization of axial polarity, inside-out layer pattern, and species-specific progenitor dynamics in human ES cell-derived neocortex. *Proc. Natl. Acad. Sci.* **110**, 20284–20289 (2013).
96. Koutsopoulos, S. & Zhang, S. Long-term three-dimensional neural tissue cultures in functionalized self-assembling peptide hydrogels, Matrigel and Collagen I. *Acta Biomater.* **9**, 5162–9 (2013).
97. Pasca, S. P. The rise of three-dimensional human brain cultures. *Nature* **553**, 437–445 (2018).
98. Camp, J. G. *et al.* Human cerebral organoids recapitulate gene expression programs of fetal neocortex development. *Proc. Natl. Acad. Sci. U. S. A.* **112**, 15672–7 (2015).
99. Lancaster, M. a. *et al.* Cerebral organoids model human brain development and microcephaly. *Nature* (2013). doi:10.1038/nature12517
100. Sakaguchi, H. *et al.* Generation of functional hippocampal neurons from self-organizing human embryonic stem cell-derived dorsomedial telencephalic tissue. *Nat. Commun.* **6**, 8896 (2015).
101. Birey, F. *et al.* Assembly of functionally integrated human forebrain spheroids. *Nature* **545**, 54–59 (2017).
102. Mansour, A. A. *et al.* An in vivo model of functional and vascularized human brain organoids. *Nat. Biotechnol.* **36**, (2018).



# Chapter 2

## A simplified protocol for differentiation of electrophysiologically mature neuronal networks from human induced pluripotent stem cells

N. Günhanlar<sup>1,\*</sup>, G. Shpak<sup>1,\*</sup>, M. van der Kroeg<sup>1</sup>, L.A. Gouty-Colomer<sup>1,4</sup>, S.T. Munshi<sup>1</sup>, B. Lendemeijer<sup>1</sup>, M. Ghazvini<sup>2,3</sup>, C. Dupont<sup>2</sup>, W.J.G. Hoogendijk<sup>1</sup>, J. Gribnau<sup>2,3</sup>, F.M.S. de Vrij<sup>1,#</sup> and S.A. Kushner<sup>1,#</sup>

<sup>1</sup> Dept of Psychiatry, Erasmus MC, Wytemaweg 80, 3015 CN Rotterdam, the Netherlands

<sup>2</sup> Department of Developmental Biology, Erasmus MC, Wytemaweg 80, 3015 CN Rotterdam, the Netherlands

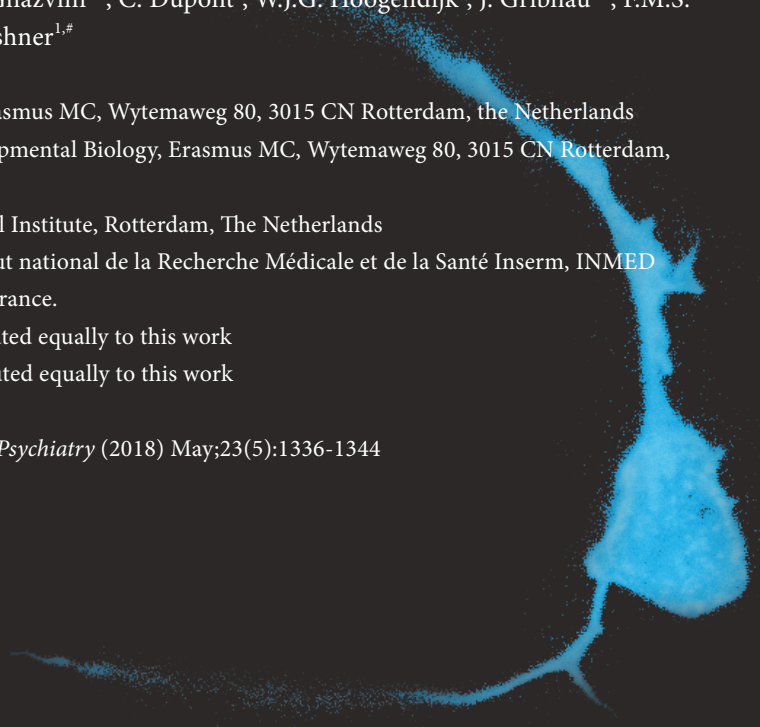
<sup>3</sup> Erasmus MC Stem Cell Institute, Rotterdam, The Netherlands

<sup>4</sup> Present address: Institut national de la Recherche Médicale et de la Santé Inserm, INMED UMR 901, Marseille, France.

\* These authors contributed equally to this work

# These authors contributed equally to this work

Published in *Molecular Psychiatry* (2018) May;23(5):1336-1344



## ABSTRACT

Progress in elucidating the molecular and cellular pathophysiology of neuropsychiatric disorders has been hindered by the limited availability of living human brain tissue. The emergence of induced pluripotent stem cells (iPSCs) has offered a unique alternative strategy using patient-derived functional neuronal networks. However, methods for reliably generating iPSC-derived neurons with mature electrophysiological characteristics have been difficult to develop. Here, we report a simplified differentiation protocol that yields electrophysiologically mature iPSC-derived cortical lineage neuronal networks without the need for astrocyte co-culture or specialized media. This protocol generates a consistent 60:40 ratio of neurons and astrocytes that arise from a common forebrain neural progenitor. Whole-cell patch-clamp recordings of 114 neurons derived from three independent iPSC lines confirmed their electrophysiological maturity, including resting membrane potential ( $-58.2 \pm 1.0$  mV), capacitance ( $49.1 \pm 2.9$  pF), action potential (AP) threshold ( $-50.9 \pm 0.5$  mV), and AP amplitude ( $66.5 \pm 1.3$  mV). Nearly 100% of neurons were capable of firing APs, of which 79% had sustained trains of mature APs with minimal accommodation (peak AP frequency:  $11.9 \pm 0.5$  Hz) and 74% exhibited spontaneous synaptic activity (amplitude,  $16.03 \pm 0.82$  pA; frequency,  $1.09 \pm 0.17$  Hz). We expect this protocol to be of broad applicability for implementing iPSC-based neural network models of neuropsychiatric disorders.



## INTRODUCTION

A detailed knowledge of the pathophysiology underlying the majority of human neuropsychiatric disorders remains largely enigmatic. However, functional genomic studies have begun to offer novel insights into many forms of neurological and psychiatric illness<sup>1–5</sup>. There is widespread consensus that validated and robust human cellular models for brain disorders would be of considerable benefit<sup>6,7</sup>.

The discovery of induced pluripotent stem cells (iPSCs) has provided the opportunity to investigate the physiology of living human neurons derived from individual patients<sup>8</sup>. Several protocols have been reported for generating iPSC-derived neurons based on a variety of different methods. One of the most commonly employed approaches is neural induction through embryoid body (EB) formation<sup>9,10</sup>. Another widely implemented method for neural induction is inhibition of the transforming growth-factor- $\beta$ -SMAD signaling pathway by Noggin and SB431542, which provides highly efficient neural conversion of iPSCs into midbrain dopamine and spinal motor neurons<sup>11,12</sup>. More recently, protocols have been developed for generating three-dimensional (3D) neural cultures using cerebral organoids cultured in a spinning bioreactor<sup>13</sup>, cortical spheroids in free-floating conditions<sup>14</sup>, or in 3D Matrigel culture<sup>15</sup>.

In establishing optimized and standardized methods for neuronal differentiation of iPSCs, one of the most important questions is the functional maturity of the resulting neuronal networks. The design of optimized neural differentiation protocols is critical for the reliable generation of functional neurons that can form active networks and demonstrate mature electrophysiological properties. Bardy et al. recently reported a significant advance in achieving functionally mature iPSC-derived neural networks<sup>16</sup>. However, the major limitation with this approach is the requirement for a non-standard culture medium and extracellular recording solution during the differentiation process and electrophysiological recordings.

Neuron-astrocyte interactions are critical both during early neurodevelopment and in the adult brain<sup>17</sup>. Astrocytes are involved in the guidance of neuronal precursors and for increasing the length of neuronal fiber projections during development<sup>18</sup>. In addition, astrocytes dynamically modulate synaptic transmission<sup>19,20</sup>. Consequently, the functional maturation of human pluripotent stem cell-derived neurons is substantially improved by the presence of astrocytes<sup>14,21</sup>. For the derivation of iPSC-derived neural networks, astrocytes can either be introduced through co-culture<sup>22</sup> or differentiated from a common neural progenitor which gives rise to both neurons and astrocytes as occurs *in vivo*<sup>10</sup>. The co-culture approach allows more flexibility in having experimental control over the neuron-to-astrocyte ratio and the source of the co-cultured astrocytes. The major drawback, however, is the potential for introducing a source of variability, especially concerning species differences when using co-cultures of rodent astrocytes with human iPSC-derived neurons. In contrast, differentiation protocols based on a common progenitor giving rise to both neurons and astrocytes proceed more similarly to *in vivo* neurodevelopment<sup>9,10</sup>.

Using the latter approach, we now report a simplified differentiation protocol for deriving functionally mature neural networks from iPSCs without the need for astrocyte co-culture or specialized media.

## MATERIAL AND METHODS

### Human iPSC lines

Reprogramming of human primary skin fibroblasts from two adult donors (Line 1: male, age 57; line 2: female, age 54) was performed as described previously using a single, multicistronic lentiviral vector encoding OCT4, SOX2, KLF4, and MYC<sup>23</sup>. Both donors provided written informed consent, in accordance with the Medical Ethical Committee of the Erasmus University Medical Center. Quality control of iPSC clones was performed by karyotyping, real-time quantitative PCR, and embryoid body differentiation<sup>24</sup>. Line 3 (male, newborn) was reprogrammed from cord blood CD34<sup>+</sup> cells using episomal reprogramming (Axol Biosciences).

### Differentiation of human iPSCs to neural networks

#### *Generation of Neural Precursor Cells (NPCs)*

Human iPSC lines 1 and 2 were dissociated from MEFs with collagenase (100 U/ml, Thermo Fisher Scientific) for 7 minutes at 37°C/5% CO<sub>2</sub>. Embryoid bodies (EBs) were generated by transferring dissociated iPSCs to non-adherent plates in human embryonic stem cell medium [DMEM/F12 (Thermo Fisher Scientific), 20% knockout serum (Thermo Fisher Scientific), 1% MEM-NEAA (Sigma-Aldrich), 7 nl/ml β-mercaptoethanol (Sigma), 1% L-glutamine (Thermo Fisher Scientific), 1% penicillin/streptomycin (P/S, Thermo Fisher Scientific)] on a shaker in an incubator at 37°C/5% CO<sub>2</sub>. EBs were grown for two days in human embryonic stem cell medium, changed into neural induction medium [DMEM/F12, 1% N2 supplement (Thermo Fisher Scientific), 2 µg/ml heparin (Sigma-Aldrich), 1% P/S] on day 2, and cultured for another four days in suspension (d3-d6). For generation of NPCs, EBs were slightly dissociated at d7 by trituration and plated onto laminin-coated 10 cm dishes [20 µg/ml laminin (Sigma-Aldrich) in DMEM for 30 min at 37°C], initially using neural induction medium (d7-14), and then from d15 in NPC medium [DMEM/F12, 1% N2 supplement, 2% B27-RA supplement (Thermo Fisher Scientific), 1 µg/ml laminin, 20 ng/ml FGF2 (Merck-Millipore), and 1% P/S]. On d15, cells were considered pre-NPCs (passage 1) and able to be passaged (1:4) and cryopreserved when confluent. From passage 5, cells were considered NPCs and used for neural differentiation.

Line 3 NPCs were derived using the protocol reported by Shi et al.<sup>10</sup> with modifications (Axol Biosciences, line ax0015) to examine the generalizability of our neural differentiation protocol.

### *Neural Differentiation*

For neural differentiation, NPCs (passage 5-11) were plated on sterile coverslips in 6-or 12-well plates, coated with polyornithine (Sigma-Aldrich) for 1 hour at room temperature. Coated coverslips were washed 3 times with sterile water and dried for 30 min. Subsequently, a 100  $\mu$ l drop of laminin solution (50  $\mu$ g/ml in water) was placed in the middle of each coverslip, incubated for 15-30 min at 37°C/5% CO<sub>2</sub>, and then replaced with a 100  $\mu$ l drop of DMEM until plating of NPCs. Immediately prior to plating, NPCs were washed with Dulbecco's phosphate buffered saline (DPBS) and dissociated with collagenase (100 U/ml). One fully confluent 10 cm dish of NPCs was divided over a 12-well plate. A 100  $\mu$ l drop of NPC cell suspension was placed on the laminin-coated spot for 1 hour to allow for attachment of NPCs on coverslips in neural differentiation medium [Neurobasal medium, 1% N2 supplement, 2% B27-RA supplement, 1% MEM-NEAA, 20 ng/ml BDNF (ProSpec Bio), 20 ng/ml GDNF (ProSpec Bio), 1  $\mu$ M db-cAMP (Sigma-Aldrich), 200  $\mu$ M ascorbic acid (Sigma-Aldrich), 2  $\mu$ g/ml laminin, and 1% P/S]. After 1 hour, 900  $\mu$ l of neural differentiation medium was added to each well. Cells were refreshed with medium 3 times per week. During weeks 1-4, medium was fully refreshed. After 4 weeks of neural differentiation, only half of the volume of medium per well was refreshed. Electrophysiology and confocal imaging were performed between 8-10 weeks after plating of NPCs.

### **Immunocytochemistry and quantification**

Cell cultures were fixed using 4% formaldehyde in PBS. Primary antibodies were incubated overnight at 4°C in labelling buffer containing 0.05 M Tris, 0.9% NaCl, 0.25% gelatin, and 0.5% Triton-X-100 (pH 7.4). The following primary antibodies were used: SOX2, Nestin, MAP2, TBR1, GAD67, NeuN and glial fibrillary acidic protein (GFAP) (Merck-Millipore); FOXG1 (ProSci); Vimentin (Santa Cruz Biotechnology); AFP (R&D Systems); TRA-1-81 and Nanog (Beckton Dickinson); OCT4, BRN2, SATB2, CUX1, CUX2 and CTIP2 (Abcam); Synapsin, MAP2 (Synaptic Systems); and PSD95 (Thermo Fisher Scientific). The following secondary antibodies were used: Alexa-488, Alexa-546, Alexa-555 and Cy3 antibodies (Jackson ImmunoResearch). Samples were imbedded in Mowiol 4-88 (Sigma-Aldrich) after which confocal imaging was performed with a Zeiss LSM700 confocal microscope using ZEN software (Zeiss, Germany).

### **Electrophysiology**

#### *Whole-cell patch clamp recordings*

Culture slides were collected from 12-well culture plates. Whole-cell patch clamp recordings were performed at 8-10 weeks following the initiation of NPC differentiation. Recording micropipettes (tip resistance 3–6 M $\Omega$ ) were filled with internal solution composed of (mM): 130 K-gluconate, 0.1 EGTA, 1 MgCl<sub>2</sub>, 2 MgATP, 0.3 NaGTP, 10 HEPES, 5 NaCl, 11 KCl, 5 Na<sub>2</sub>-phosphocreatine (pH 7.4). Recordings were made at room temperature using a Multi-

Clamp 700B amplifier (Molecular Devices). Signals were sampled and filtered at 10 kHz and 3 kHz, respectively. The whole-cell capacitance was compensated and series resistance was monitored throughout the experiment in order to confirm the integrity of the patch seal and the stability of the recording. Voltage was corrected for liquid junction potential (-14 mV). The bath was continuously perfused with oxygenated artificial cerebrospinal fluid (ACSF) composed of (mM): 110 NaCl, 2.5 KCl, 2 CaCl<sub>2</sub>, 10 glucose and 1 NaH<sub>2</sub>PO<sub>4</sub>, 25 NaHCO<sub>3</sub>, 0.2 ascorbic acid, 2 MgCl<sub>2</sub> (pH 7.4). For voltage-clamp recordings, cells were clamped at -80 mV. Spontaneous postsynaptic currents (sPSCs) were recorded for 3 minutes. Fast sodium and potassium currents were evoked by voltage steps ranging from -80 to +50 mV in 10 mV increments. Capacitance was derived from the Clampex 10.2 membrane-test function. For current-clamp recordings, voltage responses were evoked from a holding potential of -75 mV using 500 msec steps ranging from -20 to +150 pA in 10 pA intervals delivered at 0.5 Hz. Single action potential properties were calculated from the first evoked AP in response to a depolarizing step.

Spontaneous AP activity was measured for 3 minutes using the minimum hyperpolarizing holding current in which spiking was evident (0–10 pA), from an initial holding potential of -80 mV. Action potential threshold was calculated as the second derivative of the AP waveform. AP rise and decay times were calculated at 10% and 90% of the AP amplitude, respectively. Data analysis was performed by Clampfit 10.2 (Molecular devices). Spontaneous postsynaptic currents were analyzed by MiniAnalysis software (Synaptosoft).

#### *Equilibration procedure from cell culture medium to ACSF*

Before initiating whole-cell recordings, cell culture medium was gradually replaced with oxygenated ACSF in order to minimize the impact of the relative difference in osmolarity (culture medium, 220 mOsm/L; ACSF, 305 mOsm/L). Into the 1 mL volume of culture medium per well, 300 µl of oxygenated ACSF was added for 5 minutes, after which 300 µl was removed. This replacement procedure was repeated 5 times at room temperature. Slides were placed immediately thereafter into the recording chamber with continuous perfusion of oxygenated ACSF.

#### *Biocytin labeling*

Juxtosomal labeling of neurons was performed using biocytin (5% w/v internal solution) at 8 weeks following the initiation of NPC differentiation. With a GΩ seal on the cell soma, neurons were subjected to 15–20 min of 100–150 pA square-wave current pulses delivered at 2 Hz. Cultures were fixed using 4% formaldehyde in phosphate-buffered saline. Secondary staining with Alexa-488- streptavidin (Jackson ImmunoResearch) was performed in labeling buffer overnight at 4 °C, after which slides were mounted in Mowiol 4-88 and imaged with a Zeiss LSM700 confocal microscope using ZEN software (Zeiss). Sholl analysis and den-

drite length quantification were performed using Fiji (ImageJ, National Institutes of Health, Bethesda, MD, USA) software<sup>25</sup>.

### Electron Microscopy

Fixation was performed for 1 h in 2% glutaraldehyde and 0.1 M sodium cacodylate (NaCac). After rinsing in 0.1 M NaCac, cells were pelleted in 2% agar and postfixed in 2% glutaraldehyde for 15 min. Subsequently, cells were osmicated for 1 h with 1% OsO<sub>4</sub>, dehydrated with EtOH and propylene oxide, followed by embedding in Durcupan Plastic (Fluka) for 72 h. Ultrathin sections (60 nm) were cut using an ultramicrotome (Leica), mounted on nickel grids and counterstained with uranyl acetate and lead citrate. Imaging was performed with a CM100 Transmission Electron Microscope (Philips).

### Statistical analysis

Statistical comparisons of continuous variables were performed using analysis of variance (ANOVA) with post-hoc Tukey's test, using SPSS (Version 21, IBM). For categorical parameters, Fisher's Exact Test was used. The threshold for statistical significance was set at  $P < 0.01$  in order to correct for the 17 different electrophysiological parameters measured.

## RESULTS

### Generation of forebrain-patterned NPCs from iPSCs

Neural Precursor Cells (NPCs) are capable of generating a diversity of neural lineages, including both neurons and astrocytes. To generate iPSC-derived NPCs (lines 1 and 2), iPSCs were detached from feeder cells using collagenase and suspended colonies were transferred to non-adherent plates (**Supplementary Figure 1**). Suspended colonies were cultured on a shaker, which promoted the formation of spherical embryoid bodies (EBs) (**Figure 1a**). EBs were cultured for six days (d1-d6), of which the first two days (d1-d2) were in human embryonic stem cell (hESC) medium (Knock-out serum based) and then four days (d3-d6) in neural induction medium (Advanced DMEM with heparin and N-2 supplement). On the seventh day of differentiation (d7), EBs were gently dissociated and plated onto laminin-coated dishes in neural induction medium for eight days (d7-d14), resulting in a population of pre-NPCs (passage 1). At d15, pre-NPCs were dissociated by collagenase and replated onto laminin-coated dishes in NPC medium (Advanced DMEM with N-2, B-27 supplement and laminin) containing FGF2 to promote selection and proliferation of precursor cells. The medium was changed every other day. Once confluent, cells were passaged 1:4 and could be cryopreserved in liquid nitrogen. From passage five, the cells exhibited a homogeneous morphology and marker profile of mature NPCs, expressing SOX2, Nestin, Vimentin, and the forebrain-specific NPC marker FoxG1 (**Figure 1b**).

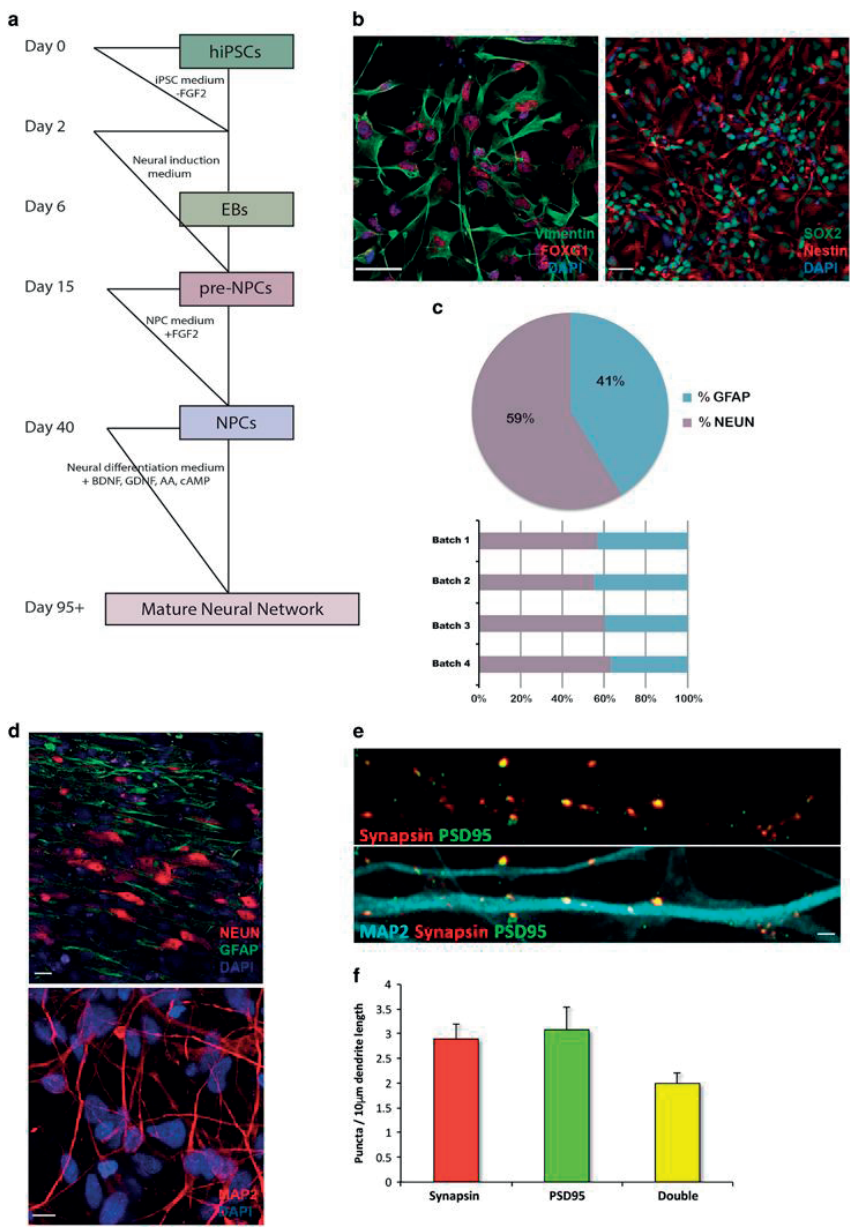


**Figure 1. Generation and characterization of NPCs and neuronal networks from iPSCs.** (a) Scheme illustrating the major developmental stages of the protocol for generating NPCs and neuronal networks. (b) Immunostaining for NPC markers Nestin, SOX2, Vimentin and FOXG1 (scale bars=30  $\mu$ m). (c) Proportion of NeuN<sup>+</sup> and GFAP<sup>+</sup> cells (days 56–70). (d) Immunostaining for glial marker GFAP, and mature neuronal markers MAP2 and NeuN (top, scale bar=20  $\mu$ m; bottom, scale bar=10  $\mu$ m). (e) Co-labeling of pre- and postsynaptic marker proteins, Synapsin and PSD95 (scale bar=2  $\mu$ m). (f) Quantification of Synapsin<sup>+</sup>, PSD95<sup>+</sup> and double-labeled puncta density (n=20 neurons). EB, embryoid body; GFAP, glial fibrillary acidic protein; iPSC, induced pluripotent stem cells; NPC, neural precursor cells.

## Differentiation of neural network cultures

NPCs were utilized between passages 5-11 for neural differentiation. NPCs were plated onto polyornithine/laminin-coated coverslips in neural differentiation medium (Neurobasal medium with N-2, B27-RA) supplemented with growth factors BDNF, GDNF, db-cAMP, and ascorbic acid. Throughout the entire period of neural differentiation, medium was replaced 3 times per week. During weeks 1-4, the medium was fully exchanged. From week 5 onwards, only half of the medium was replaced per exchange. Electrophysiological recordings and confocal imaging were performed at 8–10 weeks following the initiation of NPC differentiation. Neurons were positive for the neuron-specific cytoskeletal marker  $\beta$ -III-tubulin, nuclear marker NeuN, dendritic marker MAP2, presynaptic marker Synapsin and postsynaptic marker PSD95 (**Figures 1d and e**). Quantification of Synapsin and PSD95 puncta confirmed their frequent colocalization, consistent with synaptic network connectivity, of which ~70% were glutamatergic PSD95-labeled synapses (**Figures 1e and f**). Moreover, electron microscopy confirmed a classical synaptic morphology, including presynaptic vesicle pools and postsynaptic density (**Supplementary Figures 2a and b**). Furthermore, the majority of neurons were CTIP2<sup>+</sup>, consistent with a glutamatergic lineage identity, and mutually exclusive of neurons exhibiting GAD67 labeling (**Supplementary Figure 2c**). Both glutamatergic and GABAergic synapses were immunohistochemically confirmed by labeling for VGLUT1 and GAD67, respectively (**Supplementary Figure 2d**). The proportion of immature neurons, mature neurons and astroglia was quantified by staining for doublecortin (DCX), NeuN and GFAP, respectively. Overall, NeuN<sup>+</sup> cells constituted 15.9% of all DAPI<sup>+</sup> nuclei, and 10.8% expressed the astrocyte marker GFAP. The ratio of NeuN<sup>+</sup> (mature neurons) to GFAP<sup>+</sup> (astrocytes) was 59.5 to 40.5% (**Figure 1c**). The remaining cells were SOX2-expressing NPCs (59.7%) and DCX-expressing immature neurons (13.6%) (**Supplementary Figure 3**).

We next studied the expression of cortical layer-specific markers in the differentiated neurons (**Figure 2**)<sup>26,27</sup>. Subsets of neurons were positive for the transcription factor BRN2 that is expressed in late cortical progenitors and upper layer neurons (II-IV) (**Figure 2a**), the cortical-layer marker TBR1 that is expressed in deep layer neurons (V and VI) and the subplate (**Figure 2b**), FOXP2 that is expressed in layers V and VI (**Figure 2c**), CUX1 and CUX2 expressed in upper layer neurons (II–IV), SATB2 expressed in layers II-V, FOXP1 expressed in forebrain neural progenitors and widely in neurons of the developing telencephalon, and CTIP2 expressed in glutamatergic projection neurons from layers V and VI (**Figures 2d–f**). Juxtasomal neuronal biocytin labeling demonstrated an elaborate axonal and dendritic morphology. Sholl analysis was performed to quantify dendritic branching and total dendritic dendritic length (**Supplementary Figure 4**).



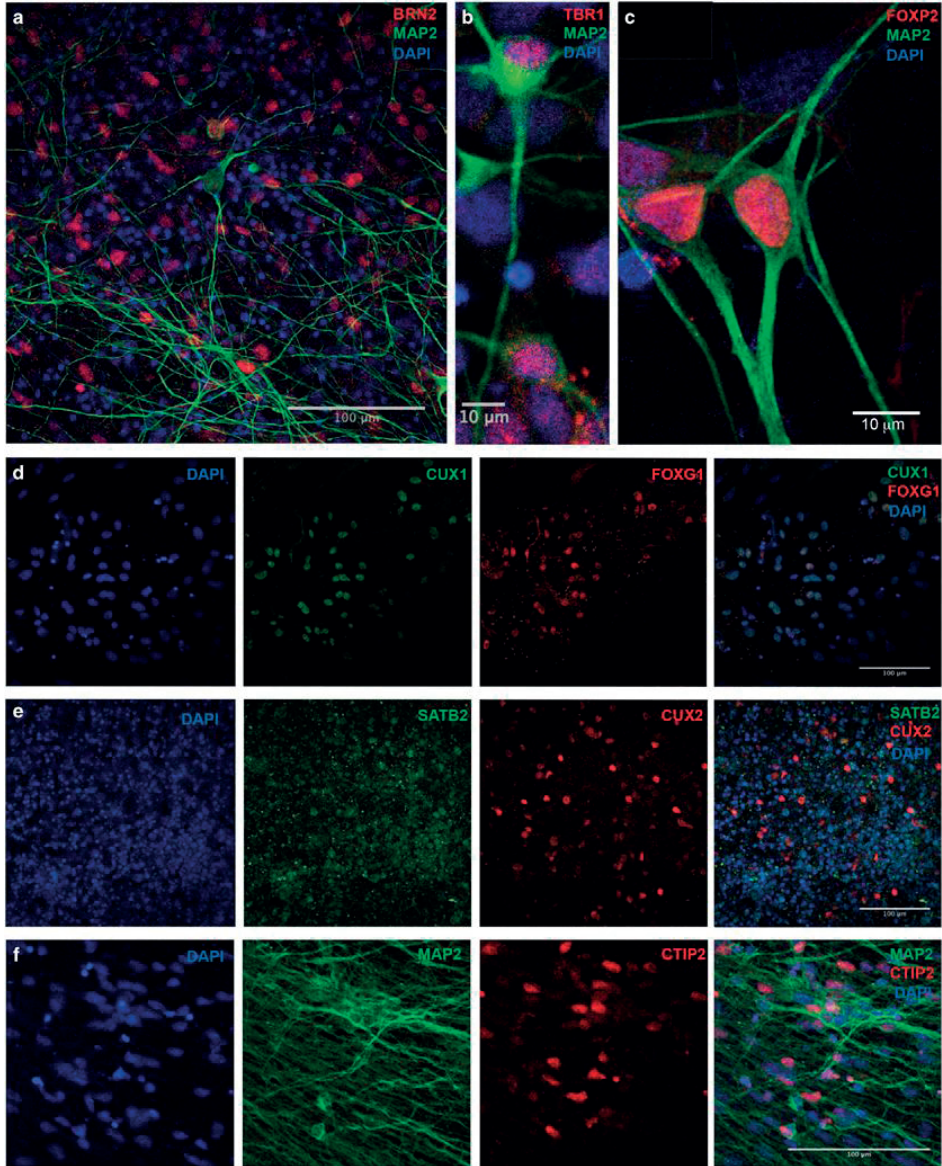


**Figure 2. Cortical layer markers in neuronal networks.** Cultures were stained at day 56 following the initiation of NPC differentiation for (a) BRN2 marker of late cortical progenitors and upper layer (II-IV) neurons, and mature dendritic marker MAP2, (b) TBR1 that is expressed by deep layer neurons (V and VI) and in the subplate, (c) FOXP2 expressed in deep layer (V and VI) neurons, (d) CUX1 marker of upper layer (II-IV) neurons and telencephalic marker FOXG1 and (e) CUX2 marker of upper layer (II-IV) neurons and SATB2 expressed in corticocortical projection neurons from layer V and upper layers. (f) CTIP2 expression in deep layer glutamatergic projection neurons. NPC, neural precursor cells.



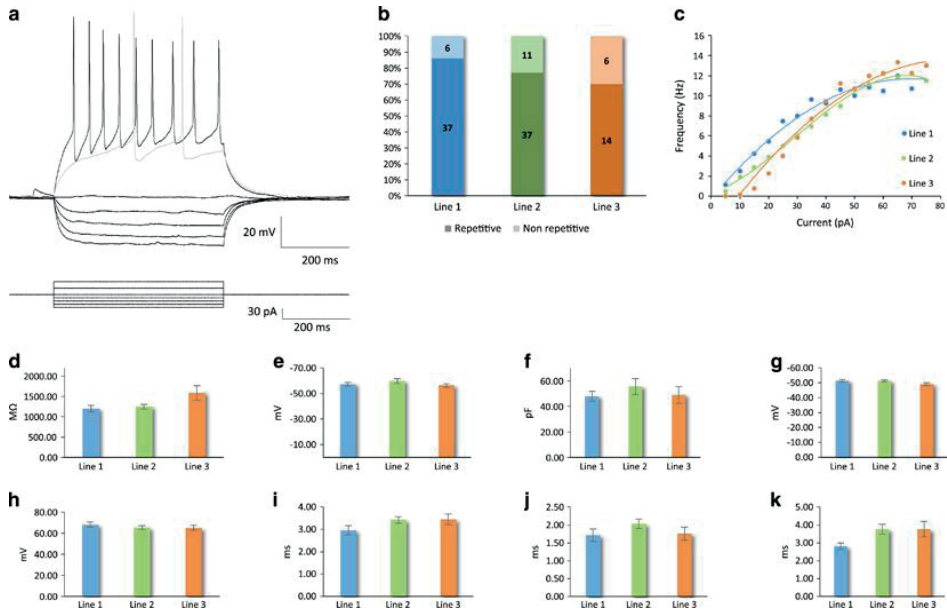


**Figure 3. Active and passive electrophysiological properties.** (a) Representative traces from a neuron firing repetitive mature APs during depolarizing constant-current injections. Current steps are shown in the bottom panel ( $V_m = -75$  mV). The lowest depolarizing step indicates the minimal current needed to evoke an action potential, and the highest step corresponds to the current at which the response frequency became saturated. (b) Percentage of repetitive versus nonrepetitively firing neurons. (c) Frequency–current (F–I) plot among repetitively firing neurons. (d–k) Active and passive membrane properties. AP parameters were calculated from the first evoked spike. (d) Input resistance ( $F = 3.65$ ,  $P = 0.03$ ), (e) resting membrane potential ( $F = 0.82$ ,  $P = 0.44$ ), (f) capacitance ( $F = 0.18$ ,  $P = 0.84$ ), (g) AP threshold ( $F = 1.25$ ,  $P = 0.29$ ), (h) AP amplitude ( $F = 1.01$ ,  $P = 0.37$ ), (i) AP half-width ( $F = 4.70$ ,  $P = 0.012$ ), (j) AP rise time ( $F = 1.23$ ,  $P = 0.30$ ) and (k) decay time ( $F = 4.62$ ,  $P = 0.013$ ). AP, action potential.

## Electrophysiology results

Whole-cell patch-clamp recordings confirmed the functional maturity of the neurons, as suggested from the immunocytochemical stainings. Electrophysiological recordings of iPSC-derived neurons were compared across three independent lines.

Most protocols that have been reported for neuronal differentiation of human pluripotent stem cells employ a semi-defined culture medium, while electrophysiological recordings are performed either in the same culture medium or after transferring from the culture medium directly into a defined artificial cerebrospinal fluid (ACSF). Importantly, the use of culture medium for electrophysiological recordings of neurons has previously been found to impair spontaneous and evoked firing of action potentials, network-level spontaneous calcium activity, and synaptic activity<sup>16</sup>. Notably however, those experiments involved an immediate switch from culture medium to ACSF, whereas a substantial acute increase in extracellular osmolarity (from 220 mOsm/kg in culture medium to 305 mOsm/kg in ACSF) is known to be highly stressful for neurons<sup>28</sup>. Therefore, we implemented a gradual transition from the

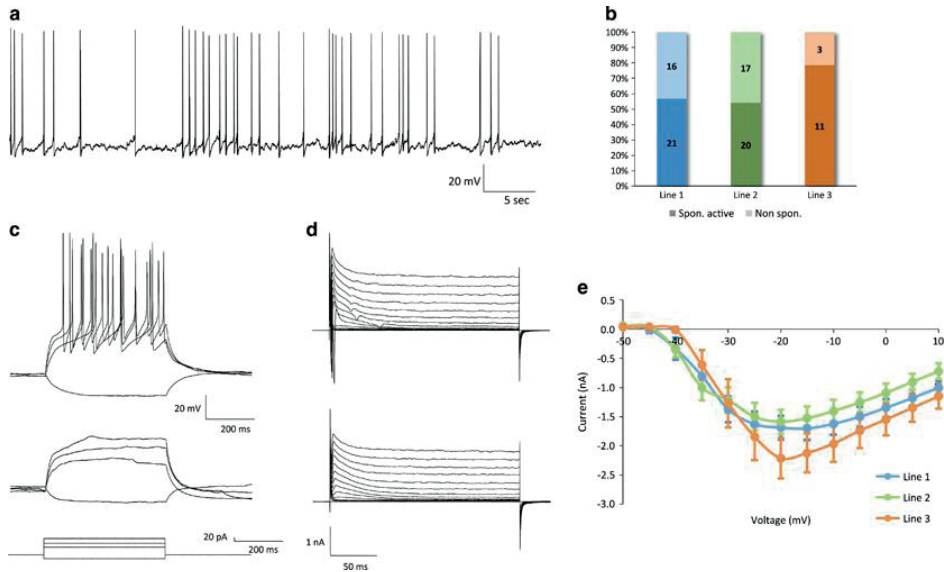


**Figure 4. Spontaneous action potentials.** (a) Representative current-clamp recording from a spontaneously active neuron ( $V_m = -68$  mV). (b) Percentage of neurons with spontaneous AP firing. (c) Voltage responses of the same neuron in (a) to hyperpolarizing or depolarizing current injections (bottom panel), before (top panel) and after (middle panel) TTX application ( $V_m = -75$  mV). (d) Sodium currents were abolished by TTX (before, top panel; after, bottom panel) ( $V_m = -80$  mV). (e) Voltage dependence of the peak amplitude of the sodium current.

culture medium to the ACSF recording medium over 25 minutes by 5 serial partial exchanges (see Materials and Methods section for details).

Mature APs were defined as being those which reached a membrane potential above 0 mV, with a fast depolarization ( $\leq 5$  ms rise time), and rapid repolarization ( $\leq 10$  ms decay time). Nearly all recorded cells were capable of firing mature APs in response to depolarizing current injections (111/114 cells, 97.4%). Among these cells, 79.3% (88/111) exhibited repetitive firing of mature APs (**Figure 3a and b**), with a peak frequency of  $\sim 13$  Hz (**Figure 3c**). The remaining 20.7% (23/111 neurons) fired an initial mature AP followed by a sequence of APs that exhibited rapid accommodation and no longer met the criteria for AP maturity.

Detailed electrophysiological measurements of intrinsic properties were performed among the group of neurons that were defined as mature based on their ability to fire mature APs repetitively in response to current injection. Passive and active membrane properties were quantified and compared in order to evaluate both the physiological maturity of the neurons and the variability between lines. The mean input resistance was  $1.28 \pm 0.05$  G $\Omega$  (**Figure 3d**). Resting membrane potential was  $-58.2 \pm 1.0$  mV (**Figure 3e**). The average capacitance was  $49.1 \pm 2.9$  pF (**Figure 3f**). AP threshold was  $-50.9 \pm 0.5$  mV (**Figure 3g**). AP amplitude, measured from voltage threshold to peak, was  $66.5 \pm 1.3$  mV (**Figure 3h**). AP half-width was

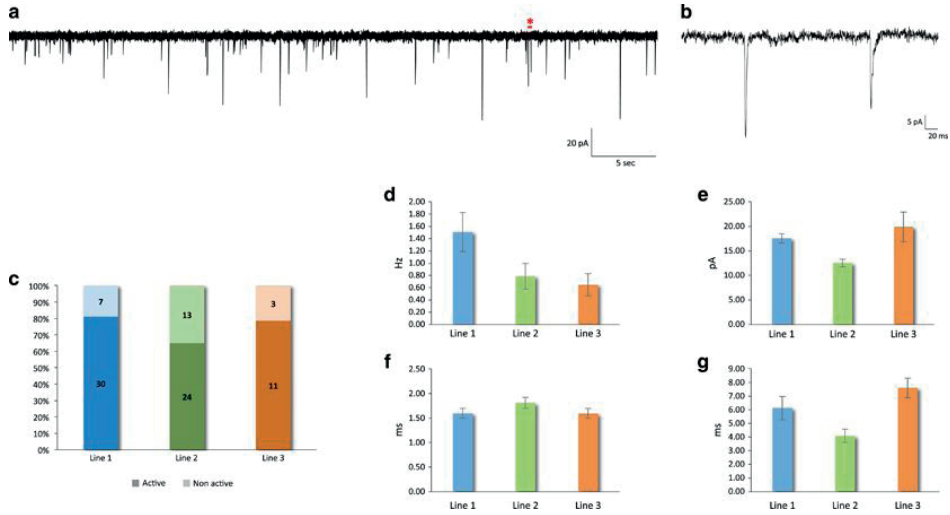


**Figure 5. Neuronal network synaptic activity.** (a) Representative voltage-clamp recording from a neuron with spontaneous synaptic input ( $V_m = -80$  mV). (b) Zoom-in of the region in (a) marked by the red asterisk, containing two postsynaptic events. (c) Percentage of neurons exhibiting spontaneous synaptic input. (d–g) Spontaneous postsynaptic currents: (d) frequency ( $F = 2.55$ ,  $P = 0.09$ ), (e) amplitude ( $F = 7.25$ ,  $P = 0.001$ ; post hoc Tukey:  $P = 0.01$  for line 1 vs 2,  $P = 0.004$  for line 2 vs 3 and  $P = 0.52$  for line 1 vs 3), (f) rise time ( $F = 1.24$ ,  $P = 0.30$ ) and (g) decay time ( $P = 0.023$ ,  $F = 4.01$ ).

$3.18 \pm 0.11$  ms (**Figure 3i**). AP rise and decay times were  $1.9 \pm 1.0$  ms (**Figure 3j**) and  $3.36 \pm 0.16$  ms (**Figure 3k**), respectively.

Another important aspect of neuronal network maturity is spontaneous AP firing<sup>28–30</sup>. The majority of neurons exhibited spontaneous APs (59.1%, 52/88 neurons) (**Figure 4, a and b**). Importantly, sustained high-quality whole-cell recordings could be maintained for more than 30 minutes (longest recording time examined) with a stable membrane potential and AP waveform, confirming that the presence of spontaneous APs was not the result of poor health (**Supplementary Figure 5a**). Moreover, spontaneous firing of APs was also evident in non-permeating cell-attached recordings, thereby establishing that the presence of spontaneous APs was not an artifact of the whole-cell configuration (**Supplementary Figure 5b**).

In order to confirm that the observed APs were driven by active sodium channel conductance, we blocked voltage-gated sodium channels by applying TTX to the bath solution in a subset of recordings. As expected, action potentials were completely abolished (**Figure 4c**). Voltage-clamp recordings demonstrated the presence of fast sodium currents, as evident from the fast inward current observed in response to depolarized membrane potentials (**Figure 4, d [upper panel] and e**). Inward voltage-gated sodium currents were also completely blocked by TTX (**Figure 4d [lower panel]**).

Another important aspect of neuronal maturity is synaptic connectivity. Spontaneous synaptic activity was evident in 73.8% of neurons (**Figure 5a–c**). The frequency and amplitude of

synaptic events was  $1.09 \pm 0.17$  Hz (**Figure 5d**) and  $16.03 \pm 0.82$  pA (**Figure 5e**), respectively. Line 2 exhibited significant pairwise differences in the amplitude of synaptic events compared to lines 1 and 3 ( $F=7.25$ ,  $p=0.001$ ; post-hoc Tukey:  $p=0.01$  for line 1 vs. 2,  $p=0.004$  for line 2 vs. 3,  $p=0.52$  for line 1 vs. 3). The kinetics of these events resembled those typically observed from neuronal recordings in acute *ex vivo* neocortical tissue slices, with an average rise time of  $1.66 \pm 0.65$  ms (**Figure 5f**) and decay time of  $5.59 \pm 0.48$  ms (**Figure 5g**). Blockade of  $\alpha$ -amino-3-hydroxy-5-methyl-4-isoxazolepropionic acid (AMPA) and N-Methyl-D-aspartic acid (NMDA) receptors using 6-cyano-7-nitroquinoxaline-2,3-dione (CNQX, 50  $\mu$ M) and (2R)- amino-5-phosphonovaleric acid (APV, 50  $\mu$ M) confirmed the dominant contribution of glutamatergic transmission to the synaptic network activity (**Supplementary Figure 6**).

## DISCUSSION

We describe the results of a robust simplified protocol for neural network differentiation from human iPSCs with a particular focus on electrophysiological maturity. The observed electrophysiological maturity was achieved using a common iPSC-derived neural progenitor to obtain both neurons and astrocytes, and therefore obviated the need for exogenous glial cell co-culture. We observed a consistent 60:40 ratio of neurons-to-glia, which included neurons representative of both upper and deep cortical layers. The maturity of the resulting neural networks was further evident by reducing the volume of medium changes over the course of differentiation, following the rationale that the emerging neural networks become increasingly self-sufficient.

This protocol requires no specialized media to obtain high-quality whole-cell patch-clamp recordings from iPSC-derived neurons with mature electrophysiological properties. We implemented a gradual equilibration procedure to transition cultures from standard neural differentiation medium to ACSF. The significance of the osmotic environment to the electrophysiological properties of iPSC-derived neurons was recently demonstrated by Bardy et al., who introduced a specialized medium for neural cell culture and electrophysiological recordings<sup>16</sup>. While the use of a specialized medium was implemented by Bardy et al. to facilitate neuronal differentiation, we demonstrate the feasibility of using standard neural differentiation media while minimizing the physiological response to acute osmotic changes through a gradual equilibration from culture medium to ACSF.

Electrophysiological properties define neuronal maturation. Many neuronal electrophysiological parameters exhibit significant alterations over the course of neurodevelopment<sup>32–34</sup>. Resting membrane potential ( $V_m$ ) tends to become progressively more hyperpolarized during neurodevelopment and stabilizes at approximately -70 mV in human neocortical *ex vivo* tissue slices<sup>35</sup>, for which our protocol generated neurons with a comparable average  $V_m$  of -58 mV. Input resistance also decreases throughout neurodevelopment, as a result of both a higher

ion channel density and a more complex cell morphology<sup>33,34</sup>. Neurons from adult human neocortex have an input resistance on the order of 50-150 M $\Omega$ <sup>35</sup> while that of second trimester human neocortical neurons is approximately 2 G $\Omega$ <sup>32</sup>. Our protocol generated neurons with an average input resistance of 1.27 G $\Omega$ , consistent with a late gestational or early postnatal neurodevelopmental period. As neurons mature, their AP firing threshold becomes increasingly hyperpolarized, and the AP waveform exhibits more rapid kinetics with larger amplitudes<sup>34,35</sup>. Consistent with our observed input resistance, the AP threshold and half-width are also comparable with neurons recorded from *ex vivo* human mid-to-late gestational neocortical tissue<sup>32</sup>.

The emergence of synaptic transmission is another defining aspect of neuronal network maturation which is continuously and dynamically regulated by short- and long-term forms of plasticity, and considered among the latest developing aspects of neuronal physiology<sup>36</sup>. Consistent with the estimated neurodevelopmental stage of the passive membrane properties and active AP characteristics in neurons derived using the current protocol, the synaptic parameters we measured are also comparable to those observed in mid-to-late gestational human neocortex<sup>32</sup>. But in contrast to the low variability that we observed across different lines regarding passive membrane and AP characteristics, synaptic properties exhibited a generally higher variance, although spontaneous postsynaptic current amplitude was the only parameter that demonstrated statistically significant differences between lines. Synapse formation and synaptic function develop over an extended period in neurodevelopment and are governed by a sizeable proportion of the genome, with ~9% of all protein-coding genes expressed at mammalian excitatory synapses<sup>37,38</sup>. Accordingly for iPSC-based disease modeling of defined genetic factors, isogenic controls may be particularly important for studies designed to investigate synaptic function. In contrast, AP parameters and passive membrane properties appear to be more robust across differing genetic backgrounds.

In summary, we have developed a reliable differentiation protocol for generating electrophysiologically-mature iPSC-derived neuronal networks without the need for astrocyte co-culture or specialized media. Moreover, our findings provide a quantitative basis for considering the variability of distinct electrophysiological parameters for iPSC-based disease modeling. We envision this protocol to be of considerable utility for implementing cellular modeling approaches to the study of human neuropsychiatric disease pathogenesis.

## ACKNOWLEDGMENTS

Funding was provided by ZonMw Vidi (017.106.384) and Middelgroot (40-00506-98-10026) and ALW (834.12.002) from the Netherlands Organization for Scientific Research, Dutch Technology Foundation STW applied science division of NWO and the Technology Programme of the Ministry of Economic Affairs [Project 12197], and NeuroBasic Pharma-

Phenomics consortium to S.A.K., and Hersenstichting Fellowship [F2012(1)-39] to F.M.dV.  
We thank Gerard Borst for helpful discussions and Elize Haasdijk for technical assistance.

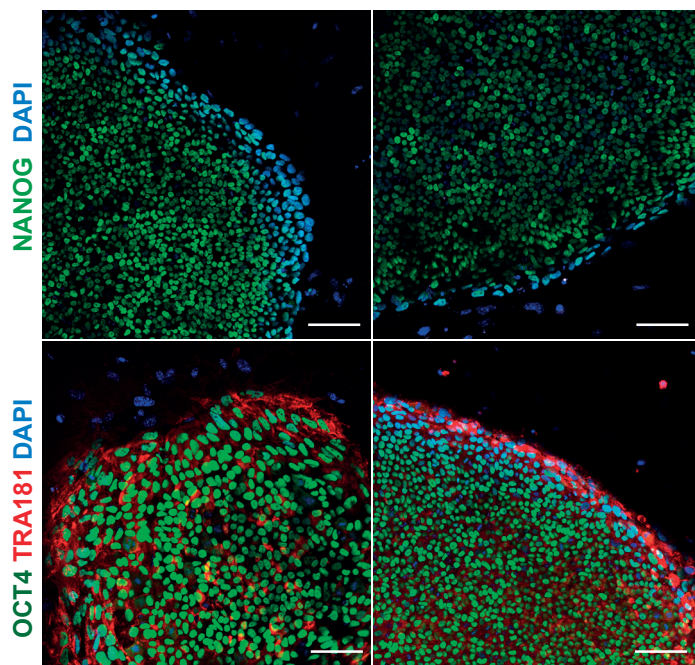
## REFERENCES

- 1 Sekar A, Bialas AR, de Rivera H, Davis A, Hammond TR, Kamitaki N *et al.* Schizophrenia risk from complex variation of complement component 4. *Nature* 2016; **530**: 177–183.
- 2 Sztainberg Y, Chen H, Swann JW, Hao S, Tang B, Wu Z *et al.* Reversal of phenotypes in MECP2 duplication mice using genetic rescue or antisense oligonucleotides. *Nature* 2015; **528**: 123–6.
- 3 Willem M, Tahirovic S, Busche MA, Ovsepian S V, Chafai M, Kootar S *et al.*  $\eta$ -Secretase processing of APP inhibits neuronal activity in the hippocampus. *Nature* 2015; **526**: 443–7.
- 4 Cirulli ET, Lasseigne BN, Petrovski S, Sapp PC, Dion PA, Leblond CS *et al.* Exome sequencing in amyotrophic lateral sclerosis identifies risk genes and pathways. *Science* 2015; **347**: 1436–41.
- 5 Meng L, Ward AJ, Chun S, Bennett CF, Beaudet AL, Rigo F. Towards a therapy for Angelman syndrome by targeting a long non-coding RNA. *Nature* 2014. doi:10.1038/nature13975.
- 6 Kelava I, Lancaster MA. Stem Cell Models of Human Brain Development. *Cell Stem Cell* 2016; **18**: 736–748.
- 7 Wen Z, Christian KM, Song H, Ming G li. Modeling psychiatric disorders with patient-derived iPSCs. *Curr Opin Neurobiol* 2016; **36**: 118–127.
- 8 Takahashi K, Yamanaka S. Induction of pluripotent stem cells from mouse embryonic and adult fibroblast cultures by defined factors. *Cell* 2006; **126**: 663–76.
- 9 Pankratz MT, Li X-J, Lavaute TM, Lyons E a, Chen X, Zhang S-C. Directed neural differentiation of human embryonic stem cells via an obligated primitive anterior stage. *Stem Cells* 2007; **25**: 1511–20.
- 10 Shi Y, Kirwan P, Livesey FJ. Directed differentiation of human pluripotent stem cells to cerebral cortex neurons and neural networks. *Nat Protoc* 2012; **7**: 1836–46.
- 11 Nguyen HN, Byers B, Cord B, Shcheglovitov A, Byrne J, Gujar P *et al.* LRRK2 mutant iPSC-derived DA neurons demonstrate increased susceptibility to oxidative stress. *Cell Stem Cell* 2011; **8**: 267–80.
- 12 Chambers SM, Fasano C a, Papapetrou EP, Tomishima M, Sadelain M, Studer L. Highly efficient neural conversion of human ES and iPS cells by dual inhibition of SMAD signaling. *Nat Biotechnol* 2009; **27**: 275–80.
- 13 Lancaster M a., Renner M, Martin C-A, Wenzel D, Bicknell LS, Hurles ME *et al.* Cerebral organoids model human brain development and microcephaly. *Nature* 2013. doi:10.1038/nature12517.
- 14 Paşca AM, Sloan SA, Clarke LE, Tian Y, Makinson CD, Huber N *et al.* Functional cortical neurons and astrocytes from human pluripotent stem cells in 3D culture. *Nat Methods* 2015; **12**: 671–678.
- 15 Kim YH, Choi SH, D’Avanzo C, Hebisch M, Sliwinski C, Bylykbashi E *et al.* A 3D human neural cell culture system for modeling Alzheimer’s disease. *Nat Protoc* 2015; **10**: 985–1006.
- 16 Bardy C, van den Hurk M, Eames T, Marchand C, Hernandez R V, Kellogg M *et al.* Neuronal medium that supports basic synaptic functions and activity of human neurons in vitro. *Proc Natl Acad Sci U S A* 2015; **112**. doi:10.1073/pnas.1504393112.
- 17 Zuchero JB, Barres BA. Glia in mammalian development and disease. *Development* 2015; **142**: 3805–9.
- 18 Sultan S, Li L, Moss J, Petrelli F, Cassé F, Gebara E *et al.* Synaptic Integration of Adult-Born Hippocampal Neurons Is Locally Controlled by Astrocytes. *Neuron* 2015; **88**: 957–972.
- 19 Chung W-S, Allen NJ, Eroglu C. Astrocytes Control Synapse Formation, Function, and Elimination. *Cold Spring Harb Perspect Biol* 2015; **7**: a020370.
- 20 Clarke LE, Barres BA. Emerging roles of astrocytes in neural circuit development. *Nat Rev Neurosci* 2013; **14**. doi:10.1038/nrn3484.
- 21 Johnson MA, Weick JP, Pearce RA, Zhang S-C. Functional neural development from human embryonic stem cells: accelerated synaptic activity via astrocyte coculture. *J Neurosci* 2007; **27**: 3069–77.

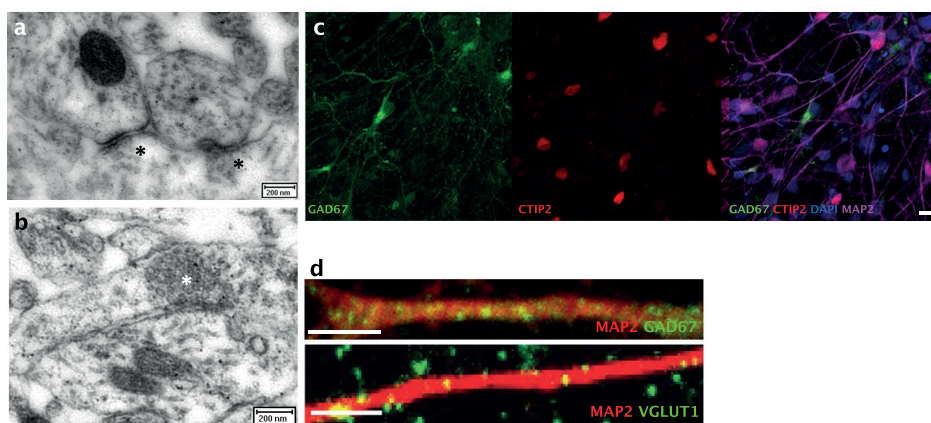
- 22 Brennand KJ, Simone A, Jou J, Gelboin-Burkhart C, Tran N, Sangar S *et al.* Modelling schizophrenia using human induced pluripotent stem cells. *Nature* 2011; **473**: 221–5.
- 23 Warlich E, Kuehle J, Cantz T, Brugman MH, Maetzig T, Galla M *et al.* Lentiviral vector design and imaging approaches to visualize the early stages of cellular reprogramming. *Mol Ther* 2011; **19**: 782–9.
- 24 De Esch CEF, Ghazvini M, Loos F, Schelling-Kazaryan N, Widagdo W, Munshi ST *et al.* Epigenetic characterization of the FMR1 promoter in induced pluripotent stem cells from human fibroblasts carrying an unmethylated full mutation. *Stem Cell Reports* 2014; **3**: 548–555.
- 25 Schindelin J, Arganda-Carreras I, Frise E, Kaynig V, Longair M, Pietzsch T *et al.* Fiji: an open-source platform for biological-image analysis. *Nat Methods* 2012; **9**: 676–682.
- 26 Gaspard N, Bouschet T, Herpoel A, Naeije G, van den Ameel J, Vanderhaeghen P. Generation of cortical neurons from mouse embryonic stem cells. *Nat Protoc* 2009; **4**: 1454–63.
- 27 Espuny-Camacho I, Michelsen K a, Gall D, Linaro D, Hasche A, Bonnefont J *et al.* Pyramidal neurons derived from human pluripotent stem cells integrate efficiently into mouse brain circuits in vivo. *Neuron* 2013; **77**: 440–56.
- 28 Pasantes-Morales H. Volume regulation in brain cells: cellular and molecular mechanisms. *Metab Brain Dis* 1996; **11**: 187–204.
- 29 Spitzer NC. Electrical activity in early neuronal development. *Nature* 2006; **444**: 707–712.
- 30 Khazipov R, Luhmann HJ. Early patterns of electrical activity in the developing cerebral cortex of humans and rodents. *Trends Neurosci* 2006; **29**: 414–418.
- 31 Luhmann HJ, Sinning A, Yang J-W, Reyes-Puerta V, Stüttgen MC, Kirischuk S *et al.* Spontaneous Neuronal Activity in Developing Neocortical Networks: From Single Cells to Large-Scale Interactions. *Front Neural Circuits* 2016; **10**: 40.
- 32 Moore AR, Filipovic R, Mo Z, Rasband MN, Zecevic N, Antic SD. Electrical excitability of early neurons in the human cerebral cortex during the second trimester of gestation. *Cereb Cortex* 2009; **19**: 1795–805.
- 33 Frick A, Feldmeyer D, Sakmann B. Postnatal development of synaptic transmission in local networks of L5A pyramidal neurons in rat somatosensory cortex. *J Physiol* 2007; **585**: 103–16.
- 34 Oswald A-MM, Reyes AD. Maturation of intrinsic and synaptic properties of layer 2/3 pyramidal neurons in mouse auditory cortex. *J Neurophysiol* 2008; **99**: 2998–3008.
- 35 Testa-Silva G, Verhoog MB, Linaro D, de Kock CPJ, Baayen JC, Meredith RM *et al.* High bandwidth synaptic communication and frequency tracking in human neocortex. *PLoS Biol* 2014; **12**: e1002007.
- 36 Moore AR, Zhou W-L, Jakovcevski I, Zecevic N, Antic SD. Spontaneous electrical activity in the human fetal cortex in vitro. *J Neurosci* 2011; **31**: 2391–8.
- 37 Morciano M, Beckhaus T, Karas M, Zimmermann H, Volknandt W. The proteome of the presynaptic active zone: from docked synaptic vesicles to adhesion molecules and maxi-channels. *J Neurochem* 2009; **108**: 662–75.
- 38 Bayés A, van de Lagemaat LN, Collins MO, Croning MDR, Whittle IR, Choudhary JS *et al.* Characterization of the proteome, diseases and evolution of the human postsynaptic density. *Nat Neurosci* 2011; **14**: 19–21.



## SUPPLEMENTARY FIGURES



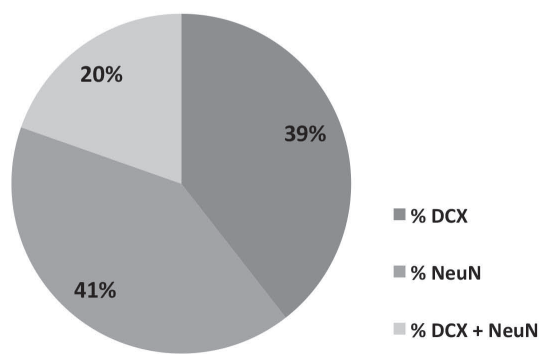
**Supplementary Figure 1. Characterization of iPSCs.** iPSCs exhibit robust expression of the pluripotency markers NANOG, TRA181, and Oct4 (scale bars = 100µm).



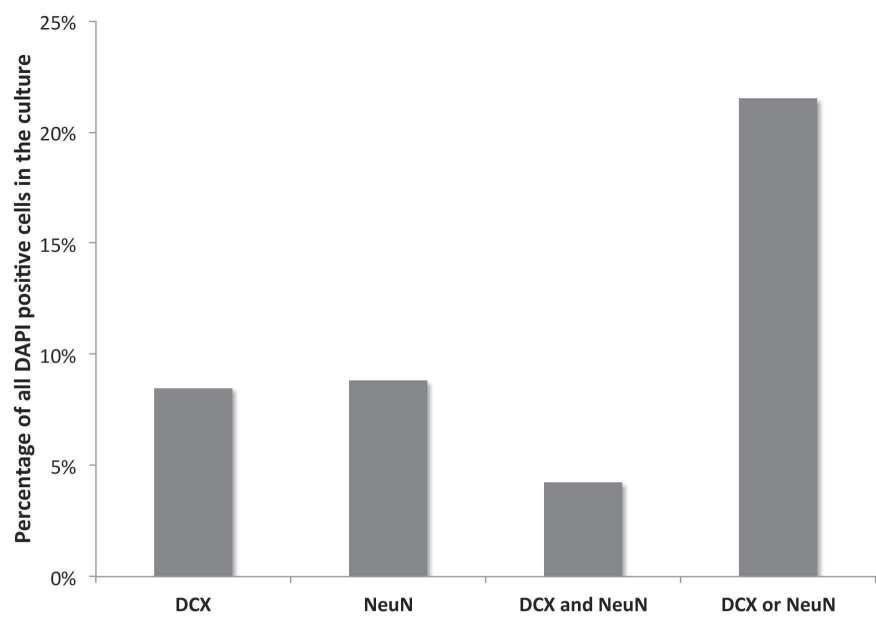
**Supplementary Figure 2. Synapse ultrastructure and neurotransmitter specification.** (a,b) Transmission electron microscopy confirms a normal synaptic ultrastructure. Asterisks indicate synaptic vesicles in presynaptic terminals. (c) Mutually exclusive expression of GABAergic and glutamatergic markers, GAD67 and CTIP2 respectively, in MAP2<sup>+</sup> neurons. (d) High magnification images of VGLUT1<sup>+</sup> and GAD67<sup>+</sup> synaptic puncta (scale bars = 3µm).

**a**

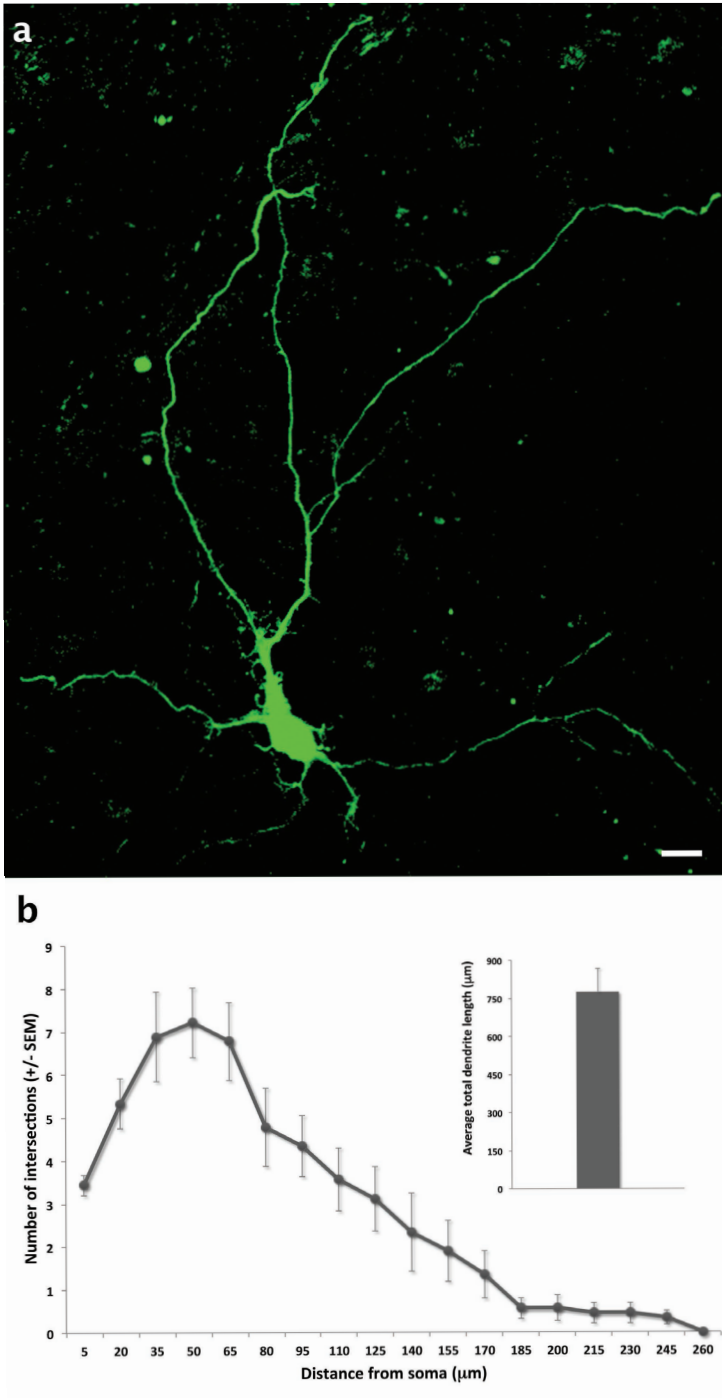
**Distribution of immature and mature neurons**



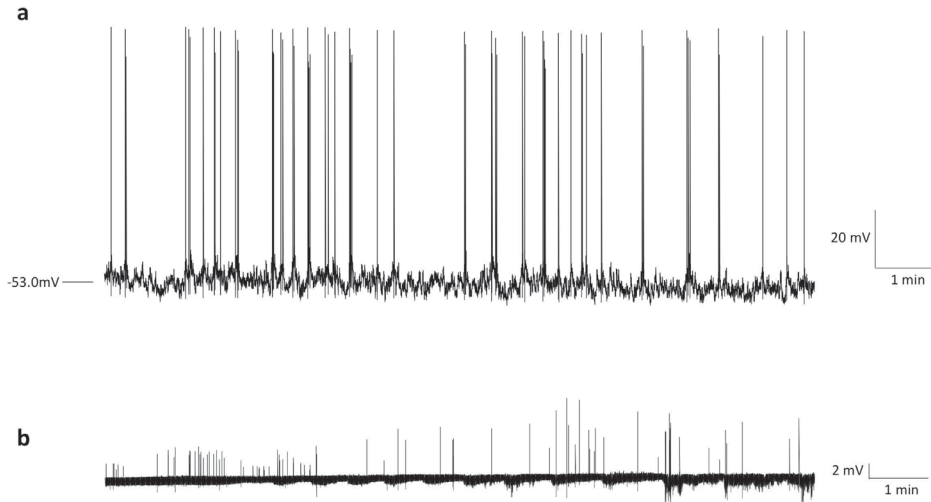
**b**



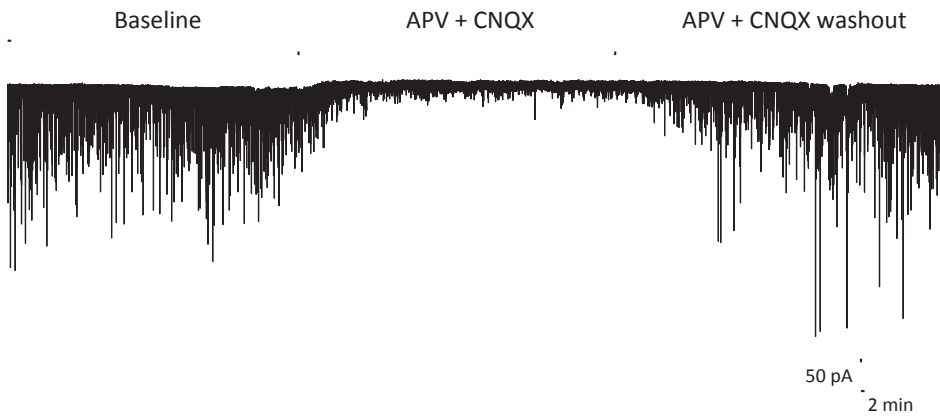
**Supplementary Figure 3. Immunohistochemical markers of neuronal maturation.** (a) Distribution of neuronal lineage differentiation subdivided between DCX<sup>+</sup> (immature) and NeuN<sup>+</sup> (mature) neurons. (b) Overall distribution of neuronal maturation within the entire population of DAPI<sup>+</sup> cells following NPC differentiation.



**Supplementary Figure 4. Neuronal morphology.** (a) Representative image of a biocytin-labelled neuron (scale bar = 10  $\mu\text{m}$ ). (b) Sholl analysis of dendritic branching and total dendrite length ( $n = 9$  neurons).



**Supplementary Figure 5. Extended recordings of spontaneous APs.** (a) Representative 12 min whole-cell recording at resting membrane potential ( $V_m = -53$  mV) demonstrating stable spontaneous AP firing. (b) Loose-patch recording (12 min) of an independent neuron demonstrating stable spontaneous AP firing, confirming that the patch-clamp configuration is not responsible for the spontaneous AP activity.



**Supplementary Figure 6. Pharmacological confirmation of synaptic activity and neurotransmitter identity.** Transient (10 min) blockade of glutamatergic AMPA and NMDA receptors through extracellular bath application of 50  $\mu$ M CNQX and 50  $\mu$ M APV strongly reduced the amplitude of spontaneous postsynaptic currents, which returned to baseline levels upon washout ( $V_m = -80$  mV).





# Chapter 3

## Identification of novel activity-dependent human *BDNF* transcripts

S.T. Munshi<sup>1</sup>, A.A. Martin<sup>1</sup>, C. Bouwkamp<sup>1</sup>, G. van Woerden<sup>2</sup>, B. Lendemeijer<sup>1</sup>, N. Günhanlar<sup>1</sup>, A.J.A. Kievit<sup>3</sup>, Y. Elgersma<sup>2</sup>, V. Bonifati<sup>3</sup>, F.M.S. de Vrij<sup>1#</sup>, S.A. Kushner<sup>1#</sup>

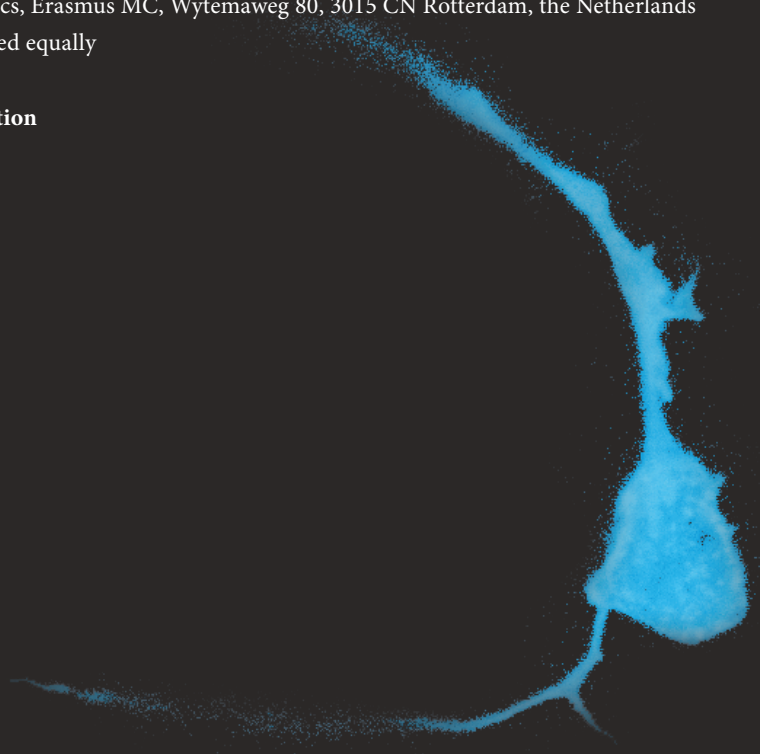
<sup>1</sup>Dept of Psychiatry, Erasmus MC, Wytemaweg 80, 3015 CN Rotterdam, the Netherlands

<sup>2</sup>Dept of Neuroscience, Erasmus MC, Wytemaweg 80, 3015 CN Rotterdam, the Netherlands

<sup>3</sup>Dept of Clinical Genetics, Erasmus MC, Wytemaweg 80, 3015 CN Rotterdam, the Netherlands

<sup>#</sup>Both authors contributed equally

**Manuscript in preparation**



## ABSTRACT

The brain-derived neurotrophic factor (*BDNF*) gene exhibits high evolutionary conservation. However, the genomic architecture of human *BDNF* is structurally and functionally more complex than in non-primate species. Few studies have investigated the transcriptional regulation of the human *BDNF* gene. Here, we demonstrate that human *BDNF* exon VIII-containing transcripts are strongly upregulated upon depolarization in multiple neural lineage cell types, most notably neural progenitor cells. Additionally, we identify three previously unreported *BDNF* exon VIII-containing transcripts (*BDNF* IV-VIII-IX, *BDNF* VIa-VIII-IX, *BDNF* VIb-VIII-IX,) that are not detected in mice, thereby bringing to 20 the total number of human *BDNF* transcripts identified to date. Lastly, we ascertained a previously unreported family with a Mendelian pattern of schizophrenia inheritance segregating a 2-basepair frameshift deletion within the coding sequence of exon VIII, providing support for the functional relevance of human *BDNF* exon VIII-containing transcripts. Our findings provide novel insight into the genomic architecture and transcriptional regulation of the human *BDNF* gene.



## INTRODUCTION

Brain-derived neurotrophic factor (*BDNF*) is a fundamental regulator of brain development facilitating proliferation, differentiation, axonal and dendritic outgrowth, synaptogenesis, synaptic functioning and plasticity of neurons<sup>1-3</sup>. There is considerable evidence that human *BDNF* dysregulation is related to neurological and psychiatric disorders<sup>4-9</sup>.

The human *BDNF* gene is highly complex which is reflected in the existence of multiple promoters, expression of multiple transcripts through alternative splicing and polyadenylation patterns, and synthesis of several *BDNF* protein precursor isoforms. The majority of prior studies on *BDNF* transcriptional regulation have been performed in rodent species, particularly *Mus musculus* (mouse) and *Rattus norvegicus* (rat). The human *BDNF* gene however has distinct features from rodent *Bdnf* (**Figure 1a**). The rodent *Bdnf* gene has 9 exons, while human *BDNF* has 11 exons. Thus far, 17 alternatively-spliced human *BDNF* transcripts have been reported (**Figure 1b**)<sup>10</sup>, whilst in both mouse and rat, 11 transcripts have been recognized. The majority of the transcripts are bipartite, containing a non-translating 5' exon spliced to a coding common-for-all 3' exon. Most known transcripts code for the same pro-*BDNF* protein, except transcripts I-IX in mouse and rats, and transcripts I-IX, VIIb-IX and VIII-IX in humans. Because of an in-frame translation start site, these transcripts allow production of an alternative longer protein called prepro-*BDNF* (**Figure 1c**).

The human *BDNF* VIII-IX transcript is a particular exception, as translation of this transcript is predicted to lead to a prepro-*BDNF* protein with a significantly longer alternative N-terminus. Interestingly, although exon VIII of rodent *Bdnf* also contains a homologous ATG, a nearby downstream 2-basepair deletion results in an intra-exonic stop codon that is out-of-frame for translation of mature *BDNF* (**Figure 1d**). The function of a potentially longer alternative N-terminus remains unknown. Recently, an independent ligand function for the pro-domain of *BDNF* was postulated<sup>11,12</sup>.

In mouse and rat, transcript *BDNF* VIII-IX is expressed at low levels in the developing brain, but prominently present in different parts of the brain in adults<sup>13</sup>. Like many of the *BDNF* transcripts in mouse and rat, its expression is activity-dependent<sup>13,14</sup>. In humans however, few studies have reported detection of *BDNF* VIII-IX expression<sup>10,15</sup> which show contradicting findings. Additionally, the transcriptional regulation of human *BDNF* VIII-IX is completely unknown.

This study focuses on human *BDNF* exon VIII-containing transcripts. Making use of human pluripotent stem cell technology, we find that exon VIII-containing transcripts are upregulated upon depolarization in neural cells and most prominently in human neural progenitor cells. Additionally, we identified two novel human *BDNF* exon VIII-containing transcripts absent in mice. Also, we identified a 2-basepair frameshift deletion in the coding part of exon VIII that segregates with schizophrenia in a family with a Mendelian pattern of disease inheritance, in support of the functional relevance of *BDNF* human exon VIII-containing transcripts.

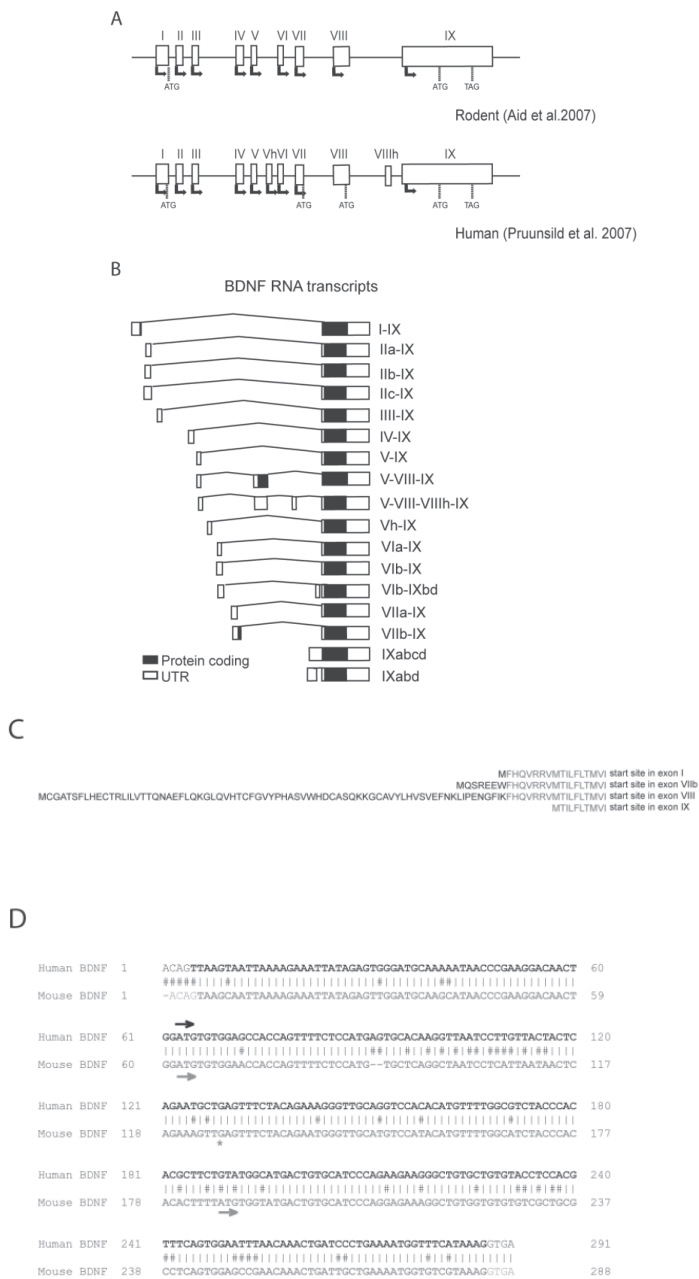


**Figure 1. Characteristics of the *BDNF* gene.** (A) Rodent and human *BDNF* gene structure. Human *BDNF* contains open-reading frames in exon VIb and VIII which are absent in mice and rats. (B) Alternative transcripts of human *BDNF*. (C) Amino acid sequences of different human prepro-*BDNF* N-termini. Amino acids encoded by exon IX are in grey and sequences encoded by alternative 5' exons are in black (adapted from Pruunsild et al. 2007<sup>16</sup>). (D) Sequence alignment of mouse and human *BDNF* exon VIII. Human *BDNF* exon VIII contains an open-reading frame while mouse *BDNF* exon VIII contains an in frame stop-codon.

## RESULTS

### Human *BDNF* exon VIII transcription exhibits strong activity-dependent regulation

Human *BDNF* exon VIII-containing transcripts were first identified by Pruunsild et al. 2007<sup>16</sup>. Moreover, they reported that exon VIII was rarely identified in *BDNF* transcripts in the adult human brain. Because of *BDNF*'s substantial involvement in neurodevelopment, we hypothesized that its appearance may be more prominent in developing neural lineages. We generated human neural progenitor cells (NPCs), neurons, and astrocytes from the H9 human embryonic stem cell (hESC) line (**Figure 2a**). Using qRT-PCR and exon-specific primers (**Table S2**) we detected *BDNF* transcripts spliced from exon VIII to IX (*BDNF* VIII-IX) at very low levels in all cell types examined. Since rodent *BDNF* is upregulated upon neuronal depolarization<sup>17,18</sup>, we hypothesized that expression of human *BDNF* exon VIII-containing transcripts may be activity-dependent. Therefore we stimulated NPCs with varying concentrations of KCl to induce depolarization (**Figure 2b**). *BDNF* transcript levels were quantified by normalizing to *GAPDH*, which we confirmed was similar between depolarized and non-depolarized conditions (mean Ct treated cultures:  $17.7 \pm 0.2$ , mean Ct untreated cultures:  $17.7 \pm 0.2$ , Student *t*-test,  $p=0.54$ ,  $n=3$ , 2 independent cultures). Compared to the Ctrl (4.2 mM) KCl concentration in the cell culture medium, *BDNF* exon VIII-containing transcripts were 10-fold and 48-fold upregulated in the 50 mM and 100 mM KCl condition, respectively (fold change 50 mM KCl:  $10.5 \pm 1.9$ , mean dCt treated cultures:  $13.9 \pm 0.3$ , mean dCt untreated cultures:  $17.2 \pm 0.3$ , Student *t*-test,  $p=1.2E-05$ ; fold change 100 mM KCl:  $48.5 \pm 2.4$ , mean dCt treated cultures:  $11.6 \pm 0.1$ , mean dCt untreated cultures:  $17.2 \pm 0.3$ , Student *t*-test,  $p=2.8E-09$ ). Total human *BDNF* levels (exon IX) were significantly upregulated in the 50 mM condition (mean relative fold change:  $2.2 \pm 0.3$ , mean dCt treated cultures:  $8.7 \pm 0.2$ , mean dCt untreated cultures:  $9.7 \pm 0.1$ , Student *t*-test,  $p<0.01$ ). Together, these findings suggest that the transcription of human *BDNF* exon VIII is strongly activity-dependent.

We next sought to examine the activity-dependence of human *BDNF* exon VIII transcription in other neural lineage cell types. To allow for the possibility of observing increased or decreased transcript levels compared to NPCs, we proceeded with the intermediate 50 mM KCl concentration (**Figure 2c**). In baseline (4.2 mM) KCl, neurons and astrocytes exhibited similarly low levels of both total and exon VIII-containing *BDNF* transcripts. However, upon administration of 50 mM KCl, exon VIII-containing *BDNF* transcript levels were significantly upregulated in neurons (relative fold change:  $9.8 \pm 2.7$ , mean dCt treated cultures:  $12.3 \pm 0.4$ , mean dCt untreated cultures:  $15.3 \pm 0.3$ , Student *t*-test,  $p<0.001$ ) and astrocytes (relative fold change:  $10.3 \pm 2.7$ , mean dCt treated cultures:  $11.6 \pm 0.6$ , mean dCt untreated cultures:  $14.5 \pm 0.2$ , Student *t*-test,  $p<0.001$ ), whereas total *BDNF* levels were 2-fold (mean relative fold change:  $1.9 \pm 0.2$ , mean dCt treated cultures:  $8.3 \pm 0.1$ , mean dCt untreated cultures:  $9.2 \pm 0.1$ , Student *t*-test,  $p<0.001$ ) and 3-fold (mean relative fold change:  $3.0 \pm 0.8$ , mean dCt treated cultures:  $7.1 \pm 0.5$ , mean dCt untreated cultures:  $8.3 \pm 0.4$ , Student *t*-test,  $p=0.06$ ) upregulated in

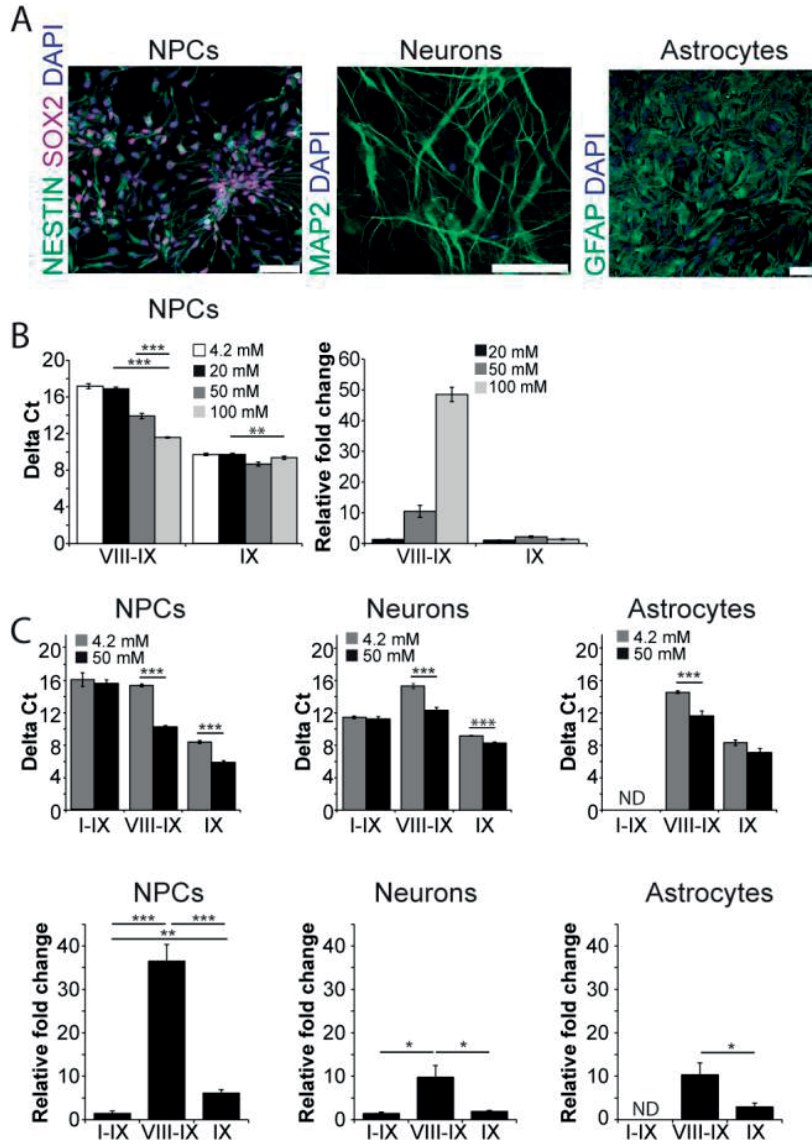


**Figure 2. BDNF exon VIII is upregulated upon depolarization in human neural lineages.** (A) Immunostainings of NPCs for SOX2 and nestin, and neurons for MAP2, and astrocytes for GFAP derived from H9 hESCs. Scale bars, 50  $\mu$ m. (B) NPCs were treated for 3hs with 20 mM, 50 mM or 100 mM KCl and *BDNF* expression was measured by qRT-PCR using transcript-specific primers, normalized to *GAPDH* transcript levels. Delta Ct values and relative fold change values are shown. Relative fold change values are calculated with respect to untreated cultures. (C) NPCs, neuronal cultures and astrocytes were treated for 3hs with 50 mM KCl and *BDNF* expression was measured by qRT-PCR using transcript-specific primers, normalized to *GAPDH* transcript levels. Delta Ct and relative fold change values are shown. Relative fold change values are calculated with respect to untreated cultures. Error bars represent SEM. Statistical significance is denoted by asterisks (\*\*\* $p$ <0.001; \*\* $p$ <0.01; \* $p$ <0.05; NS; Student *t*-test, ANOVA).

neuronal cultures and astrocytes. The *BDNF* I-IX transcript, previously shown to be strongly upregulated in rodent neurons following depolarization<sup>18–20</sup>, was not upregulated in human neurons following depolarization (mean dCt treated cultures:  $11.3 \pm 0.3$ , mean dCt untreated cultures:  $11.5 \pm 0.2$ , Student *t*-test,  $p=0.58$ ) and was undetectable in human astrocytes.

In order to further validate our findings, we performed multiple additional replications. First, we repeated the quantification of *BDNF* VIII-IX levels with a new primer set containing no overlapping primer sequence compared to those originally used. Results using this additional primer pair was highly similar in all three neural lineage cell types to those obtained with the initial *BDNF* VIII-IX primers (**Figure S1a**). Second, we repeated the experiment using human iPSC-derived NPCs, which showed similar results as H9-derived cultures (**Figure S1b**), thereby confirming that our findings appear to be generalizable, at least among human pluripotent stem cell-derived neural progenitors. Third, in order to ensure that the observed activity-dependent upregulation of *BDNF* VIII-IX is not the result of excitotoxicity due to the administration of increased extracellular KCl, we exposed NPCs to 50 mM KCl for 3h and then replaced the culture medium with baseline (4.2 mM) KCl (**Figure S1c**). *BDNF* VIII-IX and total *BDNF* levels were measured at 3 and 18hs following medium replacement. *GAPDH* levels remained unchanged. Moreover, both *BDNF* VIII-IX and IX levels returned to baseline within three hours, thereby suggesting that upregulation of *BDNF* VIII-IX was not associated with excitotoxicity.

Taken together, transcriptional activation of *BDNF* exon VIII is strongly activity-dependent in multiple human neural lineage cell types, including neurons, astrocytes, and neural progenitors.

### No evidence for activity-dependent regulation of mouse *Bdnf* exon VIII

The *Bdnf* VIII-IX transcript has been previously reported in mice<sup>13</sup>. However, it remains unknown whether activity-dependent regulation of human *BDNF* exon VIII is also observed for the mouse *Bdnf* gene. We exposed human ES-derived NPCs, mouse ES-derived NPCs, and mouse primary hippocampal neurons to 50 mM KCl for 3h. *BDNF* VIII-IX, I-IX, and IX transcript levels were robustly increased in human NPCs (**Figure 3a,b**). In contrast, *Bdnf* IX levels were decreased in mouse NPCs (mean relative fold change:  $4.2 \pm 0.2$ , mean dCt treated:  $8.1 \pm 0.1$ , mean dCt untreated:  $6.1 \pm 0.4$ , Student *t*-test,  $p<0.01$ ), while *Bdnf* I-IX and VIII-IX transcripts were undetectable at baseline and following 50 mM KCl. Moreover, although *Bdnf* IX (mean relative fold change:  $2.4 \pm 0.6$ , mean dCt treated:  $1.16 \pm 0.3$ , mean dCt untreated:  $2.3 \pm 0.2$ , Student *t*-test,  $p<0.05$ ) and *Bdnf* I-IX (mean relative fold change:  $5.2 \pm 2.3$ , mean dCt treated:  $1.7 \pm 0.5$ , mean dCt untreated:  $3.6 \pm 0.3$ , Student *t*-test,  $p<0.01$ ) were upregulated in mouse primary hippocampal neurons following 50 mM KCl, *Bdnf* VIII-IX remained undetectable. Therefore, the robust activity-dependent regulation of human *BDNF* VIII-IX does not appear to extend to mice.

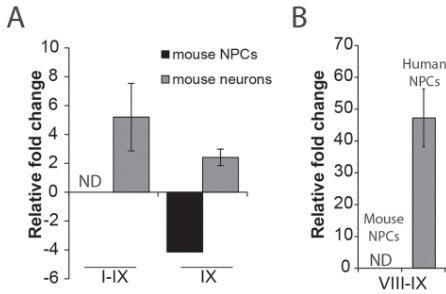


**Figure 3. No detection of *BDNF* exon VIII in depolarized neural lineages of mice.** (A, B) Mouse and human NPCs as well as primary mouse neurons were treated for 3hs with 50 mM KCl. *BDNF* expression was measured by qRT-PCR using transcript-specific primers. *BDNF* VIII-IX was measured using a primer pair that recognized mouse and human *BDNF* VIII-IX. Fold changes are relative to untreated cultures. Error bars represent SEM.

### Identification of novel human *BDNF* exon VIII-containing transcripts

Pruunsild et al. 2007 reported human *BDNF* exon VIII to be contained within a tripartite transcript in which the transcriptional start site was exclusively contained within exon V<sup>16</sup>. Despite using multiple independent primer pairs for PCR and qPCR, we were unable to detect *BDNF* V-VIII-containing transcripts in human pluripotent stem cell-derived neural lineage cell types. Therefore, we designed primers to measure hypothetical transcripts starting from all possible upstream exons spliced to exon VIII. Using human NPCs, we found transcripts joining exon IV to exon VIII and exon VI to exon VIII (**Figure 4a**), both of which were upregulated following 50 mM KCl depolarization. Sanger sequencing of the PCR products confirmed that exons IV, and VI (VIa and VIb) each spliced to exon VIII. Next, we tested if these transcripts were also present in neuronal cultures and astrocytes. Upon depolarization with 50 mM KCl, all three exon VIII-containing transcripts (*BDNF* IV-VIII-IX, *BDNF* VIa-VIII-IX and *BDNF* VIb-VIII-IX) were upregulated in human NPCs, neuronal cells and astrocytes (**Figure 4b**, **Table S1**). These findings establish three activity-dependent human *BDNF* transcripts that to our knowledge have not been previously reported.

### Candidate pathogenic variant in exon VIII segregating with the development of schizophrenia in a Dutch family

We ascertained a family of Dutch ancestry with a Mendelian pattern of inheritance for schizophrenia (SCZ) (**Figure 5**). No copy number variants were identified that segregated with the disease. Parametric linkage analysis under an autosomal dominant model yielded ~407 Mb of shared genomic regions (**Table S3**). Whole exome sequencing was performed in three individuals (**Figure 5**, PED IDs 1, 2, 5) at 100x average genomic coverage. The results of linkage analysis were used to filter the exome data for heterozygous variants within the genomic regions shared among the affected individuals. The resulting variants were filtered for those with minor allele frequency <0.1%, predicted to affect protein coding, called in both affected individuals while absent in the unaffected father, and absent from dbSNP129. In the resulting list of variants (**Table 1**), only one heterozygous variant stood out to potentially result in a severe loss-of-function, within a loss-of-function intolerant gene (pLI  $\geq 0.9$ <sup>21</sup> in Exome Aggregation Consortium browser, ExAC)<sup>22</sup>: a frameshift mutation involving a 2-base

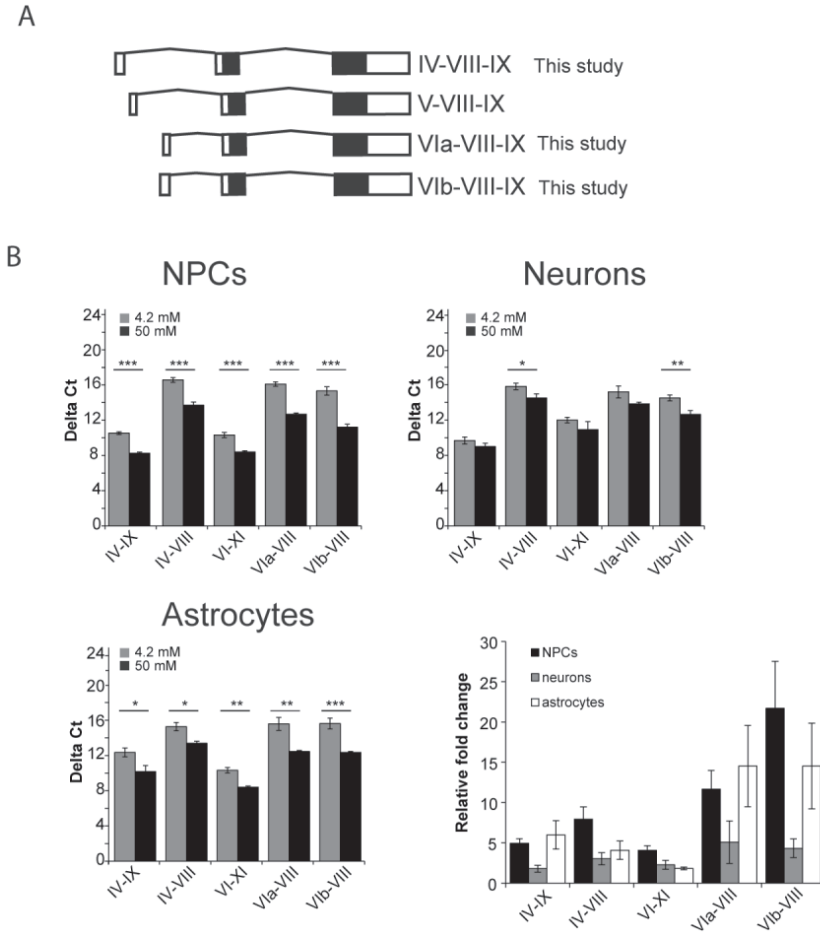


**Figure 4. Detection of novel, activity-dependent exon VIII-containing transcripts.** (A) Newly discovered *BDNF* transcripts in human neural lineages. (B) Human NPCs, neurons and astrocytes were treated for 3hs with 50 mM KCl. *BDNF* expression was measured by qRT-PCR using transcript-specific primers. Delta Ct and relative fold change values are shown. Relative fold change values are calculated with respect to untreated cultures. Error bars represent SEM. Statistical significance is denoted by asterisks (\*\*\* $p$ <0.001; \*\* $p$ <0.01; \* $p$ <0.05; NS; Student *t*-test, ANOVA).

pair deletion in *BDNF* exon VIII (Chr11:27,695,731-27,695,733, cDNA position c.99\_100del2, p.Cys34PhefsTer12, **Table 1**). Sanger sequencing confirmed the presence of the mutation in all affected family members for whom DNA was available. In addition, one unaffected family member was also found to carry the same mutation, consistent with incomplete penetrance. We found the same mutation in the Swedish Schizophrenia Exome Sequencing Study (db-GAP; phs000473.v1.p1)<sup>23</sup> but the mutation was not enriched in cases vs controls (case:carriers 2536:0, control:carriers 2543:2, Fisher's Exact Test,  $p$ =0.4999).

Table 1, candidate variants in Dutch family with high incidence of schizophrenia.

Chr	Start	End	Gene	Ref	Alt	Zygosity	RS-number	cDNA	prot. pos.	Amino acid change	Mutation type	Amino acid change	Exac frequency (non-Finnish Europeans)	pLI score (ExAC)
11	27695731	27695733	BDNF	CAT	C	het	n/a	242	34	C34PhefsTer12	frameshift	C34PhefsTer12	0.0009052	0.95
4	1348905	1348905	UVSSA	C	T	het	n/a	1495	350	R350C	Nonsynonymous (missense,splicing)	R/C	1.55E-05	0.00
5	86703854	86703854	CCNH	T	G	het	rs199815978	689	155	N155T	Nonsynonymous (missense)	N/T	4.50E-05	0.00
8	17503464	17503464	MTUS1	A	G	het	rs202148873	1845	509	F509L	Nonsynonymous (missense)	F/L	0.0002013	0.00
8	94811972	94811972	TMEM67	A	G	het	n/a	2298	743	I743V	Nonsynonymous (missense)	I/V	absent	0.00
10	128974407	128974407	FAM196A	G	A	het	rs549319983	809	85	R85C	Nonsynonymous (missense)	R/C	0.0001349	0.85
11	33374977	33374977	HIPK3	C	T	het	n/a	3718	1150	R1150C	Nonsynonymous (missense)	R/C	0	0.89
12	105605088	105605088	APPL2	A	G	het	n/a	511	98	L98P	Nonsynonymous (missense)	L/P	absent	0.00
19	13915689	13915689	ZSWIM4	C	T	het	rs375720071	628	147	R147C	Nonsynonymous (missense)	R/C	absent	0.17
19	56538591	56538591	NLRP5	G	T	het	rs369791138	992	331	S331I	Nonsynonymous (missense)	S/I	0.0002152	0.00



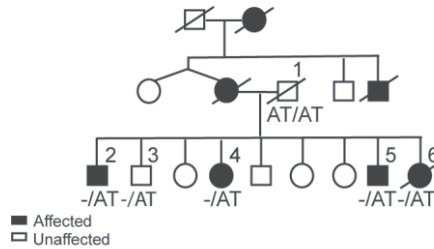


**Figure 5. Familial segregation of *BDNF* mutation with schizophrenia.** Pedigree of discovery family with schizophrenia. Number 1 to 5 (PED ID) indicate participating individuals. -/AT, heterozygous carrier of the *BDNF* c.99\_100del2 mutation (*BDNF*<sup>Cys34PhefsTer12</sup>), AT/AT, homozygous reference.

## DISCUSSION

Here we report the identification of novel activity-dependent human *BDNF* transcripts in pluripotent stem cell-derived neural lineage cell types. We focused on exon VIII-containing transcripts potentially encoding a prepro-*BDNF* isoform with a long alternative N-terminus. We show that exon VIII-containing transcripts levels are expressed at low baseline levels in human NPCs, neurons and astrocytes. However, upon KCl-induced depolarization the expression of exon VIII-containing transcripts increased substantially in all three cell types, and most prominently in NPCs. Lastly, we identified a 2-base pair frameshift deletion in *BDNF* exon VIII exhibiting familial co-segregation with SCZ, highlighting the potential functional relevance of human *BDNF* exon VIII-containing transcripts.

We measured *BDNF* transcripts in human pluripotent stem cell derived-NPCs, neurons, and astrocytes. To the best of our knowledge, these results are the first to report the activity-dependent regulation of *BDNF* in human neural lineage cell types. Our findings suggest that human NPCs, neurons, and astrocytes exhibit robust upregulation of *BDNF* expression upon KCl depolarization. The largest increase (over 30-fold upregulation) of exon VIII-containing transcript expression was found in NPCs suggesting that *BDNF* exon VIII-IX transcripts may have a particularly important function during neurodevelopment. Importantly, the strong response in upregulation was confirmed using multiple independent primer sets and in NPCs derived from both ES and iPSC cell lines.

Using primers compatible with detection of both human and mouse exon VIII-containing transcripts, we could not detect *Bdnf* VIII-IX in mouse neuronal lineage cell types. Although Aid et al. 2007 report the presence of *Bdnf* VIII-IX in developing and adult mouse brain<sup>13</sup>, we could not detect *Bdnf* VIII-IX expression in either mouse ES-derived NPCs or primary hippocampal mouse neurons. Notably, a recent report also failed to detect *Bdnf* VIII-IX expression in primary hippocampal mouse neurons<sup>24</sup>. However, since Aid et al. 2007 used brain lysates, we cannot exclude that other brain cell types may express *Bdnf* VIII-IX<sup>15</sup>. Species-specific regulation of the other *BDNF* transcripts was also observed. Although several studies report

robust increases of *BDNF* I-IX, IV-IX and VI-IX in rodent neurons upon depolarization<sup>18–20,25</sup>, we could detect upregulation of *BDNF* I-IX, IV-IX or VI-IX in human neurons. Although *BDNF* I-IX was undetectable in mouse NPCs, it was present in human NPCs but without evidence of strong activity-dependent regulation. *BDNF* I-IX was undetectable in human astrocytes, both under standard baseline conditions as well as following KCl depolarization. Expression of *BDNF* transcripts IV-IX and VI-IX was activity-dependent, but only in NPCs and astrocytes. Moreover, we observed an unexpected decrease of total *Bdnf* expression in mouse NPCs following KCl depolarization. Overall, these data show marked differences in the regulation of human *BDNF* expression compared to mouse. Earlier results already hinted towards dissimilar time course of upregulation, level of upregulation and relative ratios of transcripts in depolarized and non-depolarized condition between human and mouse cells<sup>18</sup>. Nonetheless, as stem cell-derived cells represent at best first trimester human cells<sup>26,27</sup>, *BDNF* transcript expression may be different in more mature neural lineages.

A prior study reported the identification of a human *BDNF* exon V-VIII-IX transcript in adult brain tissue<sup>10,15</sup>. Although we could not detect this transcript in human NPCs, neurons, or astrocytes, we did find expression of three novel human *BDNF* transcripts: *BDNF* IV-VIII-IX, VIa-VIII-IX and VIb-VIII-IX. Taken together, these results suggest that the expression of human *BDNF* transcripts is likely to be neurodevelopmentally-regulated<sup>28</sup>, for which transcripts IV-VIII-IX and VI-VIII-IX may predominantly be expressed in the developing brain, while transcript V-VIII-IX is more abundant in the adult brain. Moreover, given the activity-dependent expression of human *BDNF*, it is not unreasonable to presume that additional transcripts may also remain to be identified. For example, given the quadripartite transcript V-VIII-VIIIh-IX<sup>10</sup>, IV-VIII-VIIIh-IX and VI-VIII-VIIIh-IX splicing are not unlikely to be found. Moreover, as rodents express a bipartite *Bdnf* VIII-IX transcript, it is possible that human exon VIII may also contain an analogous transcriptional initiation site. *In silico* prediction algorithms indeed annotate the likely existence of human *BDNF* VIII-IX transcripts (XM\_011520280.2), but empirical confirmation has not yet been realized.

The function of the various human *BDNF* 5' UTRs remain poorly characterized. In rodents, several 5' UTRs have been shown to influence transcript localization and facilitate localized translation<sup>29–31</sup>. In rats, exon IV-containing transcripts are found in proximal dendrites, whereas exon VI-containing transcripts are targeted to distal dendrites. Exon VIII-containing transcripts remain in the soma<sup>31</sup>. 5' UTRs also influence the amount of protein produced. Several elements in the 5' UTR are involved in regulating translation levels such as secondary structures, multiple open-reading frames, upstream open-reading (uORF) frames and internal ribosomal entry-sites (IRES)<sup>32</sup>. Exon IV, VI and VIII contain several uORFs<sup>33</sup> and IRES sequences<sup>34</sup>. uORFs downregulate expression of the main ORF<sup>35</sup>, whereas IRES sequences facilitate translation initiation after the ribosomal complex has disengaged. Of note, exon VIII-containing transcripts have two open-reading frames. Given that the effectivity of an AUG as start-site depends on the context nucleotides surrounding it<sup>36</sup>, the in-frame AUG

in exon VIII lies in a weak context for translation initiation<sup>10</sup>, whereas the AUG in exon IX occurs within a more classical translation initiation sequence. The mechanisms underlying the post-transcriptional regulation of the various human *BDNF* transcripts remain an important topic to be unraveled further.

Another open question concerns the downstream processing of exon VIII prepro-*BDNF* protein. Pro*BDNF* contains a highly conserved ER-localization signal (KAAP) that mediates its translocation over the ER membrane<sup>37</sup>. The pro-domain of *BDNF* also influences packaging and sorting in the Golgi as well as secretion<sup>38–40</sup>. *In silico* prediction by the SignalP 4.1 server<sup>41</sup> does not indicate an ER-localization signal in exon VIII prepro-*BDNF*. It remains to be determined empirically if the pre-domain of *BDNF* VIII-IX contains an ER-localization signal and what its effect may be on translocation, the amount of protein synthesized and secreted, sensitivity towards convertases, and where along the secretion path it might be cleaved. Likewise, its ability to form homo or heterodimers with other *BDNF* protein isoforms, as well as its consequences for secretion, remains to be determined.

Many studies have proposed an association between genetic variation in *BDNF* and SCZ pathophysiology<sup>42,43</sup>. Differential expression of *BDNF* has been reported in postmortem brain tissue and serum of SCZ patients<sup>42,43</sup>. Several antipsychotics appear to alter *BDNF* levels<sup>44</sup>. Moreover, SCZ is widely considered a disease of neurodevelopment<sup>45</sup>, in which synaptic dysfunction is a prominent pathophysiological mechanism<sup>46,47</sup>. Extensive findings have demonstrated the critical importance of *BDNF* in synaptic plasticity<sup>2,48–50</sup>. However studies on *BDNF* and SCZ have yielded inconsistent results<sup>42,43,51,52</sup>, leaving open the question of whether and the extent to which variation in *BDNF* might influence SCZ disease risk or its phenotypic manifestation.

We identified a frameshift mutation in the *BDNF* protein coding part of exon VIII that segregated with SCZ in a Dutch family. However, we did not find enrichment for the mutation in cases in the Swedish Schizophrenia Exome Sequencing Study (dbGAP; phs000473.v1.p1)<sup>23</sup>. Incomplete penetrance of the mutation could be a reason for the lack of enrichment in the Swedish Schizophrenia Exome Sequencing Study. Next to this, severe loss-of-function mutations in *BDNF* are extremely rare (ExAC pLI=0.95)<sup>22</sup>. This indicates that *BDNF* has extreme selective constraints for functional alterations. As such, heterozygous mutation carriers may be at elevated risk for SCZ. Moreover, no homozygous individuals for this alternate allele have yet been found<sup>22</sup>. To prove causality however additional genetic and functional evidence are needed.

In conclusion, in this study we examined the transcriptional regulation of human *BDNF* exon VIII-containing transcripts. We find exon VIII-containing transcripts to be upregulated upon depolarization in human neural cells, particularly NPCs. We identified three novel exon VIII-containing human *BDNF* transcripts and find a loss-of-function mutation in exon VIII exhibiting familial co-segregation with SCZ, suggesting the neurobiological significance of human *BDNF* exon VIII-containing transcripts.

## EXPERIMENTAL PROCEDURES

### Cell culture

H9 human embryonic stem cells (hESCs) were maintained on mouse embryonic fibroblasts (MEFs) according to standard protocols<sup>53</sup>. Induced pluripotent stem cells (iPSCs) were reprogrammed from human primary skin fibroblasts (female, age 54) according to Warlich et al. using a single, multicistronic lentiviral vector encoding OCT4, SOX2, KLF4, and MYC<sup>54,55</sup>. The donor provided written informed consent in accordance with the Medical Ethical Committee of the Erasmus University Medical Center. Quality control of iPSC clones was performed by karyotyping, real-time quantitative PCR and embryoid body differentiation<sup>55,56</sup>.

Neural progenitor cells (NPCs) were generated according to previous publications<sup>55,57</sup>. In short, ES and induced pluripotent stem cell (iPSC) colonies were dissociated from MEFs with collagenase. iPSC colonies were transferred to non-adherent plates for embryoid body (EB) formation. For two days EBs were grown in human ES medium after which the medium was replaced with neural induction medium for an additional 4 days in suspension. To obtain NPCs, EBs were slightly triturated at day 7 and plated onto laminin-coated 10 cm dishes in neural induction medium for 8 days. At day 15, cells were considered pre-NPCs (passage one, p1). NPCs between p6 and p9 were used for experiments. Neuronal cultures were generated by terminally differentiating p6-9 NPCs according to Gunhanlar et al. 2017<sup>55</sup>. In brief, NPCs were plated on polyornithine/laminin-coated coverslips in neuronal differentiation medium. After 4 weeks of differentiation, only half of the medium of the cultures was replenished. Neuronal cultures were differentiated for 8-10 weeks. For generation of astrocyte cultures, NPCs (p5-p10) were differentiated for 3 weeks in NPC medium supplemented with human LIF (10 ng/ml, Peprotech) and human BMP4 (10 ng/ml, Biovision)<sup>58</sup>. Mouse NPCs were derived from 46C embryonic stem cells<sup>59</sup> and cultured as described in Conti et al. 2005<sup>60</sup>. For mouse primary neuronal cultures, FvB/NHsD females were crossed with FvB/NHsD males (both ordered at 8-10 weeks old from Envigo) and isolated at E18 according Banker and Goslin, 1998<sup>61</sup>. All animal procedures were approved by the local institutional review board and Dutch Animal Ethical Committee.

### Quantitative real-time PCR

RNA was isolated from cell cultures using the RNeasy mini kit (Qiagen) or Allprep RNA/protein kit (Qiagen) according manufacturer instructions. RNA quality was assessed with nanodrop (A260/A280>2.0, A260/A230 2.0-2.2) and rRNA was checked with gel electrophoresis for a 28S/18S ratio of 2:1. RNA was stored at -80°C. First-strand cDNA synthesis was performed with the iScript (<sup>™</sup>) cDNA Synthesis kit (BioRad) according to the manufacturer's protocol with 300 ng RNA template and stored at -20°C. Quantitative RT-PCR primers were designed with Primer Express and Primer3Plus. All primers were blasted and were not homologous to other targets than the one intended. RT-PCR amplification mixtures (20 µl) contained 3-15

ng template cDNA, 7.5 µl 2x Sybr® Green PCR Master mix (Applied Biosciences), 2.5 µl H<sub>2</sub>O and 20 nM forward and reverse primer. For each primer pair a 4-step 2-fold dilution curve was made to check for replication efficiency, except for *GAPDH* where a 10-fold dilution curve was made. Efficiency between 75-100% was measured (**Table S2**). Reactions were run on an ABI 7300 (Applied Biosystems) in microseal PCR plates (MSS9601, Bio-Rad). The cycling conditions comprised 10 min polymerase activation at 95°C, 40 cycles at 95°C for 15 sec, 60°C for 60 sec followed by one cycle of 10 sec at 95°C, 60 sec at 60°C, 15 sec at 95°C, and 60°C for 15 sec. Each assay contained a no-template control, where average  $\leq 5$  cycle threshold (Ct) cycles was accepted as the threshold. The detection limit was set to Ct=34, above which signals could not be measured reliably. Per plate, three technical replicates were measured. Ct values were determined by automatically determining the threshold and background values using the ABI7300 SDS software (version 1.3). SDS results were exported as tab-delimited text files and imported into Microsoft Excel 2010 for further analysis.

### Statistical analysis

Each set of experiments was performed in duplicate in n=3 wells for both treated and non-treated conditions. Delta Ct values (dCt) were determined by subtracting *GAPDH* Ct values from the Ct values of the transcript of interest. Delta dCt (ddCt) values were calculated by subtracting average dCt values in non-treated conditions from each individual dCt value in treated conditions. Delta dCt values were transformed to relative fold change values using the following formula:  $2^{(-ddCt)}$ . Statistical analysis was performed by unpaired Student *t*-test using Microsoft Excel 2010. Differences were considered statistically significant if the P-value was  $<0.05$ .

### Immunocytochemistry

Cell cultures were fixed using 4% formaldehyde in PBS. Primary antibodies were incubated overnight at 4°C in labelling buffer containing 0.05 M Tris, 0.9% NaCl, 0.25% gelatin, and 0.5% Triton-X-100 (pH 7.4). The following primary antibodies were used: SOX2, Nestin, MAP2, GFAP (Millipore); secondary antibodies Alexa-488 and Cy3 were used (Jackson ImmunoResearch). Samples were embedded in Mowiol 4-88 (Sigma-Aldrich) after which images were obtained with Zeiss LSM700 confocal microscope using ZEN software (Zeiss, Germany).

### Genetic analyses

A non-consanguineous family of Dutch ancestry was identified with a pattern of SCZ inheritance compatible with autosomal dominant transmission. Linkage and copy number variant (CNV) analysis was performed with Illumina HumanOmniExpress 700k SNP-arrays on DNA isolated from venous blood. Linkage analysis was performed using an autosomal dominant affected-only model with an assumption that the pathogenic allele was inherited through the affected mother. Linkage analysis was conducted for the purpose of identifying

the genome-wide set of chromosomal regions shared by all affected family members. This analysis revealed a total of ~407 Mb of shared genomic region (**Table S3**). Linkage analysis was performed using Allegro<sup>62</sup>. CNV analysis was performed using NEXUS discovery edition, version 7 (BioDiscovery, El Segundo, CA). Whole exome sequencing was performed on two affected siblings and their unaffected father (**Figure 8**, PED IDs 1, 2 and 5) at 90x average coverage. Exome sequencing was performed using in-solution capture (Agilent SureSelect V4 Human 50 Mb kit, Agilent Technologies) and paired-end sequencing on an Illumina Hi-Seq 2000 sequencer at LGC Berlin. Reads were aligned to the human reference genome version 19 using Burrows-Wheeler Aligner. SNPs and indels were called using the Genome Analysis Toolkit (GATK). The heterozygous variants were filtered based on the following criteria: a) present within the shared genomic regions, b) predicted to affect protein coding (missense, nonsense, frameshift, splice site), c) called in both affected individuals (Ped IDs 2 and 5) and absent from their unaffected father (Ped ID 1), d) absent from dbSNP129, and e) with a minor allele frequency (MAF) of < 0.1% in public databases 1000G<sup>63</sup>, ExAC<sup>22</sup>, GoNL<sup>64</sup>. The remaining variants for all participating family members were genotyped by Sanger sequencing (for primers, see **Table S4**).

## ACKNOWLEDGEMENTS

We thank Martí Quevedo Calero and Raymond Poot for providing mouse NPCs.

## REFERENCES

1. Murer, M., Yan, Q. & Raisman-Vozari, R. Brain-derived neurotrophic factor in the control human brain, and in Alzheimer's disease and Parkinson's disease. *Prog. Neurobiol.* **63**, 71–124 (2001).
2. Panja, D. & Bramham, C. R. BDNF mechanisms in late LTP formation: A synthesis and breakdown. *Neuropharmacology* **76 Pt C**, 664–76 (2014).
3. Zagrebelsky, M. & Korte, M. Form follows function: BDNF and its involvement in sculpting the function and structure of synapses. *Neuropharmacology* **76 Pt C**, 628–38 (2014).
4. Martínez-Levy, G. a & Cruz-Fuentes, C. S. Genetic and epigenetic regulation of the brain-derived neurotrophic factor in the central nervous system. *Yale J. Biol. Med.* **87**, 173–86 (2014).
5. Boule, F. *et al.* Epigenetic regulation of the BDNF gene: implications for psychiatric disorders. *Mol. Psychiatry* **17**, 584–96 (2012).
6. Castrén, M. L. & Castrén, E. BDNF in fragile X syndrome. *Neuropharmacology* **76 Pt C**, 729–36 (2014).
7. Li, W. & Pozzo-Miller, L. BDNF deregulation in Rett syndrome. *Neuropharmacology* **76 Pt C**, 737–46 (2014).
8. Buckley, P. F., Pillai, A. & Howell, K. R. Brain-derived neurotrophic factor: findings in schizophrenia. *Curr. Opin. Psychiatry* **24**, 122–7 (2011).
9. Autry, A. E. & Monteggia, L. M. Brain-derived neurotrophic factor and neuropsychiatric disorders. *Pharmacol Rev* **64**, 238–258 (2012).
10. Pruunsild, P., Kazantseva, A., Aid, T., Palm, K. & Timmusk, T. Dissecting the human BDNF locus: bidirectional transcription, complex splicing, and multiple promoters. *Genomics* **90**, 397–406 (2007).
11. Yang, B. *et al.* Regional differences in the expression of brain-derived neurotrophic factor (BDNF) pro-peptide, proBDNF and preproBDNF in the brain confer stress resilience. *Eur. Arch. Psychiatry Clin. Neurosci.* **266**, 1–5 (2016).
12. Anastasia, A. *et al.* Val66Met polymorphism of BDNF alters prodomain structure to induce neuronal growth cone retraction. *Nat. Commun.* **4**, 2490 (2013).
13. Aid, T., Kazantseva, A., Piirsoo, M. & Palm, K. Mouse and Rat BDNF Gene Structure and Expression Revisited. *J of Neuroscience res.* **535**, 525–535 (2007).
14. Baj, G. *et al.* Regulation of the spatial code for BDNF mRNA isoforms in the rat hippocampus following pilocarpine-treatment: A systematic analysis using laser microdissection and quantitative real-time PCR. *Hippocampus* **000**, 1–11 (2013).
15. Herrfurth, N. *et al.* Relevance of polymorphisms in MC4R and BDNF in short normal stature. *BMC Pediatrics* **18:278**, 5–9 (2018).
16. Pruunsild, P., Kazantseva, A., Aid, T., Palm, K. & Timmusk, T. Dissecting the human BDNF locus: bidirectional transcription, complex splicing, and multiple promoters. *Genomics* **90**, 397–406 (2007).
17. Vaghi, V. *et al.* Pharmacological Profile of Brain-Derived Neurotrophic Factor (BDNF) Splice Variants Translation Using a Novel Drug Screening Assay: a "Quantitative Code". *J. Biol. Chem.* (2014). doi:10.1074/jbc.M114.586719
18. Pruunsild, P., Sepp, M., Orav, E., Koppel, I. & Timmusk, T. Identification of cis-elements and transcription factors regulating neuronal activity-dependent transcription of human BDNF gene. *J. Neurosci.* **31**, 3295–308 (2011).
19. Marmigère, F., Rage, F. & Tapia-Arancibia, L. Regulation of brain-derived neurotrophic factor transcripts by neuronal activation in rat hypothalamic neurons. *J. Neurosci. Res.* **66**, 377–89 (2001).
20. Koppel, I. *et al.* Tissue-specific and neural activity-regulated expression of human BDNF gene in BAC transgenic mice. *BMC Neurosci.* **10**, 68 (2009).

21. Pardiñas, A. F. *et al.* Common schizophrenia alleles are enriched in mutation-intolerant genes and in regions under strong background selection. *Nat. Genet.* **50**, 381–389 (2018).
22. Lek, M. *et al.* Analysis of protein-coding genetic variation in 60,706 humans. *Nature* **536**, 285–291 (2016).
23. Purcell, S. M. *et al.* A polygenic burden of rare disruptive mutations in schizophrenia. *Nature* **506**, 185–190 (2014).
24. Rousseaud, A., Delépine, C., Nectoux, J., Billuart, P. & Bienvenu, T. Differential Expression and Regulation of Brain-Derived Neurotrophic Factor (BDNF) mRNA Isoforms in Brain Cells from Mecp2308/y Mouse Model. *J. Mol. Neurosci.* **56**, 758–767 (2015).
25. Tao, X., Finkbeiner, S., Arnold, D. B., Shaywitz, A. J. & Greenberg, M. E. Ca<sup>2+</sup> influx regulates BDNF transcription by a CREB family transcription factor-dependent mechanism. *Neuron* **20**, 709–726 (1998).
26. Mariani, J., Vittoria, M., Palejev, D. & Tomasini, Livia; Coppola, G.; Szekeley, A.M.; Horvath, T.L.; Vaccarino, M. V. Modeling human cortical development in vitro using induced pluripotent stem cells. *Proc. Natl. Acad. Sci.* **109**, 12770–12775 (2012).
27. van de Leemput, J. *et al.* CORTECON: A Temporal Transcriptome Analysis of In Vitro Human Cerebral Cortex Development from Human Embryonic Stem Cells. *Neuron* **83**, 51–68 (2014).
28. Wong, J., Webster, M. J., Cassano, H. & Weickert, C. S. Changes in alternative brain-derived neurotrophic factor transcript expression in the developing human prefrontal cortex. *Eur. J. Neurosci.* **29**, 1311–22 (2009).
29. Chiaruttini, C., Sonogo, M., Baj, G., Simonato, M. & Tongiorgi, E. BDNF mRNA splice variants display activity-dependent targeting to distinct hippocampal laminae. *Mol. Cell. Neurosci.* **37**, 11–9 (2008).
30. Pattabiraman, P. P. *et al.* Neuronal activity regulates the developmental expression and subcellular localization of cortical BDNF mRNA isoforms in vivo. *Mol. Cell. Neurosci.* **28**, 556–70 (2005).
31. Baj, G., Leone, E., Chao, M. V & Tongiorgi, E. Spatial segregation of BDNF transcripts enables BDNF to differentially shape distinct dendritic compartments. *Proc. Natl. Acad. Sci. U. S. A.* **108**, 16813–8 (2011).
32. Mignone, F., Gissi, C., Liuni, S. & Pesole, G. Untranslated regions of mRNAs. *Genome Biology* **vol 3 No 3**, 1–10 (2002).
33. Pedersen, A. G. & Nielsen, H. Neural network prediction of translation initiation sites in eukaryotes: perspectives for EST and genome analysis. *Proceedings. Int. Conf. Intell. Syst. Mol. Biol.* **5**, 226–33 (1997).
34. Grillo, G. *et al.* UTRdb and UTRsite (RELEASE 2010): a collection of sequences and regulatory motifs of the untranslated regions of eukaryotic mRNAs. *Nucleic Acids Res.* **38**, D75–D80 (2010).
35. Kidane, A. H. *et al.* Differential neuroendocrine expression of multiple brain-derived neurotrophic factor transcripts. *Endocrinology* **150**, 1361–1368 (2009).
36. Kozak, M. Point mutations define a sequence flanking the AUG initiator codon that modulates translation by eukaryotic ribosomes. *Cell* **44**, 283–292 (1986).
37. Tettamanti, G. *et al.* Phylogenesis of brain-derived neurotrophic factor (BDNF) in vertebrates. *Gene* **450**, 85–93 (2010).
38. Egan, M. F. *et al.* The BDNF val66met polymorphism affects activity-dependent secretion of BDNF and human memory and hippocampal function. *Cell* **112**, 257–69 (2003).
39. Jiang, X., Zhou, J., Mash, D. C., Marini, A. M. & Lipsky, R. H. Human BDNF isoforms are differentially expressed in cocaine addicts and are sorted to the regulated secretory pathway independent of the Met66 substitution. *Neuromolecular Med.* **11**, 1–12 (2009).
40. Koppel, I., Tuvikene, J., Lekki, I. & Timmusk, T. Efficient use of a translation start codon in BDNF exon I. *J. Neurochem.* n/a–n/a (2015). doi:10.1111/jnc.13124



41. Petersen, T. N., Brunak, S., Heijne, G. Von & Nielsen, H. correspondence SignalP 4.0 : discriminating signal peptides from transmembrane regions. *Nat. Publ. Gr.* **8**, 785–786 (2011).
42. Favalli, G., Li, J., Belmonte-de-Abreu, P., Wong, A. H. C. & Daskalakis, Z. J. The role of BDNF in the pathophysiology and treatment of schizophrenia. *J. Psychiatr. Res.* **46**, 1–11 (2012).
43. Nieto, R., Kukuljan, M. & Silva, H. BDNF and schizophrenia: from neurodevelopment to neuronal plasticity, learning, and memory. *Front. Psychiatry* **4**, 45 (2013).
44. L. Huang, T. Effects of Antipsychotics on the BDNF in Schizophrenia. *Curr. Med. Chem.* **20**, 345–350 (2013).
45. Ross, C. A., Margolis, R. L., Reading, S. A. J., Pletnikov, M. & Coyle, J. T. Neurobiology of Schizophrenia. *Neuron* **52**, 139–153 (2006).
46. Wang, X., Christian, K. M., Song, H. & Ming, G. li. Synaptic dysfunction in complex psychiatric disorders: From genetics to mechanisms. *Genome Med.* **10**, 9–11 (2018).
47. Osimo, E. F., Beck, K., Reis Marques, T. & Howes, O. D. Synaptic loss in schizophrenia: a meta-analysis and systematic review of synaptic protein and mRNA measures. *Mol. Psychiatry* 1–13 (2018). doi:10.1038/s41380-018-0041-5
48. Lu, B., Pang, P. T. & Woo, N. H. The yin and yang of neurotrophin action. *Nat. Rev. Neurosci.* **6**, 603–614 (2005).
49. Leal, G., Comprido, D. & Duarte, C. B. BDNF-induced local protein synthesis and synaptic plasticity. *Neuropharmacology* **76 Pt C**, 639–56 (2014).
50. Lu, B. BDNF and Activity-Dependent Synaptic Modulation. *Learning & Memory* **10**, 86–98 (2003)
51. Cui, H., Jin, Y., Wang, J., Weng, X. & Li, C. Serum brain-derived neurotrophic factor ( BDNF ) levels in schizophrenia : A systematic review. *Shanghai Arch. of Psychiatry* **24**, 250–261 (2012).
52. Green, M. J., Matheson, S. L., Shepherd, A., Weickert, C. S. & Carr, V. J. Brain-derived neurotrophic factor levels in schizophrenia : a systematic review with meta-analysis. *Mol. Psychiatry* **16**, 960–972 (2010).
53. Cowan, C. A. *et al.* Derivation of Embryonic Stem-Cell Lines from Human Blastocysts. *N Engl J Med* 350:13 1353–1356 (2004).
54. Warlich, E. *et al.* Lentiviral Vector Design and Imaging Approaches to Visualize the Early Stages of Cellular Reprogramming. *Mol. Ther.* **19**, 782–789 (2011).
55. Gunhanlar, N. *et al.* A simplified protocol for differentiation of electrophysiologically mature neuronal networks from human induced pluripotent stem cells. *Mol. Psychiatry* 1–9 (2017). doi:10.1038/mp.2017.56
56. De Esch, C. E. F. *et al.* Epigenetic characterization of the FMR1 promoter in induced pluripotent stem cells from human fibroblasts carrying an unmethylated full mutation. *Stem Cell Reports* **3**, 548–555 (2014).
57. de Vrij, F. M. *et al.* Candidate CSPG4 mutations and induced pluripotent stem cell modeling implicate oligodendrocyte progenitor cell dysfunction in familial schizophrenia. *Mol. Psychiatry* 1–15 (2018).
58. Kondo, T. *et al.* Modeling Alzheimer's disease with iPSCs reveals stress phenotypes associated with intracellular A $\beta$  and differential drug responsiveness. *Cell Stem Cell* **12**, 487–96 (2013).
59. Ying, Q.-L., Stavridis, M., Griffiths, D., Li, M. & Smith, A. Conversion of embryonic stem cells into neuroectodermal precursors in adherent monoculture. *Nat. Biotechnol.* **21**, 183–6 (2003).
60. Conti, L. *et al.* Niche-independent symmetrical self-renewal of a mammalian tissue stem cell. *PLoS Biol.* **3**, 1594–1606 (2005).
61. Banker, G. & Goslin, K. Culturing nerve cells. *Cambridge MA MIT Press* (1991).
62. Lindner, T. H. & Hoffmann, K. easyLINKAGE: A PERL script for easy and automated two-/multi-point linkage analyses. *Bioinformatics* **21**, 405–407 (2005).

63. Abecasis GR. A map of human genome variation from population-scale sequencing. *Nature* **467**, 1061–73 (2010).
64. The Genome of the Netherlands Consortium. Whole-genome sequence variation, population structure and demographic history of the Dutch population. *Nat. Genet.* **46**, 1–95 (2014).

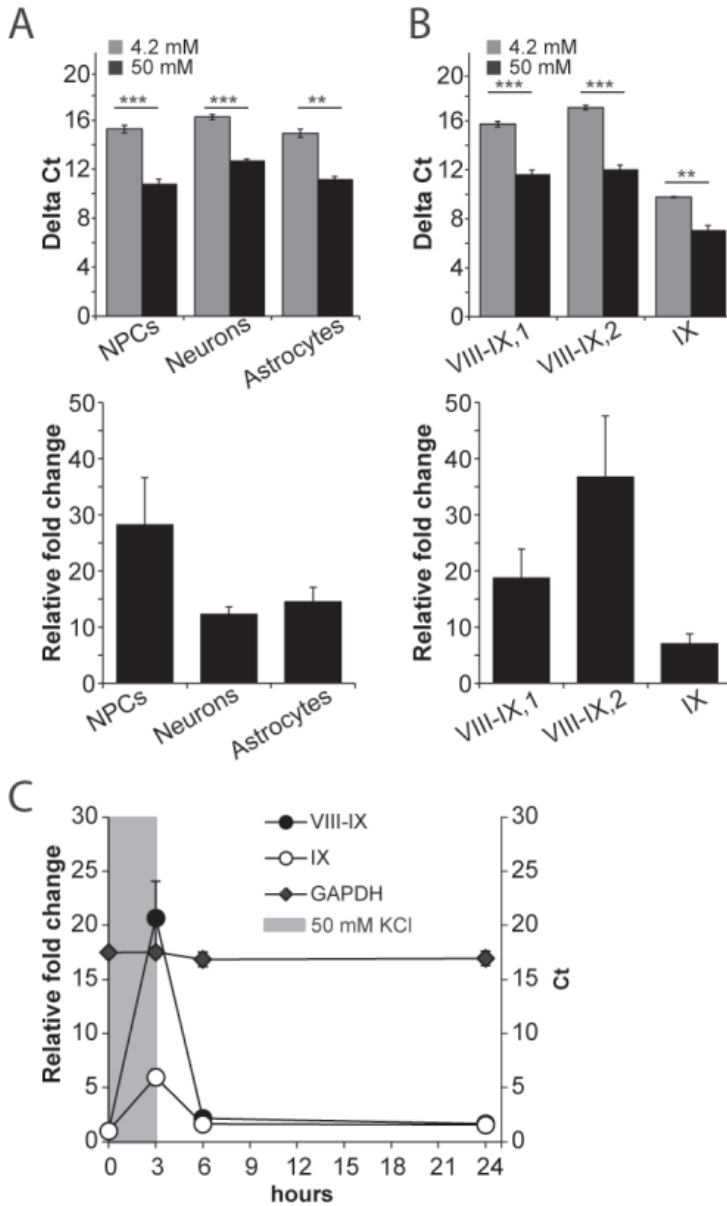


**Figure S1. Validation of *BDNF* VIII-IX upregulation** (A) ES-derived NPCs, neuronal cultures and astrocytes and (B) iPSC-derived NPCs were treated for 3hs with 50 mM KCl and *BDNF* transcript VIII-IX and IX were measured by qRT-PCR using transcript-specific primers, normalized to *GAPDH*. Delta Ct values and relative fold change values are shown. Relative fold change values are calculated with respect to untreated cultures. (C) NPCs were treated for 3hs with 50 mM KCl after which the medium was replaced with fresh medium. *BDNF* VIII-IX and IX levels were measured 3hs and 18hs after replenishment. Fold changes are relative to untreated cultures. The *GAPDH* Ct values stay constant over time. Error bars represent SEM. Statistical significance is denoted by asterisks (\*\* $p < 0.001$ ; \* $p < 0.01$ ;  $p < 0.05$ ; NS; Student *t*-test, ANOVA).

**Table S1, Related to figure 4, relative fold change and dCt values**

		Relative fold change	dCt treated cultures	dCt untreated cultures	P-value
NPCs	IV-IX	4.94 ± 0.56	8.26 ± 0.16	10.53 ± 0.12	1.04E-06
	IV- VIII	7.94 ± 1.52	13.71 ± 0.27	16.57 ± 0.36	8.26E-05
	VI-XI	4.08 ± 0.56	8.40 ± 0.30	10.32 ± 0.12	1.41E-04
	VIa-VIII	11.67 ± 2.32	12.68 ± 0.25	16.10 ± 0.13	2.86E-07
	VIb-VIII	21.69 ± 5.85	11.21 ± 0.47	15.31 ± 0.33	3.15E-05
Neurons	IV-IX	1.78 ± 0.43	9.00 ± 0.40	9.68 ± 0.39	3.48E-01
	IV- VIII	3.02 ± 0.76	14.51 ± 0.37	15.83 ± 0.46	4.96E-02
	VI-XI	2.27 ± 0.54	10.93 ± 0.31	12.01 ± 0.91	2.13E-01
	VIa-VIII	5.07 ± 2.63	13.86 ± 0.68	15.20 ± 0.18	1.34E-01
	VIb-VIII	4.32 ± 1.16	12.65 ± 0.34	14.51 ± 0.43	6.39E-03
Astrocytes	IV-IX	5.99 ± 1.76	10.16 ± 0.51	12.34 ± 0.68	2.81E-02
	IV- VIII	4.08 ± 1.14	13.37 ± 0.46	15.27 ± 0.23	2.06E-02
	VI-XI	1.82 ± 0.16	8.41 ± 0.30	10.32 ± 0.12	7.29E-03
	VIa-VIII	14.53 ± 5.04	12.45 ± 0.74	15.58 ± 0.12	1.83E-03
	VIb-VIII	14.53 ± 5.31	12.34 ± 0.61	15.61 ± 0.10	3.68E-04

Table S2, Related to Figure 2, 3, 4, primers for different BDNF isoforms

Transcript		Forward primer	Reverse primer	Efficiency (%)
Human	BDNF I-IX	CAGCATCTGTTGGGAGACGAGA	ATGGGGCAGCCTTCATGCA	91
	BDNF IV-IX	AGTGACTGAAAAGTTCCACCAG	GTAGGCCAAGCCACCTTGT	98
	BDNF VI-IX	ACCCGTGAGTTCCACCAG	GTAGGCCAAGCCACCTTGT	82
	BDNF IV-VIII-IX	CGAAGTCTTTCGCCGAGCAG	TGGCTCCACACATCCAGTTG	76
	BDNF VIa-VIII-IX	GGACCCGTGAGTTAAGTAATTAAAAG	GGAGAAAACCTGGTGGCTCCA	92
	BDNF VIIb-VIII-IX	GGTTTGTGTGGACCCGAG	GGAGAAAACCTGGTGGCTCCA	89
	BDNF VIII-IX, primer pair 1	AAGGGCTGTGCTGTGTACCTCC	TGGTCATCACTCTTCTCACCTGG	101
	BDNF VIII-IX, primer pair 2	TGTGCATCCCAAGAAAGG	CTGGTGAACTTTATGAAACCA	89
	BDNF VIII-IX, common mouse human	TAACCCGAAGGACAACTGGA	AAGGATGGTCATCACTCTCTCA	91
	BDNF IX	AGTGCCGAACCTACCCAGTCGTA	CTTATGAATCGCCAGCCAATTC	106
	GAPDH	TGCACCACCAACTGCTTAGC	GGCATGGACTGTGGTCATGAG	117
Mouse	BDNF I-IX	AGTCTCCAGGACAGCAAAAGC	GCCTTTCATGCAACCGAAGTA	103
	BDNF VIII-IX, common mouse human	TAACCCGAAGGACAACTGGA	AAGGATGGTCATCACTCTCTCA	91
	BDNF IX	TTGTTTGTGCCGTTTACCA	TGTGATGGGGATCCTTTTGT	89
	Gapdh	TGCACCACCAACTGCTTAGC	GGCATGGACTGTGGTCATGAG	117

Table S3, Related to Figure 5, shared chromosomal regions under an autosomal dominant, affected-only model

Chr.	Start SNP	End SNP	cM Start	cM End	Physical start	Physical End	Size cM	Size Mb
2	rs870638	rs12469652	44.95	61.07	21484754	36977116	16.12	15.49
3	rs6799673	rs11707471	56.87	69.71	31701082	46498865	12.84	14.80
4	rs3829	rs4637403	0.16	17.89	134851	7554721	17.73	7.42
4	rs1463842	rs7671645	51.07	56.8	31209875	38019302	5.73	6.81
4	rs1433418	rs4693933	73.82	95.88	58984954	89139002	22.06	30.15
4	rs4416516	rs17080259	187.87	205.06	184783233	190838050	17.19	6.05
5	rs12658051	rs11958855	81.1	119.32	68003457	113641145	38.22	45.64
5	rs265993	rs2287716	194.59	206.25	174846909	180666276	11.66	5.82
7	rs6950505	rs6462017	21.76	43.43	11033756	27516318	21.67	16.48
8	rs2003497	rs1915418	0.26	32.73	176818	19093006	32.47	18.92
8	rs4363185	rs12681417	86.98	112.22	74275261	105635003	25.24	31.36
9	rs10814410	rs10810110	0.01	28.4	46587	14199422	28.39	14.15
9	rs3780136	rs12684856	58.63	74.31	36845973	79818630	15.68	42.97
10	rs1772810	rs6537616	137.81	179.57	119157485	135428246	41.76	16.27
11	rs1484444	rs697315	23.98	52.36	15752803	35638772	28.38	19.89
11	rs2000605	rs4945383	76.69	86.25	70353848	79598935	9.56	9.25
12	rs10879636	rs2268389	87.11	124.4	73961218	109643152	37.29	35.68
14	rs1307538	rs12589785	56.22	69.66	56920207	71690700	13.44	14.77
15	rs6599770	rs11632150	3.95	44.28	20161372	46052390	40.33	25.89
17	rs11656081	rs2587507	117.76	129.41	75222048	77790135	11.65	2.57
19	rs475112	rs2886790	12.81	37.08	3745546	15099441	24.27	11.35
19	rs8108275	rs893185	92.59	110.92	53141566	58989495	18.33	15.49
						Total	490.01	407.23

Table S4, Related to Figure 5, sanger sequencing primers

Chr	Start	End	Gene	Amino acid change	Forward primer	Reverse primer
11	27695731	27695733	BDNF	C34PhefsTer12	GCTGGGAGCTGGGGTAGAGC	TGCCCTCTAGAGACCAAGAATAACACTCC
4	1348905	1348905	UVSSA	R350C	GCAGCTTTGTCTCTGGATCC	AGCTGCACCTGTCCCCTCTGC
5	86703854	86703854	CCNH	N155T	AACAATTTCTTGCAATGTCTAGCAGTC	CAGGCCAGACCCACACAGGTTG
8	17503464	17503464	MTUS1	F509L	CAATGGGGACCTGTGTAGCC	TGAAAAAGGCAATGAACAAAGATGC
8	94811972	94811972	TMEM67	I743V	TTTTTCAAGGTGAGTAGGGAGAGG	TTCTGCTACAGAAAGAGGATGTGG
10	128974407	128974407	FAM196A	R85C	GTGCAGTTGACCCCCAAAGG	CCTGCAGGTGCGGTTTAAGG
11	33374977	33374977	HIPK3	R1150C	TGGGCATCAAGAGTGGAAATGG	TGGATACTGGCTGAGTTTGTGTGG
12	105605088	105605088	APPL2	L98P	GGCATTTCTCAGCGATCCACA	GGCCCAAGAGTGGGAACACAG
19	13915689	13915689	ZSWIM4	R147C	AGTGACTCGGCTGGGCTTTG	AGCTGGTCCCGGTTTCATCTG
19	56538591	56538591	NLRP5	S33II	AAACGTTGGCTGGTGCTTTTG	TGAACGGAGGCTGCTTCTCAG





# Chapter 4

## Subcellular localization of mouse and human UBE3A protein isoforms

S.T. Munshi<sup>1,§</sup>, R.A. Trezza<sup>2,3,4,§</sup>, M. Sonzogni<sup>2,3</sup>, R. Ballarino<sup>1</sup>, H. Smeeks<sup>1</sup>, B. Lendemeijer<sup>1</sup>, J. Stedehouder<sup>1</sup>, B. Distel<sup>2,3,4</sup>, Y. Elgersma<sup>2,3</sup>, F.M.S. de Vrij<sup>1</sup>, S.A. Kushner<sup>1,3</sup>

<sup>1</sup>Dept of Psychiatry, Erasmus MC, Wytemaweg 80, 3015 CN Rotterdam, The Netherlands

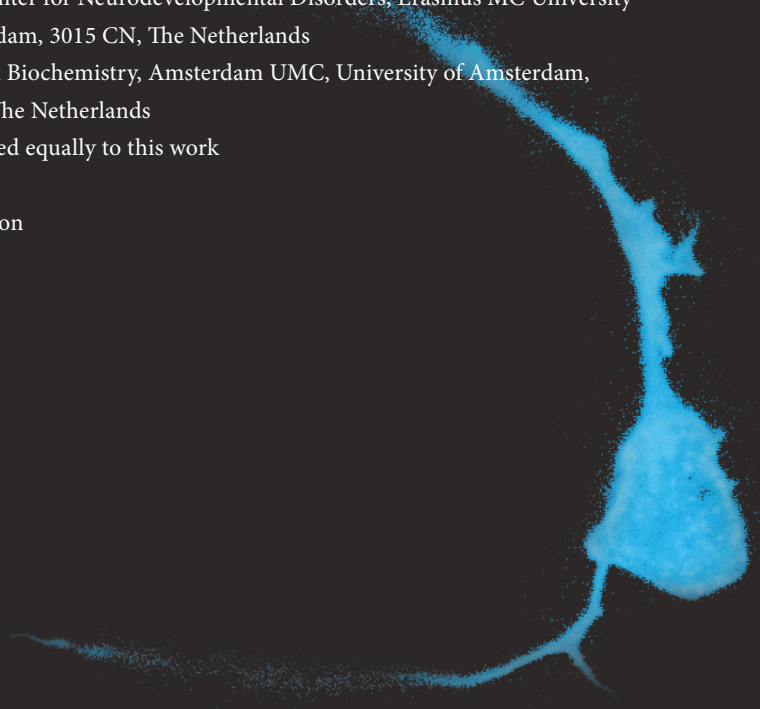
<sup>2</sup>Dept of Neuroscience, Erasmus MC, Wytemaweg 80, 3015 CN Rotterdam, The Netherlands

<sup>3</sup>ENCORE Expertise Center for Neurodevelopmental Disorders, Erasmus MC University Medical Center, Rotterdam, 3015 CN, The Netherlands

<sup>4</sup>Department of Medical Biochemistry, Amsterdam UMC, University of Amsterdam, Amsterdam, 1105AZ, The Netherlands

<sup>§</sup>Both authors contributed equally to this work

Manuscript in preparation



## ABSTRACT

Maternal loss of functional UBE3A protein causes the neurodevelopmental disease Angelman Syndrome (AS). Despite the identification of the causative gene (*UBE3A*), the precise function of UBE3A in the pathophysiology of AS remains unknown. In mice, three *Ube3a* transcriptional isoforms have been reported, of which two appear to be translated (mouse UBE3A protein isoform 2 and 3). Mouse UBE3A protein isoform 2 is predominantly localized to the cytoplasm, while mouse UBE3A protein isoform 3 is almost exclusively nuclear. In contrast, little is known about the localization of human UBE3A. Using human post-mortem tissue lysates, we examined the expression of UBE3A protein isoforms. We find at least two different UBE3A protein isoforms, which most likely correspond to human UBE3A protein isoform 1 (ortholog of mouse UBE3A protein isoform 3) and human UBE3A protein isoform 2 (no mouse ortholog) and/or human UBE3A protein isoform 3 (ortholog of mouse UBE3A protein isoform 2). To examine potential differences in UBE3A between mouse and human, we examined the localization of transiently transfected mouse and human UBE3A protein isoforms in UBE3A-null mouse hippocampal neurons and human neurons derived from induced pluripotent stem cells. We found that mouse UBE3A isoform 3 and human ortholog UBE3A isoform 1 have a predominantly nuclear localization in both mouse and human neurons. Conversely, mouse UBE3A isoform 2 has a predominantly cytoplasmic localization in both mouse and human neurons. Notably however, human UBE3A isoform 3, the ortholog of mouse UBE3A isoform 2, has a predominantly nuclear localization in both mouse and human neurons. Taken together, we conclude that the mouse versus human cellular context does not appear to be a critical modulator of the distinct cytoplasmic or nuclear localization of the various UBE3A isoforms. Rather, the highly distinct localizations of the orthologous mouse UBE3A isoform 2 and human UBE3A isoform 3 is likely a result from the few differences in their protein sequences.

## INTRODUCTION

In 1997, genetic abnormalities of maternally inherited *UBE3A* were established to cause Angelman Syndrome (AS)<sup>1,2</sup>, a rare neurodevelopmental disease that affects between 1:15.000 – 1:30.000 children. Children with AS exhibit a range of neurodevelopmental impairments, including severe intellectual disability, movement and balance problems, happy demeanor and absence of speech<sup>3</sup>. The *UBE3A* gene is parentally imprinted. In nearly all expressing cell types it is transcribed bi-allelically. In neurons, however, *UBE3A* expression occurs almost exclusively from the maternal allele, while the paternal allele is silenced by a long non-coding RNA transcript (*UBE3A-ATS*)<sup>4-7</sup>. The protein product of the *UBE3A* gene is a HECT domain ubiquitin E3 ligase, which functions to target proteins for proteasomal degradation<sup>8,9</sup>. Although several cytoplasmic and nuclear targets of *UBE3A*-mediated ubiquitination have been proposed<sup>8-10</sup>, very few have been confirmed, leaving a major open question regarding how lack of functional *UBE3A* causes Angelman Syndrome.

*UBE3A* has mostly been studied in mice. In mouse neurons, *UBE3A* is weakly localized to synapses, dendrites, endoplasmic reticulum, and mitochondria, while the nuclear localization is particularly high<sup>11-14</sup>. *UBE3A* localization appears dependent on developmental age. Immature neurons exhibit moderate *UBE3A* expression within both the cytoplasm and nucleus, while *UBE3A* expression in mature neurons is predominantly nuclear<sup>11,13,14</sup>.

AS mouse models replicate many of the core features of AS, including motor dysfunction, inducible epilepsy, learning deficiencies, anxiety- and autism-related phenotypes and repetitive behavior<sup>15-19</sup>. Anxiety- and autism-related phenotypes, as well as repetitive behavior and epilepsy, can be rescued when *Ube3a* expression is re-established before 3 weeks of age<sup>17</sup>. As such, *Ube3a* appears essential in early development. Since *UBE3A* localization is age-dependent and its expression is crucial in development, *UBE3A*'s cellular localization could reveal mechanistic details about its involvement in disease pathology.

Mice express three different *Ube3a* isoforms<sup>11,20</sup>. Mouse *UBE3A* isoforms 2 and 3 differ only in a 21-amino-acid N-terminus. Mouse *UBE3A* isoform 1 resembles isoform 3, however misses a large part of the catalytic HECT-domain at the C-terminus (**Figure 1**). Mouse *UBE3A* isoform 2 resides mostly in the cytoplasm in HEK293 cells and primary mouse neurons<sup>11,20</sup>. In contrast, the localization of mouse *UBE3A* isoform 3 is predominantly nuclear<sup>11,20</sup>. Mouse isoform 1 has functions at RNA level<sup>21</sup>. The human *UBE3A* gene contains three open-reading frames, corresponding to three different *UBE3A* protein isoforms<sup>22</sup>. Human *UBE3A* isoform 1 and 3 show high amino-acid similarity to mouse *UBE3A* isoform 3 and 2 respectively (**Figure 1**), yet so far human *UBE3A* isoform expression and function has not been investigated. Human *UBE3A* isoform 2 does not have a mouse orthologue, and its existence remains to be empirically determined. *UBE3A-005* (ENST00000604860), an *in silico* predicted human transcript, mostly resembles mouse *UBE3A* isoform 1.

In this study, we use human post-mortem tissue and neural cultures derived from human induced pluripotent stem (iPSCs) cells to investigate the expression of human UBE3A. We find that human neurons express at least two different UBE3A protein isoforms, similar to mice. However, we also find that although mouse UBE3A isoform 2 and human UBE3A isoform 3 share high amino-acid homology, their localization is strongly divergent, suggesting distinct functions for human *UBE3A*.

## MATERIALS AND METHODS

### Cell Culture

Female *Ube3a*<sup>tm1Alb</sup> (*Ube3a*<sup>m+/p-</sup>) mice in the 129 background were crossed with wildtype B6 males and primary hippocampal neurons were isolated from the *Ube3A*<sup>m-/p+</sup> pups at E18 according Banker and Goslin<sup>23</sup>. All animal procedures were approved by a Dutch Ethical Committee for animal experiments. Primary skin fibroblasts were obtained from a 39-year-old female AS patient carrying a point mutation of *UBE3A* (c.1730G>A, p.W577X). The donor's caregiver provided written informed consent in accordance with the Medical Ethical Committee of the Erasmus University Medical Center. Stem cells were derived from fibroblasts as described previously using a single, multicistronic lentiviral vector encoding *OCT4*, *SOX2*, *KLF4* and *MYC*<sup>24</sup>. Quality control of iPS clones was performed by karyotyping, real-time quantitative PCR and embryonic body (EB) differentiation. Derivation and quality control of Ctrl line (Line 2<sup>25</sup>) as well as neuronal differentiation was previously described by Gunhanlar et al<sup>25</sup>. Neural precursors cells (NPCs) were generated using an EB stage to induce neuroectoderm<sup>25</sup>. Resulting NPCs were sorted using a serial gating strategy using multiple markers to obtain a homogeneous population of forebrain-specific NPCs<sup>26</sup>. In short, NPCs at passage 3-5 were detached with accutase for 2 min at 37°C, collected and washed using PBS+2% serum. Cells were resuspended in 100-200 µl PBS+2% serum and stained on ice for 30 min with 1:100 CD15 V450 (561584, BD Bioscience), 1:250 CD24 PE-Cy7 (561646, BD Bioscience), 1:100 CD44 FITC (560977, BD Bioscience), 1:250 CD184 APC (560936, BD Bioscience), and 1:500 CD271 PE (560927, BD Bioscience)<sup>26</sup>. After staining, cells were washed twice using PBS+2% serum. Stained cells were passed through a 100 µm filter and sorted on a FACS Aria III (BD Biosciences). CD184+/CD44-/CD271-/CD24+ cells were collected in laminin-coated plates and expanded in NPC medium<sup>25</sup>. The WTC-11 NPC line (Gladstone Institute) was used as a Ctrl to compare AS-derived NPCs to. To obtain human neurons, NPCs were plated on polyornithine/laminin-coated coverslips in neuronal differentiation medium<sup>25</sup>. After 4 weeks of differentiation, only half of the medium of the cultures was replenished. Neuronal cultures were differentiated for 3-12 weeks.

## Western blot

To generate lysates for western blot, cortex of adult mice (n=3, 10-12 weeks old) and fresh-frozen human postmortem tissue blocks of three subjects (table 1) were treated as described in Wang et al<sup>27</sup>. A total of 20 ug of each sample was loaded on the gel and a wet transfer was performed. The blotted nitrocellulose membrane was probed with antibodies directed against UBE3A (E8655, Sigma–Aldrich; 1:1,000) and Actin (MAB1501R, Millipore; 1:20,000). A fluorophore-conjugated secondary goat anti-mouse antibody (IRDye 800CW, Westburg; 1:15,000) was used and the protein was detected using Li-cor Odyssey Scanner system.

**Table 1**, Demographics human postmortem tissue for western blot analysis and immunohistochemistry

	Experiment	Gender	Age	Region
1	Western blot	male	66	Right superior frontal gyrus
2	Western blot	female	58	Left superior frontal gyrus
3	Western blot	male	50	Left superior frontal gyrus
4	Immunohistochemistry	female	61	Left superior temporal gyrus
5	Immunohistochemistry	male	79	Left superior temporal gyrus

## Human brain immunohistochemistry

Left superior temporal gyrus tissue blocks of two subjects were obtained from the pathology department of Erasmus MC and stored at -80°C (table 1). These samples were fixed for 3 days in 4% paraformaldehyde (0.1M phosphate buffer, pH 7.3) at 4°C. Tissue was subsequently transferred to 10% sucrose (0.1M phosphate buffer, pH 7.3) overnight at 4°C, and stored in 30% sucrose (0.1M phosphate buffer, pH 7.3) for a maximum of 7 days at 4°C. Serial 40 µm sections were collected perpendicular to the cortical surface using a freezing microtome (Leica, Wetzlar, Germany; SM 2000 R) and stored at 4°C in 0.1M phosphate buffer for a maximum of 7 days. Free-floating sections were washed with PBS at room temperature preceding pre-incubation. Sections were pre-incubated with a blocking PBS buffer containing 0.5% Triton X-100 and 5% bovine serum albumin (BSA) for 1h at room temperature. Primary antibody labeling was performed in PBS buffer containing 0.5% Triton X-100 and 1% BSA for 72h at 4°C. The following primary antibodies were used: Mouse anti-UBE3A (SAB1404508, Sigma; 1:150), and rabbit anti-MAP2 (AB5622, Millipore; 1:300). Following primary antibody labeling, sections were washed with PBS and incubated with the following secondary antibodies: Alexa-488 anti-rabbit and Cy3 anti-mouse (Jackson ImmunoResearch; 1:200) in PBS buffer containing 0.5% Triton X-100, 1% BSA for 6 h at room temperature. Nuclear staining was performed using DAPI (1:10,000, Thermo Fisher Scientific, Waltham, MA, USA) in 0.1M phosphate buffer for 1h. Subsequently, sections were washed twice in 0.1M phosphate buffer, submerged in chromalin solution and mounted using Vectashield antifade medium. Images were acquired using a Zeiss LSM 700 confocal microscope (Carl Zeiss, Oberkochen, Germany).

### Plasmid DNA constructs and cloning

Mouse Ube3A constructs were amplified from mouse cDNA using a combination of forward and reverse primers introducing AscI and PacI restriction sites at the 5' and 3' end of the gene fragments respectively. Human UBE3A constructs were amplified from the p4053 HA-E6AP isoform1 (Addgene #8657) and p4055 HA-E6AP isoform III (Addgene #8659) using a combination of forward and reverse primers introducing AscI and NotI sites at the 5' and 3' end of the gene fragment respectively. PCR products were cloned by A-tailing into pGEMTeasy (Promega) and sequenced. PCR products were then cloned in the dual promoter vector CAGG-tdTomato (Clontech) described in Kury et al.<sup>28</sup>. To prohibit production of protein products of the second in-frame methionine in the mouse UBE3A isoform 2 and human UBE3A isoform 3 constructs, the methionine was replaced with an alanine (M22A, M21A, respectively).

### Transfections in mouse and human neurons

Primary mouse hippocampal neurons were transfected after 7 days *in vitro* (DIV) with one of the mouse or human UBE3A constructs (in total 1.8 µg DNA per 12-well coverslip). Lipofectamine 2000 was used to transfect neurons, according to the manufacturer's instructions (Invitrogen). Neurons were fixed 4 days post-transfection with 4% paraformaldehyde (PFA)/4% sucrose and stained for UBE3A and MAP2. The following primary antibodies were used: anti-MAP2 (188004, Synaptic Systems; 1:500) and anti-UBE3A (SAB1404508, Sigma; 1:200). Human neurons were differentiated for 3 weeks and transfected with 2 µg DNA per 12-well coverslip, using Lipofectamine 3000 (Invitrogen) according manufacturer's protocol. Three days post-transfections human neurons were fixed and stained using 4% formaldehyde in phosphate-buffered saline. Primary antibodies were incubated overnight at 4 °C in labeling buffer containing 0.05M Tris, 0.9% NaCl, 0.25% gelatin and 0.5% Triton-X-100 (pH 7.4). The following primary antibodies were used: anti-MAP2 (188004, Synaptic Systems; 1:200) and anti-UBE3A (SAB1404508, Sigma; 1:200). The following secondary antibodies were used: Alexa-488 anti-guinea pig and Cy3 anti-mouse (Jackson ImmunoResearch; 1:200). Samples were imbedded in Mowiol 4-88 (Sigma-Aldrich), after which confocal imaging was performed with a Zeiss LSM700 confocal microscope using ZEN software (Zeiss, Oberkochen, Germany). Of each condition 12-15 transfected cells were examined.

## RESULTS

### UBE3A isoform expression in human brain

Mouse *Ube3a* and human *UBE3A* both contain open-reading frames for three different E3 ubiquitin ligase protein (UBE3A) isoforms (**Figure 1**). These isoforms are indicated as mouse isoform 1 (NM\_173010), 2 (NM\_011668) and 3 (NM\_001033962) and human isoform 1

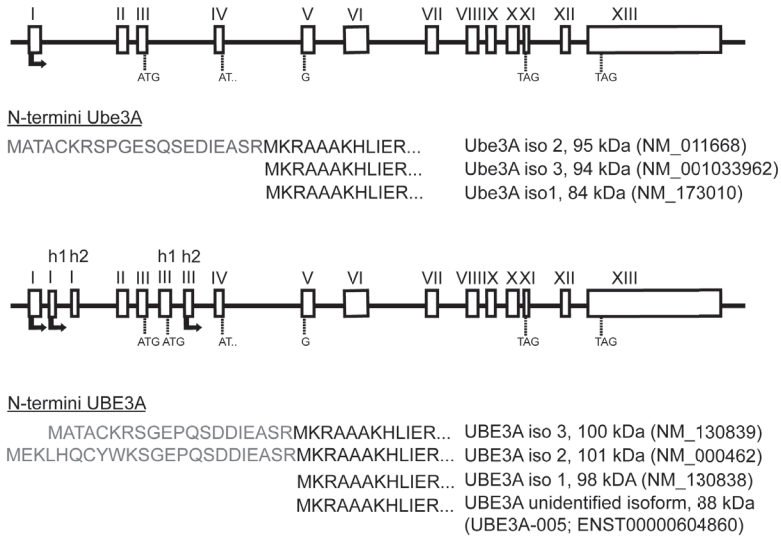


**Figure 1. Mouse *UBE3A* and human *UBE3A* gene structure and protein isoforms**

(NM\_130838), 2 (NM\_000462) and 3 (NM\_130839)<sup>22</sup>. Mouse UBE3A isoform 2 is orthologous to human UBE3A isoform 3 (96% identity in amino acid sequence). Mouse UBE3A isoform 3 is orthologous to human UBE3A isoform 1 (96% identity in amino acid sequence). Human UBE3A isoform 2 does not have a mouse orthologue, due to the usage of a human-specific promoter. Mouse UBE3A isoform 1 mostly resembles UBE3A-005, ENST00000604860, an *in silico* predicted transcript, which has not yet been confirmed experimentally. Similarly, mouse UBE3A isoform 1 protein has also not been confirmed experimentally, though RNA functionality has been reported<sup>21</sup>.

Mouse UBE3A protein localization and expression has been extensively studied<sup>11,12,29</sup>, however human UBE3A protein localization and expression remains poorly characterized. We therefore stained human post-mortem brain slices (superior temporal gyrus, n=2 different individuals) for *UBE3A* expression. We found UBE3A predominantly in the nucleus (**Figure 2A**), comparable to mouse UBE3A<sup>12-14</sup>. We did not observe UBE3A staining in astrocytes.

Given the importance of confirming the translatability of mouse UBE3A biology for understanding the pathophysiology of human UBE3A mutations in Angelman Syndrome, we assessed the isoform-specific expression of *UBE3A* in post-mortem human cortex. **Figure 2B** shows a western blot of lysates of three adult mouse and three adult human post-mortem cerebral cortex samples. We found that, comparable to mice, human cerebral cortex lysates contain two protein isoforms. Considering the open reading frames of *UBE3A*, these isoforms most likely correspond to human UBE3A isoform 1 and human UBE3A isoform 2 and/or isoform 3, given that the latter two would be indistinguishable by size. Human UBE3A isoform 1 and mouse UBE3A isoform 3 are the most abundant protein isoforms in each species.

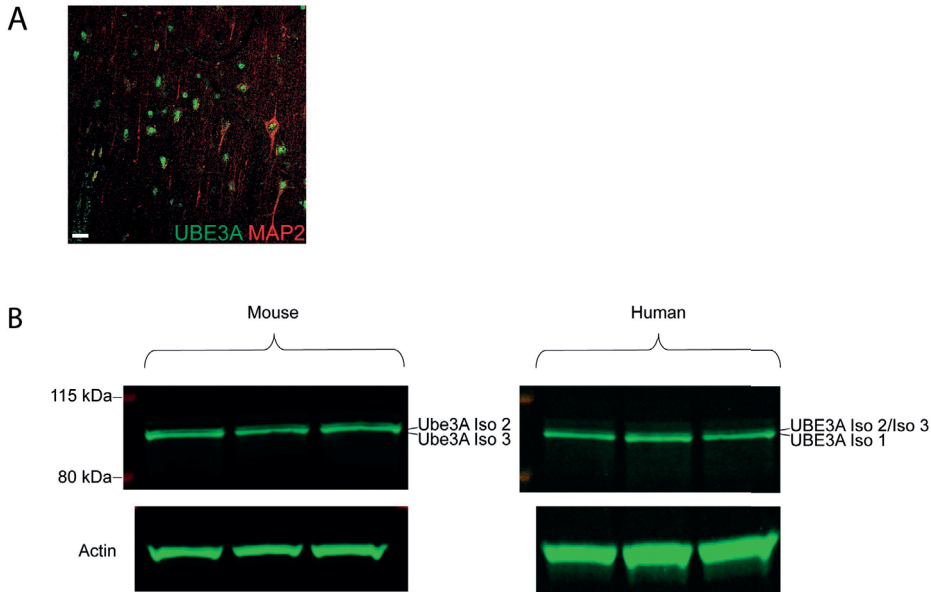


**Figure 2. Two UBE3A protein isoforms discernable in mouse and human brain.** (A) Immunohistochemical labeling of UBE3A and MAP2 in human superior temporal gyrus showing prominent nuclear labeling of UBE3A in neurons. Scale bar 20 μm. (B) Western blot analysis of UBE3A protein in WT mouse brain and post-mortem human brain samples. Each lane represents one test animal or human subject. The bands ca. 100 kDa represent the different UBE3A protein isoforms.

### Human neurons derived from induced pluripotent stem cells recapitulate UBE3A localization from cerebral cortex

In order to examine human neurodevelopmental *UBE3A* expression and subcellular localization, we utilized human iPSC-derived neural precursor cells (NPCs) and neurons that were differentiated for successively longer intervals<sup>25</sup>. In control NPCs, UBE3A was distributed throughout both the cytoplasm and nucleus, whereas in neurons UBE3A was predominantly localized to the nucleus with minimal cytoplasmic labeling (**Figure 3A,B**), consistent with previous studies in mice<sup>11,13,14</sup> and our findings in human post-mortem tissue. No discernible UBE3A labeling was observed in dendrites, synapses, or in astrocytes.

We also generated iPSC-derived neuronal lineage cells from an AS patient carrying a point mutation (c.1730 G>A, p.W577X) resulting in a premature stop codon in the HECT-domain of UBE3A. Whereas UBE3A localization was similar to controls in NPCs (**Figure 3A**), *UBE3A* expression was undetectable in AS patient-derived neurons differentiated for 3, 6, 9 or 12 weeks (**Figure 3B**). Taken together, these findings confirm that human iPSC-derived neural lineage cells retain the imprinting mechanism governing *UBE3A* paternal allele silencing specifically during neurogenesis, and faithfully models the cell-type specific localization of UBE3A protein observed in human brain tissue.



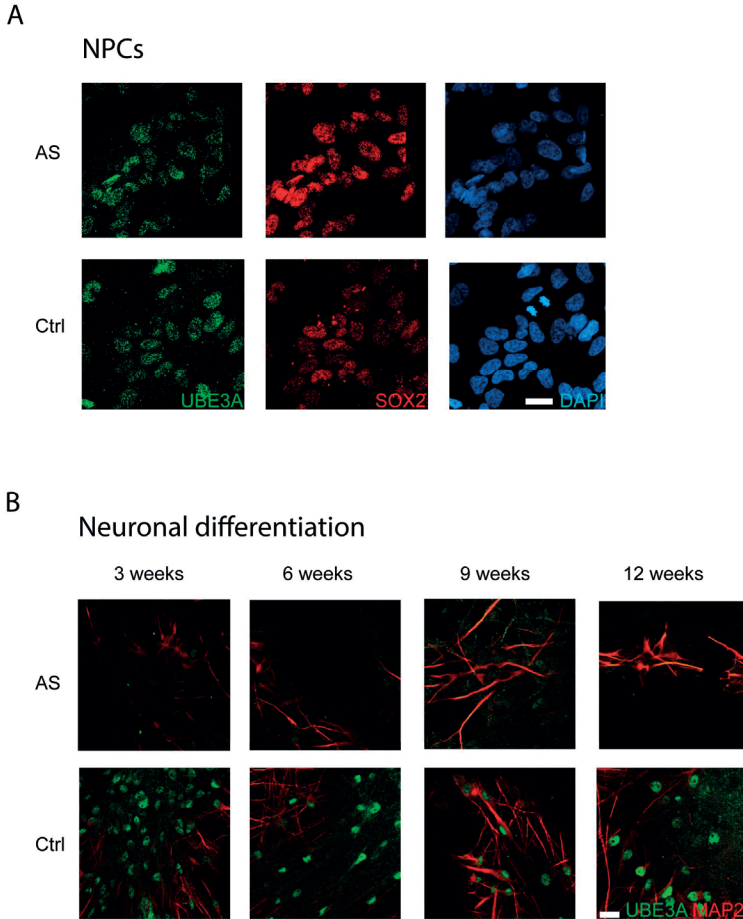


**Figure 3. Nuclear localization of UBE3A in Ctrl iPSC-derived neurons but no UBE3A in AS iPSC-derived neurons.** (A) Immunocytochemical labeling of UBE3A and neural progenitor marker SOX2 in Ctrl and AS NPCs (B) UBE3A and MAP2 labeling of 3-, 6-, 9- and 12-week-old human neurons derived from iPSCs from Ctrl subject and AS patient. Scale bar 20  $\mu$ m.

### Distinct subcellular localization of mouse UBE3A isoform 2 and the orthologous human UBE3A isoform 3

A previous study reported that mouse UBE3A isoforms 2 and 3 are predominantly localized to the cytoplasm and nucleus, respectively in both HEK293 cells and neurons<sup>11,20</sup>. We asked whether the orthologous human UBE3A isoforms exhibit a similar subcellular localization. We transfected primary hippocampal neurons from *Ube3a* knockout mice to assess isoform-specific localization in a *UBE3A* null background. As expected, mouse UBE3A isoform 2 was predominantly localized to the cytoplasm, while mouse UBE3A isoform 3 was localized to the nucleus (**Figure 4A**). The human ortholog of mouse UBE3A isoform 3, human UBE3A isoform 1, similarly was predominantly localized in the nucleus. However, human UBE3A

isoform 3 was also predominantly found in the nucleus, making its localization highly distinct from the cytoplasmic localization of its ortholog mouse UBE3A isoform 2 (**Figure 4A**).

We next considered whether the discordant localization between human UBE3A isoform 3 and its orthologue mouse UBE3A isoform 2 resulted from *cis*- or *trans*-acting factors. In particular, we considered whether the localization of human UBE3A isoform 3 might be different in mouse versus human neurons. Therefore, we individually expressed the mouse and human isoforms in human AS patient (*UBE3A* null) iPSC-derived neurons (**Figure 4B**). Mouse isoform 2 was consistently found in the cytoplasm and mouse isoform 3 was localized to the nucleus when expressed in human neurons, consistent with their respective localization in mouse neurons. Moreover, both human isoform 3 and human isoform 1 were constantly found in the nucleus, again consistent with their localization in mouse neurons. Therefore, the distinct localization of mouse UBE3A isoform 2 (cytoplasmic) and orthologous human UBE3A isoform 3 (nuclear) is likely due to a differential *cis*-acting mechanism within the protein itself.

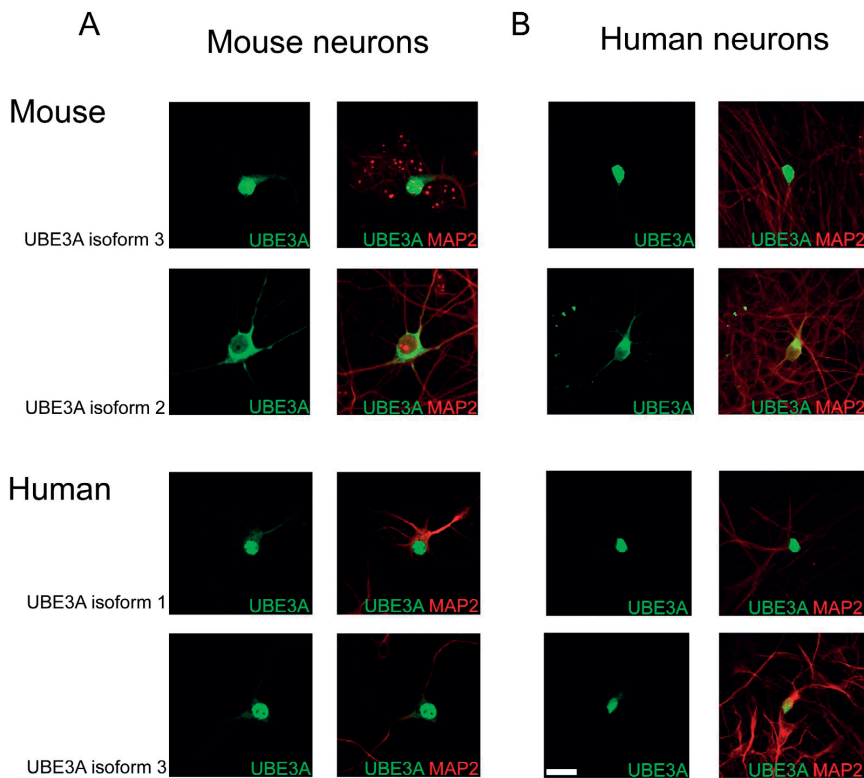


**Figure 4. Localization of mouse and human UBE3A protein isoforms in mouse and human neurons.** (A), (B) Representative immunocytochemical UBE3A and MAP2 stainings of (A) primary hippocampal neurons from AS mouse and (B) human neurons derived from iPSCs from AS patient transfected with constructs over-expressing indicated UBE3A protein isoforms. Scale bar 20  $\mu$ m.

## DISCUSSION

Loss of function of the maternal *UBE3A* gene is responsible for the neurodevelopmental disorder Angelman Syndrome<sup>1,2</sup>. Mice with a deletion of *Ube3a* show AS-related phenotypes and have served as a model to study UBE3A<sup>15,17,19,30</sup>. Given the high orthology between the protein-coding sequences of mouse and human UBE3A (96% protein sequence homology), it has widely been assumed that knowledge of the mouse UBE3A biology is valid for humans. Here we reveal a potentially important discordance between the subcellular localization of orthologous mouse and human UBE3A isoforms. The dissimilar localization suggests that the few differences between the mouse *Ube3a* and human *UBE3A* gene sequence might be the critical determinants of their distinct subcellular localization.

Analogous to mice<sup>11</sup>, humans express at least two major UBE3A protein isoforms in brain. In mature neurons of mice, UBE3A is predominantly localized to the nucleus<sup>11,13,14</sup>. Notably, using both post-mortem brain tissue and iPSC-derived neurons, we find a similar localization in human neurons. Prior studies have shown that in mice UBE3A localization is dynamic during brain development<sup>13,14</sup>: in immature neurons UBE3A is distributed broadly across the cytoplasm and nucleus, while in mature neurons it concentrates within the nucleus. The development of the cortical layers results in a transient simultaneous existence of mature and immature neurons<sup>14</sup>. As AS symptoms emerge in the early postnatal period, a spatiotemporal expression analysis of early neurodevelopmental human *UBE3A* expression may provide the opportunity to elucidate the early neurodevelopmental processes in which UBE3A is indispensable.

Our western blot data shows the expression of at least two UBE3A isoforms. Similarly, we replicated earlier reports of two mouse UBE3A isoforms, mouse UBE3A isoform 2 and isoform 3, which constitute approximately 75-80% and 20-25% of total UBE3A protein, respectively<sup>20</sup>. Human UBE3A isoform expression ratios are similar<sup>20</sup>, yet we cannot specify the contribution of the different human isoform 2 and 3 as they are indistinguishable on a western blot. Unfortunately the lack of isoform-specific antibodies for mouse or human UBE3A has frustrated attempts to examine the relative expression and localization of the various isoforms *in situ*. However, in lieu of isoform-specific antibodies, we individually expressed the mouse and human UBE3A isoforms in primary mouse neurons or iPSC-derived neurons lacking maternal UBE3A expression.

For over 15 years, several AS mouse models have been used to study AS<sup>15-17,19</sup>. On the basis of the high homology between the mouse and human UBE3A protein sequence, mice have traditionally been assumed to be sufficient for studying UBE3A neurobiology and the pathophysiology of AS. Notably however, we have now discovered a major difference in the subcellular localization of mouse isoform 2, which is predominantly cytoplasmic<sup>11,20</sup>, and the orthologous human isoform 3, which is predominantly nuclear. Importantly, we observed the same differential pattern of subcellular localization in both primary mouse neurons and hu-

man iPSC-derived neurons, excluding species-specific *trans*-acting factors as the underlying cause. Therefore, we conclude that the few differences in their protein sequence are likely to be the critical determinants of their differential subcellular localization. In particular, an intriguing candidate region is the N-terminus of the protein, which has been shown by Trezza et al.<sup>20</sup> to robustly determine the subcellular localization of UBE3A. Compared to mouse isoform 2, the N-terminus of human isoform 3 contains differences at three amino acid positions: ΔP9, S12P, and E15D (**Figure 1**). As the latter comprises a conservative amino acid change between acidic residues, this substitution may not have a strong effect on protein function. In contrast, the ΔP9 and S12P substitution are particularly notable candidates that could influence dissimilar localization.

What the function of alternatively localized human UBE3A protein is, remains to be seen. In mice, several substrates in cytoplasm and nucleus have been proposed, but few have been independently confirmed<sup>8–10</sup>. Also, a previous report suggested that UBE3A functions as a nuclear co-transcriptional activator<sup>31</sup>. Notably, both human and mouse UBE3A contain a zinc-finger domain, which may mediate RNA, DNA and/or protein interactions. Since the majority of studies have been performed in mice, independent validation in human neurons remains necessary. Additionally, a recent report has proposed that the subcellular localization of UBE3A may be further regulated by neuronal activity<sup>32</sup>, a possibility that requires further mechanistic investigation.

In our experiments we did not detect UBE3A in astrocytes, yet other studies have reported some limited expression of *UBE3A* in glial cells<sup>13,14</sup>. Notably however, UBE3A isoform-specific subcellular localization has remained largely unexplored in glial cells, leaving open the possibility of an unrecognized function of UBE3A in glial cells.

The function of the individual UBE3A isoforms remains poorly understood. In mice, UBE3A isoform 2 rescued impaired dendrite polarity in neurons with knock-down of *Ube3A*<sup>11</sup>. The function of mouse isoform 3 is unknown, yet its RNA is increased with neural activity<sup>32</sup>. A recent study shows that in mice with isoform-specific deletions, AS phenotypes were recapitulated in mice lacking isoform 3, whereas mice lacking isoform 2 were phenotypically comparable to wild types<sup>20</sup>. Analogously in humans, Sadhwani et al. reported an AS patient with a T>C variant point mutation in the start-codon of human UBE3A isoform 1 (ortholog of mouse isoform 3) that causes AS<sup>33</sup>. This mutation is predicted to abrogate translation of UBE3A isoform 1, but also introduces a methionine to threonine substitution in both human UBE3A isoform 2 and 3. Accordingly, it cannot be excluded that the altered or compensatory function of the remaining UBE3A isoform 2 and/or 3 are also contributing to the phenotype.

With the advent of human iPSC technology, the study of human neurobiology has become more tractable. Several groups have utilized iPSCs to investigate AS pathophysiology<sup>34,35</sup>. Previous models demonstrated several molecular characteristics of *UBE3A* biology, including imprinting and allele-specific silencing<sup>7,34</sup>. A recent study also reported electrophysiological alterations in neurons derived from iPSCs of AS patients<sup>35</sup>. Our findings from AS patient

iPSC-derived neurons are also consistent with imprinting and allele-specific silencing. iPSC-derived NPCs were UBE3A positive, despite a nonsense mutation in the maternal *UBE3A*, consistent with bi-allelic expression. In contrast, in iPSC-derived neurons no UBE3A was detected following just 3 weeks of differentiation from NPCs, as would be expected following paternal allele silencing in cells harboring a nonsense mutation in maternal *UBE3A*.

Trezza et al. highlight the importance of nuclear UBE3A for proper neurodevelopment<sup>20</sup>. As our iPSC-derived neural cultures likely reflect late gestational or early postnatal neurons<sup>25</sup>, it is possible that human UBE3A may localize to the nucleus prenatally. As such, investigation of the early neurodevelopmental subcellular localization in human neurons may also be important for understanding AS pathophysiology and identifying efficacious therapeutic interventions.

## REFERENCES

1. Kishino, T., Lalande, M. & Wagstaff, J. UBE3A/E6-AP mutations cause Angelman syndrome. *Nat. Genet.* **15**, (1997).
2. Matsuura, T. *et al.* De novo truncating mutations in E6-AP ubiquitin-protein ligase gene (UBE3A) in Angelman syndrome. *Nat. Genet.* **15**, (1997).
3. Williams, C. A., Beaudet, A. L. & Clayton-Smith, Ji. Angelman syndrome 2005: updated consensus for diagnostic criteria. *Am. J. Med. Genet. A* **140A**, 413–418 (2006).
4. Rougeulle, C., Glatt, H. & Lalande, M. The Angelman syndrome candidate gene, UBE3A/E6-AP, is imprinted in brain. *Nat. Genet.* **17**, (1997).
5. Rougeulle, C., Cardoso, C., Fontés, M., Colleaux, L. & Lalande, M. An imprinted antisense RNA overlaps UBE3A and second maternally expressed transcript. *Nat. Genet.* **19**, (1998).
6. Chamberlain, S. J. *et al.* Induced pluripotent stem cell models of the genomic imprinting disorders Angelman and Prader – Willi syndromes. *PNAS.* **107**:41, 17668–17673 (2010).
7. Martins-taylor, K. *et al.* Imprinted expression of UBE3A in non-neuronal cells from a Prader-Willi syndrome patient with an atypical deletion. *Human Mol Gen* 1–31 (2013).
8. Sell, G. L. & Margolis, S. S. From UBE3A to Angelman syndrome: A substrate perspective. *Front. Neurosci.* **9**, 1–6 (2015).
9. LaSalle, J. M., Reiter, L. T. & Chamberlain, S. J. Epigenetic regulation of UBE3A and roles in human neurodevelopmental disorders. *Epigenomics* **7**, 1213–28 (2015).
10. Mabb, A. M., Judson, M. C., Zylka, M. J. & Philpot, B. D. Angelman syndrome: insights into genomic imprinting and neurodevelopmental phenotypes. *Trends Neurosci.* **34**, 293–303 (2011).
11. Miao, S. *et al.* The Angelman Syndrome Protein Ube3a Is Required for Polarized Dendrite Morphogenesis in Pyramidal Neurons. *J. Neurosci.* **33**, 327–333 (2013).
12. Dindot, S. V., Antalffy, B. a., Bhattacharjee, M. B. & Beaudet, A. L. The Angelman syndrome ubiquitin ligase localizes to the synapse and nucleus, and maternal deficiency results in abnormal dendritic spine morphology. *Hum. Mol. Genet.* **17**, 111–118 (2008).
13. Burette, A. C. *et al.* Subcellular organization of UBE3A in neurons. *J. Comp. Neurol.* **00**, 1–19 (2016).
14. Judson, M. C., Sosa-Pagan, J. O., Del Cid, W. A., Han, J. E. & Philpot, B. D. Allelic specificity of Ube3a expression in the mouse brain during postnatal Development. *J. Comp. Neurol.* **522**, 1874–1896 (2014).
15. Jiang, Y. H. *et al.* Mutation of the Angelman ubiquitin ligase in mice causes increased cytoplasmic p53 and deficits of contextual learning and long-term potentiation. *Neuron* **21**, 799–811 (1998).
16. Meng, L. *et al.* Truncation of Ube3a-ATS Unsilences Paternal Ube3a and Ameliorates Behavioral Defects in the Angelman Syndrome Mouse Model. *PLoS Genet.* **9**, (2013).
17. Silva-santos, S. *et al.* Ube3a reinstatement identifies distinct developmental windows in a murine Angelman syndrome model. *J of Clinical Invest.* **125**, 1–8 (2015).
18. Huang, H. S. *et al.* Behavioral deficits in an Angelman syndrome model: Effects of genetic background and age. *Behav. Brain Res.* **243**, 79–90 (2013).
19. van Woerden, G. M. *et al.* Rescue of neurological deficits in a mouse model for Angelman syndrome by reduction of alphaCaMKII inhibitory phosphorylation. *Nat. Neurosci.* **10**, 280–2 (2007).
20. Rossella Trezza, A. *et al.* Loss of nuclear UBE3A causes electrophysiological and behavioral deficits in mice and is associated with Angelman syndrome. *Nat Neuroscience.* **22**(8):1235–1247 (2019)
21. Valluy, J. *et al.* A coding-independent function of an alternative Ube3a transcript during neuronal development. *Nat. Neurosci.* **18**, 666–673 (2015).
22. Yamamoto, Y., Huibregtse, J. M. & Howley, P. M. The human E6-AP gene (UBE3A) encodes three potential protein isoforms generated by differential splicing. *Genomics* **41**, 263–266 (1997).

23. Banker, G. & Goslin, K. Culturing nerve cells. *Cambridge MA MIT Press* (1991).
24. Warlich, E. *et al.* Lentiviral vector design and imaging approaches to visualize the early stages of cellular reprogramming. *Mol. Ther.* **19**, 782–9 (2011).
25. Gunhanlar, N. *et al.* A simplified protocol for differentiation of electrophysiologically mature neuronal networks from human induced pluripotent stem cells. *Mol. Psychiatry* 1–9 (2017). doi:10.1038/mp.2017.56
26. Yuan, S. H. *et al.* Cell-surface marker signatures for the Isolation of neural stem cells, glia and neurons derived from human pluripotent stem cells. *PLoS One* **6**, (2011).
27. Wang, T., van Woerden, G. M., Elgersma, Y. & Borst, J. G. G. Enhanced Transmission at the Calyx of Held Synapse in a Mouse Model for Angelman Syndrome. *Front. Cell. Neurosci.* **11**, 1–19 (2018).
28. Kürty, S. *et al.* De Novo Mutations in Protein Kinase Genes CAMK2A and CAMK2B Cause Intellectual Disability. *Am. J. Hum. Genet.* **101**, 768–788 (2017).
29. Burette, A. C. The subcellular organization of UBE3A in neurons. *J. Comp. Neurol.* **520**, 633–655 (2011).
30. Meng, L., Person, R. E. & Beaudet, A. L. Ube3a-ATS is an atypical RNA polymerase II transcript that represses the paternal expression of Ube3a. *Hum. Mol. Genet.* **21**, 3001–3012 (2012).
31. Nawaz, Z. *et al.* The Angelman syndrome-associated protein, E6-AP, is a coactivator for the nuclear hormone receptor superfamily. *Mol. Cell. Biol.* **19**, 1182–1189 (1999).
32. Filonova, I., Trotter, J. H., Banko, J. L. & Weeber, E. J. Activity-dependent changes in MAPK activation in the Angelman Syndrome mouse model. *Learn. Mem.* **21**, 98–104 (2014).
33. Sadhwani, A. *et al.* Two Angelman families with unusually advanced neurodevelopment carry a start codon variant in the most highly expressed UBE3A isoform. *American J of Med Gen* 1–7 (2018).
34. Chamberlain, S. J. *et al.* Induced pluripotent stem cell models of the genomic imprinting disorders Angelman and Prader-Willi syndromes. *Proc. Natl. Acad. Sci. U. S. A.* **107**, 17668–73 (2010).
35. Fink, J. J. *et al.* Disrupted neuronal maturation in Angelman syndrome-derived induced pluripotent stem cells. *Nat. Commun.* **8**, 15038 (2017).





# Chapter 5

## Epigenetic Characterization of the *FMR1* Promoter in Induced Pluripotent Stem Cells from Human Fibroblasts Carrying an Unmethylated Full Mutation

C.E.F. de Esch<sup>1</sup>, M. Ghazvini<sup>2,3</sup>, F. Loos<sup>3</sup>, N. Schelling-Kazaryan<sup>4</sup>, W. Widagdo<sup>1</sup>, S.T. Munshi<sup>5</sup>, E. van der Wal<sup>6</sup>, H. Douben<sup>1</sup>, N. Günhanlar<sup>5</sup>, S.A. Kushner<sup>5</sup>, W.W.M.P. Pijnappel<sup>6</sup>, F.M.S. de Vrij<sup>5</sup>, N. Geijsen<sup>4,7</sup>, J. Gribnau<sup>3,8</sup>, and R. Willemsen<sup>1</sup>

<sup>1</sup>Department of Clinical Genetics, Erasmus Medical Center, Rotterdam, the Netherlands

<sup>2</sup>iPS Cell Facility, Erasmus Medical Center, Rotterdam, the Netherlands

<sup>3</sup>Department of Reproduction and Development, Erasmus Medical Center, Rotterdam, the Netherlands

<sup>4</sup>KNAW Hubrecht Institute and UMC Utrecht, Utrecht, the Netherlands

<sup>5</sup>Department of Psychiatry, Erasmus Medical Center, Rotterdam, the Netherlands

<sup>6</sup>Molecular Stem Cell Biology, Department of Clinical Genetics and Department of Pediatrics, Division of Metabolic Diseases and Genetics, Center for Lysosomal and Metabolic Diseases, Erasmus Medical Center, Rotterdam, the Netherlands

<sup>7</sup>Department Companion Animals, Utrecht University School for Veterinary Medicine, Utrecht, the Netherlands

Published in Stem Cells Reports (2014), 3: 548–555



## ABSTRACT

Silencing of the *FMR1* gene leads to fragile X syndrome, the most common cause of inherited intellectual disability. To study the epigenetic modifications of the *FMR1* gene during silencing in time, we used fibroblasts and induced pluripotent stem cells (iPSCs) of an unmethylated full mutation (uFM) individual with normal intelligence. The uFM fibroblast line carried an unmethylated *FMR1* promoter region and expressed normal to slightly increased *FMR1* mRNA levels. The *FMR1* expression in the uFM line corresponds with the increased H3 acetylation and H3K4 methylation in combination with a reduced H3K9 methylation. After reprogramming, the *FMR1* promoter region was methylated in all uFM iPSC clones. Two clones were analyzed further and showed a lack of *FMR1* expression, whereas the presence of specific histone modifications also indicated a repressed *FMR1* promoter. In conclusion, these findings demonstrate that the standard reprogramming procedure leads to epigenetic silencing of the fully mutated *FMR1* gene.

## INTRODUCTION

The most common inherited form of intellectual disability, fragile X syndrome (FXS), is caused by the absence of the *FMR1* gene product, the fragile X mental retardation protein (FMRP). In the majority of FXS patients, the transcriptional silencing of the *FMR1* gene is initiated by an expansion of a naturally occurring CGG repeat in the 5' UTR of the *FMR1* gene, to more than 200 units<sup>1,2</sup>. This so-called full mutation results in hypermethylation of the cytosines in the repeat region and the *FMR1* promoter region during early human embryonic development<sup>3,4</sup>. This results in a lack of *FMR1* transcription and consequently an absence of FMRP. Along with hypermethylation, the *FMR1* promoter in FXS is characterized by additional epigenetic marks specific for transcriptionally repressed chromatin including reduced histone H3 and H4 acetylation, reduced histone H3K4 methylation, and increased histone H3K9 methylation<sup>5-8</sup>. However, the timing and molecular mechanisms involved in the CGG expansion, the concomitant DNA methylation, and the additional epigenetic changes that occur during embryonic development are not yet fully understood.

Insights into these processes may lead to a more complete understanding of the developmental processes underlying fragile X syndrome, which, in turn, could lead to new therapeutic strategies. Because murine fragile X models cannot be used to investigate epigenetic *FMR1* inactivation as methylation of the full mutations does not occur, human FXS embryonic stem cells have been studied. These studies showed that FMRP is expressed during early embryonic development, but that epigenetic silencing of *FMR1* occurs upon differentiation<sup>9,10</sup>. A further attempt to study the epigenetic changes over time made use of induced pluripotent stem cells (iPSCs) generated from human FXS fibroblasts. In contrast to human embryonic FX stem cells, these pluripotent cells were shown to already carry a fully methylated *FMR1* promoter and additional heterochromatin marks, so the epigenetic silencing mechanisms in time could not be studied<sup>11-13</sup>.

In 1991, a familial case was reported in which two brothers with normal intelligence were shown to have a full *FMR1* mutation without the concomitant hypermethylation of the CGG repeat and the promoter region<sup>14</sup>. In order to unravel the molecular mechanisms behind the epigenetic silencing in fragile X syndrome, we derived iPSCs from these human fibroblasts, to analyze the epigenetic characteristics of the *FMR1* promoter after reprogramming and during differentiation. Here, we report the characterization of these iPSCs and show, unexpectedly, that the *FMR1* promoter of the unmethylated full mutation cell line becomes methylated during reprogramming and stays methylated after differentiation into neural progenitor cells.

## RESULTS

### *Fibroblast Characterization*

Fibroblasts from a normal male carrying an unmethylated full mutation first described by Smeets et al. (1995)<sup>14</sup> (uFM) and fibroblasts from a clinically diagnosed male fragile X syndrome patient (14 years old, FXS) and an unrelated unaffected male control line (3 years old, control) were analyzed for *FMR1* 5' UTR CGG repeat length, methylation status, *FMR1* expression, and the histone marks associated with the *FMR1* promoter. As expected, the control line showed a CGG repeat length within the normal range (<55), whereas the uFM and the FXS line showed CGG repeat lengths in the full mutation range (approximately 233 and 380 repeats, respectively) (**Figure S1**). Also, as expected, the part of the *FMR1* promoter analyzed after bisulfite conversion was not methylated in the control and the uFM cell lines, whereas in the FXS cell line the *FMR1* promoter was methylated (**Figures 1A** and **S2** for location of the primers). Because the methylation status is predictive of *FMR1* expression, indeed the control line showed normal expression levels and the uFM line showed normal to slightly increased *FMR1* expression, whereas the FXS cell line did not express *FMR1* transcripts (**Figure 1B**). Additionally, bisulfite Sanger sequencing of a region of the *FMR1* promoter containing 22 CpGs was carried out, which confirmed the absence of methylation of the *FMR1* promoter in the uFM fibroblast line (**Figure 1C**).

### *Fibroblast Reprogramming and iPSC Characterization*

The fibroblasts were reprogrammed to iPSC lines according to established protocols<sup>15,16</sup>. First, four iPSC clones were generated that showed typical characteristics of pluripotent stem cells: morphology similar to that of embryonic stem cells (data not shown), expression of alkaline phosphatase (data not shown), silencing of the multicistronic lentiviral transgene (data not shown), reactivation of genes indicative of pluripotency (data not shown), immunoreactivity for OCT4, NANOG, TRA-1-60, TRA-1-81, and SSEA4 (**Figure S3**), propagation for a long time in culture (up to passage 30), and maintenance of a normal diploid karyotype (data not shown). All four cell lines generated embryonic bodies that, after differentiation *in vitro*, expressed markers of endoderm, mesoderm and ectoderm (**Figure S3**). These four lines were extensively characterized and the results are described below. Second, we generated eight additional iPSC clones from the uFM fibroblast line solely in order to confirm the methylation status of the *FMR1* promoter by quantitative PCR (**Figure 2D**). These additional iPSC clones were generated from the uFM fibroblast line by the same methods as described, except this time we used naive human stem cell medium (WIS-NHSM) as defined by Gafni et al. (2013)<sup>17</sup>. This medium facilitates the derivation of naive pluripotent iPSCs with properties highly similar to mouse naive ES cells.

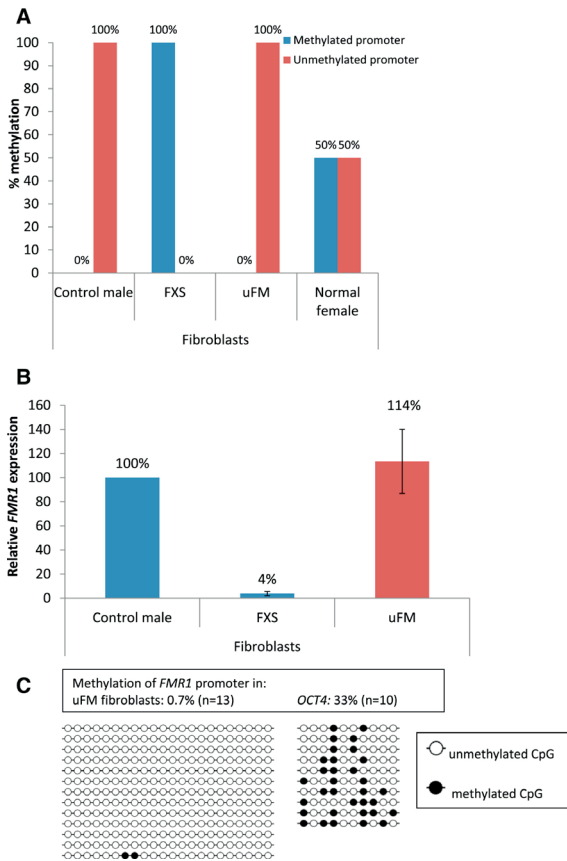


**Figure 1. Methylation Status and *FMR1* Expression Levels in the Fibroblast Cell Lines**

(A) Methylation status of a region of the *FMR1* promoter in fibroblasts of the male control line, fragile X line (FXS), and the unmethylated full mutation line (uFM). Values were normalized to CLK2 promoter activity first. The normalized exponential values were then presented as a percentage relative to the female fibroblast control line, for which the normalized exponential values were set to 50% for each primer set ( $n = 2-3$  separate measurements). (B) Real-time quantitative PCR data showing *FMR1* transcript levels in fibroblasts of the male control line, fragile X line (FXS), and the unmethylated full mutation line (uFM) normalized to CLK2 expression. Values are means  $\pm$  SEM relative to appropriate male control line ( $n = 2-3$  separate measurements). (C) The percentage of methylated CpGs in the *FMR1* promoter and as a control the *OCT4* promoter, in 13 and ten clones, respectively, after Sanger sequencing of bisulfite converted DNA of the uFM fibroblast line. Each line represents a clone, and each circle represents a CpG site, which is methylated (closed circle) or unmethylated (open circle). See also Figures S1 and S2.

### **Reprogramming Effects on CGG Repeat Length, *FMR1* Expression, and Methylation**

Analysis of the CGG repeat in the 5' UTR of the *FMR1* promoter indicated that the repeat length in the cell lines carrying a full mutation did not contract to levels below 200 CGGs during reprogramming (Figure S1). The iPSC clone of the control cell line contained a CGG length under 55 repeats. Nonetheless, the CGG repeat length contracted slightly in the FXS iPSC line after reprogramming, from 380 repeats to approximately 290 repeats. In contrast, the repeat was expanded in the two uFM iPSC clones to approximately 330 and 380 repeats (Figure S1). As expected, the iPSC clone of the control cell line showed *FMR1* expression, in contrast to the FXS iPSC clone that did not show *FMR1* expression. Unexpectedly, the two uFM iPSC clones did not express *FMR1* either (Figure 2A). Further analysis showed that the bisulfite converted *FMR1* promoter region was methylated in the FXS iPSC clone as well as in both uFM iPSC clones, whereas the control iPSC cell line did not show any methylation (Figure 2B). Bisulfite Sanger sequencing confirmed the methylation status of the two uFM iPSC clones (Figure 2C). The additional eight iPSC clones generated from the uFM fibroblast line

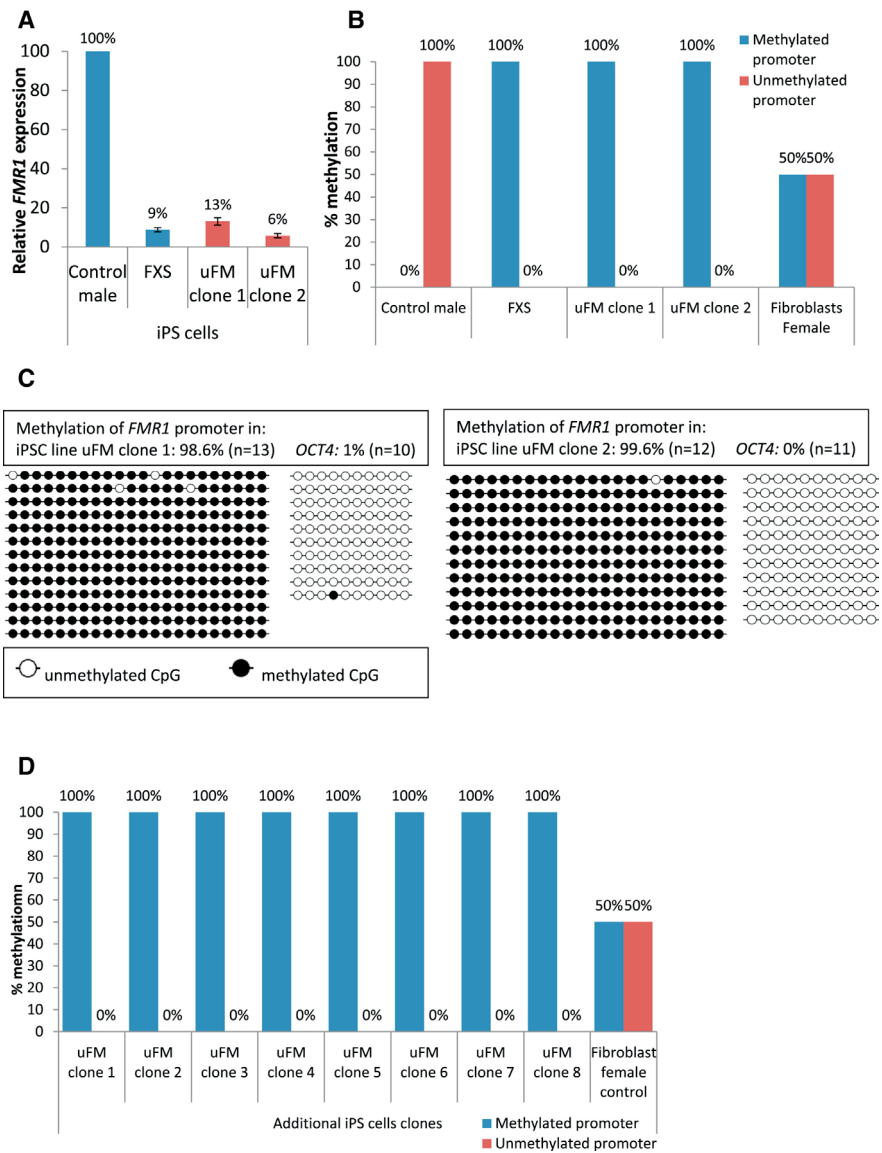


**Figure 2 Methylation Status and *FMR1* Expression Levels in the Induced Pluripotent Stem Cells**

(A) Real-time quantitative PCR data showing *FMR1* transcript levels in induced pluripotent stem cells (iPSCs) of the male control line, fragile X line (FXS), and the unmethylated full mutation clones (uFM clone 1 and clone 2) normalized to *CLK2* expression. Values are mean  $\pm$  SEM relative to appropriate male control line (n = 2–3 separate measurements).

(B) Methylation status of a region of the *FMR1* promoter in iPSCs of the male control line, fragile X line (FXS), and the unmethylated full mutation clones (uFM clone 1 and clone 2). Values were normalized to *CLK2* promoter activity first. The normalized exponential values were then presented as a percentage relative to the female fibroblast control line, for which the normalized exponential values were set to 50% for each primer set (n = 2–3 separate measurements).

## Figure 2 Methylation Status and *FMRI* Expression Levels in the Induced Pluripotent Stem Cells

(continued)

(C) The percentage of methylated CpGs in the *FMRI* promoter and as a control the *OCT4* promoter, after Sanger sequencing of bisulfite converted DNA of the uFM iPSC clones. Each line represents a clone, and each circle represents a CpG site, which is methylated (closed circle) or unmethylated (open circle).

(D) Methylation status of a region of the *FMRI* promoter in additionally generated iPSC clones of the unmethylated full mutation fibroblast line in naive human stem cell medium. Values were normalized to *CLK2* promoter activity first. The normalized exponential values were then presented as a percentage relative to the female fibroblast control line, for which the normalized exponential values were set to 50% for each primer set (n = 2 separate measurements). See also Figures S1–S3.

in WIS-NSHM medium also showed complete methylation of the bisulfite converted *FMRI* region (**Figure 2D**). Thus, the originally unmethylated extended CGG repeat found in the uFM fibroblasts became methylated at some point during the reprogramming process.

Chromatin immunoprecipitation (ChIP) experiments with the fibroblast lines showed that the *FMRI* promoter of the control line carried active histone marks, H3 acetylation and H3K4 dimethylation with values similar to the positive control, namely, the active gene *APRT*, and values much higher than the negative control *CRYAA* (crystalline), which only serves as a positive control for repressed genes. The inactive mark H3K9 trimethylation was not enriched in the control fibroblasts (**Figures 3A–3C**). The uFM fibroblast line carried histone marks representative of an actively transcribed gene, namely, H3 acetylation and H3K4 methylation at similar levels as the control line. The inactive mark H3K9 methylation could not be detected in the uFM fibroblast line (**Figures 3A–3C**). The *FMRI* promoter of the FXS cell line only showed enrichment of the repressive mark H3K9 methylation (**Figures 3A–3C**). ChIP analysis of the *FMRI* promoter in iPSCs showed enrichment of the active marks H3 acetylation and H3K4 methylation in the control iPSC clone, to levels higher than the positive control *APRT*. The FXS iPSCs and clone 1 of the uFM iPSCs showed an increase of the repressive mark H3K9 methylation to values above the repressive control *CRYAA*, whereas enrichment of the active marks could not be detected in FXS iPSCs and uFM iPSC clones 1 and 2 (**Figures 3D–3F**).

Next, we investigated the effects of differentiation into neural progenitor cells (NPCs) on *FMRI* expression and methylation (see **Figure S4** for staining with marker *SOX2*). NPCs derived from the FXS and uFM iPSCs lacked *FMRI* expression and carried a methylated *FMRI* promoter. The NPCs derived from the control iPSC clone showed clear *FMRI* expression and an unmethylated promoter region (**Figures 4A and 4B**). These findings indicate that the reprogramming process leads to methylation of the expanded *FMRI* CGG repeat sequence, which results in a stable shut down of *FMRI* gene expression.

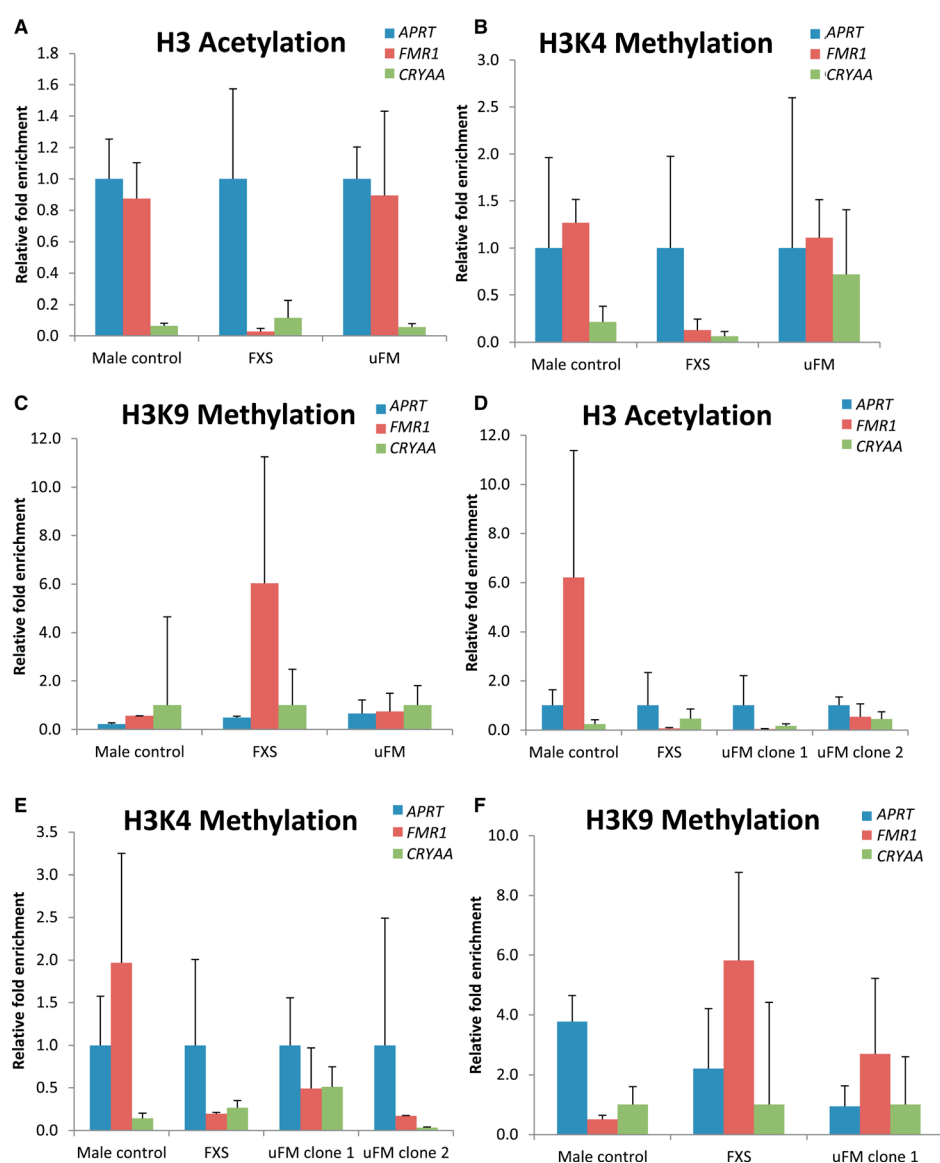


**Figure 3 Chromatin Immunoprecipitation Analysis of H3 Acetylation, H3K4 Methylation, and H3K9 Methylation in the *FMR1* Promoter of Fibroblasts and iPSCs**

Chromatin immunoprecipitation analysis of H3 acetylation, H3K4 methylation, and H3K9 methylation in the *FMR1* promoter of fibroblasts (A–C) and iPSCs (D–F), respectively. Results were normalized to the appropriate positive control (*APRT* or *CRYAA*), averaged from at least two different experiments and shown with their respective SEs.



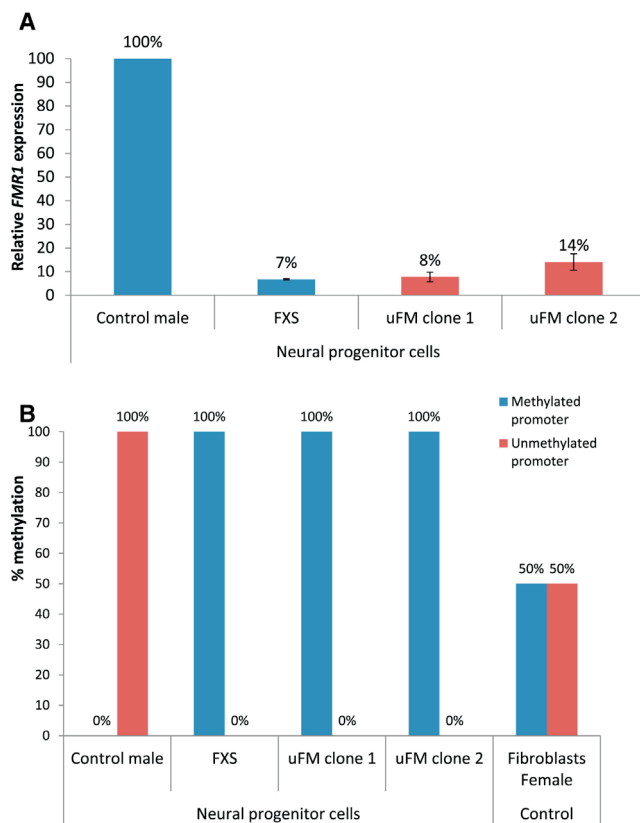


**Figure 4 Methylation Status and *FMR1* Expression Levels in Neural Progenitor Cells**

(A) Real-time quantitative PCR data showing *FMR1* transcript levels in neural progenitor cells (NPCs) of the male control line, fragile X line (FXS), and the unmethylated full mutation clones (uFM clone 1 and clone 2) normalized to *CLK2* expression. Values are mean  $\pm$  SEM relative to appropriate male control line ( $n = 2$  separate measurements).

(B) Methylation status of a region of the *FMR1* promoter in NPCs of the male control line, fragile X line (FXS), and the unmethylated full mutation clones (uFM clone 1 and clone 2). Values were normalized to *CLK2* promoter activity first. The normalized exponential values were then presented as a percentage relative to the female fibroblast control line, for which the normalized exponential values were set to 50% for each primer set ( $n = 2-3$  separate measurements). See also Figures S2 and S4.

## DISCUSSION

We undertook this study in an attempt to unravel the epigenetic mechanisms involved in the silencing of the *FMR1* gene in fragile X syndrome by the use of a fibroblast line carrying an unmethylated full mutation. There have been several attempts to study epigenetic silencing in fragile X syndrome. Eigset et al. (2007)<sup>9</sup> have shown that FXS human embryonic stem cells (hESCs) still express FMRP at a level similar to that in unaffected hESCs, whereas the FMRP level decreases as the hESCs were differentiated. Based on these results, it was expected that

by reprogramming FXS fibroblasts into pluripotent stem cells, the hypermethylated state of the *FMR1* promoter region would be reversed. However, by now several research groups have shown that iPSCs derived from FXS patients show epigenetic marks characteristic for heterochromatin similar to the full mutation fibroblasts they originated from<sup>11-13</sup>. These observations could be explained by the fact that the FXS iPSCs may not have all the characteristics of early pluripotency, but that they represent a later stage of human development<sup>11-13,17</sup>.

Another approach was used in studies with human fragile X lymphoblastic cells; here, a fully mutated and hypermethylated *FMR1* gene was reactivated by treatment with 5-azadeoxycytidine, a hypomethylating agent. Although such treatment significantly reduced DNA methylation in some cells, it could not restore all remaining epigenetic marks to control levels<sup>5,6,18,19</sup>. Drugs such as 4-phenylbutyrate, sodium butyrate or trichostatin A, which block the activity of histone deacetylases, did not restore *FMR1* expression to normal levels<sup>5,6,8,19</sup>. In addition, treatment with a compound that reduces the *in vitro* expression of the FRAXA fragile site, acetyl-l-carnitine, did not restore the *FMR1* expression either<sup>8</sup>. Recently, 5-azadeoxycytidine treatment was also tested on fragile X iPSCs, and it appeared to restore *FMR1* expression in both iPSCs and differentiated neurons, which offers possibilities to use these cells as an epigenetic model<sup>13</sup>.

The availability of a fibroblast cell line carrying an unmethylated full mutation (uFM) provided a new opportunity to study the epigenetic silencing mechanisms in time. We first characterized the uFM fibroblast cell line together with a normal male fibroblast control line and a FXS fibroblast cell line carrying a fully methylated *FMR1* promoter. Although increased *FMR1* mRNA levels (up to five times) were reported in lymphoblastoid cells of premutation carriers (55~200 unmethylated CGGs), our findings of normal to slightly increased *FMR1* mRNA levels in the uFM fibroblasts are similar to the findings of Pietrobono et al. (2005)<sup>7</sup>, who examined a lymphoblastic cell line from the same individual. The lack of DNA methylation ensures that the chromatin is less densely packed and more accessible for transcription, which explains the *FMR1* expression in this cell line. Our ChIP results differ from the original ChIP analysis of the uFM lymphoblastoid cell line<sup>8</sup>. We found a similar increase in H3K4 methylation; however, we did not find decreased H3 acetylation levels or intermediate H3K9 levels in the uFM fibroblasts. These differences could be explained by the fact that we have analyzed a distinct cell type (fibroblasts versus lymphoblastoid cells), and by differences in the ChIP protocol (e.g., quantification methods and reference genes used). Because the uFM fibroblast line lacked methylation of the *FMR1* promoter site despite the high number of CGG repeats, we expected to find an unmethylated *FMR1* promoter and normal levels of *FMR1* mRNA after reprogramming into iPSCs. Surprisingly, we found the promoter region of *FMR1* to be hypermethylated in all iPSC clones. Other epigenetic chromatin marks also indicated a repressed *FMR1* promoter similar to the marks observed in the fragile X iPSC line. After differentiation of these iPSCs into neural progenitor cells, the *FMR1* promoter remained methylated and thus silenced.

There are three possible explanations for our findings. First, it is possible that the reprogramming process resulted in iPSCs that were solely derived from methylated FM fibroblasts and not of the unmethylated cells. This assumes that methylated FM fibroblasts were present in our culture, which according to our bisulfite sequencing results seems highly unlikely. Second, there may be an unknown genetic factor present in this individual that was protective against DNA methylation during embryonic development but which was absent in his fibroblasts or which was altered or blocked during the reprogramming process. In our case, the brother of this individual was also carrier of an unmethylated full mutation. Being a carrier of an unmethylated full mutation is already a very rare phenomenon, but the fact that two children escaped methylation in one family clearly points towards the involvement of a maternal-paternal genetic component or environmental factors. Finally, the reprogramming process might activate genes that induce de novo methylation of the *FMR1* promoter. Although the *FMR1* gene in this individual escaped methylation during embryonic development, the full mutation in his fibroblasts might be recognized by epigenetic remodelers, e.g., by histone and/or DNA methyltransferases (DNMTs) that are not recruited in embryonic development. This would also explain the unmethylated full mutation observed in human embryonic FXS stem cells because these cells never went through this reprogramming process. A strategy to test this hypothesis would be, for example, to perform the reprogramming of the uFM fibroblasts as well as FXS fibroblast lines under conditions that inhibit the functioning of DNMT 3a and 3b.

In conclusion, standard reprogramming of somatic uFM fibroblasts into pluripotent stem cells by the use of four transcription factors did not lead to demethylation of the expanded CGG repeat and even induced methylation of an unmethylated template. Very recently, Gafni et al. (2013)<sup>17</sup> suggested that a more naive ground state pluripotent stem cell in which epigenetic memory is completely erased could be obtained by a unique combination of cytokines and small molecule inhibitors (WIS-NHS medium). Their study also demonstrated the reactivation of the *FMR1* gene in FXS iPSCs after the reprogramming of FXS fibroblast under naive conditions. However, in contrast to these findings, the use of this WIS-NHS medium did not prevent the occurrence of the de novo methylation of the extended *FMR1* repeat in our uFM iPS clones. In conclusion, our results show that although this fibroblast line may offer a unique system to study the de novo methylation of an extended *FMR1* repeat during reprogramming, the mechanism behind the silencing of the *FMR1* gene in fragile X syndrome remains elusive.

## EXPERIMENTAL PROCEDURES

### *Cell Culture*

The rare fibroblast cell line established from a normal male carrying an unmethylated full mutation first described by Smeets et al. (1995)<sup>14</sup> (uFM) was used. This line has been subcloned,

so that a homogenous population of cells that carry a fully extended repeat was obtained. Fibroblasts from a clinically diagnosed male fragile X syndrome patient (14 years, FXS), and an unrelated unaffected male (3 years, control) and female control fibroblast line (9 years) were all obtained from the cell repository of the department of Clinical Genetics, Erasmus MC, Rotterdam. For culture conditions, see the Supplemental Experimental Procedures.

### ***iPSC Generation***

Reprogramming of human primary skin fibroblasts was performed as described previously<sup>16</sup>. Briefly, fibroblasts were infected with a single, multicistronic lentiviral vector encoding OCT4, SOX2, KLF4, and MYC and cultured on  $\gamma$ -irradiated mouse embryonic feeder (MEF) cells until iPSC colonies could be picked<sup>16</sup>. The second round of reprogramming of the uFM fibroblast line was done in naive ES medium (WIS-NHSM medium) according to Gafni et al. (2013)<sup>17</sup> (see the Supplemental Experimental Procedures). These cells were used to affirm the methylation status of the *FMR1* promoter after reprogramming by methylation specific quantitative PCR. For further details, see the Supplemental Experimental Procedures.

### ***In Vitro Differentiation of Embryonic Bodies***

To form embryonic bodies (EBs), iPSC colonies from two wells per line were broken up by collagenase IV treatment and transferred to ultralow attachment 6-well plates (Corning). For the germ layer differentiation conditions, see the Supplemental Experimental Procedures. After 2 weeks in culture, the cells were fixed with formalin and immunostainings were performed (see the Supplemental Experimental Procedures).

### ***Neural Differentiation***

Human iPSCs were differentiated according to Brennand et al. (2011)<sup>20</sup>, with modifications (see the Supplemental Experimental Procedures). After 1 week, NPCs were dissociated with collagenase (100 U/ml), replated, and used for staining and methylation analysis after three to five passages.

### ***Karyotype Analysis and Immunocytochemistry***

Standard staining procedures were followed; for details, see Supplemental Experimental Procedures.

### ***CGG Repeat Length, FMR1 Expression, and Methylation Analysis***

CGG repeat size was determined in a PCR using the primers 5'-CGGAGGCGCCGCTGC-CAGG-3' and 5'-TGCGGGCGCTCGAGGCCAG-3' with the Expand high fidelity PCR kit (Roche) supplemented with 2.5 M betaine (see the Supplemental Experimental Procedures). For details of the *FMR1* expression analysis, see the Supplemental Experimental Procedures. Genomic DNA was modified by bisulfite treatment according to the EpiTect Bisulfite Kit.

The diluted converted DNA was then measured using quantitative PCR with two different primer set designed specifically for a region of the *FMRI* promoter (see **Figure S1** for the locations). One primer set contained the methylated DNA sequence and the other contained the unmethylated DNA sequence of a region of the *FMRI* promoter after bisulfite conversion (see the Supplemental Experimental Procedures).

### ***Bisulfite Sanger Sequencing***

Genomic DNA (1,000 ng) was modified by bisulfite treatment according to the EpiTect Bisulfite Kit. Then a region of the *FMRI* promoter containing 22 CpGs was amplified using PlatinumTaq (Invitrogen) (see **Figure S1** for location of the primers). PCR products were cloned into pGEM-T Easy (Promega), and single clones were sequenced by Sanger sequencing (see Supplemental Experimental Procedures).

### ***Chromatin Immunoprecipitation***

Chromatin immunoprecipitation (ChIP) was performed according to the Upstate ChIP protocol with some small modifications (see Supplemental Experimental Procedures). Eluted DNA fragments were used for quantitative PCR analysis (see **Figure S1** for location of the primers). The Ct values of the histone modifications were first normalized for the nonspecific immunoglobulin G antibody treatment and then for the amount of input DNA. Data were then presented in relative fold enrichment after further normalization to the APRT gene for H3 acetylation and H3K4 methylation and CRYAA for H3K9 methylation. Data from at least two separate experiments were averaged, and both reference genes were previously used by Urbach et al. (2010)<sup>11</sup> and Bar-Nur et al. (2012)<sup>13</sup>.

## **ACKNOWLEDGMENTS**

The authors thank Dr. A. Schambach for kindly sharing the iPSC reprogramming vector. This work was supported by the Netherlands Organisation for Health Research and Development (R.W.; ZonMw; 912-07-022), E-Rare program entitled “Cure FXS” (R.W.; no. EU/FISPS09102673), the Prinses Beatrix Spierfonds (W.W.M.P.P. and E.v.d.W., project number: W.OR13-21), a fellowship of the Hersenstichting Nederland (F.M.S.d.V.) and the NeuroBasic-PharmaPhenomics consortium (S.A.K.), and NWO VICI and ERC grants (J.G.).

## REFERENCES

1. Verkerk, A.J., Pieretti, M., Sutcliffe, J.S., Fu, Y.H., Kuhl, D.P., Pizzuti, A., Reiner, O., Richards, S., Victoria, M.F., Zhang, F.P., et al. (1991). Identification of a gene (FMR-1) containing a CGG repeat coincident with a breakpoint cluster region exhibiting length variation in fragile X syndrome. *Cell* 65, 905–914.
2. Pearson, C.E., Nichol Edamura, K., and Cleary, J.D. (2005). Repeat instability: mechanisms of dynamic mutations. *Nat. Rev. Genet.* 6, 729–742.
3. Sutcliffe, J.S., Nelson, D.L., Zhang, F., Pieretti, M., Caskey, C.T., Saxe, D., and Warren, S.T. (1992). DNA methylation represses FMR-1 transcription in fragile X syndrome. *Hum. Mol. Genet.* 1, 397–400.
4. Willemsen, R., Bontekoe, C.J., Severijnen, L.A., and Oostra, B.A. (2002). Timing of the absence of FMR1 expression in full mutation chorionic villi. *Hum. Genet.* 110, 601–605.
5. Coffee, B., Zhang, F., Warren, S.T., and Reines, D. (1999). Acetylated histones are associated with FMR1 in normal but not fragile X-syndrome cells. *Nat. Genet.* 22, 98–101.
6. Coffee, B., Zhang, F., Ceman, S., Warren, S.T., and Reines, D. (2002). Histone modifications depict an aberrantly heterochromatinized FMR1 gene in fragile x syndrome. *Am. J. Hum. Genet.* 71, 923–932.
7. Pietrobono, R., Tabolacci, E., Zalfa, F., Zito, I., Terracciano, A., Moscato, U., Bagni, C., Oostra, B., Chiurazzi, P., and Neri, G. (2005). Molecular dissection of the events leading to inactivation of the FMR1 gene. *Hum. Mol. Genet.* 14, 267–277.
8. Tabolacci, E., Pietrobono, R., Moscato, U., Oostra, B.A., Chiurazzi, P., and Neri, G. (2005). Differential epigenetic modifications in the FMR1 gene of the fragile X syndrome after reactivating pharmacological treatments. *Eur. J. Hum. Genet.* 13, 641–648.
9. Eiges, R., Urbach, A., Malcov, M., Frumkin, T., Schwartz, T., Amit, A., Yaron, Y., Eden, A., Yanuka, O., Benvenisty, N., and Ben-Yosef, D. (2007). Developmental study of fragile X syndrome using human embryonic stem cells derived from preimplantation genetically diagnosed embryos. *Cell Stem Cell* 1, 568–577.
10. Gerhardt, J.I., Tomishima, M.J., Zaninovic, N., Colak, D., Yan, Z., Zhan, Q., Rosenwaks, Z., Jaffrey, S.R., and Schildkraut, C.L. (2013). The DNA replication program is altered at the FMR1 locus in fragile X embryonic stem cells. *Mol. Cell* 53, 19–31.
11. Urbach, A., Bar-Nur, O., Daley, G.Q., and Benvenisty, N. (2010). Differential modeling of fragile X syndrome by human embryonic stem cells and induced pluripotent stem cells. *Cell Stem Cell* 6, 407–411.
12. Sheridan, S.D., Theriault, K.M., Reis, S.A., Zhou, F., Madison, J.M., Daheron, L., Loring, J.F., and Haggarty, S.J. (2011). Epigenetic characterization of the FMR1 gene and aberrant neurodevelopment in human induced pluripotent stem cell models of fragile X syndrome. *PLoS ONE* 6, e26203.
13. Bar-Nur, O., Caspi, I., and Benvenisty, N. (2012). Molecular analysis of FMR1 reactivation in fragile-X induced pluripotent stem cells and their neuronal derivatives. *J. Mol. Cell Biol.* 4, 180–183.
14. Smeets, H.J., Smits, A.P., Verheij, C.E., Theelen, J.P., Willemsen, R., van de Burgt, I., Hoogeveen, A.T., Oosterwijk, J.C., and Oostra, B.A. (1995). Normal phenotype in two brothers with a full FMR1 mutation. *Hum. Mol. Genet.* 4, 2103–2108.
15. Takahashi, K., Okita, K., Nakagawa, M., and Yamanaka, S. (2007). Induction of pluripotent stem cells from fibroblast cultures. *Nat. Protoc.* 2, 3081–3089.
16. Warlich, E., Kuehle, J., Cantz, T., Brugman, M.H., Maetzig, T., Galla, M., Filipczyk, A.A., Halle, S., Klump, H., Scholer, H.R., et al. (2011). Lentiviral vector design and imaging approaches to visualize the early stages of cellular reprogramming. *Mol. Ther.* 19, 782–789.
17. Gafni, O., Weinberger, L., Mansour, A.A., Manor, Y.S., Chomsky, E., Ben-Yosef, D., Kalma, Y., Viukov, S., Maza, I., Zviran, A., et al. (2013). Derivation of novel human ground state naive pluripotent stem cells. *Nature* 504, 282–286.

18. Chiurazzi, P., Pomponi, M.G., Willemsen, R., Oostra, B.A., and Neri, G. (1998). In vitro reactivation of the FMR1 gene involved in fragile X syndrome. *Hum. Mol. Genet.* 7, 109–113.
19. Chiurazzi, P., Pomponi, M.G., Pietrobono, R., Bakker, C.E., Neri, G., and Oostra, B.A. (1999). Synergistic effect of histone hyperacetylation and DNA demethylation in the reactivation of the FMR1 gene. *Hum. Mol. Genet.* 8, 2317–2323.
20. Brennand, K.J., Simone, A., Jou, J., Gelboin-Burkhart, C., Tran, N., Sangar, S., Li, Y., Mu, Y., Chen, G., Yu, D., et al. (2011). Modelling schizophrenia using human induced pluripotent stem cells. *Nature* 473, 221–225.

# SUPPLEMENTAL DATA SUPPLEMENTAL FIGURES

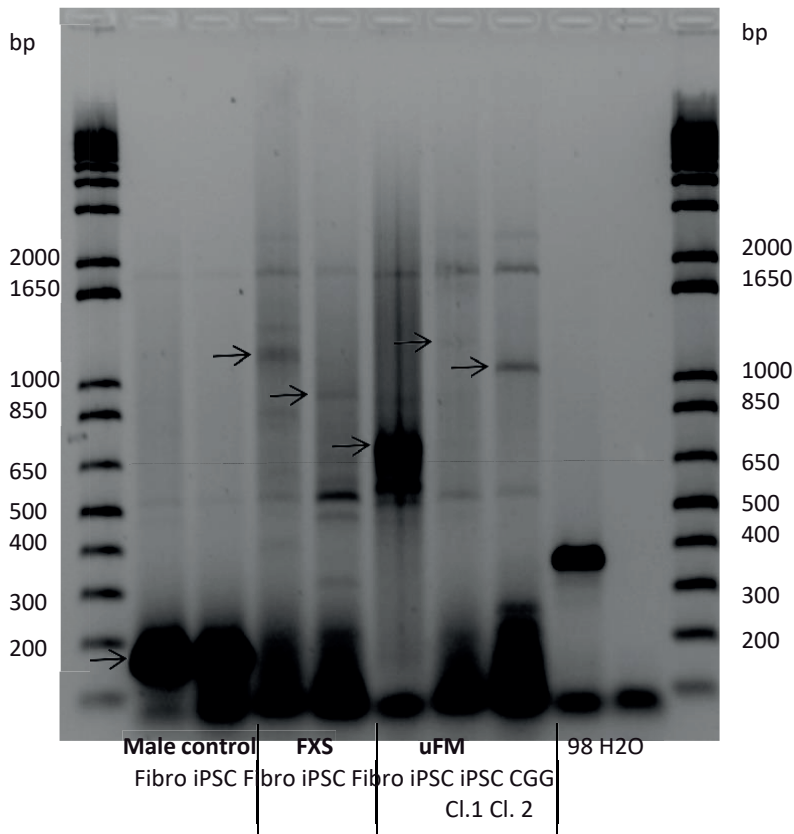


**Figure S1: Repeat length analysis before and after reprogramming into iPS cells**

The male control fibroblasts and the derived control iPS cells show a repeat length below 55. The fragile X (FXS) fibroblast line shows a repeat length of approximately 380 repeats. The derived FXS iPSs show a small contraction of the repeat length to approximately 290 repeats. The unmethylated full mutation (uFM) fibroblast line has a repeat length of approximately 233 repeats (~750bp). The two uFM iPS cell clones show an expanded repeat length of approximately 380 (clone 1) and 330 repeats (clone 2). A DNA sample containing 98 CGG repeats was run on the same gel, in addition to a water control. All products of the CGG repeat PCR were run on one agarose gel with a ladder on both sides. A band at the marker level of 650 base pairs corresponds with a CGG repeat length of 200 repeats. Related to Figures 1 and 2.



13261 ccactccacc tcccgtcag tcagactcg ctactttgaa ccggaccaa ccaaacaaa

ChIP F -----> F1 -----> <-----

13381 gggataaccg gatgcattg atttccacg ccaactgagtg cacctctgca gaaatggcg

<-ChIP R BSM F---->

13441 ttctggccct cgcgaggcag tgcgacctgt caccgccctt cagccttccc gcctccacc

<---BSM R

13501 aagcccgcgc acgccggcc cgcgcgtctg tcttcgacc cggcaccgc gccggttccc

<-----R1

13561 agcagcgcgc atgcgcgcgc tcccaggcca ctgaagaga gaggcgggg cgcgaggct

BSNM F--->

13621 gagcccgcgc ggggaggga cagcgttgat cagtgacgt ggtttcagtg ttacaccgc

Start of transcription

13681 cagcgggcgc ggggttcggc ctacgtcagg cgtcagctc gtttcggtt tcacttcgcg

<---BSNM R

13741 tggaggcgcc cctctgagcg ggcgcgggcg cgacgcgag cgcggcgccg ggcggtgacg

CGG-repeat

13801 gagcgccgc tgcaggggg cgtgcggcag cgcggcgccg gcggcgccg cgcggcgccg

13861 ggaggcgccg gcggcgccg cgcggcgccg ggctgggcct cagcgcgccg cagcccact

Start of translation

13921 ctcggggcg ggctccgcg gctagcagg ctgaagaga gatggaggag ctggtggtg

start of intron 1

13981 aagtgcggg ctccaatgc gcttttaca aggtacttg cttagggca ggccccatc

**Figure S2: The promoter region of the *FMRI* gene with the location of the primers used in this study**

Sequence numbering from GenBank L29074. Primers used in this study are indicated by the underlined sequence in combination with the name and arrow above the sequence. Individual cytosines belonging to methylation sites are indicated in bold as well as the CGG repeat. In addition, the start of transcription, translation and intron 1 are indicated as well. For the methylation-specific qPCR we analysed 11 methylation sites using the methylation specific primers (BSM F and R) and 15 sites with the unmethylated primers set (BSNM F and R). Bisulfite sequencing by using the F1 and R1 primers was based on Pietrobono *et al*, 2002, and contained 22 methylation sites. Related to Figures 1, 2, and 4.

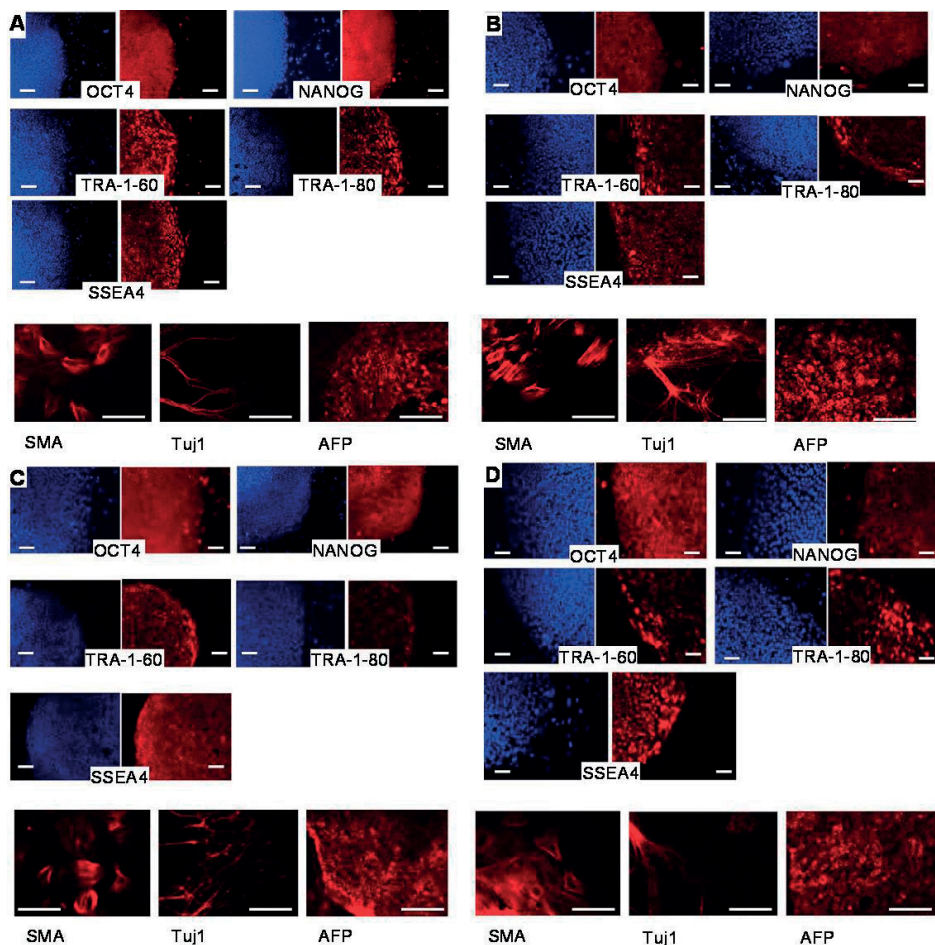


**Figure S3: Expression of pluripotency markers by iPSCs and germ layer marker expression after *in vitro* differentiation**

From left to right and top to bottom you can see images showing OCT4, NANOG, Tra-1-60, Tra-1-80 and SSEA4 expression as well as expression of the mesodermal marker smooth muscle actin (SMA), the ectodermal marker Tuj1 (or B-tubulin III) and endodermal marker alpha fetoprotein (AFP) (all in red) in the control line (A), fragile X cell line (B) and the uFM clones (C and D, clone 1 and clone 2 respectively). For each pluripotency marker a nuclear Hoechst staining is displayed in blue. Scale bars: 50  $\mu$ m for the pluripotency markers and 100  $\mu$ m for the germ layer markers. Related to Figure 2.

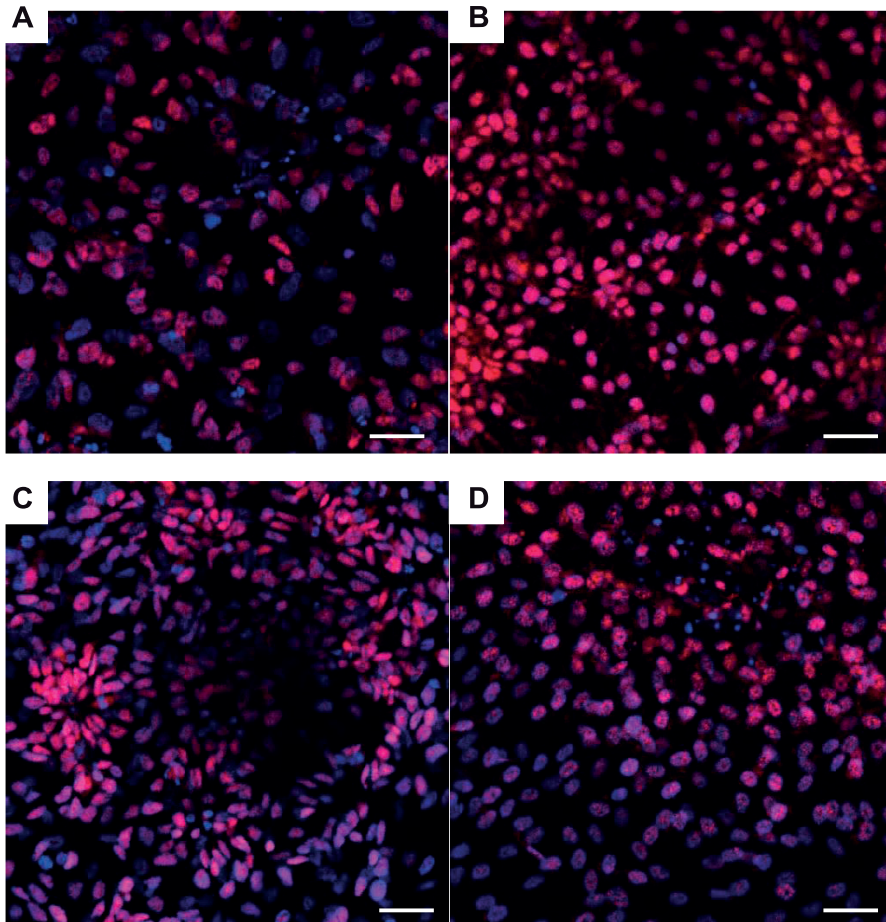


**Figure S4: SOX2 expression by neural progenitor cells**

Expression of SOX2 in red by neural progenitor cells of the control line (A), fragile X cell line (B) and the uFM clones (C and D, clone 1 and clone 2 respectively). In each image a nuclear DAPI staining (in blue) is displayed as well. Scale bar 100 μm. Related to Figure 4.

## SUPPLEMENTAL EXPERIMENTAL PROCEDURES CELL CULTURE CONDITIONS

The fibroblasts were cultured in Dulbecco's Modified Eagle Medium (DMEM) (Gibco-Invitrogen) containing 10% fetal calf serum and 1% penicillin/streptomycin.

The first set of generated iPS cell lines, namely the male control line, the FXS line and the uFM iPS clone 1 and 2 were cultured in conventional ES cell culture medium containing DMEM/F12 (Gibco-Invitrogen) supplemented with 20% knock-out serum replacement (Gibco-Invitrogen), 2 mM L-glutamine, 50 units of penicillin/streptomycin/glutamine, 0.1 mM MEM-non-essential amino acids (PAA Laboratories GmbH), 0.1 mM B-mercaptoethanol, and 10 ng/ml bFGF (Invitrogen) filtered through a 0.22  $\mu$ m filter (Corning). Human iPS lines growing on conventional medium were passaged weekly using collagenase IV (1 mg/ml, Invitrogen) on  $\gamma$ -irradiated MEFs.

The second round of iPS cells were grown in WIS-NHSM medium containing 475 ml knockout DMEM (Invitrogen), 20% knockout serum (invitrogen), human insulin (Sigma, 12.5  $\mu$ g/ml), 10  $\mu$ g recombinant human Lif (Peprotech), 8 ng/ml recombinant bFGF (Peprotech) and 1 ng/ml recombinant TGF- $\beta$ 1 (Peprotech), 1 mM glutamine (Invitrogen), 1% MEM-non-essential amino acids (Invitrogen), 0.1 mM  $\beta$ -mercaptoethanol (Sigma), Penicillin-Streptomycin (Invitrogen) and small molecule inhibitors: PD0325901 (1  $\mu$ M, ERK1/2i, Axon Medchem); CHIR99021 (3  $\mu$ M, GSK3i, Axon Medchem); SP600125 (10  $\mu$ M, JNKi, TORCIS) and SB203580 (10  $\mu$ M, p38i, Axon Medchem) Y-27632 (5  $\mu$ M, Axon Medchem) and protein kinase C inhibitor G06983 (5  $\mu$ M, TOCRIS). Naive human iPS clones were grown on  $\gamma$ -irradiated MEFs on gelatin-coated plates and passaged by single-cell trypsinization (0.05% EDTA) every 4 days. These naive cells also showed the main characteristics of induced pluripotent stem cells including morphology similar to that of embryonic stem cells, silencing of retroviral transgenes and reactivation of pluripotency genes (data not shown).

### ***In vitro* differentiation of embryonic bodies**

Floating EBs were cultured in iPSC medium without bFGF for a minimum of 6 days with supplemented SB431542 for ectoderm conditions only. The embryonic bodies (EBs) designated for endoderm were then transferred to gelatin coated 12-wells plates containing the following medium: RPMI 1640 (Gibco-Invitrogen), supplemented with 20% FBS, 1: 100 dilution of penicillin/streptomycin/glutamine and alpha-thioglycerol (0.4mM). Mesoderm differentiation from the EBs was induced in gelatin-coated 12-wells plates with DMEM low glucose medium supplemented with 15% FBS, 1:100 dilution of penicillin/streptomycin/glutamine and 1:100 dilution of MEM-non-essential amino acids. The formation of ectoderm was induced in matrigel-coated plates with the following medium: neurobasal medium (Gibco) and DMEM/F12 (v/v 50/50) supplemented with 1:100 dilution of penicillin/streptomycin/

glutamine and 1:100 dilution of MEM-non-essential aminoacids, 0.02% BSA (Gibco), 1:200 N2 (Gibco) and 1:100 B27 (Gibco).

### **Neural differentiation**

Briefly, iPS colonies were dissociated from MEFs with collagenase (100 U/ml) and transferred to non-adherent plates in hES cell medium on a shaker in an incubator at 37°C/5% CO<sub>2</sub>. After two days, embryonic bodies (EBs) were placed in neural induction medium (DMEM/F12, 1x N2, 2 µg/ml heparin, penicillin/streptomycin) and cultured for another four days in suspension. EBs were gently dissociated and plated onto laminin-coated dishes in NPC medium (DMEM/F12, 1x N2, 1x B27-RA, 1 µg/ml laminin and 20 ng/ml FGF2, penicillin/streptomycin). All cell culture reagents were obtained from Invitrogen.

### **Karyotype analysis**

For karyotype analysis, cells in a well of a 6-wells plate were treated with colcemid (100 ng/ml) for 1 hour. Then cells were harvested with trypsin, treated with hypotonic solution and fixed. Metaphases were spread onto glass slides and stained with DAPI (Dako). Chromosomes were classified according to the International System for Human Cytogenetic Nomenclature. At least 10 metaphases were analyzed per cell line.

### **Immunocytochemistry and antibodies used in this study**

iPS cells or NPCs were washed with PBS once, fixed with 4% formalin solution for 5 min and washed again with PBS. Cells were then incubated with 50 mM glycine for 5 min, washed with PBS and permeabilized with 0.5% Triton X-100 for 5 min (only for OCT4 and NANOG). After blocking for 45 min at room temperature with 0.1% PBS-Tween containing 2% fetal bovine serum (Invitrogen), primary antibody staining was performed for 1 hour in room temperature with antibodies diluted in blocking solution. Cells were then washed and incubated with the appropriate secondary Cy3 or Alexa Fluor A555 antibody (1:200, Jackson ImmunoResearch Laboratories or Invitrogen) for 45 min. Afterwards, cells were washed with twice 0.1% PBS-Tween, with a nuclear staining step in between (Hoechst or DAPI). Cells were covered with Mowiol and a glass slide. Staining for alkaline phosphatase was carried out using the Alkaline Phosphatase kit (Sigma-Aldrich) according to the manufacturer's instructions. The antibodies used for pluripotency stainings or neural marker stainings were goat anti-human OCT3/4 (1:100, Santa Cruz Biotechnology), goat anti-human NANOG (1:50, R&D Systems), mouse anti-human TRA-1-60, TRA-1-80, and SSEA4 (1:100 Santa Cruz Biotechnology) and rabbit anti-SOX2 (1:1000 Millipore). Antibodies used for *in vitro* differentiation stainings were anti-human smooth muscle actin (SMA, 1:50, DAKO), rabbit anti-human alpha-fetoprotein (AFP, 1:200, Dako), mouse anti-human β-tubulin III (TujI) (1:200, Sigma-Aldrich).

## CGG repeat length, *FMR1* expression and methylation analysis

### CGG length PCR

In order to isolate total genomic DNA, cells were treated with lysis buffer containing 100 mM NaCl, 10 mM Tris, 15 mM EDTA, 0.5% SDS, and 5% Proteinase K. After overnight incubation at 55°C, DNA was extracted and precipitated using a standard protocol containing saturated salt solution and ethanol. PCR was performed with 35 cycles of 35 seconds denaturing at 98°C, 35 seconds of annealing at 55°C, and 5 minutes elongation at 72°C. PCR products were analyzed with standard agarose gel electrophoresis.

### *FMR1* expression

RNA was isolated using the RNeasy kit (Qiagen), and 1 µg of RNA was reverse transcribed using iScript (BioRad). Real-time PCR was carried out in triplicate using Kappa mix and a 7300 Real-time PCR system (Applied Biosystems). A forward primer located in exon 4 was used in combination with a reverse primer located in exon 5 to measure *FMR1* expression: 5'-GGTGGTTAGCTAAAGTGAGGA-3' and 5'-GTGGCAGGTTTGTGTGGGATTA-3'.

*CLK2* was used as reference gene with forward primer 5'-CCTACAACCTAGAGA-AGAAGCGAG-3' and reverse primer 5'-CACTGCCAAAGTCTACCACC-3' (de Brouwer *et al.* 2006). *FMR1* expression was normalized to *CLK2* expression and data was presented as an average value from 2 to 3 independent measurements. The expression values of the male control and the female control cell lines were combined and their average relative fold enrichment was set to 100%.

### *FMR1* methylation analysis

The primers for the methylated sequence are F 5'-GGTCGAAAGATAGACGCGC-3', R 5'-AAACAATGCGACCTATCACCG-3'; and for the unmethylated sequence are F 5'-TGTTGGTTTGTGTGTGTAG-3', R 5'-AACATAATTTCAATATTTACACCC-3' and for the promoter of the unmethylated bisulfite converted reference gene *CLK2*: F 5'-CGGTTGATTTTGGGTGAAGT-3' and R 5'-TCCCGACTAAAATCCACAA-3'. All reactions were carried out in triplicate using SYBR Green ROX mix and a 7300 Real-time PCR system. Experiments were only analyzed when the Ct values of the female control sample were under 30 for both primer sets, as an indication for an efficient bisulfite conversion and DNA recovery. For each sample, the values for the methylated and the unmethylated sequences were normalized to *CLK2* promoter activity first to obtain delta Cts. The normalized exponential values from the measurements of both primers sets were then set to 50% for the female control cell line. These values represent the random X-inactivation in female control cells. The normalized exponential data of the remaining samples was then presented as a percentage relative to the female control data. Average ratios from at least two independent measurements were used for each sample.

### Bisulfite Sanger sequencing

The following primers were used *FMRI* F1 5'-GAGTGTATTTTGTAGAAATGGG-3' and R1 5'-TCTCTCTTCAAATAACCTAAAAAC-3' (see supplemental figure 1 for location of primers), while the *OCT4* promoter containing 10 CpG sites was amplified using the forward primer 5'-GAGGGAGAGAGGGGTTGAGTAG-3' and the reverse primer 5'-CCTC-CAAAAAACCTTAAAACTTAAC-3' (based on Al-khtib *et al.* 2012).

### Chromatin immunoprecipitation assay

In short, approximately 2.5 million cells were crosslinked with 1% formaldehyde for 5 minutes at room temperature. After quenching the reaction with 125 mM glycine, cells were subsequently suspended in lysis buffer (1% SDS, 10 mM EDTA, 50 mM Tris pH 8.1) containing proteinase inhibitor (Roche, Complete). Chromatin was then sonicated using the Bioruptor (Diagonide) to create 200bp-1000bp DNA fragments. All chromatin was pre-cleared by treatment with salmon sperm agarose beads (Millipore) for 0.5 hour at room temperature. Immunoprecipitation was performed overnight using 7.5 µg anti-acetylated histone H3 (Millipore), anti-dimethyl histone H3K4 (Millipore), anti-trimethyl histone H3K9 (Millipore), or anti-IgG antibody (Millipore) in dilution buffer. Next, crosslinking was reversed by incubation with 0.2M NaCl at 65°C and DNA was purified using a PCR clean-up kit (Mobio). Quantitative PCR analysis was carried out using primers for the *FMRI* promoter region F 5'-AACTGGGATAACCGGATGCAT-3' and R 5'-GGCCAGAACGCCATTTTC-3' (see supplemental figure 1 for location) as well as appropriate positive and negative controls namely *APRT* F 5'-GCCTTGACTCGCACTTTT-3', and R 5'-TAGGCGCCATCGATTTTA-3' and *CRYAA* F 5'-CCGTGGTACCAAAGCTGA-3', and R 5'-AGCCGGCTGGGGTAGAA-3'.





# Chapter 6

## A functional variant in the miR-142 promoter modulating its expression and conferring risk of Alzheimer's disease

M. Ghanbari<sup>1,2</sup>, S.T. Munshi<sup>3</sup>, B. Ma<sup>4</sup>, B. Lendemeijer<sup>3</sup>, S. Bansal<sup>3</sup>, H.H. Adams<sup>1</sup>, W. Wang<sup>4</sup>, K.Goth<sup>5</sup>, D.E. Slump<sup>3</sup>, M. C.G.N van den Hout<sup>6</sup>, W.F.J. van IJcken<sup>6</sup>, S.Bellusci<sup>5</sup>, Q.Pan<sup>4</sup>, S.J. Erkeland<sup>7</sup>, F.M.S. de Vrij<sup>3</sup>, S.A. Kushner<sup>3</sup>, M. A.Ikram<sup>1</sup>

1. Department of Epidemiology, Erasmus MC, University Medical Center Rotterdam, 3000 CA Rotterdam, the Netherlands.
2. Department of Genetics, School of Medicine, Mashhad University of Medical Sciences, Mashhad, Iran.
3. Department of Psychiatry, Erasmus MC, University Medical Center Rotterdam, 3000 CA Rotterdam, the Netherlands.
4. Department of Gastroenterology, Erasmus MC, University Medical Center Rotterdam, 3000 CA Rotterdam, the Netherlands.
5. Excellence Cluster Cardio-Pulmonary System (ECCPS), University Justus Liebig Giessen, 35392 Giessen, Germany.
6. Erasmus MC Center for Biomics, Erasmus MC, University Medical Center Rotterdam, 3000 CA Rotterdam, the Netherlands.
7. Department of Immunology, Erasmus MC, University Medical Center Rotterdam, 3000 CA Rotterdam, the Netherlands.

Published in Human Mutation (2019), in press

## ABSTRACT

Non-coding RNAs have been widely recognized as essential mediators of gene regulation. However, in contrast to protein-coding genes, much less is known about the influence of non-coding RNAs on human diseases. Here we examined the association of genetic variants located in primary microRNA sequences and long non-coding RNAs (lncRNAs) with Alzheimer's disease (AD) by leveraging data from the largest genome-wide association meta-analysis of late-onset AD. Variants annotated to five miRNAs and ten lncRNAs (in 7 distinct loci) exceeded the Bonferroni-corrected significance threshold ( $p$ -value  $<1.02 \times 10^{-6}$ ). Among these, a leading variant (rs2526377:A>G) at the 17q22 locus annotated to two non-coding RNAs (*MIR142* and *BZRAP1-AS*) was significantly associated with a reduced risk of AD and fulfilled predefined criteria for being functional. Our functional genomic analyses revealed that rs2526377 affects the promoter activity and decreases the expression of miR-142. Moreover, differential expression analysis by RNA-Seq in human iPSC-derived neural progenitor cells and the hippocampus of miR-142 knockout mice demonstrated multiple target genes of miR-142 in the brain that are likely to be involved in the inflammatory and neurodegenerative manifestations of AD. These include *TGFBR1* and *PICALM*, of which their derepression in the brain due to reduced expression levels of miR-142-3p may reduce risk of AD.

## INTRODUCTION

Alzheimer's disease (AD) is the most common age-related neurodegenerative disease worldwide manifested by the progressive loss of memory and cognitive decline<sup>1</sup>. Enormous efforts have been made over the past decades to discover risk factors for developing AD and to identify biomarkers for early diagnosis of the disease<sup>2-4</sup>. The determinants of early-onset AD have been primarily associated with mutations in one of three genes: *APP*, *PSEN1* and *PSEN2*<sup>5</sup>. In contrast, late-onset AD (after 65 years of age), the most common form of AD with a heritability of 60-80%, is a genetically heterogeneous disease<sup>6</sup>. In addition to apolipoprotein E (*APOE*) polymorphisms that explain ~25% of the heritability, more than 30 genetic loci have so far been established as contributing to late-onset AD risk<sup>7,8</sup>. However, they explain only a fraction of the estimated heritability and the genetics of AD are yet to be fully understood<sup>9</sup>. To fully grasp the contribution of genetic factors to AD, we must go beyond classical genetics, and explore the multiple interacting layers that regulate the genome. This includes the analysis of not only the protein-coding sequences, but the vast non-coding regions as well.

Recent developments in omics technologies have revealed the complexity of the human genome, displaying that protein-coding RNAs constitute only ~2% of the human transcriptome, highlighting the distinct possibility that non-coding RNAs (ncRNAs) might meaningfully contribute to human disease<sup>10,11</sup>. Non-coding RNAs are functional RNA molecules that are transcribed from DNA but not translated into proteins. They are frequently categorized, on the basis of transcript size, as small (less than 200 nucleotides (nt)) or long non-coding RNAs (over 200 nt). Among these, microRNAs (miRNAs), with approximately 21-23 nt in length, are currently the best-characterized ncRNAs. Many studies have shown the crucial role of miRNAs in neurodevelopmental regulation and disease-related neuropathology including AD<sup>12,13</sup>. Long non-coding RNAs (lncRNAs) comprise a large and diverse class of transcribed RNA molecules that are classified into different subtypes (e.g., antisense and intergenic) according to the position and direction of transcription with regard to other genes<sup>14</sup>. It has become increasingly evident that lncRNAs impact disease pathogenesis primarily through post-transcriptional regulation of gene expression<sup>15</sup>. Despite constituting the majority of non-coding transcriptome, few lncRNAs most notably *BACE1-AS* and *BC200* have been so far characterized to play a role in the pathogenesis of AD to date<sup>16,17</sup>.

In the present study, we conducted a genome-wide scan to identify miRNAs and lncRNAs associated with AD by leveraging data from the largest available GWAS of late-onset AD<sup>7</sup>. We found several ncRNA loci significantly associated with AD, including a newly identified susceptibility locus on 17q22. We performed various *in silico* and *in vitro* studies to determine the functionality of ncRNA variant in this locus and to gain insight into the role of associated ncRNA in AD pathogenesis.

## MATERIALS AND METHODS

### Genome-wide association study on AD

Summary statistics data were retrieved from a recent large-scale GWAS meta-analysis of late-onset AD including 455,258 individuals of European ancestry, meta-analyzed in three phases<sup>7</sup>. Phase 1 consisted of 24,087 clinically diagnosed late-onset AD cases and 55,058 controls of European ancestry, which are collected by 3 independent consortia (Alzheimer disease working group of the Psychiatric Genomics Consortium (PGC-ALZ), the International Genomics of Alzheimer Project (IGAP), and the Alzheimer Disease Sequencing Project (ADSP)), and investigating 9,862,738 genetic variants. Phase 2 consisted of 376,113 individuals of European ancestry from the UK Biobank with parental AD status available (N proxy cases = 47,793; N proxy controls = 328,320). Phase 3 was the meta-analysis of phase 1 and 2, including 71,880 (proxy) AD cases and 383,378 (proxy) controls. More details about the consortia and participants are described elsewhere<sup>7</sup>. All participating studies in the AD GWAS had provided informed consent for participation in genetics studies and were approved by their local ethical committees.

### Genetic variants in non-coding RNAs

Genetic variants in human lncRNA transcripts were extracted using lncRNASNP, a comprehensive database including 495,729 SNPs in 32,108 lncRNA transcripts of 17,436 lncRNAs<sup>18</sup>. Moreover, as primary transcript of miRNAs has been suggested to be 3-4kb in length<sup>19</sup>, we used dbSNP database (<https://www.ncbi.nlm.nih.gov/SNP/>) to extract 16,178 SNPs located in +/-2kb of 1,318 mature miRNA sequences reported in miRBase v21 (<http://www.mirbase.org/>). We excluded SNPs with minor allele frequency (MAF) < 0.01. Of the remaining SNPs, we analyzed the association with AD of 96,950 SNPs in 14,790 lncRNA transcripts and 12,404 SNPs in 1,237 primary miRNA transcripts that were present in the GWAS summary statistics data<sup>7</sup>. To obtain the number of independent SNPs, we used the LD based SNP pruning in PLINK (<http://pngu.mgh.harvard.edu/~purcell/plink/>), where we excluded the SNPs with  $R^2 > 0.7$ . The Bonferroni correction was used to adjust  $p$ -value for the number of tests (0.05/49,323 independent SNPs) and the significance threshold was set at  $1.02 \times 10^{-6}$ . Regional plots showing the association of ncRNA SNPs and flanking variants in the corresponding loci with AD were generated by the LocusZoom web tool<sup>20</sup>.

### Assessing biological functionality of non-coding RNA variants

For the ncRNA SNPs associated with AD, the LD region ( $R^2 > 0.7$ ) was determined using the 1000 Genomes Phase 3. We investigated whether known protein-coding variants were in strong LD with the associated ncRNA SNPs. Further, we examined whether the associated SNPs in ncRNAs are annotated to regulatory features, including promoter and enhancer regulatory motifs, DNase footprinting sites and conserved sequences using HaploReg (v4.1)<sup>21</sup>.

For each set of variants in strong LD with a given ncRNA SNP, we also investigated whether the SNP was located in a potential regulatory region using the Roadmap consortium reference epigenomes dataset<sup>22</sup>. To test the association of ncRNA SNPs with gene expression, we used expression quantitative trait loci (eQTL) data provided by GTEx (<https://www.gtexportal.org/home/>) and BBMRI-NL atlas (<http://atlas.bbmrirp3-lumc.surf-hosted.nl/#query>)<sup>23</sup>. The UCSC genome browser was used for visualization of the ncRNA SNP location in the genome. The ncRNA secondary structure and the effect of a SNP on the minimum free energy (MFE) of the predicted ncRNA structure were investigated using the Vienna RNA Package 2.0<sup>24</sup>.

### Plasmids, miRNA promoter constructs and cell culture transfection

To compare the activity of miR-142 promoter containing either rs2526377 alleles, the full-length 589-bp fragment corresponding to the upstream region of the pri-miR-142 transcript was synthesized by Integrated DNA Technologies (IDT) and cloned into pGreenFire-CMV-EF1-puro (System Biosciences) digested with *EcoR I* and *Spe I*. DNA sequencing verified all constructs. HEK293 cells were then used to generate the lentivirus with co-transfection of reporter gene vectors, HIV gag-pol and VSV-G in a ratio of 1:0.8:0.2. For transduction assay, cells were seeded into 24-well plates and transduced with lentiviral particles. With selection by puromycin at a concentration of 2 µg/ml, cells were calculated and seeded into 96-well. After incubation for 24-hours, the cell supernatant was harvested and the luciferase activity was then measured on a luminometer (LB960; Berthold) using the Dual-Luciferase Reporter Assay System (Promega). The ratio of firefly luciferase to Renilla luciferase was calculated for each well. The experiments were performed five times.

### Quantitative RT-PCR

Total RNA from human induced pluripotent stem cell (iPSC)-derived neural progenitor cells (NPCs) and human brain cryopreserved sections was isolated using Trizol LS reagent (Invitrogen, Carlsbad, CA, USA) according to the manufacturer's protocols. The concentration of total RNA was determined using a NanoDrop ND-1000 spectrophotometer (NanoDrop, Wilmington, DE). TaqMan qPCR Assays were performed according to the manufacturer's protocols (Applied Biosystems, Foster City, CA, USA) to determine the expression levels of miR-142-3p, miR-142-5p, and *BZRAP1-AS1*. The assays were run using Applied Biosystems 7900HT Real-Time PCR system. RNU6B was used as an internal control for miRNA expression analysis. All the experiments were performed in triplicates. The human frozen brain tissues (n=3 gray matter and n=3 white matter) were obtained from the Netherlands Brain Bank (Amsterdam, the Netherlands). All samples were free of neurological disease.

### Putative target genes of miR-142

TargetScan V7.1 (<http://www.targetscan.org/>)<sup>25</sup> was used to identify the putative targets of miR-142-3p and -5p in human and mouse. This program predicts biological targets of miR-

NAs by searching for conserved 7/8-mer sites that match the miRNA seed region. The predictions are ranked based on the putative efficacy of targeting as calculated using context scores of the sites, the higher context score, the greater the probability that a miRNA could target a particular gene. For our analysis, we used the predicted targets that had a recommended context score  $< -0.01$ . Further, we retrieved the list of putative target genes of miR-142 (3p and 5p) from two other widely used online miRNA target prediction databases, miRtarget2<sup>26</sup> and DIANA-microT<sup>27</sup>. Then, RNA-Seq data from the Human Body Map 2.0<sup>28</sup> was used to check which of the miR-142 putative target genes are expressed in the human brain (Fragments Per Kilobase Million, FPKM  $\geq 1$ ), target genes not expressed in the brain were excluded.

Pathway analysis was performed using KEGG and IPA databases. KEGG incorporates knowledge of known gene networks and identifies significant enrichment of miRNA putative targets in these networks according to a t-test<sup>29</sup>. IPA is a knowledge database generated from peer-reviewed scientific publications that enables the discovery of highly represented biological mechanisms, pathways or functions most relevant to the genes of interest from large, quantitative datasets. We uploaded the list of the miR-142 target genes and performed a core analysis with the default settings in IPA. We mapped the miRNA target genes to biological functions or canonical pathways to see whether they are enriched in specific networks. The p-values are calculated using the right-tailed Fisher Exact Test and a p-value of less than 0.05 indicates a statistically significant, nonrandom association.

### RNA-Seq analysis in human iPSC-derived neural progenitor cells (NPCs)

NPCs derived from human control iPSCs (Sigma-Aldrich line iPSC0028) were cultured to 70% confluency in 6-well plates (Corning) according to standard protocols<sup>30</sup>. NPCs were transfected with 10 nM miRNA mimics (mirVanaTM Mimics, Thermo Fisher Scientific) including miR-142-3p, miR-142-5p, and the standard negative control #1 (Catalog nr. 4464060), or without any mimic (untreated). Transfections were performed using X-treme GENE<sup>TM</sup> transfection reagent (Merck) according to manufacturer's instructions. The experiment was run in triplicate. Total RNA was isolated 72 hours after transfection from the four groups of NPC samples using the RNeasy mini kit (Qiagen, 74104). The RNA quality was checked by Agilent's 2100 Bioanalyzer (using Eukaryote Total RNA Nano kit). RNA-Seq analysis was performed at Erasmus MC Center for Biomics to test the changes in gene expression pattern in NPCs after overexpression of either miR-142-3p or -5p compared to controls.

### RNA-Seq analysis in the hippocampus of miR-142 KO mice and Wt littermates

MiR-142 in mice is located on chromosome 11 and in the vicinity of the second exon belonging to Mir142hg (ENSMUSG00000084796). The miR-142<sup>-/-</sup> knockout mouse is a model with complete deletion of miR-142, with a significant decrease in the expression levels of both miR-142-3p and -5p isoforms<sup>31</sup>. The expression of *Bzrap1*, a gene immediately flanking miR-142 is not altered in the miR-142-null mice, while the expression of a long non-coding RNA

(Mir142hg) embedded within the miR-142 gene is decreased. We confirmed the homo- and heterozygosity of miR-142 KO mice by qPCR. The hippocampi of miR-142<sup>-/-</sup>, miR-142<sup>+/-</sup> and miR-142<sup>+/+</sup> littermates (n=4 for each group, age 13-14 weeks, gender balanced in all groups) were collected and total RNA was extracted using the RNeasy lipid tissue kit (Qiagen, 74804). RNA quality was checked by Agilent's 2100 Bioanalyzer (using Eukaryote Total RNA Nano kit). RNA-Seq analysis was performed at Erasmus MC Center for Biomix to identify target genes of mmu-miR-142a-3p and mmu-miR-142a-5p that are differentially expressed in the hippocampus samples of mice in the different groups. Animal experiments were approved by the Federal Authorities of Animal Research of the Regierungspräsidium Giessen, Hessen, Germany (Approved Protocol No. 613\_M).

### Data analysis and statistics

The nonparametric Mann-Whitney test was used to compare miR-142 expression between the genotype groups, and an unpaired/independent t-test was used to compare reporter gene activities. *In vitro* experiments were repeated at least three times and histograms represent mean  $\pm$  S.D. Statistical differences were measured using unpaired two-sided Student's *t*-test.  $P < 0.05$  was considered as statistically significant. Data analysis was performed using Excel Software Version 14.4.5.

RNA-Seq was performed with the Illumina TruSeq Stranded mRNA Library prep kit. The resulting DNA libraries were sequenced on the HiSeq2500, for single-end reads of 50bp length. Reads were generated of 50 base-pairs in length. Reads were mapped against the GRCm38 reference genome using HiSat2 (version 2.0.4)<sup>32</sup>. We called gene expression values (reads per gene) using htseq-count (version 0.6.1)<sup>33</sup>. We took only expressed genes into account, genes with at least 5 reads in at least 7 samples (half of the samples plus one). This filtering in iPSC-derived NPCs resulted in 17,181 genes. Differential expression analysis of the RNA-Seq data in human iPSC-derived NPCs was performed using R (version 3.3.2) and DESeq2 (version 1.14.1)<sup>34-36</sup>. Briefly, DESeq2 generated three values for each gene that were used for subsequent analysis: 1. Log2 fold change (Log2FC), 2. *p*-value based on the Wald test, and 3. Corrected *p*-value controlling the false discovery rate to 5%. Genes were considered differentially expressed if the corrected *p*-value was lower than 0.05. For the biological interpretation of the results, we placed an additional cut-off of fold change  $\geq 1.2$ .

## RESULTS

### Non-coding RNAs associated with AD

In total, we examined the associations of 108,862 unique SNPs in primary miRNA sequences and lncRNAs with AD. Of these, SNPs annotated to 5 miRNAs and 10 lncRNAs, located in 7 distinct loci (each locus defined as 1 Mb), exceeded the significance threshold (*p*-value  $< 1.02$

$\times 10^{-6}$ ) (**Table 1**). We assessed whether the associated ncRNA SNPs are likely to be functional in their corresponding loci based on a set of criteria recommended by previous studies to assess the potential functionality of ncRNA SNPs in GWAS results<sup>37,38</sup>. These criteria include an established association between SNP and the trait, the correlation of SNP with expression of the host ncRNA, the localization of SNP in the ncRNA regulatory regions and the potential of SNP for structural perturbations in the host ncRNA.

**Table 1. Top variants in 15 non-coding RNAs significantly associated with Alzheimer's disease**

SNP ID	ncRNA ID	Annotated gene	Chr:position	Locus	A1>A2	MAF	Beta	p-value
rs7384878	miR-6840	<i>PMS2P1</i>	7:100334426	1	C>T	0.32	-0.018	$3.98 \times 10^{-15}$
rs611418	miR-6503	<i>MS4A4E</i>	11:60243540	2	C>T	0.35	-0.016	$2.46 \times 10^{-13}$
rs10792264	lnc-MS4A4A-1	NA	11:60318017	2	A>C	0.36	0.012	$2.29 \times 10^{-8}$
rs636355	lnc-CCDC83-1	<i>PICALM</i>	11:86013618	3	T>A	0.44	-0.019	$1.25 \times 10^{-17}$
rs77162419	lnc-SLTM-2	<i>SLTM</i>	15:58926990	4	C>A	0.07	-0.021	$8.06 \times 10^{-7}$
rs850520	lnc-ABI3-2:5	<i>FLJ40194</i>	17:49255705	5	A>G	0.46	0.010	$9.25 \times 10^{-7}$
rs56229705	lnc-USP6-1	<i>LOC101928000</i>	17:5111494	5	G>A	0.12	0.018	$1.09 \times 10^{-7}$
rs75511804	lnc-USP6-2	<i>LOC100130950</i>	17:5235009	5	C>T	0.12	0.020	$1.68 \times 10^{-9}$
rs2632516	lnc-BZRAP1-1	<i>TSPOAP1-AS1/</i> <i>MIR142</i>	17:58331728	6	G>A	0.47	-0.010	$9.66 \times 10^{-7}$
rs2526377	miR-142	<i>TSPOAP1-AS1/</i> <i>MIR142</i>	17:58332680	6	A>G	0.46	-0.011	$9.13 \times 10^{-7}$
rs203709	miR-4531	<i>LOC107985305</i>	19:44658298	7	T>A	0.49	-0.020	$4.15 \times 10^{-17}$
rs12459810	lnc-ZNF180-2	<i>BCL3</i>	19:44746404	7	C>T	0.27	0.083	$4.08 \times 10^{-44}$
rs2965169	miR-8085	<i>BLC3</i>	19:44747899	7	A>C	0.47	-0.034	$3.13 \times 10^{-57}$
rs3760628	lnc-ZNF296-1	<i>CLPTM1</i>	19:44953968	7	G>A	0.46	0.012	$9.31 \times 10^{-10}$
rs1114831	lnc-NKPD1-1	<i>PPP1R37</i>	19:45133061	7	C>A	0.10	0.044	$9.04 \times 10^{-37}$

Shown are the top variants in 5 miRNAs and 10 lncRNAs (located in 7 distinct loci), exceeding the significance threshold ( $p\text{-value} < 1.02 \times 10^{-6}$ ) to be associated with AD. The associations are based on the data from meta-analysis of phase 1 and 2 of the recent AD GWAS.<sup>7</sup> The table is sorted based on Chr and position (GRCh38.p12). Annotated gene, reported in dbSNP database; Chr, Chromosome; A1, Reference allele; A2, Alternative allele; MAF, Minor allele frequency; Beta, Effect estimate.

As shown in the regional association plots (Supp.**Figure S1**), in 6 of the 7 identified non-coding RNA loci were coding variants in strong LD ( $R^2 > 0.7$ ) with the ncRNA SNPs more significantly associated with AD (Supp.**Table S1**), which complicating interpretations of the coding versus non-coding variants in these loci. In contrast, in the 17q22 locus, the top-associated variant (rs2526377:A>G, chr17:58332680) localized in two ncRNAs, *MIR142* and *BZRAP1-AS1*, and exhibited with no proxy variants in high LD in coding regions. We thus focused our further investigations on the 17q22 locus (**Figure 1**). Evaluation of the LD pattern in 17q22 revealed four SNPs in LD with an  $R^2 > 0.7$ . Of these, rs2632516 and rs2526377, in very high LD ( $R^2 = 1.0$ ), are annotated to *MIR142* and, on the reverse DNA strand, located in



the last intron of *BZRAP1-AS1*. The other two SNPs, rs2526378 and rs2526380, are located in the first and last introns of *BZRAP1*, a coding gene ~3kb away from the top-associated SNP rs2526377 (**Figure 2**). Regulome DB and HaploReg showed that three of the SNPs (rs2526378, rs2526380 and rs2632516) are intronic and without any predicted functions. Conversely, the top SNP rs2526377 is located in a highly conserved promoter region upstream of miR-142, which could control the expression of miR-142<sup>39</sup> (**Figure 2**). Using the UCSC genome browser and ENCODE data, we further found that rs2526377 overlaps with the well-conserved binding sites of multiple transcription factors (Supp. **Table S2** and Supp. **Figure S2**), which their bindings to the miR-142 promoter might be perturbed by the SNP. Moreover, the eQTL data from the BBMRI-NL consortium showed that the rs2632577 minor allele is associated with lower miR-142 expression levels in blood ( $p$ -value =  $4.84 \times 10^{-11}$ , Z-score = -6.58).

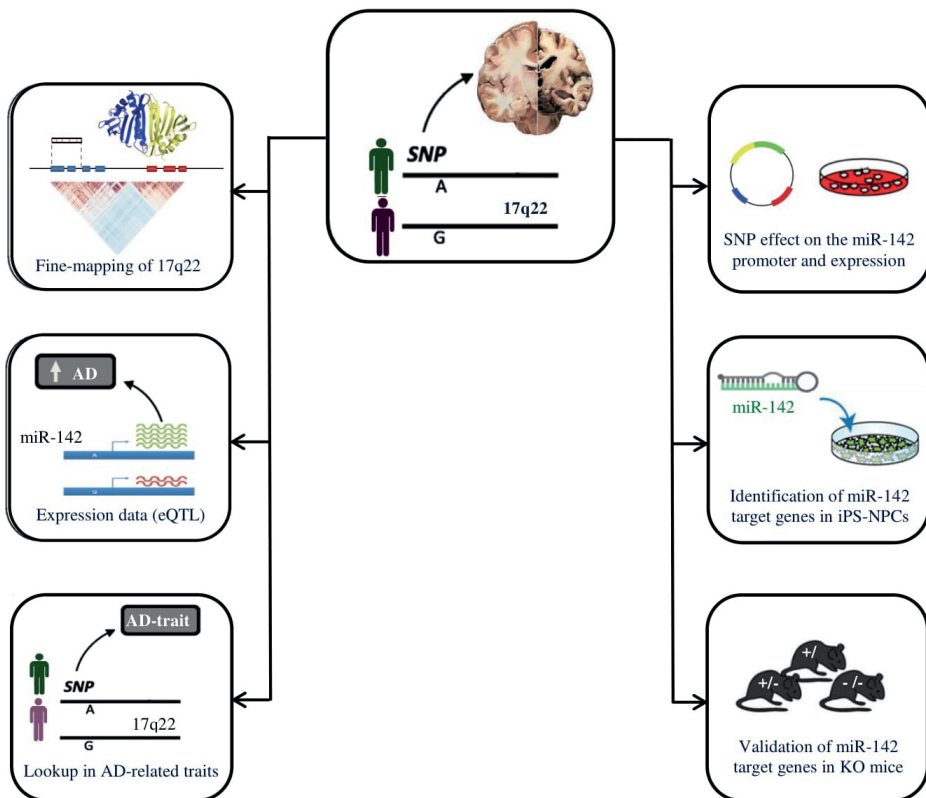


**Figure 1. *In silico* and *in vitro* studies to elucidate the role of SNPs in 17q22 and miR-142 in AD.** The figure summarizes our analyses to test the functionality of non-coding RNA variants at the 17q22 locus associated with AD and the role of miR-142 in AD pathogenesis. GWAS, Genome-wide association study; SNP, Single-nucleotide polymorphism; KO, Knock-out (miR-142<sup>-/-</sup>); NPCs, human iPS-derived neural progenitor cells; eQTL, expression quantitative trait loci; AD-related traits, Look-up in GWAS of cognitive ability and educational attainment.

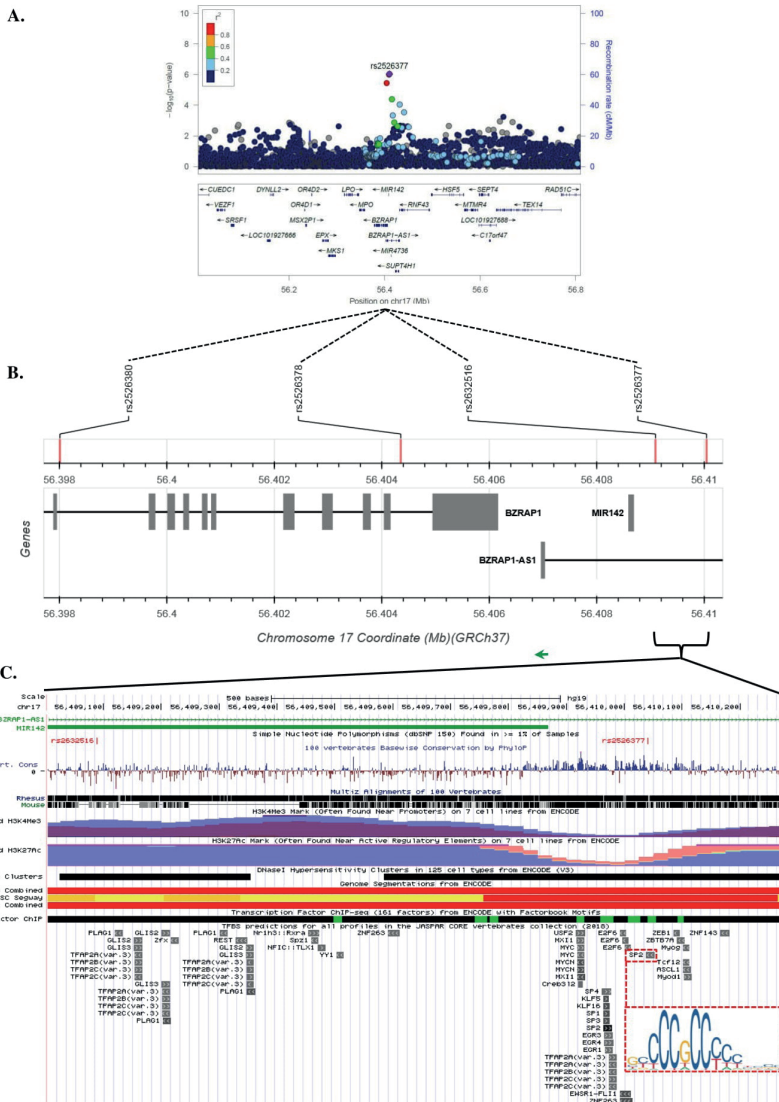


**Figure 2. Fine-mapping of SNPs in the 17q22 locus associated with AD.** **A)** The regional association plot shows the association of rs2526377 and its proxies at the 17q22 locus with AD based on the meta-analysis of phase 1 and 2 of the Jansen et al. paper. The  $p$ -values of variants are plotted (as  $-\log_{10}$  of the  $p$ -value) against their physical position on the locus. A purple diamond represents the  $p$ -value for the top associated SNP rs2526377. Estimated recombination rates from the 1000 Genomes project (European population) show the local LD structure. The variant's colors indicate LD with the top SNP according to a scale from  $r^2 = 0$  to  $r^2 = 1$  based on pairwise  $r^2$  values from the 1000 Genomes project. **B)** The figure displays the localization of the four SNPs in strong LD ( $r^2 > 0.7$ ) at the 17q22 locus. These include two SNPs (rs2632516 and rs2526377) upstream of *MIR142*, and in the last intron of *BZRAP1-AS1*, and two SNPs (rs2526378 and rs2526380) in the first and last introns of *BZRAP1* gene. **C)** The functional mapping of the locus and gene annotations from the UCSC genome browser are also shown below.

As an additional analysis, we tested whether rs2526377 is connected to cognitive functioning prior to the clinical manifestations of AD, so that the variant can be used as early marker of disease. To this end, we examined the association of rs2526377 with cognitive ability and educational attainment using the publicly available GWAS data<sup>40,41</sup>. The SNP minor allele (G) was positively associated with cognitive function ( $P$ -value = 0.046, Beta = 0.011) and educational attainment ( $P$ -value = 0.005, Beta = 0.01), which is consistent with the protective effect of the G allele for AD risk.

Together, these data indicate that rs2526377 fulfilled predefined criteria for being a functional variant in the 17q22 locus, which possibly function by altering the expression of miR-142. We performed various *in vitro* and *in silico* studies to functionally show the impact of rs2526377 on the expression levels of miR-142 and gain insight into the function of miR-142 and its targets in the pathogenesis of AD.

### **The impact of rs2526377 on the promoter activity of miR-142**

The promoter region and transcription start site (TSS) of miR-142 have previously been characterized<sup>39</sup>, indicating that transcription of *MIR142* is initiated 1205bp upstream of the pre-miR-142 sequence and the promoter region is located between 1305 and 1570bp upstream of miR-142 (**Figure 3a**). Rs2526377 resides 1362bp upstream of the pre-miR-142 sequence and therefore within the miRNA promoter. To demonstrate whether rs2526377 alters the promoter activity of miR-142, we performed luciferase reporter assays in HEK293 cells. We generated reporter constructs containing either alleles of the SNP rs2526377 and transfected cells with the reporter plasmids, so that the effect of each allele on the promoter activity was evaluated. The construct carrying the rs2526377 major (A) allele exhibited 20% higher basal activity than the construct carrying minor (G) allele ( $P$ -value = 0.037) (**Figure 3b**). These data are consistent with the eQTL data from the BBMRI-NL consortium that show rs2526377 minor allele carriers have lower miR-142 expression levels in blood.

### **Potential miR-142 target genes implicated in AD**

A miRNA and its target genes should be expressed in the target tissue for any biological function to be exerted. Thus, we first measured the expression of miR-142 in human brain. Both strands of miR-142 were expressed in the brain, miR-142-3p with an average Ct-value of 26 and miR-142-5p with an average Ct-value of 30, relative to the endogenous control RNU6B with an average Ct-value of 21.5 (Supp. **Table S3**). To identify target genes that could mediate the function of miR-142 in the brain, we compiled a list of all putative target genes of miR-142-3p and -5p from three miRNA target prediction databases (TargetsScan, miRDB and DIANA-microT). This resulted in 885 putative target genes for miR-142-3p and 1,541 putative target genes for miR-142-5p (**Figure 4**). We filtered these target genes on the basis of human brain expression, using the Illumina's Human Body Map RNA-Seq dataset. We focused our analysis on the 814 brain-expressed putative target genes of miR-142-3p and 1,393 of miR-142-5p. To

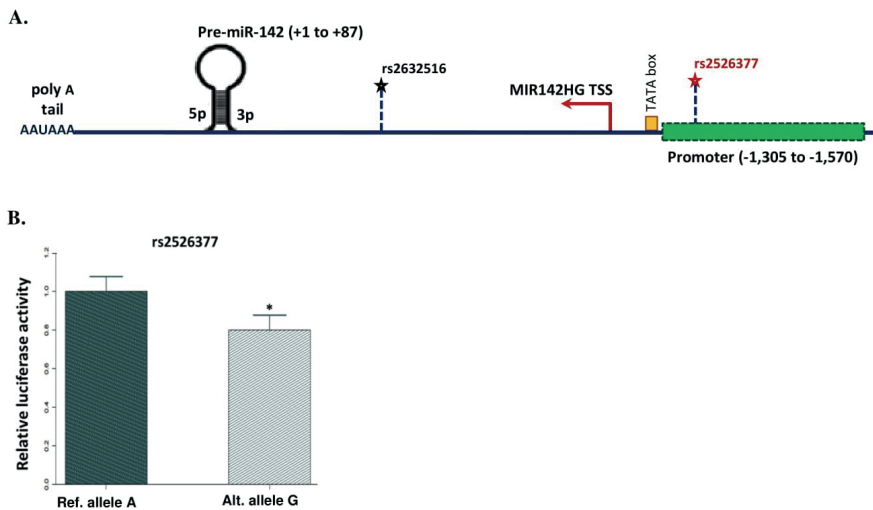


**Figure 3. The genomic location of rs2526377 and its effect on the promoter activity and expression of miR-142.** **A)** A schematic showing the position of rs2526377 upstream of pre-miR-142 sequence. The position of the miR-142 promoter region, transcription start site (TSS) and regulatory elements adapted from *Skarn et al., PLoSOne 2013*.<sup>39</sup> **B)** Luciferase reporter assay was performed to determine the effect of rs2526377 on the miR-142 promoter activity. The reporter gene constructs containing either the SNP alleles were generated and HEK293 cells were transfected with the reporter plasmids. The construct carrying the major allele A of rs2526377 had 20% higher basal activity in HEK293 cells than the construct carrying the minor allele G ( $P$ -value = 0.037). Error bars represent standard deviation (SD). \* $P$  < 0.05 compared with the control group (Student's  $t$ -test). NS, non-significant.

examine the regulatory effect of miR-142-3p and -5p on the expression levels of their putative target genes, we used human iPSC-derived neural progenitor cells (NPCs). We overexpressed either miR-142-3p or -5p in NPCs using mirVana™ miRNA Mimics and performed differential expression analysis by RNA-Seq. To elucidate miR-142 target genes implicated in the AD pathogenesis, we applied the two most commonly used methods for detecting miRNA targets.

First, we conducted a hypothesis-free differential expression analysis considering all brain-expressed target genes of miR-142. We sought to identify target genes that were significantly down-regulated after overexpression of the mature miRNA (3p or 5p) with FDR-adjusted  $P$ -value < 0.05 and fold change  $\geq 1.2$ . Of the 814 brain-expressed putative target genes of miR-142-3p, 280 genes were significantly down-regulated by the miR-142-3p mimic *vs* untreated, and 74 genes were significantly down-regulated in NPCs transfected with miR-142-3p mimic *vs* negative control (Supp. Table S4 and Table 2). We performed KEGG pathway analysis for the 74 identified target genes of miR-142-3p and observed significant enrichment in Regulation of actin cytoskeleton (*WASL*, *ITGB8*, *APC*, *GNG12*, *CFL2*, *GNG12* and *ENAH*), Adherence junction (*TGFBRI*, *WASL*, *RAC1* and *YES1*) and Axon guidance (*CFL2*, *RAC1* and *SEMA3D*) (Supp. Table S5 and Supp. Figure S3). Of the 1,393 brain-expressed putative target

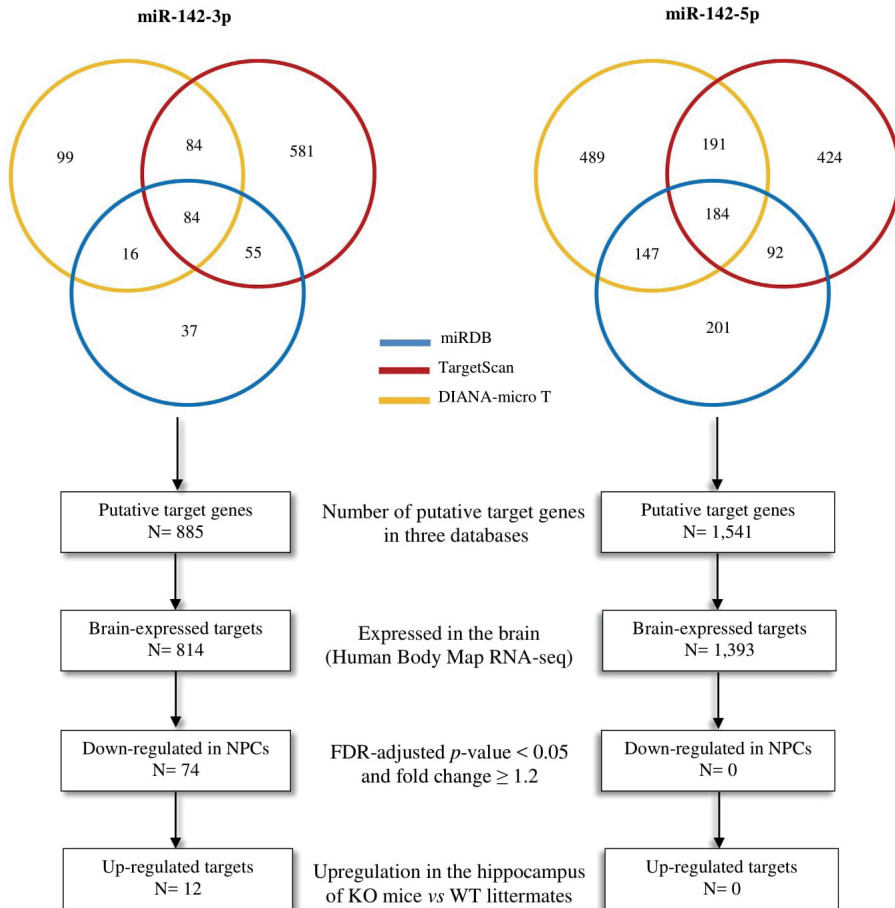


**Figure 4. Identification of potential target genes of miR-142 in the brain implicated in AD.** We compiled a list of all putative targets of miR-142-3p and -5p from three widely used miRNA target prediction databases (miRDB, TargetScan, and DIANA-micro T). The target genes found to be expressed in the human brain were included. We overexpressed miR-142 (3p or 5p) in human iPS-derived NPCs and performed RNA-Seq to examine the changes in gene expression pattern. Target genes significantly down-regulated (FDR-adjusted  $P < 0.05$  and fold change  $\geq 1.2$ ) in NPCs transfected with mature miR-142 mimic (3p or 5p) vs untreated and negative control were retrieved. Subsequently, RNA-Seq was performed on hippocampus of miR-142 KO mice and their wildtype littermates to confirm miR-142-mediated regulation of the identified target genes in human iPS-derived NPCs.

genes of miR-142-5p, none of them were significantly down-regulated (FDR-adjusted  $P$ -value < 0.05 and fold change  $\geq 1.2$ ) in NPCs transfected with miR-142-5p mimic vs negative control.

Second, we examined the association of the 814 putative target genes of miR-142-3p and 1,393 putative target genes of miR-142-5p with AD using a candidate gene approach. To this end, we extracted genetic variants located in these target genes and tested their associations

**Table 2. The top 20 target genes of miR-142-3p significantly down-regulated in human iPSC-derived NPCs**

Gene Name	miR-142-3p mimic vs untreated		miR-142-3p mimic vs negative control	
	Fold change	FDR-adj <i>p</i> -value	Fold change	FDR-adj <i>p</i> -value
<i>WASL</i>	1.7	$7.14 \times 10^{-21}$	1.6	$2.83 \times 10^{-16}$
<i>YES1</i>	1.6	$3.60 \times 10^{-21}$	1.4	$4.64 \times 10^{-11}$
<i>BOD1</i>	1.6	$4.78 \times 10^{-26}$	1.4	$4.64 \times 10^{-11}$
<i>VAMP3</i>	1.6	$2.17 \times 10^{-22}$	1.4	$9.39 \times 10^{-11}$
<i>IL6ST</i>	1.6	$2.33 \times 10^{-22}$	1.4	$1.03 \times 10^{-10}$
<i>CFL2</i>	1.5	$1.69 \times 10^{-11}$	1.5	$1.02 \times 10^{-09}$
<i>SUCO</i>	1.4	$7.46 \times 10^{-15}$	1.4	$4.24 \times 10^{-09}$
<i>CASK</i>	1.2	$3.05 \times 10^{-06}$	1.3	$8.12 \times 10^{-09}$
<i>TWFI</i>	2.0	$5.20 \times 10^{-30}$	1.5	$1.08 \times 10^{-08}$
<i>TNFRSF12A</i>	1.2	$2.58 \times 10^{-01}$	2.0	$1.12 \times 10^{-08}$
<i>CLIC4</i>	1.6	$3.06 \times 10^{-22}$	1.3	$1.13 \times 10^{-08}$
<i>TGFBR1</i>	1.4	$1.43 \times 10^{-11}$	1.3	$1.56 \times 10^{-07}$
<i>ITGB8</i>	1.6	$3.17 \times 10^{-16}$	1.4	$6.53 \times 10^{-07}$
<i>MANBAL</i>	1.3	$3.44 \times 10^{-05}$	1.4	$6.53 \times 10^{-07}$
<i>FAM127B</i>	1.3	$7.88 \times 10^{-05}$	1.4	$1.51 \times 10^{-06}$
<i>RHOBTB3</i>	1.8	$7.20 \times 10^{-33}$	1.3	$1.67 \times 10^{-06}$
<i>HEATR5A</i>	1.2	$16.0 \times 10^{-02}$	1.3	$1.74 \times 10^{-05}$
<i>RAB2A</i>	1.3	$9.41 \times 10^{-09}$	1.3	$2.00 \times 10^{-05}$
<i>HSPA1B</i>	1.8	$2.69 \times 10^{-20}$	1.4	$3.48 \times 10^{-05}$
<i>DIRC2</i>	1.2	$1.01 \times 10^{-02}$	1.4	$3.74 \times 10^{-05}$

The table shows the 20 most significantly down-regulated target genes in miR-142-3p overexpressing iPSC-derived neural progenitor cells (NPCs). Out of 814 predicted target genes of miR-142-3p, 280 were down-regulated in NPCs transfected with miR-142-3p mimic vs untreated and 74 were down-regulated in NPCs transfected with miR-142-3p mimic vs negative control (FDR-adjusted *p*-value < 0.05 and Fold change  $\geq$  1.2).

with AD using the GWAS data<sup>7</sup>. After Bonferroni correction for the number of tested variants in all target genes of miR-142-3p ( $0.05 / 62,515 = 8.0 \times 10^{-7}$ ), four target genes passed the significance threshold (Supp. **Table S6**). Among these, *PICALM* (rs867611, *P*-value =  $2.19 \times 10^{-18}$ ) was the only target gene significantly down-regulated in NPCs transfected with miR-142-3p mimic compared to both untreated (*P*-value =  $1.6 \times 10^{-8}$ , fold change = 1.2) and negative control (*P*-value =  $2.7 \times 10^{-2}$ , fold change = 1.1) conditions. We additionally confirmed the down-regulation of *PICALM* in NPCs transfected with miR-142-3p mimic by qPCR, which demonstrated ~30% reduction of the *PICALM* expression compared to untreated NPCs. A similar analysis was performed for 1,393 target genes of miR-142-5p. One target gene (*FAM63B*) passed the significance threshold ( $0.05/128,444 = 3.9 \times 10^{-7}$ ) (Supp. **Table S6**), however, the gene was not significantly down-regulated in NPCs transfected with miR-142-5p mimic compared to negative controls.

### Validation of the identified miR-142-3p target genes in the hippocampus of miR-142<sup>-/-</sup> mice

To confirm regulation of the 74 identified target genes of miR-142-3p in the brain, we performed RNA-Seq of the hippocampus from miR-142 homozygous KO mice (miR-142<sup>-/-</sup>) and compared it with heterozygous KO (miR-142<sup>+/-</sup>) and wild-type (Wt) littermates (Supp. Table S7). Twelve ( $n=12$ ) of the 74 identified target genes of miR-142-3p were up-regulated in the hippocampus of both homozygous and heterozygous KO mice vs Wt littermates ( $P$ -value  $< 0.05$ ) (Table 3). IPA (Ingenuity Pathway Analysis) revealed that five of the twelve target genes (*TGFBR1*, *CFL2*, *SEMA3D*, *ALCAM* and *RHOQ*) are over-represented in Nervous System Development and Function ( $P$ -value =  $4.98 \times 10^{-2}$ - $5.54 \times 10^{-4}$ ) (Supp. Table S8). Among the twelve target genes, miR-142-3p-mediated regulation of *TGFBR1* and *CFL2* have also been validated experimentally in the previous studies.<sup>42,43</sup>

**Table 3. Twelve target genes of miR-142-3p up-regulated in the hippocampus of miR-142 KO mice**

Gene Name	Homozygous KO vs WT		Heterozygous vs WT	
	Fold change	<i>p</i> -value	Fold change	<i>p</i> -value
<i>Tgfb1</i>	1.22	$2.43 \times 10^{-03}$	1.20	$6.68 \times 10^{-03}$
<i>Rhoq</i>	1.18	$3.46 \times 10^{-03}$	1.15	$1.50 \times 10^{-02}$
<i>Slc39a10</i>	1.15	$5.62 \times 10^{-03}$	1.15	$6.56 \times 10^{-03}$
<i>Ppp1r2</i>	1.67	$5.69 \times 10^{-03}$	1.20	$1.04 \times 10^{-03}$
<i>Cfl2</i>	1.18	$7.43 \times 10^{-03}$	1.15	$2.04 \times 10^{-02}$
<i>Pafah1b2</i>	1.11	$7.51 \times 10^{-03}$	1.12	$4.49 \times 10^{-03}$
<i>Rab1a</i>	1.10	$8.11 \times 10^{-03}$	1.12	$1.30 \times 10^{-03}$
<i>Rab18</i>	1.15	$1.49 \times 10^{-02}$	1.20	$2.25 \times 10^{-03}$
<i>Alcam</i>	1.13	$1.64 \times 10^{-02}$	1.09	$1.64 \times 10^{-02}$
<i>Hspa4l</i>	1.13	$2.33 \times 10^{-02}$	1.14	$1.81 \times 10^{-02}$
<i>Rab2a</i>	1.12	$2.55 \times 10^{-02}$	1.13	$1.70 \times 10^{-02}$
<i>Sema3d</i>	1.17	$2.79 \times 10^{-02}$	1.09	$2.42 \times 10^{-01}$

The table shows 12 target genes of miR-142-3p that are up-regulated in the hippocampus of KO mice (miR142<sup>-/-</sup>). Out of the 74 identified target genes of miR-142-3p, which were significantly down-regulated in iPS-derived NPCs, twelve were confirmed to be up-regulated in the hippocampus of KO mice (miR-142<sup>-/-</sup>) compared to their WT (miR-142<sup>+/-</sup>) littermates ( $P < 0.05$ ).

Moreover, *PICALM*, the target gene found to be significantly associated with AD in the GWAS data, was up-regulated in the hippocampus of miR-142 KO mice vs Wt littermates ( $P$ -value =  $1.5 \times 10^{-2}$ , fold change = 1.13) and heterozygous KO mice vs Wt littermates ( $P$ -value =  $7.2 \times 10^{-4}$ , fold change = 1.2) (Figure 5).



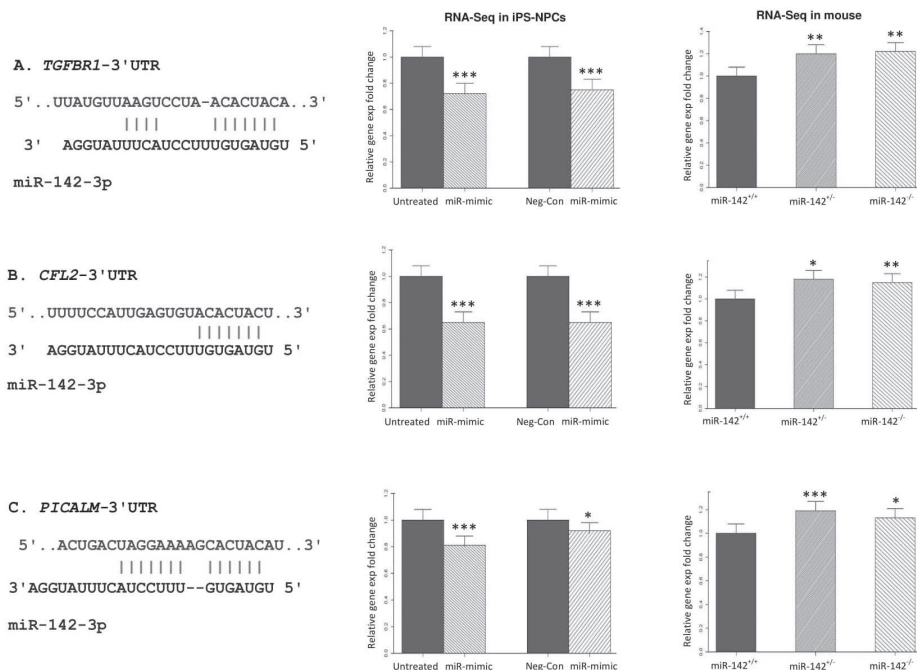


**Figure 5. The interaction and regulatory effect between miR-142-3p and its three target genes.** The figure illustrates the binding of miR-142-3p to its three highlighted target genes (*TGFB1*, *CLF2*, and *PICALM*). The expression of these target genes were significantly down-regulated in human iPS-NPCs transfected with miR-142-3p mimic vs untreated, and in iPS-NPCs transfected with miR-142-3p mimic vs negative control. In contrast, the expression of these target genes were up-regulated in the hippocampus of miR-142 KO mice vs Wt littermates. Error bars represent standard deviation (SD). \* $P < 0.05$ , \*\* $P < 0.01$  and \*\*\* $P < 0.001$  compared with the control group (Wald-test).

## DISCUSSION

Despite increasing interest in the biology of non-coding RNAs, relatively few genome-wide studies have thus far demonstrated associations with human disease. In this study, we performed a genome-wide scan to systematically investigate the association of miRNAs and lncRNAs with AD by leveraging publicly available GWAS summary statistics<sup>7</sup>. We found seven distinct ncRNA loci significantly associated with AD including a newly identified susceptibility locus on 17q22, in which the ncRNA variant leads the signal and fulfills predefined criteria for being functional. The locus has not been reported as significant in the original GWAS, because the p-value of the top SNP in the meta-analysis of phase 1 (AD case/control) and phase 2 (AD-by-proxy) was above the GWAS threshold<sup>7</sup>. However, the SNP exceeds the GWAS threshold in the phase 1 of this GWAS meta-analysis ( $P$ -value =  $1.42 \times 10^{-9}$ ), combining data from the two large-scale AD case/control consortia, IGAP and PGC-ALZ. In the phase 2, using the AD-by-proxy phenotype from the UK biobank cohort, the association between



rs2632516 and AD is less significant ( $P$ -value =  $5.0 \times 10^{-3}$ ), but still in the same direction. The lower association signal for the 17q22 locus in the UK biobank cohort could be explained by differences in case ascertainment of AD. In the UK biobank, Alzheimer dementia is ascertained via self-report information from family history (parent or first-degree relative with AD or dementia) as a proxy-phenotype for the participants<sup>44</sup>. This method relies on people to provide accurate information about whether their parents developed AD, for which misclassification of case status is of greater concern than consortia relying upon clinician reported diagnoses. In addition, a trans-ethnic GWAS, by adding more samples to the IGAP GWAS data, recently reported the significant association of 17q22 with AD<sup>45</sup>. In this trans-ethnic GWAS, however, the leading ncRNA variant in the 17q22 locus was annotated to the closest protein-coding gene (*BZRAP1*), and the potential impact of miR-142 has been overlooked. In contrast a more recent GWAS, investigating the association of rare coding variants with AD, with an even larger sample size did not find any significant association between rare variants in *BZRAP1* gene and AD<sup>46</sup>. In this line, our results demonstrated that miR-142 is the most likely functional target in the 17q22 locus implicated in AD pathogenesis.

Genetic variants in miRNA-encoding sequences have been shown previously to affect miRNAs expression and subsequently influence gene regulation in complex diseases<sup>47-49</sup>. Moreover, the functional impact of variants on the promoter activity of miRNAs has been revealed, most notably for rs57095329 located in miR-146a, by altering the miRNA processing and expression level<sup>50</sup>. Here, we demonstrated that rs2526377 affects the promoter activity and reduces the expression levels of miR-142. Previously, Skarn et al. characterized the miR-142 promoter region and demonstrated that DNA methylation of specific CpG sites in the region represses the promoter activity and reduces the expression level of miR-142 in mesenchymal stem cells<sup>39</sup>. Moreover, an independent study by Mor et al. revealed that hypomethylation of the CpGs in the miR-142 promoter region increases the miRNA expression level in the prefrontal cortex of autism patients<sup>51</sup>. These data may indicate that rs2526377 attenuates the risk of AD via reducing the miR-142 expression levels in the brain.

MiR-142 is a highly conserved miRNA amongst multiple invertebrate and vertebrate species. The role of miR-142 has extensively been studied in the hematopoietic system, lung development and cardiac hypertrophy<sup>52</sup>. Convergent evidence from multiple investigations also indicates the expression of miR-142 in the brain, suggesting that dysregulation or malfunction of miR-142 contribute to the pathogenesis of brain disorders. For instance, Junker et al. reported miR-142 among the 10 miRNAs that are more abundant in active multiple sclerosis (MS) brain lesions than normal white matter, and suggested miR-142 to be involved in the brain inflammatory and degenerative diseases<sup>53</sup>. Similarly, Mandolesi et al. observed that miR-142 is increased in the CSF of patients with active MS<sup>54</sup>. Moreover, Sorensen et al. performed miRNA expression profiles in CSF and blood of patients with AD and found a number of differentially expressed miRNAs, in which miR-142 is one of the significantly up-regulated miRNAs in AD patients compared to controls<sup>55</sup>. Two independent studies also revealed that

the expression of miR-142 is increased by age<sup>56,57</sup>. Here, our expression data confirmed that both mature miR-142-3p and -5p are expressed at relatively high levels in the brain; though, our RNA-Seq analysis proposed miR-142-3p, which is the guide strand of miR-142, to be more active on the regulation of its target genes in the brain. Consistent with this notion, Lau et al. have performed miRNA expression profiling of the hippocampus of a cohort of 41 AD patients and 23 age-matched controls and found miR-142-3p among the 15 significantly up-regulated miRNAs in the AD group<sup>58</sup>. Moreover, miR-142-3p has been reported as one of the eight miRNAs up-regulated in synaptoneurosomes from forebrains and hippocampus of mice during prion disease<sup>59</sup>. Together, these data endorse that alterations in the expression of miR-142 in the brain could confer AD risk, where higher levels of miR-142-3p increase a person's risk of developing Alzheimer's.

Up-regulation of miR-142 in the brain may influence AD risk through different mechanisms. Gene ontology analysis on the putative target genes of miR-142-3p and -5p has shown enrichment in categories related to synaptic transmission (dopaminergic synapse, neurotrophin signaling, axon guidance) and signal transduction (TGF- $\beta$  signaling, MAPK signaling, ErbB signaling)<sup>51,60</sup>. Mandolesi et al. proposed miR-142 to be related to neuro-inflammatory changes in the brain occurring during MS by regulating the expression of *IL-1 $\beta$* <sup>54</sup>. Further, Chaudhuri et al. suggested the involvement of miR-142 in autoimmune and neuro-inflammation in the brain, via miR-142-mediated repression of *SIRT1* in primary human neurons<sup>61</sup>. In an independent study, Chaudhuri et al. verified that miR-142 indirectly reduces MAOA protein level via regulating *SIRT1* expression<sup>62</sup>. Since MAOA is a neurotransmitter-metabolizing enzyme and delaminates serotonin, melanin, epinephrine and norepinephrine, they postulated that miR-142 up-regulation might contribute to change the dopaminergic neurotransmission by lowering MAOA expression and activity. In this study, we further demonstrated miR-142-3p-mediated regulation of multiple target genes in the brain that are involved in the pathways underlying AD. *TGFBRI* and *PICALM*, among others, are of particular interest (**Figure 6**). *TGFBRI* has been shown in several studies to be implicated in AD pathogenesis<sup>63-68</sup>. The regulation of *TGFBRI* expression by miR-142-3p has been experimentally confirmed at mRNA and protein levels in previous studies<sup>43,69</sup>. Our differential expression analysis for all miR-142-3p target genes demonstrated that *TGFBRI* was significantly down-regulated in miR-142-3p overexpressing human iPS-derived NPCs and the top target gene up-regulated in the hippocampus of miR-142 KO mice. Locating at the intersection of anti-inflammatory, anti-aging and neuroprotective pathways, *TGFBRI* makes a promising molecule for mediating the function of miR-142-3p in AD.

*PICALM* is ubiquitously expressed in all tissue types with prominent expression in neurons and is non-selectively distributed in pre- and postsynaptic terminals, where it plays an essential role in the fusion of synaptic vesicles to the presynaptic membrane in neurotransmitter release<sup>70</sup>. Several GWA studies have independently confirmed the association of *PICALM* with AD<sup>8,46,71</sup>. Recent studies have also shown that *PICALM* level is reduced in the AD brain

endothelium and postulated that it can potentially lead to A $\beta$  accumulation in the brain by hindering LRP1-mediated A $\beta$  transport<sup>72,73</sup>. These data strongly suggest that derepression of *PICALM* in response to the reduced miR-142 expression may decrease AD risk that deserve further and more deep investigation in future experimental work.

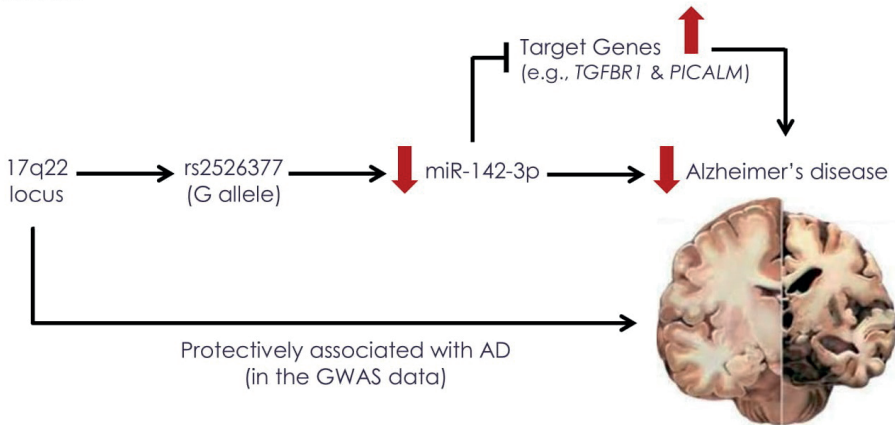


**Figure 6. Rs2526377 in the promoter of miR-142 modulating its expression and conferring risk of AD.** The SNP rs2526377 occurring within the promoter region of miR-142 alters the promoter activity and reduces the expression level of miR-142. Downregulation of miR-142-3p in the brain results in derepression of multiple target genes (e.g., *TGFBR1* and *PICALM*) that contribute to the pathogenesis of AD.

## Conclusions

In this study, we endorse 17q22 as a susceptibility locus for AD and provide evidence demonstrating that miR-142 is the most likely functional target in the locus involved in AD pathogenesis. Furthermore, we revealed miR-142-3p-mediated regulation of multiple target genes in the brain that are implicated in the inflammatory and neurodegenerative manifestations of AD. These include two well-validated AD-associated genes, *TGFBR1* and *PICALM*, of which their derepression in the brain due to reduced expression levels of miR-142-3p may decrease risk of AD. Our findings may also suggest the therapeutic potential of miR-142 inhibition for AD, which warrants further investigations in future.

## ABBREVIATIONS

AD, Alzheimer's disease; GWAS, Genome-wide association studies; SNP, Single-nucleotide polymorphism; lncRNA, long non-coding RNA; miRNA, microRNA; eQTL, expression quantitative trait loci; mRNA, messenger RNA; MFE, Minimum free energy; MAF, Minor allele frequency; LD, Linkage disequilibrium; GFP, green fluorescent protein; MSCV-BC,

Murine Stem Cell Virus-Bar Coded; TSS, Transcription start site; PCR, Polymerase chain reaction; iPSC, induced pluripotent stem cell; FPKM, Fragments Per Kilobase Million; FDR, False discovery rate; Wt, wild-type; KO, Knock-out.

## REFERENCES

1. Brookmeyer R, Johnson E, Ziegler-Graham K, Arrighi HM. 2007. Forecasting the global burden of Alzheimer's disease. *Alzheimers Dement* 3(3):186-91.
2. Crews L, Masliah E. 2010. Molecular mechanisms of neurodegeneration in Alzheimer's disease. *Hum Mol Genet* 19(R1):R12-20.
3. Hampel H, Frank R, Broich K, Teipel SJ, Katz RG, Hardy J, Herholz K, Bokde AL, Jessen F, Hoessler YC and others. 2010. Biomarkers for Alzheimer's disease: academic, industry and regulatory perspectives. *Nat Rev Drug Discov* 9(7):560-74.
4. Schmechel DE, Saunders AM, Strittmatter WJ, Crain BJ, Hulette CM, Joo SH, Pericak-Vance MA, Goldgaber D, Roses AD. 1993. Increased amyloid beta-peptide deposition in cerebral cortex as a consequence of apolipoprotein E genotype in late-onset Alzheimer disease. *Proc Natl Acad Sci U S A* 90(20):9649-53.
5. Ertekin-Taner N. 2007. Genetics of Alzheimer's disease: a centennial review. *Neurol Clin* 25(3):611-67, v.
6. Gatz M, Reynolds CA, Fratiglioni L, Johansson B, Mortimer JA, Berg S, Fiske A, Pedersen NL. 2006. Role of genes and environments for explaining Alzheimer disease. *Arch Gen Psychiatry* 63(2):168-74.
7. Jansen IE, Savage JE, Watanabe K, Bryois J, Williams DM, Steinberg S, Sealock J, Karlsson IK, Hagg S, Athanasiu L and others. 2019. Genome-wide meta-analysis identifies new loci and functional pathways influencing Alzheimer's disease risk. *Nat Genet* 51(3):404-413.
8. Lambert JC, Ibrahim-Verbaas CA, Harold D, Naj AC, Sims R, Bellenguez C, DeStafano AL, Bis JC, Beecham GW, Grenier-Boley B and others. 2013. Meta-analysis of 74,046 individuals identifies 11 new susceptibility loci for Alzheimer's disease. *Nat Genet* 45(12):1452-8.
9. Zhou X, Chen Y, Mok KY, Zhao Q, Chen K, Chen Y, Hardy J, Li Y, Fu AKY, Guo Q and others. 2018. Identification of genetic risk factors in the Chinese population implicates a role of immune system in Alzheimer's disease pathogenesis. *Proc Natl Acad Sci U S A* 115(8):1697-1706.
10. Carninci P, Kasukawa T, Katayama S, Gough J, Frith MC, Maeda N, Oyama R, Ravasi T, Lenhard B, Wells C and others. 2005. The transcriptional landscape of the mammalian genome. *Science* 309(5740):1559-63.
11. Consortium EP. 2012. An integrated encyclopedia of DNA elements in the human genome. *Nature* 489(7414):57-74.
12. Meza-Sosa KE, Valle-Garcia D, Pedraza-Alva G, Perez-Martinez L. 2012. Role of microRNAs in central nervous system development and pathology. *J Neurosci Res* 90(1):1-12.
13. O'Carroll D, Schaefer A. 2013. General principals of miRNA biogenesis and regulation in the brain. *Neuropsychopharmacology* 38(1):39-54.
14. Ma L, Bajic VB, Zhang Z. 2013. On the classification of long non-coding RNAs. *RNA Biol* 10(6):925-33.
15. Rinn JL, Chang HY. 2012. Genome regulation by long noncoding RNAs. *Annu Rev Biochem* 81:145-66.
16. Modarresi F, Faghihi MA, Patel NS, Sahagan BG, Wahlestedt C, Lopez-Toledano MA. 2011. Knock-down of BACE1-AS Nonprotein-Coding Transcript Modulates Beta-Amyloid-Related Hippocampal Neurogenesis. *Int J Alzheimers Dis* 2011:929042.
17. Mus E, Hof PR, Tiedge H. 2007. Dendritic BC200 RNA in aging and in Alzheimer's disease. *Proc Natl Acad Sci U S A* 104(25):10679-84.
18. Gong J, Wu Y, Zhang X, Liao Y, Sibanda VL, Liu W, Guo AY. 2014. Comprehensive analysis of human small RNA sequencing data provides insights into expression profiles and miRNA editing. *RNA Biol* 11(11):1375-85.

19. Saini HK, Griffiths-Jones S, Enright AJ. 2007. Genomic analysis of human microRNA transcripts. *Proc Natl Acad Sci U S A* 104(45):17719-24.
20. Pruim RJ, Welch RP, Sanna S, Teslovich TM, Chines PS, Gliedt TP, Boehnke M, Abecasis GR, Willer CJ. 2010. LocusZoom: regional visualization of genome-wide association scan results. *Bioinformatics* 26(18):2336-7.
21. Ward LD, Kellis M. 2016. HaploReg v4: systematic mining of putative causal variants, cell types, regulators and target genes for human complex traits and disease. *Nucleic Acids Res* 44(D1):D877-81.
22. Romanoski CE, Glass CK, Stunnenberg HG, Wilson L, Almouzni G. 2015. Epigenomics: Roadmap for regulation. *Nature* 518(7539):314-6.
23. Bonder MJ, Luijk R, Zhernakova DV, Moed M, Deelen P, Vermaat M, van Iterson M, van Dijk F, van Galen M, Bot J and others. 2017. Disease variants alter transcription factor levels and methylation of their binding sites. *Nat Genet* 49(1):131-138.
24. Lorenz R, Bernhart SH, Honer Zu Siederdisen C, Tafer H, Flamm C, Stadler PF, Hofacker IL. 2011. ViennaRNA Package 2.0. *Algorithms Mol Biol* 6:26.
25. Agarwal V, Bell GW, Nam JW, Bartel DP. 2015. Predicting effective microRNA target sites in mammalian mRNAs. *Elife* 4.
26. Wang X, El Naqa IM. 2008. Prediction of both conserved and nonconserved microRNA targets in animals. *Bioinformatics* 24(3):325-32.
27. Paraskevopoulou MD, Georgakilas G, Kostoulas N, Vlachos IS, Vergoulis T, Reczko M, Filippidis C, Dalamagas T, Hatzigeorgiou AG. 2013. DIANA-microT web server v5.0: service integration into miRNA functional analysis workflows. *Nucleic Acids Res* 41(Web Server issue):W169-73.
28. Kawamoto S, Yoshii J, Mizuno K, Ito K, Miyamoto Y, Ohnishi T, Matoba R, Hori N, Matsumoto Y, Okumura T and others. 2000. BodyMap: a collection of 3' ESTs for analysis of human gene expression information. *Genome Res* 10(11):1817-27.
29. Subramanian A, Tamayo P, Mootha VK, Mukherjee S, Ebert BL, Gillette MA, Paulovich A, Pomeroy SL, Golub TR, Lander ES and others. 2005. Gene set enrichment analysis: a knowledge-based approach for interpreting genome-wide expression profiles. *Proc Natl Acad Sci U S A* 102(43):15545-50.
30. Shi Y, Kirwan P, Livesey FJ. 2012. Directed differentiation of human pluripotent stem cells to cerebral cortex neurons and neural networks. *Nat Protoc* 7(10):1836-46.
31. Shrestha A, Carraro G, El Agha E, Mukhametshina R, Chao CM, Rizvanov A, Barreto G, Bellusci S. 2015. Generation and Validation of miR-142 Knock Out Mice. *PLoS One* 10(9):e0136913.
32. Kim D, Langmead B, Salzberg SL. 2015. HISAT: a fast spliced aligner with low memory requirements. *Nat Methods* 12(4):357-60.
33. Anders S, Pyl PT, Huber W. 2015. HTSeq--a Python framework to work with high-throughput sequencing data. *Bioinformatics* 31(2):166-9.
34. Cuypers B, Domagalska MA, Meysman P, Muylder G, Vanaerschot M, Imamura H, Dumetz F, Verdonck TW, Myler PJ, Ramasamy G and others. 2017. Multiplexed Spliced-Leader Sequencing: A high-throughput, selective method for RNA-seq in Trypanosomatids. *Sci Rep* 7(1):3725.
35. Love MI, Huber W, Anders S. 2014. Moderated estimation of fold change and dispersion for RNA-seq data with DESeq2. *Genome Biol* 15(12):550.
36. Tian Y, Liao IH, Zhan X, Gunther JR, Ander BP, Liu D, Lit L, Jickling GC, Corbett BA, Bos-Veneman NG and others. 2011. Exon expression and alternatively spliced genes in Tourette Syndrome. *Am J Med Genet B Neuropsychiatr Genet* 156B(1):72-8.
37. Ghanbari M, Peters MJ, de Vries PS, Boer CG, van Rooij JGJ, Lee YC, Kumar V, Uitterlinden AG, Ikram MA, Wijmenga C and others. 2018. A systematic analysis highlights multiple long non-coding RNAs associated with cardiometabolic disorders. *J Hum Genet* 63(4):431-446.

38. Ryan BM, Robles AI, Harris CC. 2010. Genetic variation in microRNA networks: the implications for cancer research. *Nat Rev Cancer* 10(6):389-402.
39. Skarn M, Baroy T, Stratford EW, Myklebost O. 2013. Epigenetic regulation and functional characterization of microRNA-142 in mesenchymal cells. *PLoS One* 8(11):e79231.
40. Davies G, Lam M, Harris SE, Trampush JW, Luciano M, Hill WD, Hagenaars SP, Ritchie SJ, Marioni RE, Fawns-Ritchie C and others. 2018. Study of 300,486 individuals identifies 148 independent genetic loci influencing general cognitive function. *Nat Commun* 9(1):2098.
41. Okbay A, Beauchamp JP, Fontana MA, Lee JJ, Pers TH, Rietveld CA, Turley P, Chen GB, Emilsson V, Meddens SF and others. 2016. Genome-wide association study identifies 74 loci associated with educational attainment. *Nature* 533(7604):539-42.
42. Schwickert A, Weghake E, Bruggemann K, Engbers A, Brinkmann BF, Kemper B, Seggewiss J, Stock C, Ebnet K, Kiesel L and others. 2015. microRNA miR-142-3p Inhibits Breast Cancer Cell Invasiveness by Synchronous Targeting of WASL, Integrin Alpha V, and Additional Cytoskeletal Elements. *PLoS One* 10(12):e0143993.
43. Yang X, Dan X, Men R, Ma L, Wen M, Peng Y, Yang L. 2017. MiR-142-3p blocks TGF-beta-induced activation of hepatic stellate cells through targeting TGFbetaRI. *Life Sci* 187:22-30.
44. Marioni RE, Harris SE, Zhang Q, McRae AF, Hagenaars SP, Hill WD, Davies G, Ritchie CW, Gale CR, Starr JM and others. 2018. GWAS on family history of Alzheimer's disease. *Transl Psychiatry* 8(1):99.
45. Jun GR, Chung J, Mez J, Barber R, Beecham GW, Bennett DA, Buxbaum JD, Byrd GS, Carrasquillo MM, Crane PK and others. 2017. Transethnic genome-wide scan identifies novel Alzheimer's disease loci. *Alzheimers Dement* 13(7):727-738.
46. Sims R, van der Lee SJ, Naj AC, Bellenguez C, Badarinarayan N, Jakobsdottir J, Kunkle BW, Bolland A, Raybould R, Bis JC and others. 2017. Rare coding variants in PLCG2, ABI3, and TREM2 implicate microglial-mediated innate immunity in Alzheimer's disease. *Nat Genet* 49(9):1373-1384.
47. Dorn GW, 2nd, Matkovich SJ, Eschenbacher WH, Zhang Y. 2012. A human 3' miR-499 mutation alters cardiac mRNA targeting and function. *Circ Res* 110(7):958-67.
48. Ghanbari M, Darweesh SK, de Looper HW, van Luijn MM, Hofman A, Ikram MA, Franco OH, Erkeland SJ, Dehghan A. 2015. Genetic Variants in MicroRNAs and their Binding Sites are Associated with the Risk of Parkinson Disease. *Hum Mutat* 37(3):292-300.
49. Ghanbari M, de Vries PS, de Looper H, Peters MJ, Schurmann C, Yaghootkar H, Dorr M, Frayling TM, Uitterlinden AG, Hofman A and others. 2014. A genetic variant in the seed region of miR-4513 shows pleiotropic effects on lipid and glucose homeostasis, blood pressure, and coronary artery disease. *Hum Mutat* 35(12):1524-31.
50. Luo X, Yang W, Ye DQ, Cui H, Zhang Y, Hirankarn N, Qian X, Tang Y, Lau YL, de Vries N and others. 2011. A functional variant in microRNA-146a promoter modulates its expression and confers disease risk for systemic lupus erythematosus. *PLoS Genet* 7(6):e1002128.
51. Mor M, Nardone S, Sams DS, Elliott E. 2015. Hypomethylation of miR-142 promoter and upregulation of microRNAs that target the oxytocin receptor gene in the autism prefrontal cortex. *Mol Autism* 6:46.
52. Shrestha A, Mukhametshina RT, Taghizadeh S, Vasquez-Pacheco E, Cabrera-Fuentes H, Rizvanov A, Mari B, Carraro G, Bellusci S. 2016. MicroRNA-142 is a multifaceted regulator in organogenesis, homeostasis, and disease. *Dev Dyn* 246(4):285-290.
53. Junker A, Krumbholz M, Eisele S, Mohan H, Augstein F, Bittner R, Lassmann H, Wekerle H, Hohlfield R, Meinel E. 2009. MicroRNA profiling of multiple sclerosis lesions identifies modulators of the regulatory protein CD47. *Brain* 132(Pt 12):3342-52.

54. Mandolesi G, De Vito F, Musella A, Gentile A, Bullitta S, Fresegna D, Sepman H, Di Sanza C, Haji N, Mori F and others. 2017. miR-142-3p Is a Key Regulator of IL-1 $\beta$ -Dependent Synaptopathy in Neuroinflammation. *J Neurosci* 37(3):546-561.
55. Sorensen SS, Nygaard AB, Christensen T. 2016. miRNA expression profiles in cerebrospinal fluid and blood of patients with Alzheimer's disease and other types of dementia - an exploratory study. *Transl Neurodegener* 5:6.
56. Huan T, Chen G, Liu C, Bhattacharya A, Rong J, Chen BH, Seshadri S, Tanriverdi K, Freedman JE, Larson MG and others. 2018. Age-associated microRNA expression in human peripheral blood is associated with all-cause mortality and age-related traits. *Aging Cell* 17(1).
57. Zhang X, Azhar G, Wei JY. 2012. The expression of microRNA and microRNA clusters in the aging heart. *PLoS One* 7(4):e34688.
58. Lau P, Bossers K, Janky R, Salta E, Frigerio CS, Barbash S, Rothman R, Sierksma AS, Thathiah A, Greenberg D and others. 2013. Alteration of the microRNA network during the progression of Alzheimer's disease. *EMBO Mol Med* 5(10):1613-34.
59. Boese AS, Saba R, Campbell K, Majer A, Medina S, Burton L, Booth TF, Chong P, Westmacott G, Dutta SM and others. 2016. MicroRNA abundance is altered in synaptoneurosomes during prion disease. *Mol Cell Neurosci* 71:13-24.
60. Shrestha A, Mukhametshina RT, Taghizadeh S, Vasquez-Pacheco E, Cabrera-Fuentes H, Rizvanov A, Mari B, Carraro G, Bellusci S. 2017. MicroRNA-142 is a multifaceted regulator in organogenesis, homeostasis, and disease. *Dev Dyn* 246(4):285-290.
61. Chaudhuri AD, Yelamanchili SV, Marcondes MC, Fox HS. 2013b. Up-regulation of microRNA-142 in simian immunodeficiency virus encephalitis leads to repression of sirtuin1. *FASEB J* 27(9):3720-9.
62. Chaudhuri AD, Yelamanchili SV, Fox HS. 2013a. MicroRNA-142 reduces monoamine oxidase A expression and activity in neuronal cells by downregulating SIRT1. *PLoS One* 8(11):e79579.
63. Caraci F, Spampinato S, Sortino MA, Bosco P, Battaglia G, Bruno V, Drago F, Nicoletti F, Copani A. 2012. Dysfunction of TGF- $\beta$ 1 signaling in Alzheimer's disease: perspectives for neuroprotection. *Cell Tissue Res* 347(1):291-301.
64. Chen JH, Ke KF, Lu JH, Qiu YH, Peng YP. 2015. Protection of TGF- $\beta$ 1 against neuroinflammation and neurodegeneration in Abeta1-42-induced Alzheimer's disease model rats. *PLoS One* 10(2):e0116549.
65. Flanders KC, Lippa CF, Smith TW, Pollen DA, Sporn MB. 1995. Altered expression of transforming growth factor- $\beta$  in Alzheimer's disease. *Neurology* 45(8):1561-9.
66. Lippa CF, Flanders KC, Kim ES, Croul S. 1998. TGF- $\beta$  receptors-I and -II immunoexpression in Alzheimer's disease: a comparison with aging and progressive supranuclear palsy. *Neurobiol Aging* 19(6):527-33.
67. Tesseur I, Zou K, Esposito L, Bard F, Berber E, Can JV, Lin AH, Crews L, Tremblay P, Mathews P and others. 2006. Deficiency in neuronal TGF- $\beta$  signaling promotes neurodegeneration and Alzheimer's pathology. *J Clin Invest* 116(11):3060-9.
68. Wyss-Coray T, Yan F, Lin AH, Lambris JD, Alexander JJ, Quigg RJ, Masliah E. 2002. Prominent neurodegeneration and increased plaque formation in complement-inhibited Alzheimer's mice. *Proc Natl Acad Sci U S A* 99(16):10837-42.
69. Talebi F, Ghorbani S, Chan WF, Boghazian R, Masoumi F, Ghasemi S, Voigani M, Power C, Noorbakhsh F. 2017. MicroRNA-142 regulates inflammation and T cell differentiation in an animal model of multiple sclerosis. *J Neuroinflammation* 14(1):55.
70. Ando K, Brion JP, Stygelbout V, Suain V, Authalet M, Dedecker R, Chanut A, Lacor P, Lavaur J, Sazdovitch V and others. 2013. Clathrin adaptor CALM/PICALM is associated with neurofibrillary tangles and is cleaved in Alzheimer's brains. *Acta Neuropathol* 125(6):861-78.



71. Naj AC, Jun G, Reitz C, Kunkle BW, Perry W, Park YS, Beecham GW, Rajbhandary RA, Hamilton-Nelson KL, Wang LS and others. 2014. Effects of multiple genetic loci on age at onset in late-onset Alzheimer disease: a genome-wide association study. *JAMA Neurol* 71(11):1394-404.
72. Parikh I, Fardo DW, Estus S. 2014. Genetics of PICALM expression and Alzheimer's disease. *PLoS One* 9(3):e91242.
73. Zhao Z, Sagare AP, Ma Q, Halliday MR, Kong P, Kisler K, Winkler EA, Ramanathan A, Kanekiyo T, Bu G and others. 2015. Central role for PICALM in amyloid-beta blood-brain barrier transcytosis and clearance. *Nat Neurosci* 18(7):978-87.

## SUPPLEMENTARY DATA

**Table S1.** Functional annotation of the 15 AD-associated ncRNA SNPs and their proxies in high LD ( $R^2 > 0.7$ ) using HaploReg v4 (Excel file)

**Table S2.** Transcription factor binding sites (TFBSs) might be perturbing by rs2526377

**Table S3.** Expression of miR-142-3p and -5p in the human brain regions

**Table S4.** Downregulated target genes of miR-142-3p in human iPSC-derived NPCs

**Table S5.** Putative miR-142-3p target genes that are involved in AD-relevant pathways

**Table S6.** Target genes of miR-142 with the most significant association with AD

**Table S7.** Differentially expressed target genes of miR-142-3p in the hippocampus of KO mice vs Wt littermates

**Table S8.** IPA pathway analysis for 12 target genes of miR-142-3p upregulated in the hippocampus of KO mice

**Figure S1.** Regional association plots showing the association of 15 ncRNA SNPs with AD using the phase 3 of AD GWAS

**Figure S2.** Transcription factor binding sites overlap with rs2526377 (using UCSC browser)

**Figure S3.** KEGG pathways analysis for some of the putative miR-142-3p target genes (orange boxes) involved in AD

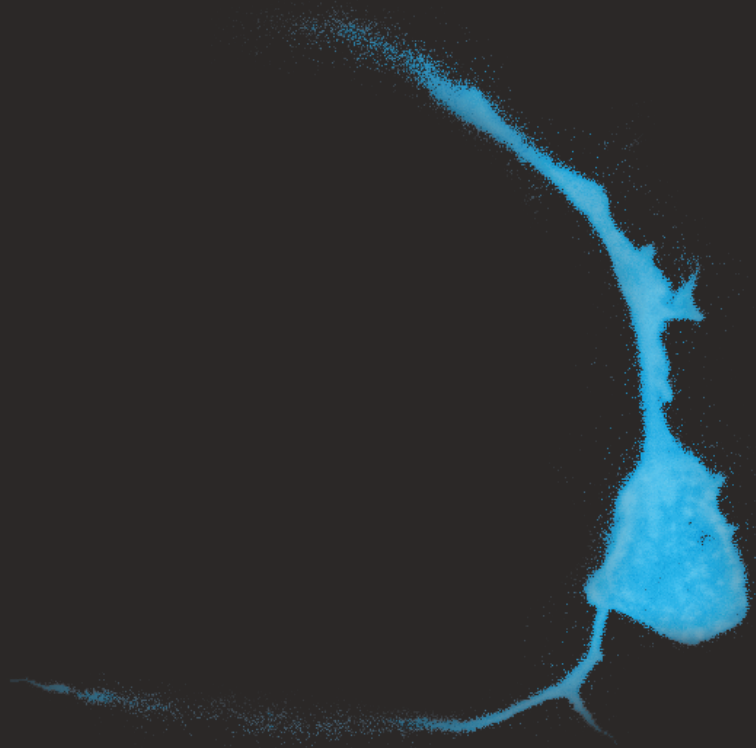
**All supplementary data can be found online: doi 10.1002/humu.23872.**





# Chapter 7

## General discussion





This thesis set out to test the functionality of human iPS technology for human brain disease modeling. In the preceding chapters I reported on several studies where we successfully used iPS technology to answer questions on human molecular and cellular neurobiological functioning. We established a simplified protocol for obtaining mature neuronal networks and revealed on transcriptional regulation of human *BDNF* and sublocalization of human *UBE3A*. We reported that the reprogramming procedure leads to silencing of the *FMRI* gene even in a healthy individual without concomitant methylation of the full mutation. Lastly, we identified a functional variant associated with lower risk for AD.

Nonetheless, since the emergence of iPS technology several features of its use have come to light that require proper attention. The largest and most disturbing discovery is that not all pluripotent stem cells are equal in their capacity to differentiate into desired cell types *in vitro*. Numerous studies now point towards variation at the genetic and epigenetic level between clones that result in functional variability between cell lines and heterogeneity between clones. Below I discuss the sources of this variability and how we have combatted these in our studies.

## DONOR CELL-INDUCED GENETIC VARIABILITY

The first introduction of genetic variability arises with the choice of donor cell from which an iPS line is generated. Nowadays, many different cell types have proven suitable as donor cell. In the initial publication on reprogramming by Takahashi et al. dermal fibroblasts and fibroblast-like synoviocytes were used<sup>1</sup>. Ever since other groups confirmed that also blood erythroblasts, hair keratinocytes<sup>2,3</sup>, cells from tubular networks from the ureters, bladder and urethra disposed in urine<sup>4,5</sup>, and dental pulp cells<sup>6</sup> are converted to iPS by the Yamanaka factors Oct4, Sox2, Klf4, c-Myc. Also cells derived from lesser accessible tissues proved sufficient such as neural stem cells, hematopoietic stem cells and liver cells<sup>7</sup>. Although all of these cells are originally formed from different germ layers and their conversion towards a pluripotent state is possible, increasing reports document that the efficiency differs as a function of the donor cell source<sup>7,8</sup>. This may depend on endogenous expression of the Yamanaka factors themselves<sup>9</sup>. Regardless, there seem to be no limitations depending on sex, ethnic group, disease condition, or interestingly age. This latter point however may require extra attention. As individuals age, their DNA accumulates mutations either induced by the environment or because of mistakes in the DNA proofreading process during cell division<sup>10,11</sup>. These somatic mutations not necessarily turn into harmful tissue for the individual, yet this phenomenon in iPS-based studies may pose a problem: the starting donor cell culture may be genetically heterogeneous. Several groups indeed confirm this<sup>12-14</sup>. Albeit a small population of cells, there are unique mutations not present in the culture as whole. Next to inherent heterogeneity of the used tissue, a mutational load for cell divisions (approximately 0.02 per cell division<sup>12</sup>) also applies. While the contribution of variability to the culture is small, the subsequent step

in iPS line generation requires reprogramming and colony picking. Here individual cells form individual colonies and initial neglectable variety runs the risks of being established within a cell line. Interestingly also, several studies suggest that somatic mosaicism, the presence of multiple cell clones with different genotypes in the same individual, is common in normal development<sup>15,16</sup>. This poses a dilemma on modeling. What is the reference genome or are the reference genomes? What is the contribution of each? Are somatic mutation facilitating the phenotype in an individual or are they non-functional?

In our studies we have tried to deal with donor cell variability in several ways. Firstly, our iPS lines were derived from skin fibroblasts, where our oldest donor was 57 years old and our youngest donor 3 years old. We made use of skin fibroblasts because of their large source and ease for culturing. This would keep the culture-induced mutation rate as low as possible.

Ideally, we would use younger cells, such as hematopoietic stem cells which are rare in peripheral blood, but rich in bone marrow, umbilical cord blood and placenta<sup>17</sup>. Moreover, these last two have multi-lineage differentiation potential and a low mutational load. However in practice this may pose a problem. Such cells are not commonly stored. Since a large group of psychiatric disorders and degenerative disorders present themselves only decades after birth, a large source of donor cells may be the next best option in line for modeling them with iPS. Next to fibroblasts, another convenient source of cells are urine-derived donor cells<sup>4,5</sup>. Also no medical assistance is necessary to obtain them. However little is known about this derived source. Peripheral blood also represents itself as a rich source, yet it contains erasable immunogenic marks, and may contain infections<sup>7,8</sup>. Overall, conscious decisions should be made with respect to donor cell type, and quality control checks for spotting heterogeneity in donor cell population may be of help.

## REPROGRAMMING-INDUCED GENETIC VARIABILITY

Apart from variability induced by the donor cell population, several groups have reported on additional mutations and genomic alterations after reprogramming. Gore et al. indicated that in 22 tested iPS lines an average of 6 exomic mutations per line was gained. It is unclear though at which passage number the lines were tested. Interestingly, Ji et al. indicate an average of 12 mutations per iPS cell line at passage 6<sup>13</sup>. Their study focused on the derivation of 5 individual iPS lines from one fibroblast source. Additionally, large chromosomal aberrations were also found in derived iPS lines. Several groups report on abnormal chromosomal aneuploidy (multiple copies of the same chromosome), chromosomal trisomies<sup>14,18</sup>, copy-number variants (CNV)<sup>18,19</sup>, and deletions and duplications<sup>18,20</sup>. Taapken et al.<sup>21</sup> reported that of 552 cultures of 219 iPS lines, 12.5% of the cultures have an abnormal karyotype. This indicates that significant genomic aberrations emerge during reprogramming, colony picking, and expansion.



The genes affected by these mutations were not random. Many of the mutations were found in genes related to cancer<sup>12</sup>, and culturing specifically selected for them<sup>12</sup>. These mutations may give the cells a growth advantage. CNVs were also found in genes with established roles in cancer<sup>18</sup>. Most chromosomal aberrations were detected on chromosome 12 and 17 which carry genes benefitting embryonic tumors and stem cell adaptation<sup>14</sup>. Similarly, Hussein et al. ascertained that compared to 6596 common CNVs found in 270 healthy individuals, 37% of the found CNVs were novel but enriched in maintaining an undifferentiated state, or associated with human ES differentiation and maintenance<sup>19</sup>. They also indicated that deletions were commonly found in common fragile sites in the genome and subtelomeric regions. Although others could not confirm that<sup>18</sup>. On a karyotype level trisomy 12 was the predominant abnormality in 31,9% of the hundreds of iPS lines tested. However 42% of the located chromosomal abnormalities were nonrecurrent between lines.

Testing for mutations in the gene however only represents the genomic status in that moment, as mutations seem to be acquired and lost with passaging. In a small study Ji et al. indicated that at passage 12, 2 of the 5 tested iPS lines had lost 2, and 1 point mutations, and two iPS lines had gained 1, and 3 point mutations<sup>13</sup>. In another study an increase of 4 mutations from passage 9 to passage 40 was found<sup>12</sup>. A rough estimation therefore is approximately 1 mutation per 10 passages. However both studies examined mutational burden in the exome. Additional mutations may have been incorporated in the non-coding genome as well. Apart from the exome, the DNA also holds regulatory sequences, the proper functioning of which ensures adequate transcriptional regulation of the cell<sup>22,23</sup>. Therefore, the amount and effect of acquired mutations may in fact be higher. Long-term culture also increases genomic abnormalities, where aneuploidy is rare in low passage iPS, but increase at later passages<sup>24</sup>. For example in one iPS line (hiPSC 18)<sup>25,26</sup> Marshay et al. measured a normal karyotype at passage 45, passage 58 presented a mosaic cell line with normal cells and trisomic cells containing three copies of chromosome 12. However at passage 63 the line had acquired a full trisomy of chromosome 12. Deletions were mostly found in early passages (passage 5-8), and duplications in later passages (passage 25-34)<sup>20</sup>. Some early deletions actually receded, indicating that they are positively selected for during reprogramming, but negatively selected for during passaging. With regard to CNVs Hussein et al. found that they were negatively correlated with passage numbers<sup>19</sup>. This indicated that with passaging CNVs were selected against, and their number and length decreased over passaging time. Over time, therefore, cultures were mosaic. Others however did not find an association between CNVs and passage number<sup>18</sup>.

To ensure that our iPS lines did not carry genetic abnormalities we checked their karyotype between p5-p10 after colony picking and every 10 passages. We kept our lines in culture for the least amount of time necessary. Lines with aberrant karyotypes were not used for subsequent studies. Yet we did not perform exome or whole-genome sequencing at any of the passages. A major challenge we encountered was that individual clones are selected not only in the reprogramming procedure, but also in iPS maintenance. Culture of any given line in

routine-practice therefore is highly branched. A way to combat this disadvantage is to work with highly efficient reprogramming strategies, and iPS maintenance protocols that are robust and standardized such that colony picking is prevented as much as possible. Next to this, an administrative system to keep close track of genetically surveyed lines, and their pedigree relationship between cryopreserved stocks, live cultures and cells from which data is derived may greatly benefit detecting any genetic abnormalities that may obscure experimental data.

## REPROGRAMMING-INDUCED EPIGENETIC VARIABILITY

Next to genetic variability, also epigenetic variability occurs in cell culture. In essence cellular reprogramming as is done by the Yamanaka factors, results in the repression of genes responsible for differentiation and activation of genes responsible for reprogramming. Here epigenetic marks are responsible for the gene-specific expression.

Different types of epigenetic marks exist. They are divided in two major classes<sup>27</sup>: DNA methylation and histone modifications. DNA methylation is a biochemical process where a methyl group (CH<sub>3</sub>) is covalently bound to the cytosine in the DNA. Through this modification access to the DNA is hampered. Also methyl-CG-binding domain proteins can be recruited. They remodel histones and form compact, inactive chromatin so-called heterochromatin. Regularly high repeats of CG's are found near gene promoters and transcriptional start sites. These are called CG-islands. These islands are targets for methylation. Methylation of CG-islands generally leads to inhibition of transcriptional activity of genes in their vicinity, whereas unmethylated CG-islands allow activation.

For most genetic locations DNA methylation is identical on both alleles. However, at imprinted genes and X-chromosomes though, only a single allele is methylated normally. This results in silencing and parental-specific expression of this gene. At this point about 60 human genes are known to be imprinted<sup>28</sup>. There are imprints that are established in the germline, whereas others are derived in somatic cells during early embryonic development. Imprinting defects are amongst others associated with neurodevelopmental diseases such as Silver-Russell, Beckwith-Wiedemann, Prader-Willi syndromes and Angelman Syndrome<sup>29</sup>.

The second class of epigenetic marks is histone modification. Histones are proteins around which the DNA winds itself. Wound up DNA together with the histone is called a nucleosome. Histones can also undergo covalent modifications such as acetylation, phosphorylation, methylation, SUMOylation, and ubiquitination<sup>30</sup>.

A another class of epigenetic-related processes is covered by regulation through noncoding RNA expression<sup>27</sup>. It has become evident that noncoding RNAs are involved in controlling several epigenomic phenomena. One example is the dosage compensation mechanism of the X-chromosome through the long non-coding RNA, *XIST* (X-inactive specific transcript). This mechanism ensures X-chromosome inactivation (XCI). However noncoding RNAs are

also involved with silencing genes and repetitive DNA sequences by post-transcriptional and transcriptional RNA interference-related pathways through microRNAs and siRNAs.

Cellular reprogramming requires the substitution of the donor cell epigenetic marks, which normally are stably inherited through subsequent divisions, with that of the epigenetic marks specific to iPS cells<sup>29</sup>. Subsequent modeling of human brain cells then obliges remodeling of the iPS epigenetic landscape to that of the desired brain cell. This however turns out not to be straightforward. In the original study by Takahashi et al. iPS were promoted for their comparison to ES cells with respect to morphology, proliferation, gene expression and differentiation potential<sup>1</sup>. However, at the epigenetic level iPS and ES cells share some differences. For example, when DNA methylation patterns in iPS cells are compared to those in ES cells, differentially methylated regions (DMR) in genes are detected<sup>31-34</sup>. Similarly, at several genes methylation patterns are found in iPS that are specific to the donor cell, but are not found in ES cells. This epigenetic memory phenomenon can either be labeled as aberrant or incomplete reprogramming, or as an iPS-specific epigenetic signature. Lister et al. indicated that 51-56% of 3507 DMRs in CG islands found between iPS on the one hand and donor cells or ES cells on the other hand, were specific to the iPS cells only. Sixty-nine percent of these DMRs were present in at least two iPS lines, and 16% of the DMRs were found in 5 iPS lines. These may represent iPS-specific epigenetic signatures. These iPS-specific signature marks were spread over the genome so they did not specifically disrupt certain processes. In these 5 lines 92% of the DMRs turned out to be hypomethylated compared to the donor cell, indicating that it mostly was methylation that was not properly reset.

Ohi et al. found a similar trend. They differentiated hepatocytes, newborn foreskin fibroblasts, and adult melanocytes to iPSs. In low passage iPS cells (below 20) they found that genes that were expressed at high levels in donor cells, were repressed in iPS, yet their expression remained higher than in ES cells. The same applied for poorly expressed genes in donor cells: they were more highly expressed in iPS, but not as high as in ES cells. Next to this they found that DMRs were not dependent on any of the donor cell type. However, they did find a non-random pattern of incompletely silenced genes. These genes tended to be physically isolated from other genes that did undergo silencing. This could indicate that the silencing machinery or DNA methyltransferases may be inefficient or delayed at certain donor genes.

Also, when iPS were differentiated to trophoblast lineage cells, hundreds of DMRs were found between ES cells and ES-derived trophoblasts<sup>31</sup>. The differences were attributed to donor cell DMRs, and iPS-specific DMRs. This indicated that aberrant methylation is maintained in differentiated lineages. Bar-Nur et al. reprogrammed pancreatic islet beta cells towards iPS, and found that pluripotency genes indeed were active, however donor cell genes were more methylated<sup>34</sup>. Also, hypomethylated genes in the islet cells were still hypomethylated in the iPS line, while normally methylated in lines derived from fibroblasts, or in ES cells. Next to this 29 mega-regions of dissimilar methylation were found in genomes<sup>31</sup>. Half of them were greater

than 1 MB, the largest was 4.8 MB. Many of these regions were found in close proximity to centromeres and telomeres.

Nazor et al. also found aberrant methylation in differentiated cell types<sup>35</sup>. They studied methylation in several female iPS lines, and discovered that numerous had partial or low methylation of X-chromosomes. This coincided with *XIST* expression, where a higher expression of the non-coding RNA *XIST* that mediates silencing, was related to higher methylation levels on the X-chromosome. This difference was found even though all clones were passaged and managed in the same way. Also, where the majority of lines in early passages showed XCI and *XIST* expression, at late passages they showed loss of XCI and *XIST* expression. Similar patterns were observed by Mekhoubad et al.<sup>36</sup> This loss of imprinting resulted in biallelic expression of the X-chromosomes. When these cells were differentiated to the NPC and OPC lineages, these partial methylation patterns persisted. Apart from epigenetic changes that are established during reprogramming and passed through to differentiated lineages, epigenetic changes thus also occur during passaging over time.

We did not perform assays on DNA methylation patterns in our derived iPS or differentiated neural cells. However we did experience the epigenetic altering effect of reprogramming in our studies. In chapter 5 we worked with fibroblasts from a healthy individual who carries a full mutation of the *FMR1* gene. Where a full mutation normally induces silencing of the gene by DNA methylation of the *FMR1* promoter and additional histone modifications, this individual carried unmethylated *FMR1* alleles in fibroblasts and showed *FMR1* expression. To study the effects of epigenetic silencing of *FMR1* in fragile X syndrome we reprogrammed these fibroblasts into iPS lines. However in the iPS state, the *FMR1* promoter of this healthy individual was methylated. This illustrates an example of the effect of reprogramming on the epigenome that render iPS unusable for modeling. Since in this case the epigenetic silencing process was our area of focus, this discrepancy in methylation status came to our attention. However, certain epigenetic marks may play subtle roles in disease modeling, and where the involved marks are even unknown, these as of yet unpredictable differential epigenetic marks may cause variability and faulty results.

One of the limitations of our study is that we did not evaluate the methylation pattern of the PWS-IC of the cells used for our UBE3A localization experiments (Chapter 4). A methylated PWS-IC inhibits expression of UBE3A-ATS. This long non-coding RNA silences expression of the *UBE3A* gene. The UBE3A-ATS is exclusively expressed in neurons. As such, in neurons derived from iPS with unmethylated PWS-ICs no UBE3A expression would be observed. Nonetheless, we observed UBE3A expression in NPCs derived from iPS generated from fibroblasts from an AS patient and in NPCs and neurons of a healthy control. Therefore we assume that the PWS-IC must have been methylated. However, we are not able to ascertain that UBE3A expression in neurons from the healthy control was not due to two active UBE3A alleles. Nonetheless, several studies reported on fibroblast-derived iPS lines where the PWS-IC centers in different iPS lines was methylated<sup>37–39</sup>, confirming the use of iPS for studying

UBE3A expression. However a recent study found differential methylation of PWS-IC and subsequent aberrant expression of the closely located *SNRPN* gene, pointing towards the necessity to thoroughly check methylation status in genes under investigation<sup>40</sup>.

## INHERENT GENETIC VARIABILITY

Several researchers have established acquired genetic and epigenetic variability not to be the biggest source of *in vitro* variation<sup>41–43</sup>. Inherent genetic variation between individuals seems to play a much larger part. Burrows et al. collected blood and fibroblasts for iPS reprogramming from two males, and two female individuals. Deriving multiple lines from each donor cell source allowed them to compare cell-type of origin, epigenetic memory, and their intra- and inter-individual components to variability. Their gene expression and DNA methylation data showed that the contribution of cell type of origin to variation in gene expression and methylation data was very small. There was an epigenetic memory of the donor cells in the iPS lines, but this contributed only marginally to variation. This was also confirmed by others<sup>43</sup>. Burrows et al. concluded that only a handful of differentially methylated sites influenced regulatory variation but that genetic background captured a much greater proportion of the variation seen in gene expression and methylation assays.

This fact was also supported by Kyttälä et al.<sup>42</sup> who showed that only 7-25% of the DMRs resemble those from the donor cell. On average 70% of these DMRs are equal to those found in ES cells. They find that the majority of variance found in gene expression and methylation assays is dependent on genetic background. The genes differentially expressed between donors were mostly those encoding transcriptional factors related to maintenance and differentiation of iPS. Also, when iPS were differentiated they found that the differences in gene expression in iPS were reflected in the gene expression in differentiated cells types as well.

Subsequent studies were able to more concretely define genetic variability to the outcomes of measured *in vitro* variance<sup>18</sup>. In a comparative study using hundreds of lines from 301 individuals, Kilpiken et al. calculated that 21.4-45.8% of variance measured in immunocytochemical stainings, and 7.8%-22.8% of variance measured in cellular morphology is attributable to genetic variability between individuals. In a gene expression assay were 25,434 probes were tested, variation of 46.4% of the probes was explained by gene variability. CNVs, culture conditions, passage numbers or gender explained 23.4%, 26.2%, 2%, and 1.9% of the variance, respectively. Carcamo-Orive et al. found that 50% of the variance found in gene expression data was explained by genetic background. They added to this that several expression quantitative trait loci correlated with gene expression levels. It appeared that *cis*-regulatory variants contributed more to variance than shared environment and technical processing. The genes that varied most were related to developmental processes such as pattern specification,

regionalization, and organ and embryonic morphogenesis. This indicated that developmental pathways contributed at length to variability between lines.

In our studies, to correct for variability between lines, we made use of three lines from three different individuals in Chapter 2, where we tested the robustness of our neuronal differentiation protocol. For the remaining of our studies we made use of one line per condition. Despite the reported variability we found robust and reproducible results in our experiments. The reason we asked very specific questions that did not require comparison between different iPS lines may have been the reason for that: in Chapter 2 we were testing the robustness of our protocol which was confirmed by the development of neuronal cultures from three independent lines in several rounds of differentiation. In Chapter 3 we made use of one ES line, and one iPS line for investigating transcriptional control of the *BDNF* gene. In Chapter 4 we compared overexpression of different UBE3A protein isoforms. In Chapter 5 we evaluated the epigenetic characteristics of the *FMR1* promoter of several lines before and after reprogramming. As such our experiments did not suffer from inherent genetic variability between lines.

Whenever phenotypes between iPS lines are to be compared, an alternative study design would be the use of isogenic lines: lines theoretically only differing in the genetic perturbation to be studied.

In general three types of iPS-based studies are discernable: the study of fundamental biology irrespective of genetic variations or mutations, the study of a monogenic disease, or a multigenic disease. In each study the genetic background of the stem cell line to be used needs to be considered carefully. Commonly donor cells from a healthy subject are used to generate control stem cells lines. Control cell lines are used for fundamental studies unrelated to genetic variations and mutations as well as in 'patient vs control' designs. Yet the question remains what healthy subjects entail. Individuals could be free of disease at the moment of assessment, and develop disease later in life. Collection of donor cells from aged subjects may not be accommodating because of mutational load in older cells<sup>10</sup>. In this case selection of sufficient amount of lines would mitigate line-specific effects. This makes the selection of youthful donor cells-derived lines a possibility, in that way eliminating high mutation load derived from adult somatic cells. Retrospect check-up on donors when they reach the critical age for disease development is an alternative as well.

In case of studying monogenic diseases with strong effect sizes it may suffice to select unrelated controls<sup>44–46</sup> (such as in chapter AS) or at best healthy family members to compare with the patient-specific lines<sup>47</sup>. In case of smaller effect sizes variation between lines can partially be taken away by making use of isogenic lines, lines identical other than the mutation to be studied. This solution should mitigate the unintended genetic and epigenetic variability that remains between two unrelated stem cell lines<sup>48</sup>. Yet several points have to be taken into account. Commonly used procedures for gene editing entail zinc fingers, TALENs and Caspr-Cas9 where the use of the latter nowadays becomes standard-practice in labs. Nonetheless, albeit they are being improved, these techniques can unintentionally create mutations elsewhere

in the genome in the editing procedure<sup>49</sup>. Several economical high-throughput methods are being developed to check the genome for additional mutation. Yet these would have to become standard-practice as well in laboratories as often only *in silico* predicted off-targets are examined. Unfortunately there is accumulating evidence that the current algorithms have low prediction accuracy<sup>49</sup>. Taking into account the variability induced by the *in vitro* procedures, the chance on differences between derived isogenic lines in point mutations as well as aberrant epigenetic landscapes increases with every passage (see above).

In case of studying multigenic diseases where uncertainty remains on which genetic perturbation is responsible, patient and control selection is a delicate business. Some suggest that selecting patients and controls with clustered risk-scores may create enough power for phenotype detection<sup>50</sup>. Surely high numbers of lines are necessary to tease out the phenotype.

Nonetheless, where possible the use of isogenic lines seems the best way forward to reduce genetic and epigenetic variability.

## IN VITRO DIFFERENTIATION-INDUCED VARIABILITY

Another source of variability seen in human brain modeling studies is the neural differentiation procedure itself. Most differentiation strategies are based on modulating naturally occurring specialization in the brain. In development, neurons are derived from the ectoderm, one of the three germ layers generated in early embryogenesis<sup>51</sup>. Ectoderm forms the neural tube, which gives rise to the brain and spinal cord. These developmental steps are triggered by the expression of morphogens in strict patterns along the rostral-caudal axis (Fibroblast Growth Factors (FGFs), Wingless/Int (WNTs), retinoic acid (RA)) and ventral-dorsal (WNTs, Bone Morphogenetic Proteins (BMPs), Sonic Hedgehog (Shh)). Under influence of FGF and RA ectodermal tissue develops into neuroepithelia. Subsequently, a specific combination of morphogens in the neural tube triggers the neural stem cells in that area to develop into either neuronal or glial progenitors<sup>52</sup>. These progenitors differentiate into mature neurons or astrocytes and oligodendrocytes, respectively. In the differentiation process similar developmental stages are passed. An important step is the induction of neuroectoderm. From there on, neural stem cells and precursors continue on to differentiate into specific neuronal subtypes with or without addition of specific morphogens.

There are several ways to induce neuroectoderm *in vitro*. One way is the isolation of neuroectoderm from embryoid bodies<sup>53</sup>. Embryoid bodies (EBs) are three-dimensional cellular aggregates of iPSCs, obtained when cells are grown in suspension. This method allows the spontaneous differentiation of iPSCs to cells of the three germ layers. When treated with specific growth factors or morphogens such as RA, the proliferation of neuroectoderm is promoted. Subsequently, cells are plated in neuronal supporting media. However, the drawback of this system is that embryoid bodies can vary in size, which results in inconsistent yields



of neural progenitors. Since the inner cell layers of embryoid bodies are difficult to reach for morphogens, radial concentration gradients emerge which induces heterogeneous cell types.

As EBs are derived from iPS, their homogeneity also plays an important part. *In vivo* the pluripotent state is a transient one, such that *in vitro* critical media components are necessary to maintain the pluripotent state<sup>1,54–57</sup>. Yet iPS occasionally escape the pluripotent state and randomly differentiate, thereby reducing the line's overall pluripotency. Whenever these cells are used for targeted terminal differentiation the outcome is inevitably a mixed population of desired and undesired cells.

Kilpinen et al. tested over hundreds of lines from 301 individuals and found that 84% of them are classified as pluripotent by the Pluritest, a tool for pluripotency assessment by whole genome expression analysis<sup>18</sup>. In an average iPS line 18–62% of the cells co-express the pluripotency markers NANOG, OCT4 and SOX2. Whenever an iPS line was differentiated to one of the germ layers 70%, 84% and 77% of the cells in the line would express markers specific for respectively endoderm, mesoderm, and ectoderm. This indicates that roughly one-sixth of the lines are pluripotent, and that roughly one-fourth of the cells do not differentiate to the desired germ layer.

After neural induction of EBs from iPS, EBs are commonly plated and display neural rosettes. Series of radial migration of NPCs occur, yet however not all these NPCs are the same<sup>58</sup>. They are an ensemble of several neuronal precursors such as radial glia, intermediate progenitors, symmetrically and asymmetrically dividing NPCs<sup>59</sup>, but also progenitors of oligodendrocytes, and astrocytes<sup>60</sup>. Depending on the question to be asked, treating them as one population may result in high batch-to-batch differences. Next to that, terminal neural differentiation highly depends on the composition of the original NPC population. As such, mixed NPC populations may lead to dissimilar terminally differentiated neural cultures if the ratios of the different types of progenitors are not the same. As terminally differentiated cultures derived from NPCs by dual-SMAD inhibition also go through a neural rosette stage, the same caution should be taken.

Apart from the cell type diversity of the NPC population, another point to take into account is the age of the cell. Regular passage of NPCs may contain migrated NPCs, as well as newly born NPCs. These cells represent different neurodevelopmental stages of NPCs: each of these cells may have a different temporal-spatial expression profile, such as in the brain. Practically, the first rounds of passaging of the NPC population deliver mostly neuronal precursors, where later populations produce more astrocytes. Whenever this tipping point occurs though is unknown. Yet in our studies we find this to be around 10 passages of the NPC population. During *in vivo* brain development different NPC populations co-exist simultaneously; however, for modeling neurodevelopmental diseases the fine balance of the population may be crucial.

The shortest protocols to differentiate neuronal cells with basic electrophysiological properties from a common neural progenitor need 6 weeks of *in vitro* culturing from a neuroectoder-



mal stage. As the protocols to generate neurons lengthen and several procedures ((sub)plating, refreshing, stable environmental factors) need to be performed, well-to-well variability is increased, such as differences in cell density and cellular heterogeneity. Volpato et al. tested the reproducibility of the Shi et al. protocol<sup>61,62</sup>. They used two lines: one control line, and one line containing a mutation in the *PSEN1* gene, in 5 different laboratories and examined the RNA and protein profiles of differentiated cortical neurons. Within each laboratory the differences between lines were visible (three independent neuronal induction). However across multiple laboratories differences in expression between the two lines were not consistently detectable. They indicated cell type heterogeneity as the major contributor to variability. Subsequently, they also collected 771 individual transcriptomes of cells in the culture. Here 4-5 subpopulations were identified within the neural cultures expressing neuronal, astrocytic, oligodendritic and microglial marker genes. They also found out that factors that hampered cross laboratory comparison were iPS passage number before differentiation, the number of passages before terminal differentiation plating, media volume changes, feeding at weekends, and use of frozen progenitors. They hypothesized that the factors may alter epigenetic and cellular programs that determine cell fate choice, eventually influencing the composition of the final culture.

For the majority of the studies we made use of the differentiation protocol described in Chapter 2. In this chapter we showed reproducible outcomes of neural cell composition. In Chapter 4 we made use of fluorescence-activated cell sorting (FACS) to enrich our NPC population, thereby increasing the homogeneity of the precursor population. To validate our results it may be worthwhile to test again the transcriptional activation of *BDNF* VIII-IX transcript and the methylation states of the different iPS lines used in chapter 3 and 5 respectively with FACS-sorted NPC populations to prove that the obtained results were not due to contamination of the cell population. Others have proved it to be a valuable technique to enrich the NPC population<sup>63,64</sup>. It should be taken into consideration though that even populations selected by canonical marker expression may still present a diversity within their own subclass.

We used real-time quantitative PCR and EB differentiation to test pluripotency of our iPS lines. However, determining when to call a line a pluripotent stem cell line remains a topic for debate. Several tests and assays are available yet none of these tests provides exclusive proof for all the genetic, epigenetic, transcriptional and translational assets of a stem cell<sup>65</sup>. Momentarily the community is moving towards validation of stem cell lines by gene expression data by the algorithm provided by Pluritest<sup>66</sup>. By computationally comparing the gene expression data of induced stem cells to *bona fide* stem cells, a cut-off score determines when an induced line is considered a stem cell line. However, once validated, stem cell lines need revalidation after passaging, manipulation and colony picking, making it practically impossible to control the exact composition of an iPS population. Here also studies would benefit from improved iPS maintenance protocols, such as methods to minimize contamination of pluripotency by spontaneous differentiation.

To define the different types of neural cells in the culture still remains challenging. However others are paving the way with single-cell analyses and systematic characterization on the basis of electrophysiological and transcriptomic profiles<sup>67</sup>. As the brain in development also depicts heterogeneity *in vitro* iPS-derived neural cultures may actually not stray too far from their *in vivo* counterparts<sup>68</sup>. Nonetheless, as pathways regarding cell fate decision and network formation in neuronal cultures are being explored and more knowledge on the different NPCs emerges, caution should be taken with treating every batch of NPCs and neuronal differentiation similar.

Reproducibility between labs is a concerning factor, as findings of previous researchers may prove non-repeatable and hence their results faulty. Comparable to iPS maintenance, protocols to generate reproducible neuronal cultures contain multiple steps, variables, and often, subjective judgment decisions. Clearer and more accurate experimental descriptions, improvement of induction protocols and pre-selection of NPC pools may benefit reproducibility between labs.

Overall, the extent to which acquired mutations in iPS lines, aberrant epigenomic markers, inherent genetic variability and heterogeneity in neural cultures hamper the ability to model human brain diseases seems to largely depend on the research question to be answered. Experimental conditions are to be tailored to these questions. Nonetheless, small effect sizes of genes, unidentified neural cell types, and the involvement of pathways in disease require the highest standard of iPS modeling. As such, the community at whole may do best to optimize iPS technology to its highest capacities to continue to unravel the molecular and cellular mechanisms underlying human brain disorders.

## REFERENCES

1. Takahashi, K. *et al.* Induction of pluripotent stem cells from adult human fibroblasts by defined factors. *Cell* **131**, 861–72 (2007).
2. Carey, B. W. *et al.* Reprogramming of murine and human somatic cells using a single polycistronic vector. *Proc. Natl. Acad. Sci. U. S. A.* **106**, 157–62 (2009).
3. Aasen, T. *et al.* Efficient and rapid generation of induced pluripotent stem cells from human keratinocytes. *Nat. Biotechnol.* **26**, 1276–84 (2008).
4. Wang, L. *et al.* Generation of integration-free neural progenitor cells from cells in human urine. **10**, (2013).
5. Zhou, T. *et al.* Generation of Induced Pluripotent Stem Cells from Urine. *J. Am. Soc. Nephrol.* **22**, 1221–1228 (2011).
6. Yan, X. *et al.* iPS Cells Reprogrammed From Human Mesenchymal-Like Stem/Progenitor Cells of Dental Tissue Origin. *Stem Cells Dev.* **19**, 469–480 (2010).
7. Li, J., Song, W., Pan, G. & Zhou, J. Advances in understanding the cell types and approaches used for generating induced pluripotent stem cells. *J. Hematol. Oncol.* **7**, 50 (2014).
8. Raab, S., Klingenstein, M., Liebau, S. & Linta, L. A Comparative View on Human Somatic Cell Sources for iPSC Generation. *Stem Cells Int* **2014**, 768391 (2014).
9. Tsai, S. Y. *et al.* Oct4 and Klf4 reprogram dermal papilla cells into induced pluripotent stem cells. *Stem Cells* **28**, 221–228 (2010).
10. Kennedy, S. R., Loeb, L. A. & Herr, A. J. Somatic mutations in aging, cancer and neurodegeneration. *Mech. Ageing Dev.* **133**, 118–26 (2012).
11. Milholland, B., Auton, A., Suh, Y. & Vijg, J. Age-related somatic mutations in the cancer genome. *Oncotarget* **6**, 24627–35 (2015).
12. Gore, A. *et al.* Somatic coding mutations in human induced pluripotent stem cells. *Nature* **471**, 63–67 (2011).
13. Ji, J. *et al.* Elevated Coding Mutation Rate During the Reprogramming of Human Somatic Cells into Induced Pluripotent Stem Cells. *Stem Cells* **30**, 435–440 (2012).
14. Mayshar, Y. *et al.* Identification and Classification of Chromosomal Aberrations in Human Induced Pluripotent Stem Cells. *Cell Stem Cell* **7**, 521–531 (2010).
15. Risques, R. A. & Kennedy, S. R. Aging and the rise of somatic cancer-associated mutations in normal tissues. *PLoS Genet.* **14**, 1–12 (2018).
16. De, S. Somatic mosaicism in healthy human tissues. *Trends Genet.* **27**, 217–223 (2011).
17. Haase, A. *et al.* Generation of induced pluripotent stem cells from human cord blood. *Cell Stem Cell* **5**, 434–41 (2009).
18. Kilpinen, H. *et al.* Common genetic variation drives molecular heterogeneity in human iPSCs. *bioRxiv* **546**, 055160 (2016).
19. Hussein, S. M. *et al.* Copy number variation and selection during reprogramming to pluripotency. *Nature* **471**, 58–62 (2011).
20. Laurent, L. C. *et al.* Dynamic changes in the copy number of pluripotency and cell proliferation genes in human ESCs and iPSCs during reprogramming and time in culture. *Cell Stem Cell* **8**, 106–118 (2011).
21. Taapken, S. M. *et al.* Karyotypic abnormalities in human induced pluripotent stem cells and embryonic stem cells. *Nat. Biotechnol.* **29**, 313–4 (2011).
22. Epstein, D. J. Cis-regulatory mutations in human disease. *Briefings Funct. Genomics Proteomics* **8**, 310–316 (2009).

23. Narlikar, L. & Ovcharenko, I. Identifying regulatory elements in eukaryotic genomes. *Briefings Funct. Genomics Proteomics* **8**, 215–230 (2009).
24. Mayshar, Y. *et al.* Identification and Classification of Chromosomal Aberrations in Human Induced Pluripotent Stem Cells. *Cell Stem Cell* **7**, 521–531 (2010).
25. Lowry, W. E. *et al.* Generation of human induced pluripotent stem cells from dermal fibroblasts. *Proc. Natl. Acad. Sci.* **105**, 2883–2888 (2008).
26. Chin, M. H. *et al.* Induced Pluripotent Stem Cells and Embryonic Stem Cells Are Distinguished by Gene Expression Signatures. *Cell Stem Cell* **5**, 111–123 (2009).
27. Goldberg, A. D., Allis, C. D. & Bernstein, E. Epigenetics: A Landscape Takes Shape. *Cell* **128**, 635–638 (2007).
28. [www.geneimprint.org](http://www.geneimprint.org).
29. Nashun, B., Hill, P. W. & Hajkova, P. Reprogramming of cell fate: epigenetic memory and the erasure of memories past. *EMBO J.* **34**, 1296–1308 (2015).
30. Spivakov, M. & Fisher, A. G. Epigenetic signatures of stem-cell identity. *Nat. Rev. Genet.* **8**, 263–271 (2007).
31. Lister, R. *et al.* Hotspots of aberrant epigenomic reprogramming in human induced pluripotent stem cells. *Nature* **471**, 68–73 (2011).
32. Ohi, Y. *et al.* Incomplete DNA methylation underlies a transcriptional memory of somatic cells in human iPS cells. *Nat. Cell Biol.* **13**, 541–9 (2011).
33. Doi, A. *et al.* Differential methylation of tissue- and cancer-specific CpG island shores distinguishes human induced pluripotent stem cells, embryonic stem cells and fibroblasts. *Nat. Genet.* **41**, 1350–1353 (2009).
34. Bar-Nur, O., Russ, H. A., Efrat, S. & Benvenisty, N. Epigenetic memory and preferential lineage-specific differentiation in induced pluripotent stem cells derived from human pancreatic islet beta cells. *Cell Stem Cell* **9**, 17–23 (2011).
35. Nazor, K. L. *et al.* Recurrent variations in DNA methylation in human pluripotent stem cells and their differentiated derivatives. *Cell Stem Cell* **10**, 620–634 (2012).
36. Mekhoubad, S. *et al.* Erosion of dosage compensation impacts human iPSC disease modeling. *Cell Stem Cell* **10**, 595–609 (2012).
37. Chamberlain, S. J. *et al.* Induced pluripotent stem cell models of the genomic imprinting disorders Angelman and Prader – Willi syndromes. (2010) *Proc Natl Acad Sci*, 12;107(41):17668–73 (2010).
38. Stanurova, J. *et al.* Angelman syndrome-derived neurons display late onset of paternal UBE3A silencing. *Sci. Rep.* **6**, 30792 (2016).
39. Burnett, L. C. *et al.* Induced pluripotent stem cells (iPSC) created from skin fibroblasts of patients with Prader-Willi syndrome (PWS) retain the molecular signature of PWS. *Stem Cell Res.* **17**, 526–530 (2016).
40. Pólvara-Brandão, D. *et al.* Loss of hierarchical imprinting regulation at the Prader-Willi/Angelman syndrome locus in human iPSCs. *Hum. Mol. Genet.* **00**, 1–13 (2018).
41. Burrows, C. K. *et al.* Genetic Variation, Not Cell Type of Origin, Underlies the Majority of Identifiable Regulatory Differences in iPSCs. *PLoS Genet.* **12**, 1–18 (2016).
42. Kyttilä, A. *et al.* Genetic Variability Overrides the Impact of Parental Cell Type and Determines iPSC Differentiation Potential. *Stem Cell Reports* **6**, 200–212 (2016).
43. Rouhani, F. *et al.* Genetic Background Drives Transcriptional Variation in Human Induced Pluripotent Stem Cells. *PLoS Genet.* **10**, (2014).
44. Vanhauwaert, R. *et al.* The SAC1 domain in synaptojanin is required for autophagosome maturation at presynaptic terminals. *EMBO J.* **36**, 1392–1411 (2017).

45. Yeh, E. *et al.* Patient-derived iPSCs show premature neural differentiation and neuron type-specific phenotypes relevant to neurodevelopment. *Mol. Psychiatry* 1–12 (2017).
46. Rooney, G. E. *et al.* Human iPS Cell-Derived Neurons Uncover the Impact of Increased Ras Signaling in Costello Syndrome. *J. Neurosci.* **36**, 142–152 (2016).
47. de Vrij, F. M. *et al.* Candidate CSPG4 mutations and induced pluripotent stem cell modeling implicate oligodendrocyte progenitor cell dysfunction in familial schizophrenia. *Mol. Psychiatry* 1–15 (2018).
48. Germain, P. L. & Testa, G. Taming Human Genetic Variability: Transcriptomic Meta-Analysis Guides the Experimental Design and Interpretation of iPSC-Based Disease Modeling. *Stem Cell Reports* **8**, 1784–1796 (2017).
49. Tsai, S. Q. & Joung, J. K. Defining and improving the genome-wide specificities of CRISPR–Cas9 nucleases. *Nat. Rev. Genet.* **17**, 300–312 (2016).
50. Hoekstra, S. D., Stringer, S., Heine, V. M. & Posthuma, D. Genetically-Informed Patient Selection for iPSC Studies of Complex Diseases May Aid in Reducing Cellular Heterogeneity. *Front. Cell. Neurosci.* **11**, 164 (2017).
51. Lupo, G., Harris, W. a & Lewis, K. E. Mechanisms of ventral patterning in the vertebrate nervous system. *Nat. Rev. Neurosci.* **7**, 103–114 (2006).
52. Temple, S. The development of neural stem cells. *Nature* **414**, 112–7 (2001).
53. Dhara, S. K. *et al.* Human neural progenitor cells derived from embryonic stem cells in feeder-free cultures. *Differentiation*. **76**, 454–64 (2008).
54. Manuilova, E. S., Gordeeva, O. F., Grivennikov, I. A. & Ozernikov, N. D. Embryonic stem cells: spontaneous and directed differentiation. *Izv. Akad. Nauk. Seriya Biol.* 704–10
55. Sathananthan, A. H. & Trounson, A. Human embryonic stem cells and their spontaneous differentiation. *Ital. J. Anat. Embryol.* **110**, 151–7 (2005).
56. Levenstein, M. E. *et al.* Basic Fibroblast Growth Factor Support of Human Embryonic Stem Cell Self-Renewal. *Stem Cells* **24**, 568–574 (2006).
57. Takahashi, K. & Yamanaka, S. Induction of pluripotent stem cells from mouse embryonic and adult fibroblast cultures by defined factors. *Cell* **126**, 663–76 (2006).
58. Otani, T. *et al.* 2D and 3D Stem Cell Models of Primate Cortical Development Identify Species-Specific Differences in Progenitor Behavior Contributing to Brain Size Article 2D and 3D Stem Cell Models of Primate Cortical Development Identify Species-Specific Differences in. *Stem Cell* **18**, 1–14 (2016).
59. Shi, Y., Kirwan, P., Smith, J., Robinson, H. P. C. & Livesey, F. J. Human cerebral cortex development from pluripotent stem cells to functional excitatory synapses. *Nat. Neurosci.* **15**, 477–486 (2012).
60. Gunhanlar, N. *et al.* A simplified protocol for differentiation of electrophysiologically mature neuronal networks from human induced pluripotent stem cells. *Mol. Psychiatry* 1–9 (2017). doi:10.1038/mp.2017.56
61. Volpato, V. *et al.* Reproducibility of Molecular Phenotypes after Long-Term Differentiation to Human iPSC-Derived Neurons: A Multi-Site Omics Study. *Stem Cell Reports* **11**, (2018).
62. Shi, Y., Kirwan, P., Smith, J., Robinson, H. P. C. & Livesey, F. J. Human cerebral cortex development from pluripotent stem cells to functional excitatory synapses. *Nat. Neurosci.* (2012). doi:10.1038/nn.3041
63. Pruszk, J., Sonntag, K.-C., Aung, M. H., Sanchez-Pernaute, R. & Isacson, O. Markers and methods for cell sorting of human embryonic stem cell-derived neural cell populations. *Stem Cells* **25**, 2257–68 (2007).
64. Yuan, S. H. *et al.* Cell-surface marker signatures for the Isolation of neural stem cells, glia and neurons derived from human pluripotent stem cells. *PLoS One* **6**, (2011).
65. Franz-josef, M., Kiel, I. P. & Kiel, C. Assessment of human pluripotent stem cells with PluriTest. 1–17 (2012). doi:10.3824/stembook.1.83.1

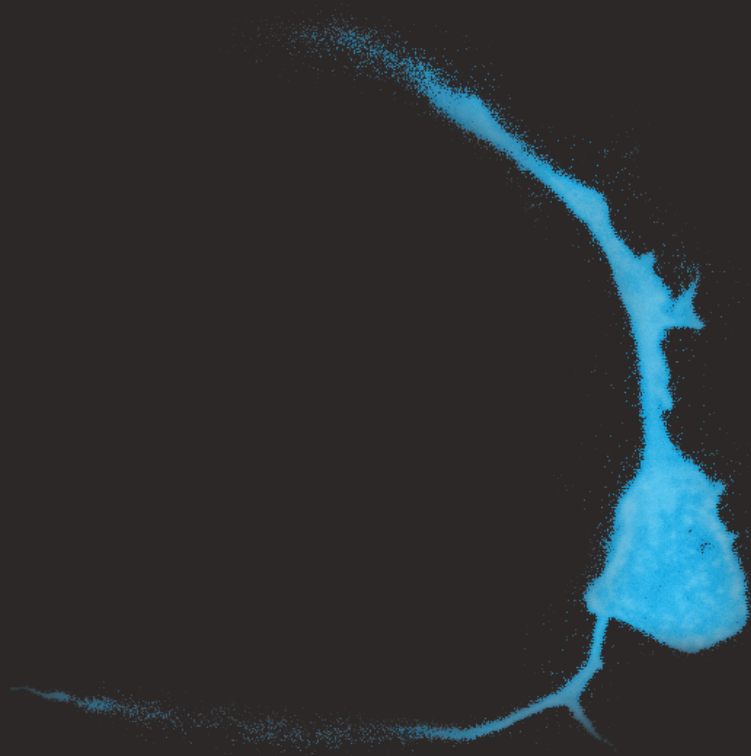
66. Muller, F. J. *et al.* A bioinformatic assay for pluripotency in human cells. *Nat Methods* **8**, 315–317 (2011).
67. Bardy, C. *et al.* Predicting the functional states of human iPSC-derived neurons with single-cell RNA-seq and electrophysiology. *Mol. Psychiatry* **21**, 1573–1588 (2016).
68. Silbereis, J. C., Pochareddy, S., Zhu, Y., Li, M. & Sestan, N. The Cellular and Molecular Landscapes of the Developing Human Central Nervous System. *Neuron* **89**, 248–268 (2016).







# Appendices





## SUMMARY

For decades the study of living human brain-derived cell types was challenging. With the advent of stem cell technology this changed. Neural cells could now be generated from somatic cell types. With this technology a new opportunity for studying human brain diseases emerged.

In chapter 1 I give a brief overview of the complexity and development of the human cerebral cortex. I introduce stem cell technology and pose the question to what extent stem cell technology can be used to model human brain disorders.

In chapter 2 we describe a protocol to generate functional neuronal networks using human iPS. We show that these networks exist of different types of neuronal cells: neurons and astrocytes. In addition we show that the neurons are electrophysiologically active and suitable for modeling living human neurons.

In chapter 3 we use this protocol to generate different types of neural cells. We study the transcriptional regulation of *BDNF* transcript VIII-IX. *BDNF* is a neurotrophic factor that is of essence for brain development and proper structure of individual cells and networks. We find that *BDNF* transcript VIII-IX is highly upregulated in neural precursor cells that are chemically activated. This is not the case in mouse neural precursor cells. We also identified several new human *BDNF* transcripts using pluripotent stem cell-derived neuronal cells.

In chapter 4 we use our protocol to study subcellular localization of human UBE3A protein isoforms. Patients with the Angelman Syndrome have a dysfunctional maternal copy of the *UBE3A* gene. Comparisons between the mouse and human isoforms show that UBE3A isoforms are differentially located in neurons. Dissimilar localization suggests that the few differences between the mouse and human *UBE3A* gene sequence might be the critical determinants of their distinct subcellular localization.

In chapter 5 we investigate the epigenetic effect of our reprogramming strategy on the *FMRI* gene. Absence of the product of this gene, the fragile X mental retardation protein (FMRP), causes the intellectual disability disorder fragile X. In the majority of the patients an expanded CGG repeat in the promoter region of this gene causes, by methylation, transcriptional silencing which leads to disease. This process takes place in early human embryonic development. We identified a healthy individual with a full mutation of the *FMRI* gene without concomitant methylation. We find that in cell lines of this individual the *FMRI* promoter becomes methylated during reprogramming and stays methylated after differentiation into neuronal progenitors.

In chapter 6 we identify a genetic variant associated with Alzheimer's disease (AD). This variant is annotated to the promoter region of the non-coding RNA miR-142. In iPS-derived neuronal progenitors we find that miR-142 regulates *PICALM*, a well-validated gene linked to AD.

In chapter 7, I discuss the limitations of iPS technology that influence its capacity to model human brain diseases. I also discuss potential solutions.

## SAMENVATTING

Decennia lang was het bestuderen van levende humane hersencellen een uitdaging. Met de komst van de induceerbare stamcel technologie veranderde dit. Hersencellen konden vanaf nu gegenereerd worden van somatische cellen. Deze technologie creëerde daarom een nieuwe mogelijkheid om humane hersenaandoeningen te bestuderen.

In hoofdstuk 1 geef ik een kort overzicht van de complexiteit en de ontwikkeling van de humane cerebrale cortex. Ik introduceer stamcel technologie en stel de vraag in hoeverre stamcel technologie gebruikt kan worden om humane hersenaandoeningen te modeleren.

In hoofdstuk 2 beschrijven we een protocol om functionele neuronale netwerken te genereren van humane geïnduceerde stamcellen. We laten zien dat deze netwerken uit verschillende neuronale cellen bestaan: neuronen en astrocyten. Deze neuronen zijn ook electrofysiologisch actief en presenteren zich als een goed model voor levende humane neuronen.

In hoofdstuk 3 gebruiken we dit protocol om verschillende neurale cellen te genereren. We bestuderen de transcriptionele regulatie van het *BDNF* transcript VIII-IX. BDNF is een neurotrofine dat van belang is voor hersenontwikkeling en opbouw van individuele cellen en netwerken. We vinden dat *BDNF* transcript VIII-IX sterk opgeregeerd wordt in neuronale voorloper cellen die chemisch geactiveerd zijn. Dit fenomeen vindt niet plaats in neuronale voorloper cellen in muizen. We identificeren ook enkele nieuwe humane *BDNF* transcripten door gebruik te maken van neuronale cellen die zijn afgeleid van stamcellen.

In hoofdstuk 4 gebruiken we ons protocol om de subcellulaire lokalisatie van het humane UBE3A eiwit te bestuderen. Patiënten met het Angelman Syndroom (AS) hebben een disfunctioneel maternaal *UBE3A* gen. Vergelijkingen tussen de isovormen van de muis en de mens van het *UBE3A* eiwit laten zien dat er verschillen in lokalisatie zijn. Het verschil in lokalisatie suggereert dat de enkele verschillen tussen de DNA-sequentie van de mens en de muis wellicht verantwoordelijk kunnen zijn voor de verschillende sublokalisaties.

In hoofdstuk 5 bestuderen we het epigenetische effect van onze reprogrammeringsstrategie op het *FMR1* gen. In afwezigheid van het product van dit gen, het fragile X mentale retardatie eiwit (FMRP), ontstaat de verstandelijke beperking fragile X Syndrome. Bij het merendeel van de patiënten zorgt een herhaling van het CGG patroon in de promoter regio van het gen door methylering transcriptionele blokkade van *FMR1* wat tot ziekte leidt. Dit proces vindt plaats in de vroege embryonale ontwikkeling. We identificeerden een gezond individu met een volledige mutatie van het *FMR1* gen zonder bijgaande methylering. We ondervonden dat door het reprogrammeren de promoter van het *FMR1* gen werd gemethyleerd in cellijnen van dit individu en dat deze gemethyleerd bleef in neuronale voorloper cellen.

In hoofdstuk 6 identificeren we een genetische variant die verband houdt met de ziekte van Alzheimer. Deze variant bevindt zich in de promoter regio van het niet-coderende RNA miR-142. In neuronale voorloper cellen die zijn afgeleid van geïnduceerde stamcellen vinden

we dat miR-142 het gen *PICALM* reguleert. Dit gen werd al eerder in verband gebracht met de ziekte van Alzheimer.

In hoofdstuk 7 bespreek ik de limitaties van induceerbare stamcel technologie en hoe dit de capaciteit om hersenaandoeningen te modeleren beïnvloedt. Ook bespreek ik enkele potentiële oplossingen.

## PHD PORTOFOLIO

Name: Shashini Munshi

PhD period: Nov 2012 - May 2018

Department of Psychiatry, Erasmus MC

Promotor: Prof. dr. S.A. Kushner

Co-promoter: Dr. F.M.S. de Vrij

Research school: Graduate school Neuroscience Amsterdam Rotterdam (ONWAR)

### PhD training

#### *Courses*

Workshop Life Science with Industry, Lorentz Center, Leiden	2014
Grant Writing, ONWAR	2015
Teach the Teacher I, Erasmus MC	2015
Research integrity in Science, Erasmus MC	2015
Workshop Famelab	2015
Masterclass Woman in medicine, ECWO	2015
ACE Venture lab Explore program on entrepreneurship	2015

#### **Presentations and conferences**

Dutch Society for Stem Cell Research (DSSCR) annual meeting	2013
Annual PhD meeting ONWAR (poster presentation)	2013
Annual PhD meeting ONWAR (blitz presentation)	2014
European Neuroscience Conference by Doctoral Students (ENCODS)	2015
Dutch Society for Stem Cell Research (DSSCR) annual meeting	2015
Annual PhD meeting ONWAR (presentation)	2016
Dutch Neuroscience meeting 2016 (presentation and co-chair session)	2016
Annual PhD meeting ONWAR (poster presentation)	2016
SFN annual meeting (poster presentation)	2016

### Teaching

Teaching assistant Journal Club Nanobiology	2013
Guiding minor students psychiatry	2015

#### *Supervising master students*

Ane Ayo Martin	2013/2016
Roberto Ballarino	2015/2017
Sakshi Badal	2016/2018

### Outreach

Brain Awareness week 2017, open day at the lab	2017
Scientist Wanted, online platform	2018
Science Battle, theatre show	2018
Studio Erasmus talkshow	2018

## CURRICULUM VITAE

Shashini Thischa Munshi was born on December 13 1988 in Schiedam. She graduated from Erasmiaans Gymnasium (Rotterdam) in 2007, after which she started her bachelor program Life Science & Technology (TU Delft, Leiden University). In 2012 she came to the Erasmus MC to do her master thesis research on Angelman Syndrome under supervision of Prof. Dr. Ype Elgersma as part of her research master Neurosciences (VU University). In 2012 she joined the lab of Prof. Dr. Steven Kushner to work on stem cell-derived models for human brain diseases.



## LIST OF PUBLICATIONS

**Munshi ST**, Martin AA, Bouwkamp C, van Woerden G, Lendemeijer B, Gunhanlar N, Kievit AJA, Elgersma Y, Bonifati V, de Vrij FMS, Kushner SA. Identification of novel activity-dependent human BDNF transcripts. (*Manuscript in preparation*)

Avagliano Trezza R, Sonzogni M, Bossuyt SNV, Zampeta FI, Punt AM, van den Berg M, Rotaru DC, Koene LMC, **Munshi ST**, Stedehouder J, Kros JM, Williams M, Heussler H, de Vrij FMS, Mientjes EJ, van Woerden GM, Kushner SA, Distel B, Elgersma Y (2019). Loss of nuclear UBE3A causes electrophysiological and behavioral deficits in mice and is associated with Angelman syndrome. *Nature Neuroscience*. 22(8):1235-1247

Ghanbari M, **Munshi ST**, Ma B, Lendemeijer B, Bansal S, Adams HH, Wang W, Goth K, Slump DE, van den Hout MCGN, van IJcken WFJ, Bellusci S, Pan Q, Erkeland SJ, de Vrij FMS, Kushner SA, Arfan Ikram M. A functional variant in the miR-142 promoter modulating its expression and conferring risk of Alzheimer's disease *Human Mutation*. 2019 Jul (*in press*)

Gunhanlar N, Shpak G, van der Kroeg M, Gouty-Colomer LA, **Munshi ST**, Lendemeijer B, Ghazvini M, Dupont C, Hoogendijk WJG, Gribnau J, de Vrij FMS, Kushner SA (2017). A simplified protocol for differentiation of electrophysiologically mature neuronal networks from human induced pluripotent stem cells. *Molecular Psychiatry*. 23(5):1336-1344.

de Esch CEF, Ghazvini M, Schelling-Kazaryan N, Widagdo W, **Munshi ST**, van der Wal E, Douben H, Gunhanlar N, Kushner SA, Pijnappel WWMP, de Vrij FMS, Geijsen N, Gribnau J, Willemsen R (2014). Epigenetic characterization of the *FMRI* promoter after reprogramming of a human fibroblast line carrying an unmethylated full mutation into pluripotent stem cells. *Stem Cell Reports*. 3(4):548-555.

### Not in this thesis:

Vanhouwaert R, Kuenen S, Masius R, Bademosi A, Manetsberger J, Schoovaerts N, Bounti L, Gontcharenko S, Swerts J, Vilain S, Picillo M, Barone P, **Munshi ST**, de Vrij FMS, Kushner SA, Gounko NV, Mandemakers W, Bonifati V, Meunier FA, Soukup SF, Verstreken P (2017). The SAC1 domain in synaptojanin is required for autophagosome maturation at presynaptic terminals. *The EMBO journal*. 36(10):1392-1411.

Higuera GA, Iaffaldano G, Bedar M, Shpak G, Broersen R, **Munshi ST**, Dupont C, Gribnau J, de Vrij FMS, Kushner SA, De Zeeuw CI (2017). An expandable embryonic stem cell-derived Purkinje neuron progenitor population that exhibits in vivo maturation in the adult mouse cerebellum. *Scientific Reports*. 7(1):1-19.

## ACKNOWLEDGEMENTS

When I started my PhD I was 24 years young. I had even more to explore than now, and was standing in the world rather ignorant (some may claim this hasn't changed much). Truth is that I spend over half of my twenties in the lab with wonderful people who have contributed significantly to who I am now, what I stand for, and what I believe in, intellectually but definitely personally. My thanks go out to all of you who have been part of this outstanding journey and my wish is that our paths keep crossing until far into the future.

Several of you I would like to acknowledge in particular. Thank you to the committee for critically reading my thesis and your valuable feedback.

Then, to my promoter Steven Kushner: thank you so much for offering me a spot in your lab. The amount of knowledge I gained in the 6 years in the lab is priceless. I was able to develop myself scientifically, work with pioneering techniques, and benefit from your breadth of knowledge on neuroscience. I thank you in particular for always treating me with respect, and giving me the space to develop my further professional career. It means a lot to me.

To Femke de Vrij, my co-promoter, but moreover the person who was always there to help me whenever I needed it. Thank you for your supervision. Your support was of utmost importance in successfully executing my experiments. I truly appreciate how you always skillfully, consciously or unconsciously, kept all of us connected as a group. It definitely made us a more effective team.

To Ype Elgersma and Edwin Mientjes: thank you for introducing me into the Erasmus MC. An extra thanks for your patience with the Shashini 'student-version' and her exceptional skill to handle animals. I express to you my gratitude for readying me for my PhD. Thanks for believing in me and the fruitful collaborations we have had in the last years.

Next to my scientific development I have to thank Ane Ayo Martin, Roberto Ballerino, and Sakshi Bansal for being my guinea-pigs for developing my planning, organization and communication skills. Thanks for being critical and patient and for the dedication you have shown to the work we did.

We did not have an office, we had a club. Thank you to my colleagues Bas, Christian, Denise, Mark, Nilhan and Jurate, who are better labeled as friends. Thank you for the Doppio coffees, the lunches, the dinners. I am proud that our repertoire of activities has extended to non-office hours. And a special thanks to Christian and Denise for accepting the paranimf position.

Specific attention goes to Priyanka Rao. I with certainty can say I have never appreciated anyone so much who has annoyed me as much as you have. Thank you for being painfully honest, speaking up when I wish you wouldn't and asking nothing in return. You are special to me.

To Bart, Tim and Linda, thank you for your friendships. This journey would have been so much more difficult and less fun without you.

Last but not least, I thank my family. Thank you for supporting my education, your understanding for unusual working hours and listening to my positive and less positive stories of

lab-life. This was a milestone I wanted to reach, and without a doubt I couldn't have done it without you. I love you all.

